Development of squeezing techniques for quantum noise reduction in gravitational-wave detectors

Catherine Nguyen

Université de Paris

École doctorale des Sciences de la Terre et de l'Environnement et Physique de l'Univers - ED560

Laboratoire AstroParticule et Cosmologie (APC) - Groupe Gravitation

Development of squeezing techniques for quantum noise reduction in gravitational-wave detectors

Par Catherine Nguyen

Thèse de doctorat de Physique de l'Univers

Dirigée par Matteo Barsuglia

présentée et soutenue publiquement le 5 octobre 2021
Avec un jury composé de :

Sara Ducci	Professeure à l'Université de Paris	Présidente
Giancarlo Cella	Chercheur INFN Pisa	Rapporteur
Myriam Zerrad	Ingénieure de recherche CNRS	Rapportrice
Martina De Laurentis	Maîtresse de conférence à l'Université de Naples Federico II	Examinatrice
Jean-Christophe Hamilton	Directeur de recherche CNRS	Examinateur
Edwige Tournefier	Directrice de recherche CNRS	Examinatrice
Matteo Barsuglia	Directeur de recherche CNRS	Directeur de thèse
Fiodor Sorrentino	Chercheur INFN Genova	Co-encadrant

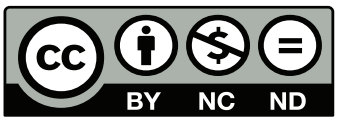

À mon père bien-aimé, Nguyên François ngọc Tú,
À ma mère chérie, Vũ Sabine thị Khiêm,

Remerciements

Autant sur le plan scientifique que personnel, ces trois années de recherche ont été très riches pour moi. Cette expérience n'aurait jamais pu être aussi passionnante, enrichissante et gratifiante si je n'avais pas été si bien entourée et je voudrais ainsi remercier toutes ces personnes qui ont contribué à cette merveilleuse aventure qu'est la thèse. Les remerciements, étant les premières pages lues dans une thèse mais étant les dernières pages que j'aurai écrites et, épuisée par la fin de thèse, je risque d'oublier certaines personnes. Je remercie ainsi par avance toutes les personnes que j'aurais pu oublier et qui ont contribué, de près ou de loin, à cette merveilleuse aventure.

À Yannick Giraud-Héraud, pour m'avoir proposé de participer au projet ExploraScience, de m'avoir ainsi aidée à créer ce lien avec mes origines et pour les discussions passionnantes que nous avions eu sur le Vietnam.

To Giancarlo Cella and Myriam Zerrad for accepting to be my referees, for carefully read my manuscript and for your very helpful comments.
À Sara Ducci, Jean-Christophe Hamilton, Edwige Tournefier d'avoir accepté d'être membres de mon jury de thèse, de m'avoir témoigné de leur intérêt sur mon sujet et pour leurs questions très intéressantes.

À Matteo Barsuglia, de m'avoir si bien accompagnée, épaulée et supportée dans cette aventure scientifique passionnante. Grâce à toutes les discussions que nous avons pu avoir, toutes les idées, les questionnements, j'ai appris comment améliorer mon travail et ma réflexion scientifique. Il a toujours cherché les meilleures solutions dans mon intérêt et a toujours fait preuve d'une très grande compréhension et pour cela, je lui en suis très reconnaissante.

To Fiodor Sorrentino for guiding me, for teaching me how to be a squeezing experimentalist and for being so patient when I misalign some parts of the bench badly, you gave me the confidence to learn without being fearful. I learnt a lot through all our discussions about the bench. To Martina De Laurentis who showed me how to be a determined experimentalist, taught me to always think by myself, helped me to better understand squeezing theory and appreciate it. I also enjoyed all the dinners we had after spending so many hours in the bench,

with you and the squeezing team, and appreciated this warm atmosphere that we had all together.

To the EPR squeezing team, in particular, to Mateusz, Imran, Sibilla, Laura, Beatrice, with whom working on the bench was so exciting, fun, stimulating and with whom I shared so many beautiful moments. To Valeria, for all your support and care, for always helping me during this past three years, always trying to find the best solution for me and for all the things you taught me in squeezing in general: it was very clear and you made me understand many things. Grazij mia cara Valeria p l'amicizia toi, pe tutt chell cà me imparat, pe sti belli mument c'amma passat aret e banc e pe tutt e risat che c'amm fatt (e tutt l'insulte c'amm imparat nziem!). Si comme na grand sor adottive pe me, me semp affiancat, sostenut e te semp fidant do lavor mij!

To all the Virgo members and all the people that always gave me a very warm welcome when I was in Pisa, and special thanks to Maurizio, for his kindness towards me.

À Eric, qui a toujours été présent pour moi depuis le tout début de ma carrière professionnelle (depuis l'entretien d'embauche, au vendredi soir en salle blanche avant le confinement et jusqu'aux dernières répétitions), qui m'a toujours poussée à me mettre en avant, m'a appris tellement de choses (à souder aussi !) et me supporte depuis presque 5 ans en co-bureau (et a donc laissé tomber d'avoir du calme dans son bureau). À Christelle, ma première cheffe, avec qui je pouvais discuter de tout, qui a toujours été d'une grande compréhension, qui est une grande source de motivation, avec qui cela a toujours été très stimulant et intéressant de travailler entre opticiennes. Elle m'a toujours aidée pour ma carrière et toujours mis mes intérêts en premier. À Eleonora, qui m'a toujours aidée, même quand elle n'était pas encore arrivée au laboratoire, a toujours trouvé le temps de me motiver quand elle sentait que je n'étais pas en forme, de m'avoir toujours écoutée en cas de besoin, grâce à qui, je me suis améliorée dans mon travail par ses explications et pour sa bonne humeur contagieuse.

À tous mes autres collègues de l'APC dont Matthieu, Miles, Damien, Ion, Olga, Alin, Stéphane, Claude, Alain, Fabrice, Aymeric avec qui j'ai passé de supers moments, à Pierre, pour m'avoir toujours aidée pour l'électronique, à Jean-Pierre, sans qui ma cavité étalon n'aurait pas été si belle, aux doctorants de l'APC, aux personnels de l'administration et en particulier, à Béatrice, Vincent et Cindy, qui ont toujours été très sympathiques, même quand je les embêtais chaque semaine.

Aux membres du NaNoWrimo PhD Discord et en particulier à Manon, à

Mélanie, à Charlotte, à Pauline, qui ont été une grande source de motivation, au début pour la rédaction et finalement pour tous les aspects de ma vie en général, pour tous les encouragements quotidiens, tous ces bons moments passés à fêter la fin du mois, pour leur amitié tout simplement.

Au PhD Discord, cette super communauté de doctorant.e.s avec qui nous pouvons discuter de tout avec bienveillance, grâce à qui, on se sent moins seul.e, à Eva et Mathilde pour avoir créé et soudé cette communauté, à tous les modérateurs qui rendent cela possible. Aux membres du *rush-final* et en particulier, à Muriel, Marine, Clémentine, Camille, Isabelle, Barnabé, Marie, Julien, Charlotte, Inès, Malina, Claudia, Pauline, Olivia, Hélène, à leur immense support quotidien depuis la rédaction de thèse, pour leur oreille attentive, pour avoir toujours été là pour me remonter le moral et pour toutes les paroles d'amour que l'on s'envoie quotidiennement. Sans ces merveilleuses personnes, mes derniers mois de thèse auraient été beaucoup plus difficiles. Une spéciale dédicace au Night Squad avec qui j'ai passé mes meilleures soirées à travailler dans une ambiance festive.

À ma mère, pour son amour inconditionnel, pour m'avoir toujours offert toutes les meilleures choses dans la vie, pour son soutien quotidien, de me gâter et de s'occuper de moi jusqu'à maintenant, pour tous les bons petits plats qui sont un facteur important dans le bon déroulement de ma thèse, d'être toujours présente dans ma vie tout simplement. À mon père, pour son amour inconditionnel, pour avoir dédié sa vie pour que la mienne soit meilleure, pour s'être battu jusqu'au bout pour moi, je t'aime fort papa et tu me manques chaque jour qui passe. À mon petit frère Pascal, pour m'avoir supporté ces 23 dernières années, de m'avoir toujours encouragée, pour son admiration qui me motive tous les jours, je suis fière d'être ta grande sœur (mais arrête de me recopier s'il te plaît !). À mes grands-parents paternels, pour leur amour. À mes tantes Tata et Út, de m'avoir gâtée de bons petits plats à chaque fois que je redescendais sur Marseille, à mon oncle Chú Truoc, à ma grande soeur Giang, pour leur amour et soutien. À mes nièces Chantal et Caroline, à mes cousines Lina et Jenny, pour leur soutien quotidien, pour les après-midis bubble tea, tteokkbokki (et autres bons petits plats), cela m'a reboostée après des moments difficiles. À mes cousins, mon neveu et à toute ma famille au Vietnam, pour leur soutien malgré la distance et pour m'avoir témoigné tant de fierté.

À tous mes amis, à Solange, Sébastien, à Fabienne, pour les encouragements quotidiens, pour m'écouter râler tous les jours, pour leur support durant les moments les plus difficiles, à Alice et Maria, pour leur amitié toutes ces années, pour le soutien moral à toute épreuve, pour la joie qu'elles me procurent à chaque fois que l'on se voit. À ma bretonne préférée Hélène, pour sa positivité, sa bonne humeur communicative, pour les supers moments passés. À mon

parrain Guillaume, pour son soutien, pour son humour et son aide en optique. À mes copines de Supoptique, Joséphine, Claire, Lina, qui m'ont montré en avance la vie de thésarde, pour leurs encouragements. À mes amis du club d'arts martiaux Lam Son Vo Dao, et particulièrement à maître Alain, à Antigoni, à Rivo, grâce à qui j'ai pris confiance en moi. Au Scooby Gang, à ma belle-famille, pour leur attention, leur accueil, qui comblent le fait d'être loin de ma famille.

A mon compagnon Liêm, pour sa patience infinie, pour avoir si bien pris soin de moi depuis le début, de s'être occupé de tout pour moi quand je n'avais plus l'énergie pour le faire (notamment préparer tous les repas durant toute la fin de thèse et pas que), pour son soutien inconditionnel et ses encouragements à toute épreuve.

Acronyms

A | B | C | E | F | G | H | I | L | M | O | P | Q | R | S | T

A

AdV Advanced Virgo. xxviii, 14, 19–22, 25, 27, 29, 74, 75, 79
AdV+ Advanced Virgo+. 136, 159
aLIGO Advanced LIGO. 19, 21, 22, 27, 29, 74
AOM acousto-optic modulator. 139, 142, 144, 145, 147, 148, 150, 152, 154

B

BAB Bright Alignment Beam. xxiv, xxix, 97–101, 104, 107, 111–113, 115, 116, 118–121, 137–140, 142, 148–153, 155, 156, 158
BBH Binary Black Holes. 23, 26, 28
BNS Binary Neutron Stars. 20, 23, 25, 30
BS beam-splitter. 12, 55, 56, 59, 62, 66, 71, 87, 92, 99, 103, 105, 111, 115, 120, 146, 149, 150, 153

C

CCB Coherent Control Beam. xxiv, xxix, 98, 99, 101, 102, 108, 115, 119, 120, 138, 152, 158
CMRR Common-Mode Rejection Ratio. 107, 148

E

EOM electro-optic modulator. 98, 151
EPR Einstein-Podolsky-Rosen. xxix, 67, 80, 81, 83, 86, 87, 90, 91, 93, 133, 134, 136, 139, 140, 148, 152, 177
ET Einstein Telescope. 29

F

FDS Frequency-Dependent Squeezing. xxix, 67, 74, 77, 78, 80, 88, 90, 92, 136

FIS Frequency-Independent Squeezing. xxix, 66, 67, 69, 70, 97, 134, 138, 139, 144, 147–149, 151, 152, 154
FSM Finite-State Machines. 107
FSR Free Spectral Range. 103–105, 134, 136, 161, 162, 173
FWHM full-width at half maximum. 103–105

G

gMC green Mode-Cleaner. 135, 147, 152
GR General Relativity. 9, 23, 26, 28
GW Gravitational-Wave. xxviii, 8, 10–13, 20–23, 25, 27–32, 51, 52, 58–60, 62, 63, 66, 68, 69, 71, 74, 76, 78, 83, 87, 88, 93–95, 122, 127, 131, 134–136, 159, 193, 194, 196

H

HD Homodyne Detector. 99, 102, 107, 109–112, 115
HR high reflectivity. 102
HWHM half-width-half-maximum. 73
HWP half-wave plate. 110, 119, 151

I

ITF interferometer. xxviii, xxxii, xxxiii, 12, 13, 18, 21, 29, 58, 60, 62, 63, 66, 68, 71, 72, 81, 83–85, 90–92, 94, 135, 156, 159

L

LCB Length Control Beam. 97–100, 104, 108, 118, 121, 123, 137, 139, 140, 142, 144, 149, 153, 158
LO Local Oscillator. xxiv, 88, 97, 101, 102, 106, 111, 113, 114, 117, 118, 137–140, 147–149, 179

M

MC mode cleaner. 92, 144, 147, 149, 154
MCG Mode-Cleaner Green. 105, 106, 119, 126, 135, 142–145, 157
MCIR Mode-Cleaner InfraRed. 98, 106, 109, 111, 126, 148, 149
MZ Mach-Zehnder. 105, 122, 126, 135, 144, 147, 152

O

OMC Output Mode Cleaner. 81, 85, 88, 90
OPA Optical Parametric Amplification. 50, 52, 53, 81
OPLL Optical Phase-Locked Loop. 144

OPO Optical Parametric Oscillation. 52–54, 80–82, 88, 90, 96–99, 102, 103, 105, 107, 113, 114, 117, 118, 126, 134, 135, 137–139, 144, 147, 148, 150, 152, 156–158

P

PBS polarizing beam splitter. 119, 120, 148, 150, 151, 158, 175
PD photodiode. 98, 107, 109, 111, 114
PDH Pound-Drever Hall. 99, 103, 126
PID Proportional Integrative Derivative. 105, 122, 125
PLL Phase-Locked-Loop. 145, 149, 152, 153
PRM Power Recycling Mirror. 12
PSD Power Spectral Density. 18
PZT piezoelectric. 102

Q

QN Quantum Noise. 18, 66
QWP quarter-wave plate. 148, 175, 176

R

RoC radius of curvature. 106
RPN Radiation Pressure Noise. 18, 66, 68–70, 72, 74, 85, 133, 136, 159
RTL Round-Trip Losses. 116

S

SHG Second-Harmonic Generation. 49, 96–98, 102, 103, 126, 140, 142–145, 147, 148, 152, 157
SIPS Suspended Interferometer for Pondemorotive Squeezing. 136, 146, 156
SN Shot Noise. 18, 19, 66, 68–70, 113
SQL Standard Quantum Limit. 63, 65, 69, 72, 82
SRC Signal Recycling Cavity. 87, 89–91
SRM Signal Recycling Mirror. 12, 90, 92

T

TEC thermoelectric cooler. 173
TM test mass. 10, 91

Development of squeezing techniques for quantum noise reduction in gravitational-wave detectors

Abstract

Quantum noise is one of the main limitations for interferometric gravitational-wave (GW) detectors as Virgo and LIGO. Reducing quantum noise has a direct impact on the science reach of future GW detectors (Advanced Virgo+, Advanced LIGO+, Einstein Telescope, Cosmic Explorer). Quantum noise originates from the quantum nature of light, from the vacuum fluctuations entering by the interferometer detection stage. The so-called *quantum shot noise* is present at frequencies higher than 100 Hz. The other quantum noise component, the so-called *quantum radiation pressure noise*, manifests itself at lower frequencies. The shot noise arises from the uncertainty on the measured phase of the laser field, while the latter arises from the uncertainty on the amplitude. The current injection of vacuum squeezed states (frequency-independent squeezing) into Virgo and LIGO leads to the quantum noise reduction in the spectral detection region corresponding to one of the two components of quantum noise. Heisenberg uncertainty relation imposes that shot noise reduction results in an increased radiation pressure noise. Squeezed states of light can be depicted with an ellipse, in a phase-amplitude space, with unbalanced uncertainties for the phase and the amplitude.
During the data taking period called O3, only moderate squeezing levels were injected to avoid the degradation of the Virgo and LIGO interferometers' sensitivities. To achieve a broadband reduction of quantum noise, it is necessary to inject a frequency-dependent squeezing inside the interferometer, i.e., to inject vacuum squeezed states in a frequency-dependent way, which will have a smaller uncertainty accordingly to the concerned quantum noise component. For the next upgrade of the current detectors Advanced Virgo and Advanced LIGO called Advanced Virgo+ and Advanced LIGO+, frequency-dependent squeezing is obtained by adding a suspended 300-meter filter cavity, with very high finesse. My thesis engages in the development of squeezing techniques for quantum noise reduction in future GW detectors.
Firstly, I contributed to an experimental work based on the automation and the improvement of a frequency-independent squeezed vacuum source located on the Virgo site, at Pisa. This was a preparatory work for the conception of a table-top experiment to study a frequency-dependent squeezing technique different from the one proposed previously and based on Einstein-Podolsky-Rosen entanglement. Based on the theory, brought forward in 2017, this technique offers significant advantages for future GW detectors, due to the absence of an external cost-intensive filter cavity. In this framework, I participated in the realization of a complete optical design for this experimental demonstrator, that can be implemented into the detector Virgo. I designed, realized, and tested a monolithic Fabry-Perot cavity (a solid etalon), at the optical laboratory of APC, necessary for the separation and detection of two entangled beams. More precisely, this cavity was optically characterized and its thermal stabilization was evaluated, which allowed to check its performances.

Keywords: gravitational-wave detector, frequency-dependent squeezing, quantum entanglement, Advanced Virgo, Fabry-Perot cavity, optical resonator, optics, astrophysics

Résumé

Le bruit quantique est une des limitations principales des détecteurs interférométriques d'ondes gravitationnelles, comme Virgo et LIGO. Réduire le bruit quantique a un impact direct sur la portée scientifique des futurs détecteurs d'ondes gravitationnelles (Advanced Virgo +, Advanced LIGO+, Einstein Telescope, Cosmic Explorer). L'origine du bruit quantique réside dans la nature quantique de la lumière, dans les fluctuations du vide qui entrent par la sortie de l'interféromètre. Actuellement, l'injection d'états de vide comprimé (squeezing indépendant de la fréquence) dans Virgo et LIGO permet de réduire le bruit quantique dans la bande spectrale de détection correspondante à une des deux composantes de ce bruit, le bruit de photons, ou shot noise, pour des fréquences supérieures à environ 100 Hz. La pression de radiation, l'autre composante, se manifeste quant à elle à de plus basses fréquences. Le shot noise émane de l'incertitude sur la phase mesurée du laser tandis que la pression de radiation, de l'incertitude sur l'amplitude. Le principe d'incertitude d'Heisenberg impose que la réduction du shot noise grâce à l'injection d'états du vide comprimé sur la phase, se traduise nécessairement par une augmentation de la pression de radiation. Cet état comprimé peut être représenté par une ellipse dans l'espace phase-amplitude, où les incertitudes sur la phase et l'amplitude sont inégales. Durant la prise de données O3, on a injecté des niveaux des squeezing modérés pour ne pas dégrader la sensibilité des interféromètres Virgo et LIGO. Afin de réduire le bruit quantique sur toute la bande spectrale de détection (et donc aussi à basse fréquence), il est nécessaire d'introduire dans l'interféromètre un squeezing dépendant de la fréquence, c'est-à-dire un état du vide comprimé, tantôt sur l'amplitude et tantôt sur la phase, permettant de réduire à la fois la pression de radiation et le shot noise. Pour Advanced Virgo+ et Advanced LIGO+ (les projets d'améliorations en cours pour les détecteurs actuels), l'ajout d'une cavité de filtrage quantique suspendue de 300 mètres et avec une très grande finesse, permettra de réaliser ce squeezing dépendant de la fréquence. Ma thèse porte sur le développement de techniques de squeezing pour la réduction du bruit quantique dans les futurs détecteurs d'ondes gravitationnelles. J'ai d'abord contribué à un travail expérimental sur l'automatisation et l'amélioration d'une source de squeezing indépendant de la fréquence, situé sur le site de Virgo, à Pise. Ce travail préparatoire a été réalisé pour la conception d'un banc de démonstration pour l'étude d'une technique de squeezing dépendant de la fréquence, alternative à celle proposée ci-dessus et basée sur l'intrication quantique (de type Einstein-Podolsky-Rosen). Les fondements théoriques de ce squeezing EPR ayant été proposés en 2017, cette technique présente des avantages pour les futurs détecteurs d'ondes gravitationnelles, notamment liés à l'absence de cavité de filtrage. Dans ce cadre, j'ai participé au design optique complet de cette expérience, qui pourra être implémentée sur le détecteur Virgo. J'ai conçu, réalisé et testé dans le laboratoire optique de l'APC, une cavité Fabry-Perot monolithique (de type étalon) nécessaire pour la séparation et la détection de deux faisceaux intriqués. Plus précisément, j'ai effectué des mesures de caractérisation optique et sur la stabilisation thermique de cette cavité, permettant de conclure sur les performances de cet étalon.

Mots clés : détecteur d'ondes gravitationnelles, squeezing, intrication quantique, Advanced Virgo, cavité Fabry-Perot, résonateur optique, optique, astrophysique

Résumé de la thèse

L'existence des ondes gravitationnelles a été prédite il y a plus de 100 ans de cela par Einstein et sa théorie de la relativité générale, en 1916. Dans celle-ci, la gravitation n'est plus une force d'attraction comme l'avait démontré Newton environ 230 ans auparavant mais elle devient une propriété de l'espace-temps : les objets massifs le déforment, l'étirent, le courbent. Cette relation entre l'espace-temps et les masses sont décrites par les équations de champ d'Einstein et peuvent être résumées par une citation célèbre de John Archibald Wheeler « L'espace-temps dit à la matière comment se déplacer ; la matière dit à l'espace-temps comment se courber. » De cette théorie découle la prédiction de l'existence des ondes gravitationnelles, qui sont des déformations de l'espace-temps émises par l'accélération d'objets massifs. Ces ondes se propageraient à la vitesse de la lumière dans le vide. Néanmoins, leur existence a longtemps été débattue et même Einstein n'était pas convaincu qu'il serait possible un jour de détecter de telles ondes.

Ce n'est que vers la fin des années 80 qu'émergent les projets de construction des détecteurs d'ondes gravitationnelles aux Etats-Unis (projet *LIGO*) et en Europe, issu d'une collaboration franco-italienne (projet *Virgo*). L'amplitude des déformations induites par les ondes gravitationnelles étant très faible, seuls des évènements cosmiques assez violents, par exemple la fusion d'une binaire de trous noirs, peuvent être détectés. Il nous faudra attendre encore plus d'une trentaine d'années pour assister à la toute première détection directe d'une onde gravitationnelle provenant de la fusion de deux trous noirs par les deux détecteurs de la collaboration de LIGO, en septembre 2015. Cette découverte marque le début de l'ère de l'astronomie gravitationnelle, en ouvrant une nouvelle fenêtre sur l'Univers. En effet, les ondes gravitationnelles constituent un nouveau type de messager pour l'astrophysique, renfermant des informations importantes sur leur source et un nouvel outil pour faire des tests de physique fondamentale. Le 17 août 2017 est une autre date historique, marquant le début de l'astronomie « multi-messagère ». En effet, le signal provenant de la détection d'une onde gravitationnelle, provoquée par la fusion de deux étoiles à neutrons (*GW170817*) est détecté par le réseau de détecteurs LIGO-Virgo, de manière

quasi-instantanée avec celle d'un sursaut gamma détecté par les satellites *Fermi* et *Integral*. L'hypothèse, qui consiste à attribuer à certains sursauts gamma une origine liée à la fusion d'étoiles à neutrons, a pu ainsi être confirmée. De plus, la précision de la localisation de la source de ce signal d'onde gravitationnelle, jamais égalée jusqu'alors, a permis à environ 70 observatoires terrestres de détecter une « kilonova », un transitoire optique, et ensuite d'étudier la source sur tout le spectre électromagnétique.

Les détecteurs d'ondes gravitationnelles et la chasse aux bruits

Les détecteurs d'ondes gravitationnelles (OG) sont des interféromètres de Michelson, des outils qui permettent de convertir la déformation de la métrique de l'espace-temps provoquée par le passage d'une onde gravitationnelle, en un signal optique. Comme expliqué précédemment, seuls les évènements d'origine cosmique génèrent des ondes gravitationnelles dont l'amplitude est assez grande pour que ces ondes soient détectables. La variation relative induite par de tels évènements est de l'ordre de 10^{-21}, ce qui est équivalent à une variation de la taille d'un atome sur une distance totale Terre-Soleil. Nous avons donc dû faire face à de nombreux défis technologiques afin de détecter une si faible variation relative. Ainsi, presque 100 ans séparent la prédiction d'Einstein et la toute première détection directe d'ondes gravitationnelles.

Actuellement, il y a un réseau de quatre détecteurs, dits de « seconde génération » : les deux détecteurs Advanced LIGO (« *Handford* » et « *Livingston* ») aux Etats-Unis, *Advanced Virgo* en Europe et *KAGRA* au Japon. Ce réseau (LIGO pour la première prise de données et LIGO-Virgo pour les deux dernières) a déjà effectué trois prises de données. Actuellement, les détecteurs sont en cours d'amélioration en vue de la quatrième phase d'observation scientifique (« O4 ») prévue pour 2022. Les détecteurs actuels sont des versions modifiées de l'interféromètre de Michelson, avec des bras kilométriques (3 km pour Advanced Virgo, 4 km pour Advanced LIGO).

Au cours des trois dernières campagnes d'observation, l'amélioration constante de la sensibilité des détecteurs Advanced LIGO et Advanced Virgo a permis d'augmenter la portée scientifique de ces détecteurs. On dénombre pour l'instant 41 détections uniquement durant la troisième campagne d'observation (« O3 »), contre 11 détections durant les deux premières campagnes. Cela s'explique par les améliorations fructueuses réalisées avant O3, campagne s'étant déroulée entre le 1er avril 2019 et le 27 mars 2020. Une des améliorations consistait en l'injection du *squeezing*, technique que nous allons décrire par la suite.

Les techniques de squeezing

Améliorer la sensibilité d'un détecteur permet de détecter des évènements

cosmiques plus lointains et avec un signal plus propre mais, requiert un travail important de réduction des bruits de l'instrument. La bande de détection des détecteurs actuels étant de 10 Hz-10 kHz, les instruments sont limités par plusieurs bruits dominants sur différentes plages de fréquences comme les bruits sismiques, les bruits thermiques et le bruit quantique. Ce dernier est une des limitations principales des détecteurs d'OG, provenant de la nature quantique de la lumière, et en particulier des fluctuations du vide qui entrent par la sortie de l'interféromètre. Le principe d'Heisenberg impose en effet une limitation sur la précision conjointe sur la phase et l'amplitude de la lumière. Ce bruit quantique est composé du « **shot noise** » ou bruit de grenaille, limitant la sensibilité entre 100 Hz et 10 kHz, et du **bruit de pression de radiation**, présent à de plus basses fréquences. Le shot noise émane de l'incertitude sur la phase et le bruit de pression de radiation, de l'incertitude sur l'amplitude. Pour réduire le shot noise, la solution naturelle consistant à augmenter la puissance d'entrée du laser est utilisée sur *LIGO-Virgo* mais elle comporte des désavantages importants. En effet, une augmentation de la puissance d'entrée du laser provoque des effets thermiques sur les miroirs, augmente la pression de radiation et requiert des changements importants sur le détecteur. Il n'est donc pas possible d'utiliser cette seule technique pour réduire le bruit quantique.

En 1981, C. Caves proposa une technique, appelée plus tard **squeezing indépendant de la fréquence**, consistant en l'injection d'états comprimés (ou *squeezed*) du vide dans l'interféromètre. Ces états comprimés du vide peuvent être représentés par une ellipse, dans l'espace phase-amplitude, où les incertitudes sur la phase sont réduites tandis que celles sur l'amplitude sont augmentées. Le principe d'incertitude d'Heisenberg impose en effet, que la réduction du shot noise grâce à ces états, s'accompagne d'une augmentation de la pression de radiation. Cet effet qu'il faut en général considérer, n'est pas gênant pour la sensibilité des détecteurs d'OG jusqu'à maintenant, étant donné que les bruits techniques sont dominants dans cette région de détection. Cette technique de squeezing a été utilisée sur tous les détecteurs durant O3 (pour LIGO et Virgo), ce qui a permis d'augmenter le taux de détection jusqu'à environ 30 % pour Virgo et atteignant 50 % pour LIGO.

Advanced Virgo (mais aussi Advanced LIGO) sera amélioré vers une version appelée Advanced Virgo+, avec une première phase opérationnelle en 2022 et une deuxième phase opérationnelle vers 2025. Cependant, les améliorations en cours permettent de réduire les bruits techniques, la pression de radiation devenant dominante pour les basses fréquences. Le *squeezing indépendant de la fréquence*, ayant pour effet secondaire d'augmenter la pression de radiation, n'est plus adapté pour améliorer la sensibilité des détecteurs d'OG. Afin de réduire le bruit quantique sur toute la bande spectrale de détection, le squeezing

doit agir en fonction de la fréquence, diminuant chacune des composantes du bruit quantique : c'est la technique du **squeezing dépendant de la fréquence**. Pour cela, la solution adoptée par LIGO et Virgo est d'injecter le vide comprimé dans une très longue *cavité de filtrage* de type Fabry-Pérot (285 mètres pour Advanced Virgo+). Une autre technique utilisant l'intrication quantique (de type *Einstein-Podolsky-Rosen* [**EPR**]) a été proposée par Ma et ses collaborateurs. Cette technique utilise les mêmes composants que la technique du *squeezing indépendant de la fréquence* mais dans une autre configuration pour générer des faisceaux intriqués du vide, appelés **signal** et **idler**, ayant des fréquences différentes. Précisons que dans le cas du *squeezing indépendant de la fréquence*, un seul faisceau comprimé du vide était généré. Ensuite, les deux faisceaux intriqués sont injectés dans l'interféromètre, ayant le même rôle qu'une cavité de filtrage. Le faisceau *signal* étant résonant alors que le bras agit comme une cavité déréglée vis-à-vis du faisceau *idler*, l'*idler* va subir une rotation de la phase dépendante de la fréquence après avoir été réfléchi par le bras de l'interféromètre. Enfin, ces faisceaux intriqués du vide doivent être séparés pour être détectés séparément. C'est le résultat de la détection de l'*idler* qui conditionne le résultat de celle du *signal* : le *squeezing dépendant de la fréquence* est ainsi produit. Ce procédé est donc plus simple que celui utilisant la cavité de filtrage, moins complexe au niveau logistique, moins coûteux et est donc une alternative prometteuse, notamment pour les détecteurs d'OG comme *Einstein Telescope*, un projet à l'étude qui commencerait à effectuer des observations dès 2035. Ce **squeezing EPR** pourrait être aussi testé sur Advanced Virgo+ après O5. Par ailleurs, deux démonstrateurs simplifiés, réalisés par deux équipes différentes, ont déjà montré la faisabilité de la technique EPR.

Mon travail sur le développement des techniques de squeezing

J'ai travaillé durant ma thèse sur la démonstration expérimentale de cette technique alternative, le *squeezing EPR*. J'ai réalisé un travail expérimental préliminaire, pour mettre en place un démonstrateur de la technique de *squeezing dépendant de la fréquence*, utilisant l'intrication EPR. Ce démonstrateur sera le premier à être conçu de façon à être compatible avec l'interféromètre Virgo. De plus, le *squeezing EPR* généré sera injecté pour la toute première fois dans un petit interféromètre suspendu (appelé *small-scale suspended interferometer* ou *SIPS*). Celui-ci a la particularité d'être limité par le bruit de pression de radiation dans la même bande de fréquence que les interféromètres d'OG (10 Hz – 1 kHz). Cela permettra de tester la réduction de ce bruit par le *squeezing EPR*, ce qui constitue une étape supplémentaire dans la réalisation d'un banc de *squeezing EPR*, directement injectable dans les détecteurs actuels.

Description de mon travail
Ma thèse est divisée en six chapitres : les trois premiers chapitres sont des chapitres de théorie, nécessaires pour la compréhension du travail expérimental que j'ai effectué et qui est décrit dans les trois derniers chapitres (4,5 et 6). Dans le **Chapitre 1**, je présente la théorie des ondes gravitationnelles, dans le contexte de la théorie de la relativité générale d'Einstein afin de donner quelques éléments pour aborder la suite des chapitres. Ensuite, je détaille les principales caractéristiques des détecteurs d'OG et les différents défis technologiques en jeu. Enfin, je récapitule toutes les détections faites jusqu'à maintenant et décris les perspectives pour l'astronomie gravitationnelle. Dans le **Chapitre 2**, je décris la lumière du point de vue de la mécanique quantique avec la quantification du champ électromagnétique, afin d'expliquer la nature des états comprimés et leur relation avec le principe d'incertitude d'Heisenberg. La représentation du champ électromagnétique dans ces états particuliers est ensuite développée. Ensuite, je donne une description très qualitative de la génération de ces états «*squeezés*» par les processus d'optique non-linéaire. La détection de ces états par un système de détection homodyne est expliquée par la suite. Finalement, je vais décrire le formalisme à deux photons, afin de pouvoir expliquer l'origine du bruit quantique dans les détecteurs d'OG et leur action dans ceux-ci. Le **Chapitre 3** est consacré à la réduction du bruit quantique dans les interféromètres gravitationnels. Je présente tout d'abord la technique du *squeezing indépendant de la fréquence*, en comparant les densités spectrales du bruit quantique dans les détecteurs avec ou sans injection de ce squeezing. Ensuite, après avoir expliqué les limites de cette technique pour nos détecteurs actuels, je présente la technique du *squeezing dépendant de la fréquence* adoptée pour les détecteurs d'OG actuels, utilisant une cavité de filtrage externe. J'illustre ensuite les performances du *squeezing indépendant de la fréquence* durant O3 (particulièrement pour Virgo) et les démonstrations de la technique de squeezing dépendant de la fréquence avec l'utilisation d'une cavité de filtrage externe. Enfin, j'explique les principes du squeezing dépendant de la fréquence en utilisant l'intrication quantique (de type *EPR*), son état de l'art et décris les deux expériences de démonstration de faisabilité de cette technique.

Concernant le travail expérimental effectué au cours de cette thèse, un travail préparatoire consistant au développement d'une expérience de R&D de squeezing indépendant de la fréquence, a d'abord été réalisé et est décrit dans le **Chapitre 4**. Un banc sur table avait été mis en place dans le but d'être le banc d'injection du *squeezing indépendant de la fréquence* d'Advanced Virgo. Cependant, l'équipe de l'institut Max-Planck à Hanovre a finalement eu la charge de la construction de ce banc car ils ont une expertise de longue date sur le squeezing.

Notre banc sur table, se trouvant en salle blanche dans le laboratoire *1500 W*, sur le site de Virgo, a donc été utilisé pour tester des techniques d'automatisation et acquérir de l'expérience en vue de la mise en place du démonstrateur EPR. J'ai ainsi travaillé sur tous les aspects techniques pour produire, mesurer et caractériser entièrement ce banc optique. Ainsi, le squeezing mesuré est de -1.6 dB et grâce notamment à la mesure expérimentale des pertes optiques par propagation (15.3 %), nous avons pu évaluer le niveau de squeezing produit à -2.5 dB. Par ailleurs, en nous appuyant sur une ancienne mesure de squeezing (effectuée il y a plus de deux ans), nous avons aussi estimé le niveau de squeezing produit. Cet écart entre le niveau de squeezing passé et actuel peut s'expliquer par un alignement non optimal et le vieillissement des cavités optiques. L'expérience acquise grâce à ce travail préliminaire nous a permis d'observer quelques paramètres critiques pour le démonstrateur EPR : la température de la salle, qui doit être mieux stabilisée, et le design optique, qui doit être réalisé de manière à faciliter les alignements très précis et réduire les pertes optiques. La future expérience doit également être régulièrement mise hors service afin d'éviter la baisse de performances due au vieillissement des cavités. De plus, nous avons ainsi pu mettre en œuvre et tester une nouvelle technique pour améliorer les stratégies de contrôle avec un logiciel basé sur des machines d'états. En effet, différentes cavités optiques sont nécessaires dans une expérience de squeezing et nous avons souhaité améliorer l'automatisation du *locking* de ces cavités. C'est la première fois qu'un logiciel temps réel basé sur des machines d'états a été testé sur une expérience de squeezing ; le but étant de simplifier le système de contrôle pour minimiser l'intervention humaine et les temps morts sur l'expérience. Cela permettrait de maximiser la période durant laquelle un détecteur d'OG utilisant la technique du squeezing est dans le mode « science » (ou « observation») sans interruption. Les tests se sont révélés concluants et compatibles avec le duty-cycle (la fraction de temps sur le temps total d'observation dans lequel le squeezing était opérationnel) requis pour l'injection du squeezing dans Virgo (plus de 99,9 %).

Avec l'expérience technique acquise sur ce banc complet de production du *squeezing indépendant de la fréquence*, j'ai contribué dans un second temps au design optique de notre démonstrateur expérimental EPR, travail qui est rapporté dans le **Chapitre 5**. Ce démonstrateur sera installé sur le même banc optique qui hébergeait la précédente expérience (*squeezing indépendant de la fréquence*) ; les contraintes qui en découlent sont dues à l'espace limité que nous avons et la stratégie est de minimiser les modifications en comparaison avec le banc précédent pour des raisons financières. De plus, nous avons essayé de faire un compromis entre minimiser les changements et optimiser le design afin d'avoir assez de puissances optiques pour les faisceaux auxiliaires, essentiels

pour cette technique de *squeezing EPR*. La première partie de l'expérience, consistant à produire du squeezing, requiert les mêmes composants que l'expérience décrite dans le Chapitre 4 mais ces composants sont utilisés dans une autre configuration. La principale différence dans cette nouvelle expérience est qu'au lieu de produire un seul faisceau comprimé du vide, nous produisons deux faisceaux intriqués du vide, ayant tous deux des fréquences différentes. Ainsi, au lieu de détecter ces faisceaux directement avec un détecteur homodyne, comme pour la technique du *squeezing indépendant de la fréquence*, ces faisceaux doivent dans un premier temps, être injectés dans une cavité de test. Cette cavité imitant le comportement d'un bras de l'interféromètre, les faisceaux intriqués sont ensuite séparés et détectés par deux détecteurs homodynes différents. Cette différence entraîne le doublement du nombre de faisceaux auxiliaires requis. Nous avons dans un premier temps réalisé un design optique qui minimisait au mieux les changements par rapport à l'expérience précédente. Nous avions réalisé ensuite qu'il était impossible d'obtenir assez de puissance optique pour tous les faisceaux auxiliaires avec ce design, ce qui nous a poussé à réaliser un second design optique, en veillant à bien prendre en compte le budget de puissances des différents faisceaux. Au moment de la rédaction de cette thèse, l'expérience est en cours d'installation, en utilisant ce dernier design.

La dernière partie de ma thèse est consacrée à un élément-clef de la technique du squeezing EPR et est décrite dans le **Chapitre 6**. J'y expose les motivations du choix d'une cavité étalon solide, les différents choix pour le design de cette cavité, le design mécanique et le design du système de contrôle thermique. L'étalon solide est utilisé en tant que résonateur optique, pour séparer les deux faisceaux intriqués générés par la technique du *squeezing EPR*. La particularité du contrôle de cette cavité est qu'elle ne nécessite pas l'utilisation d'un *faisceau brillant* pour contrôler sa longueur ; la longueur de la cavité est ici simplement contrôlée par un régulateur thermique (avec un mécanisme de rétroaction sur la temperature de l'étalon). Les spécifications sur la performance de cet étalon ont été déterminées en transmission et en réflexion, ainsi que les performances requises pour le système de stabilisation thermique afin de ne pas dégrader de manière notable le niveau de *squeezing EPR* produit. En effet, l'étalon devra transmettre une fraction de puissance suffisante de l'un des faisceaux intriqués et réfléchir une fraction suffisante de l'autre faisceau. Les performances de cet étalon doivent être maintenues dans le temps et grâce à un contrôle passif sur la longueur de la cavité étalon en utilisant un régulateur de température. Cet étalon, son support mécanique, ainsi que le système de contrôle thermique ont été testés sur un banc de caractérisation dédié au laboratoire optique du laboratoire APC. La caractérisation optique consiste en l'évaluation de la puissance de séparation de l'étalon en mesurant sa finesse, paramètre que nous avons choisi et spécifié

au fabricant. Nous avons mesuré une finesse de 14 ± 0.08, ce qui est en accord avec la valeur que nous avions choisie. La transmission pour un des faisceaux intriqués et la réflexion de l'autre faisceau ont été mesurés et sont à plus de 98 %, ce qui est suffisant pour le *squeezing EPR*. Dans un second temps, la capacité de la stabilisation thermique à maintenir le système au point de fonctionnement, sur une période d'une heure et sur une période d'une journée a été évaluée. Plus spécifiquement, les fluctuations en température doivent être inférieures à $\pm 0.01\,°C$ et nous avons mesuré des fluctuations en température 4 à 20 fois inférieures à cette spécification. Les tests réalisés ont permis de conclure que nous avons rempli le cahier des charges, que ce soit sur du court terme ou sur du long terme, et que notre étalon est donc prêt à être intégré sur le démonstrateur EPR.

Mon travail dans un contexte plus large

En inscrivant mon travail dans un contexte plus large, l'expérience de *squeezing indépendant de la fréquence* m'a permis d'acquérir une expérience cruciale sur la génération de squeezing dans la collaboration Virgo et d'en tirer quelques enseignements pour le design de futures expériences de squeezing. A propos du logiciel pour automatiser l'expérience, c'est la première fois qu'un logiciel temps réel basé sur des machines d'états est implémenté sur une expérience de squeezing et celui-ci peut potentiellement être utilisé sur Virgo pour améliorer l'efficacité des contrôles. Ces contrôles sont nécessaires dans toute expérience de squeezing. Conséquemment, ce travail peut être exploité pour l'injection de squeezing dans les futurs détecteurs d'OG tel qu'Einstein Telescope (ET). Le travail réalisé sur le démonstrateur EPR est une avancée de plus pour le test de cette technique dans un prototype suspendu (SIPS). Même si les futurs détecteurs tels qu'ET, planifient pour l'instant d'utiliser les cavités de filtrages externes pour la réduction du bruit quantique, la démonstration de la faisabilité de la technique EPR peut paver la voie vers une reconsidération d'une alternative moins coûteuse et logistiquement plus simple, en particulier quand ET sera construit sous terre.

Contents

List of Tables

List of Figures

List of Symbols

$\|0\rangle$	vacuum or ground state
$\hat{a}$	annihilation operator
$\hat{a}^\dagger$	creation operator
$\hat{a}_1$	amplitude or cosine quadrature operator
$\hat{a}_2$	phase or sine quadrature operator
$\hat{a}_\omega$	single-photon annihilation operator in the mode ω
$\hat{a}^\dagger_\omega$	single-photon creation operator in the mode ω
$\|\alpha\rangle$	quasi-classical states
A	round-trip losses
$\|A\rangle_R$	generalized annihilation operator
$\|A\rangle^\dagger_R$	generalized creation operator
B_0	magnetic field amplitude
c	speed of light in vacuum
χ	susceptibility
$\chi^{(2)}$	second-order nonlinear susceptibility
$\hat{D}(\alpha)$	displacement operator
ΔL	differential displacement of the ITF arms
ϵ_0	vacuum permittivity
$\boldsymbol{\epsilon}$	polarization vector
$\epsilon_{\mu\nu}$	polarization vector

η	amplitude reflectivity of the BS
η_{esc}	OPO escape efficiency
$\eta_{\mu\nu}$	flat spacetime metric (Minkovski metric)
η_{prop}	propagation efficiency
η_q	photodiode quantum efficiency
η_{tot}	total optical efficiency
$\mathcal{E}_0$	amplitude of the electric field
$E^{(1)}$	one-photon electric field
$\hat{E}_{in}^{dark}$	input field at the BS dark port
$\hat{E}_{out}$	output field at the BS dark port
$\hat{E}(\mathbf{r}, t)$	one-photon electric field
f_p	pole frequency of the Fabry-Perot arm cavity
$\mathcal{F}$	finesse
FSR_{etalon}	etalon free spectral range
$\mathcal{F}$	Fabry-Perot arm cavity finesse
$g_{\mu\nu}$	metric tensor
γ	ITF arm cavities half-bandwidths (or cavity pole)
$\gamma_{mes,th}$	intensity overlap integral
$g(f)$	frequency response of the Fabry-Perot arm cavity
G	Newton's gravitational constant
$G_{\mu\nu}$	Einstein Tensor
G_{pr}	power recycling cavity gain
$\hbar$	Planck constant in Js/rad
$\mathbf{k}$	wave vector
h_{SQL}^2	standard quantum limit
$h_{\mu\nu}$	small perturbation of the flat spacetime metric
$h_n(\Omega)$	noise of the Fourier transform of the GW signal
$h(t)$	GW field
$\hat{H}$	Hamiltonian of the electromagnetic field
I_0	input laser power of the GW detector
I_{SQL}	input laser power required to reach the SQL
$\mathcal{K}(\Omega)$	Kimble factor
L	length of the two orthogonal arms of the ITF
L_{et}	physical length of the etalon

m	mirror mass
μ_0	vacuum permeability
$M_\odot$	solar masses
ν	fringe visibility
$\|n\rangle$	number states or Fock states
$\hat{N}$	Number operator
ω	angular frequency of the wave
ω_0	angular frequency of the GW detector
ω_p	angular frequency of the pump field
Ω	modulation sideband frequency
Ω_{SQL}	frequency at which the ITF quantum noise equals SQL
$\|\Phi\rangle_{dark}^{in}$	dark-port input field in its vacuum state
$\boldsymbol{\mathcal{P}}$	dielectric polarization
Φ	round-trip phase
P_{bs}	input power on the BS
P_{in}	input laser power
$P(n)$	probability of finding n number of photons
r	squeezing parameter
R	scalar curvature
$R(\theta)$	rotation operator
$R_{\mu\nu}$	Ricci curvature tensor
S_h	noise spectral density for a GW detector
$\sqrt{S_{QN}(f)}$	equivalent strain sensitivity (or amplitude spectral density) for the quantum noise
$S_{RPN}(f)$	radiation pressure noise power spectral density
$S_{SN}(f)$	shot noise displacement power spectral density
$S(\xi)$	squeezing operator
$S(r,\theta)$	squeezing operator in two-photon formalism
θ	squeezing angle
T	input mirrors transmissivities
$T_{cav}(\Phi)$	transmitted field of the cavity
T_{ifo}	ITF transfer matrix
$T_{\mu\nu}$	stress-energy tensor
U	energy density of the electromagnetic field
V	volume
$V_\pm$	resp. anti-squeezing and squeezing variances
V^{meas}	measured variance
V^{prod}	achievable variance
$\hat{X}_1$	amplitude quadrature
$\hat{X}_2$	phase quadrature
z	redshift

Introduction

The existence of the GWs was predicted more than 100 years ago, by Einstein in his theory of relativity in 1916. In his theory, gravitation is no longer an attraction force, as formalized by Newton about 230 years earlier. Gravitation becomes a property of spacetime and massive objects deform it, stretch it, "curve" it. This relationship between spacetime and masses is described by Einstein's field equations and can be summarized by a famous quote from John Archibald Wheeler: "Spacetime tells matter how to move; matter tells spacetime how to curve." This theory leads to the prediction of the existence of GWs, which are ripples of spacetime emitted by the acceleration of massive objects. These waves would propagate at the speed of light in vacuum. Nevertheless, Einstein was not convinced at all that it would be possible one day to detect such waves.

We had to wait until the late 1980s to see the first projects of GW detectors in the United States (LIGO project) and in Europe, as a result of a French-Italian collaboration (Virgo project). Only cosmic and violent events such as the merger of two black holes can generate a large enough deformation (a relative deformation of the order of 10^{-21}) to have detectable GWs. We would have to wait more than thirty years to witness the first direct detection of a gravitational wave from the merger of two black holes in September 2015, by the two LIGO detectors. This discovery marked the beginning of the era of GW astronomy, opening a new window into the Universe. Indeed, GWs are a new messenger for astrophysics and a new tool for fundamental physics. August 17, 2017, is another historic date, marking the beginning of the era of multi-messenger astronomy. The signal from the detection of a GW, caused by the merger of two neutron stars (GW170817), was detected by the LIGO-Virgo detector network, in quasi-coincidence with a gamma-ray burst, detected by the Fermi and Integral

satellites. This confirmed the hypothesis of a link between the merger of neutron stars and (at least) some of short gamma-ray bursts. Moreover, the precision of the localization of the source of the GW, thanks to the detection by three detectors (LIGO and Virgo), allowed about 70 telescopes to detect a "kilonova".

Gravitational-wave detectors are modified Michelson interferometers, which convert spacetime perturbations produced by a GW into an optical phase shift that is detectable at the interferometer output. Almost 100 years separate Einstein's prediction and the very first direct detection of gravitational waves: this is partially due to the technological challenge that lies in building the detectors and obtaining the exquisite sensitivity required to detect GWs. Let's recall that events such as the merger of two black holes induce a relative deformation of a strain amplitude of $h \sim 10^{-21}$: this represents a deformation of the size of an atom over the distance Earth-Sun. There is currently a network of 4 detectors, called *second generation GW detectors*: the two *Advanced LIGO* detectors (Handford and Livingston) in the USA, *Advanced Virgo* in Europe and KAGRA in Japan. There were already three data takings. Currently, we are in an improvement phase, to get ready for the fourth science run (O4) planned for the end of 2022. The current detectors have kilometer arms (3 km for Advanced Virgo, 4 km for Advanced LIGO).

During the last three observing runs, the constant improvement of the sensitivity of the Advanced LIGO and Advanced Virgo detectors has allowed to increase the science reach of these detectors. At the time of writing, there have been 41 detections only from the third observing run (O3), against 11 detections during the first two science runs. This increase in number is explained by the successful improvements realized before O3, this science run having taken place between April 1, 2019, and March 27, 2020. One of the improvements consists in the injection of *squeezing* technique which we will describe immediately after.

Improving the sensitivity of a detector allows to detect cosmic events further away and with a cleaner signal, but requires an important work to mitigate the noise of the instrument. The detection band of the current detectors being of 10 Hz-10 kHz, the instruments are limited by several noises dominating on various ranges of frequencies such as seismic noises, thermal noises and the quantum noise. The latter is one of the main limitations of GW detectors, arising

from the quantum nature of light, particularly from the vacuum fluctuations that enter through the output of the interferometer. Heisenberg's uncertainty principle imposes that it is impossible to be precise on both the phase and the amplitude of the light. This noise is composed of the quantum shot noise, limiting the sensitivity between 100 Hz and 10 kHz, and the quantum radiation pressure noise, present at lower frequencies. The shot noise comes from the uncertainty on the phase and the radiation pressure noise from the uncertainty on the amplitude. A natural solution would be to increase the input power of the laser to reduce the shot noise. This solution is accompanied by thermal effects on the mirrors, will increase the radiation pressure noise, and requires significant changes to the detector.

In 1981, C. Caves proposed a technique, later called *frequency-independent squeezing*, consisting of injecting squeezed vacuum states into the interferometer. These squeezed states can be represented by an ellipse, in phase-amplitude space, where the uncertainties on the phase are reduced while those on the amplitude are increased. The Heisenberg uncertainty principle imposes that the reduction of the shot noise thanks to these states is accompanied by an increase in the radiation pressure noise. This effect does not affect so far the sensitivity of the detectors, since the technical noises are dominant in this region. This squeezing technique has been routinely used on all the detectors during O3 (LIGO and Virgo), which has allowed to increase the detection rate up to about 30% for Virgo and to reach 50% for LIGO.

Advanced Virgo (but also Advanced LIGO) will be upgraded to a version called Advanced Virgo+, which will be completed by 2025. The technical noises will be reduced, making the radiation pressure noise limiting for the sensitivity (in the low-frequency band) of Advanced Virgo+. The side effect of the frequency-independent squeezing technique is no longer covered by these technical noises. To obtain a broadband reduction of quantum noise, the squeezing should act in a frequency-dependent way, reducing each of the quantum noise components. For this purpose, the solution adopted by LIGO and Virgo is to inject the squeezed vacuum into a very long Fabry-Perot cavity, a *filter*

cavity (285 meters for Advanced Virgo+). An alternative using Einstein-Podolsky-Rosen (EPR) entanglement has been proposed by Ma and coworkers. This technique uses the same components as the frequency-independent squeezing technique but in a different configuration, to generate EPR-entangled vacuum fields, called *signal* and *idler*, both having different frequencies. Note that for the frequency-independent squeezing technique, only one squeezed vacuum field was generated. Then, these two fields are injected into the interferometer, one of the interferometer arms having the same role as a filter cavity. The signal is resonant while the idler beam sees the arm as a detuned cavity. The idler field will undergo a frequency-dependent phase rotation after being reflected off from the arm. Finally, these entangled beams must be separated to be detected separately. The outcome of the idler detection conditions the outcome of the signal detection. This enables to have a broadband reduction of quantum noise. This process is thus simpler than the one using the filter cavity, less complex logistically, and thus less expensive. Therefore, this is a promising alternative, especially for gravitational-wave detectors such as the Einstein Telescope, a project under study that would start making observations as early as 2035. This EPR squeezing could also be tested on Advanced Virgo+ after O4. Two simplified proof-of-principles experiments, realized by two different teams, have already shown the feasibility of the EPR technique.

In this framework, I have done a preliminary experimental work, to build a demonstrator to test the frequency-dependent squeezing technique, using EPR entanglement. This demonstrator will be designed to be compatible with the Virgo interferometer, this type of demonstrator having never existed before. The generated EPR squeezing will be injected for the very first time into a small-scale suspended interferometer (SIPS). This interferometer is limited by the radiation pressure noise, in the same frequency band as GW interferometers (10 Hz-1 kHz). This will allow to test the reduction of this noise by EPR squeezing, which is a further step towards the injection of the frequency-dependent squeezing technique with EPR entanglement into current GW detectors.

First, I did a preparatory work to develop an R&D table-top experiment for frequency-independent squeezing, in an optical laboratory at the Virgo site. This

table-top experiment has been designed with the initial goal to be the Advanced Virgo squeezer. However, the Advanced Virgo squeezer was finally provided by the Hannover Max-Plank institute team, having a long-standing experience in squeezing, and the table-top experiment was used to test automation strategies, and acquire experience in view of the EPR experiment.

In this context, I worked on all the technical aspects to produce, measure and characterize the squeezing and improve this experiment. In particular, I have worked on the estimation of the optical losses. We also implemented an automation software based on finite state machines for the cavities locking. This allows to improve the performances of the experiment. With the experimental experience acquired on this complete frequency-independent squeezer, I contributed in a second phase to the complete optical design of our experimental EPR demonstrator. Finally, one of the key elements of the EPR technique is the separation of the EPR-entangled beams, which have different frequencies. I have been responsible for the design and characterization tests of a solid etalon (a Fabry-Perot cavity) acting as an optical resonator. The particularity of this cavity control is that it does not require the use of a bright beam to perform an active length control, and a temperature feedback system simply controls the cavity length. The optical performances and the thermal stabilization of the etalon have been tested in a dedicated characterization optical bench at the APC laboratory.

The first three chapters are theory-based, necessary to understand the experimental work described in the last three chapters (4,5 and 6).

In **Chapter 1**, I will present the theory of gravitational waves, in the framework of Einstein's theory of relativity to give some elements to read the following chapters. Then, I will expose the main characteristics of the GW detection by the interferometry technique and the various technological challenges involved in the detection. Finally, I will summarize all the detections made so far and describe the future prospects for GW astronomy.

In **Chapter 2**, I will give an introduction on the quantum description of light with the quantization of the electromagnetic field, to explain the nature of squeezed states and their relation with the Heisenberg uncertainty principle.

The representation of the electromagnetic field in these particular states is then explained. Afterward, I will give a very qualitative description of the generation of these squeezed states by nonlinear optics processes. The detection of these states by a homodyne detection system is explained. Finally, I will describe the two-photon formalism, to explain the origin of quantum noise in gravitational-wave detectors and their effects.

Chapter 3 is devoted to the reduction of quantum noise in GW interferometers. I will first describe the frequency-independent squeezing technique, comparing the spectral densities of the quantum noise with and without squeezing injection. Then, after explaining the limitations of this technique for our current detectors, I will describe the frequency-dependent squeezing technique adopted for these detectors, the technique using an external filter cavity. Then, I will present the performances achieved thanks to the frequency-independent squeezing injection during O3 (especially for Virgo) and demonstrations of the frequency-dependent squeezing technique using an external filter cavity. Finally, I will explain the principles of frequency-dependent squeezing using EPR entanglement, the state of the art and describe the two proof-of-principles experiments.

In **Chapter 4**, I will present the experimental work done on the table-top experiment of the frequency-independent squeezing technique. This technique was performed in a cleanroom, in the laboratory *1500 W*, on the Virgo site. I will describe my contribution to the implementation of the coherent-control technique, the improvement of the performances of this bench and its complete characterization to test a new technique to improve the control strategies for a squeezed vacuum source, using a software based on finite-state machines. The experience gained with this bench and the tested automation is then used for our EPR squeezing demonstrator.

In **Chapter 5**, I will present our work on the realization of the complete optical design of the EPR squeezing demonstrator. I will describe in particular our strategy for the design, the different specifications and constraints we had. As the bench which will house the EPR demonstrator is the bench used for the previous experiment, described in Chapter 4, constraints are due to the limited space we have and the strategy to have minimal modifications on this previous

bench, due to financial reasons.

In **Chapter 6**, I will explain the motivations for the choice of a solid etalon as optical resonator, the different choices made for the design, the mechanical design and the design of the temperature-controlled system. Then, I will describe the optical characterization tests performed on the characterization bench, built in a cleanroom and the tests of the thermal stabilization of this etalon. The performances of the etalon needed to be evaluated as they will impact the measured level of squeezing.

I would like to underline that the experiment at the Virgo site has been carried out by a collaboration of several groups in Italy (INFN Genova, INFN Roma "Tor Vergata", INFN Roma "La Sapienza", INFN Padova, INFN Perugia, INFN Napoli, INFN Pisa), the optics and electronics groups at the European Gravitational Observatory and the APC laboratory. I have spent roughly ∼8 integrated months on the Virgo site. The EPR design has been made in collaboration with Martina De Laurentis (Università di Napoli “Federico II", I-80126 Napoli, Italy), Valeria Sequino (Università di Napoli “Federico II", I-80126 Napoli, Italy), Sibilla di Pace (Università di Roma “La Sapienza”, I-00185 Roma, Italy), Barbara Garaventa (INFN, Sezione di Genova, I-16146 Genova, Italy), Fiodor Sorrentino (INFN, Sezione di Genova, I-16146 Genova, Italy) for the optical part and with Mateusz Bawaj (INFN, Sezione di Perugia, I-06123 Perugia, Italy) who is in charge with the electronical and software implementation of the controls. The experiment at APC has been carried out in collaboration with engineers, lab technicians and researchers of APC (Eric Bréelle, Eleonora Capocasa, Jean-Pierre Baronick, Pierre Prat et Stéphane Dheilly).

Chapter 1

Gravitational-waves theory, detectors and astronomy

Outline of the current chapter

In this chapter, I will shortly introduce the GW theory, detectors and astronomy. I will first introduce GW in the context of Einstein's theory of general relativity and describe the main features of GW. Then, I will present the detection principles of GW through laser interferometry and the technological challenges those detectors face. Finally, I will make a summary of the GW detections made so far and of the future prospects for GW astronomy. The goal of this chapter is not to have an exhaustive treatment of the GW theory and sources, but rather to offer the reader some elements of context and background for the next chapters about quantum noise and *squeezing*.

1.1 Gravitational waves

Gravitational waves (GW) are oscillatory perturbations of the spacetime metrics emitted by massive accelerating objects. In 1916, Albert Einstein predicted their existence starting from the field equations of General Relativity (GR) [26].

The *Einstein Field Equations* describe the relationship between spacetime geometry, described by the *Einstein Tensor* $G_{\mu\nu}$ and matter-energy content, described by the *stress-energy tensor* $T_{\mu\nu}$:

$$G_{\mu\nu} = \frac{8\pi G}{c^4} T_{\mu\nu}, \tag{1.1}$$

where G is the Newton's gravitational constant, c is the speed of light in vacuum and where the Einstein tensor is defined as :

$$G_{\mu\nu} = R_{\mu\nu} - \frac{1}{2} g_{\mu\nu} R, \tag{1.2}$$

where $R_{\mu\nu}$ is the *Ricci curvature tensor*, a contraction of the Riemann tensor, $g_{\mu\nu}$ is the *metric tensor* and R the *scalar curvature*.

If we consider a small perturbation ($h_{\mu\nu}$) of the flat spacetime metric $\eta_{\mu\nu}$ (*Minkovski metric*):

$$g_{\mu\nu} = \eta_{\mu\nu} + h_{\mu\nu} \qquad \text{with } |h_{\mu\nu}| << 1, \tag{1.3}$$

the Einstein equations can be linearized. By further imposing some specific set of coordinates [26] and considering the absence of sources, we can demonstrate that $h_{\mu\nu}$ satisfies a wave-equation equation:

$$\left(\nabla^2 - \frac{1}{c^2}\frac{\partial^2}{\partial t^2}\right) h_{\mu\nu} = 0, \tag{1.4}$$

whose solutions are the *gravitational-waves*, transverse waves propagating in vacuum at the speed of light. The solution can be written under the form of plane waves:

$$h_{\mu\nu}(\mathbf{x}, t) = \epsilon_{\mu\nu} \exp(i\mathbf{k}\mathbf{x} - \omega t), \tag{1.5}$$

where $\epsilon_{\mu\nu}$ is the polarization vector, ω is the angular frequency of the wave, and $\mathbf{k}$ is the wave vector. We can demonstrate that a general solution can be expressed as the sum of two polarization states, traditionally called $\times$ and $+$:

$$h = \epsilon_{\times} h_{+} + \epsilon_{+} h_{\times}. \tag{1.6}$$

About the interaction between the gravitational wave and matter, it is possible to show that a GW normally arriving in a plane containing a ring of free-falling test mass (TM) makes the ring stretching in a direction and squeezing in the orthogonal direction. Fig. 1.1 shows this effect for the two GW polarizations. This property of differential stretching of the space-time is used in the interferometric gravitational-wave detectors.

We have so far discussed the propagation of the gravitational waves in vacuum. Using the Einstein Equations, we can demonstrate that, in order to produce gravitational waves, a system should have at least a non-null second derivative of the quadrupolar mass distribution. The emission in the lowest term is governed by the *quadrupole formula*, found by Einstein in 1918.

For instance, a perfect rotating sphere will not emit gravitational waves. Still, two bodies rotating one around the others are a very efficient gravitational-wave generator, as we will see in the following of the chapter. Gravitational-waves sources include compact objects systems (well before the merger and during the coalescence), spinning neutron stars with some asymmetry, processes in the early universe producing a cosmological background of gravitational waves, supernovae.

Using the quadrupole formula, applied to a binary system of two compact bodies, we can demonstrate that typical amplitudes of realistic sources are of the order of magnitude of $h = 10^{-21}$ or less, and this number immediately explains the difficulty of the gravitational-wave detection.

To conclude this introductory section, let us remind that, since the gravitational waves are produced by acceleration of bodies, rather than acceleration of charges (as for electromagnetic waves), detecting GW offers the opportunity

to have complementary information about several astronomical sources with respect to the ones obtained with electromagnetic waves (radio, infrared, visible, UV, X-, and γ-radiation), and the ones one can obtain using neutrinos and cosmic rays. For instance, as shown by the first LIGO-Virgo detections, gravitational waves made it possible to measure mass, spins and distances of binary systems of black-holes, neutron stars and mixed systems of neutron star and black-hole. These information enables new tests of general relativity, to perform cosmological measurements, measurements about matter under extreme conditions, as well as other studies about violent astrophysical phenomena, like gamma-ray bursts.

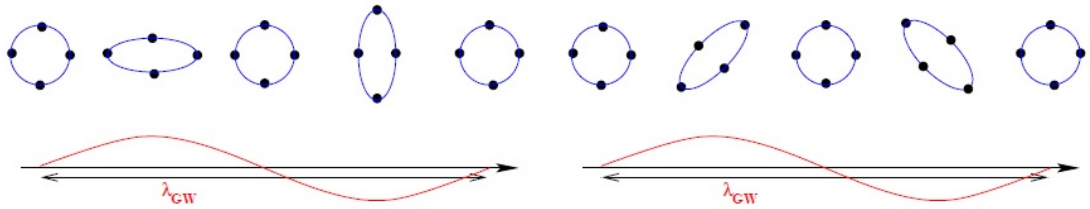

Figure 1.1 – Effect of a GW on a ring of test masses, propagating in the direction perpendicular to the plane of the ring, from [26]. The left panel refers to a wave with + polarization, the right panel with a × polarization.

1.2 Gravitational-wave interferometric detection

In this section, I will describe the GW detection principles and challenges using laser interferometry, in the particular context of the LIGO and Virgo detectors: kilometer-scale detectors with suspended test masses, Michelson interferometers-based, with Fabry-Perot cavities in the arms and techniques to increase the internal power (*power recycling*) and the signal produced by GW (*signal recycling*).

A Michelson interferometer converts space-time perturbations produced by a GW into an optical phase shift detectable at the interferometer output. Using the relation that the spacetime interval is equal to zero for light ($ds^2 = 0$) in the presence of gravitational waves, we can demonstrate [68] that the effect of a GW crossing the detector is equivalent to a differential stretch of the two arms and,

for a GW with a + polarization aligned with the two arms. Moreover, with a period higher than the round-trip time of the light in the arms, the differential displacement is expressed as:

$$\Delta L = hL, \tag{1.7}$$

where L is the length of the two orthogonal arms of the ITF and h is the GW amplitude.

Figure 1.2 shows a simplified optical layout of a standard gravitational-wave detector. This scheme is adopted by Advanced LIGO, Advanced Virgo (the signal recycling will be introduced in the O4 data taking), KAGRA (in its final design configuration) and it is also the basic scheme for the future detectors Einstein Telescope and Cosmic Explorer. It consists of a *dual recycled Fabry-Perot Michelson interferometer*:

- two Fabry-Perot cavities along each arm (called *arm cavities*) to increase the arms' optical length.
- a Fabry-Perot cavity formed by the Power Recycling Mirror (PRM) and the beam-splitter (BS) to perform a technique called *power recycling*, that increases the circulating power in the ITF.
- a Fabry-Perot cavity formed by the Signal Recycling Mirror (SRM) and the BS, to perform the *signal recycling* technique, that broadens the detection bandwidth of the instrument.
- a Fabry-Perot cavity between the laser and the main interferometer, called *input mode-cleaner*, used to suppress the beam jitter fluctuations and stabilize the laser frequency before entering in the interferometer.
- a Fabry-Perot cavity between the interferometer and the photodetectors, called *output mode-cleaner*, used for a spatial cleaning of the output beam and to remove radio-frequency fields used for the interferometer control.

Moreover, the test masses and all the interferometer components are suspended to a mixed of passive and active seismic isolation systems, formed by

chains of pendula (called *superattenuators* in the Virgo environment), and inertial platforms.

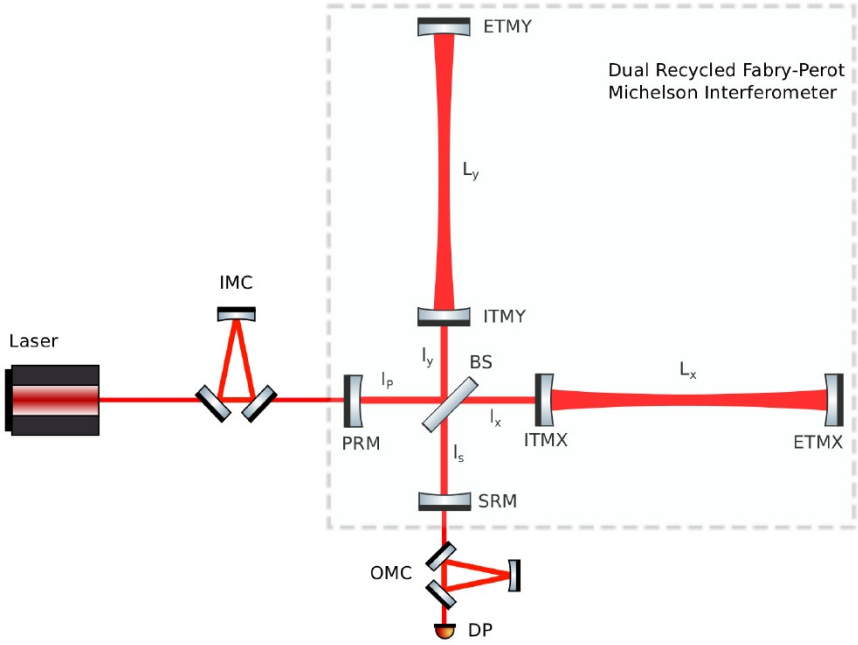

Figure 1.2 – Simplified optical layout [35] of a dual-recycled Michelson ITF with Fabry-Perot cavities in each arm. A solid state laser going through an input mode-cleaner (IMC) illuminates the ITF and the light reaches an output mode-cleaner (OMC) before the detection by the photodetectors (DP). ITMX/ITMY (respectively ETMX/ETMY) stand for input test-mass (respectively end test-mass) of the arm X and Y.

1.3 Main noises sources of a gravitational-wave interferometric detector

In this section, I will briefly describe the main noise sources of a GW interferometric detector, using Advanced Virgo as an example. Advanced Virgo is a major upgrade of the Virgo detector, and it has been operated between 2017 and 2021, during the O2 and O3 LIGO-Virgo data takings (described below). The instrument is considered as a *second generation GW detector*, together with Advanced LIGO. Advanced Virgo is currently under upgrade (becoming *Advanced*

Virgo+) and will be operated again in 2022 for the O4 data taking.

Figure 1.3 shows the planned sensitivity of Advanced Virgo (according to the Advanced Virgo technical design report [35]) with the main noise sources. As already mentioned, we used Advanced Virgo as an example, but the influence of the same noises can be roughly found in Advanced LIGO, KAGRA and future detectors. In the low frequency region (up to 40 Hz), the sensitivity is dominated by the *Newtonian noise*, *quantum noise*, *seismic noise* and *suspension thermal noise* (the thermal noise associated with the main vibrational mode of the suspensions). The mid-frequency range is mainly limited by the *thermal noise* (the suspension thermal noise and the coating Brownian noise) and the *quantum noise*. Finally, the high-frequency region (above 300 Hz) is dominated by the *shot noise*, the high-frequency component of the quantum noise.

The seismic noise, the thermal noise and the low-frequency component of the quantum noise are also called *displacement noises*, because they create a displacement of the mirrors. The shot noise (the high-frequency component of the quantum noise) and the electronic read-out noise of the photodetectors are *read-out* noises, because they are related to the measurement process.

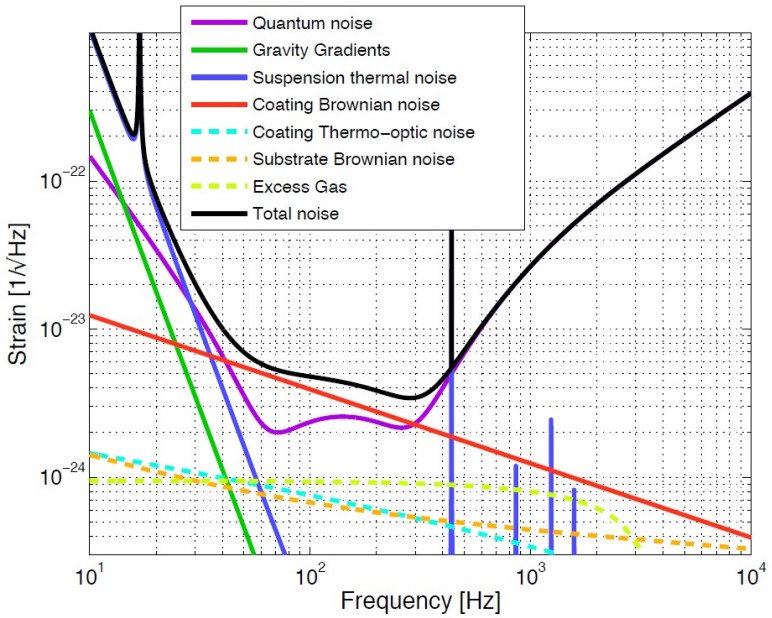

Figure 1.3 – Design sensitivity curve of AdV with its noise budget[35]

The experience accumulated with Virgo and LIGO shows that several technical noise sources limit the sensitivity of the detector, especially at low frequency. We can quote: the laser and amplitude frequency noise, the actuation electronic noise, the control noise of the auxiliary degrees of freedom, the noise related to the alignment control, the noise related to the scattered light. A careful evaluation (through simulation and measurement) is mandatory to quantify the noise sources and mitigate them. This activity called *noise hunting* is one of the main part of the *commissioning* of the detector. In Figure 1.4, we show the noise sources for the LIGO detector during the O3 data taking, where we see the several sources of noise limiting the sensitivity, especially at low frequency.

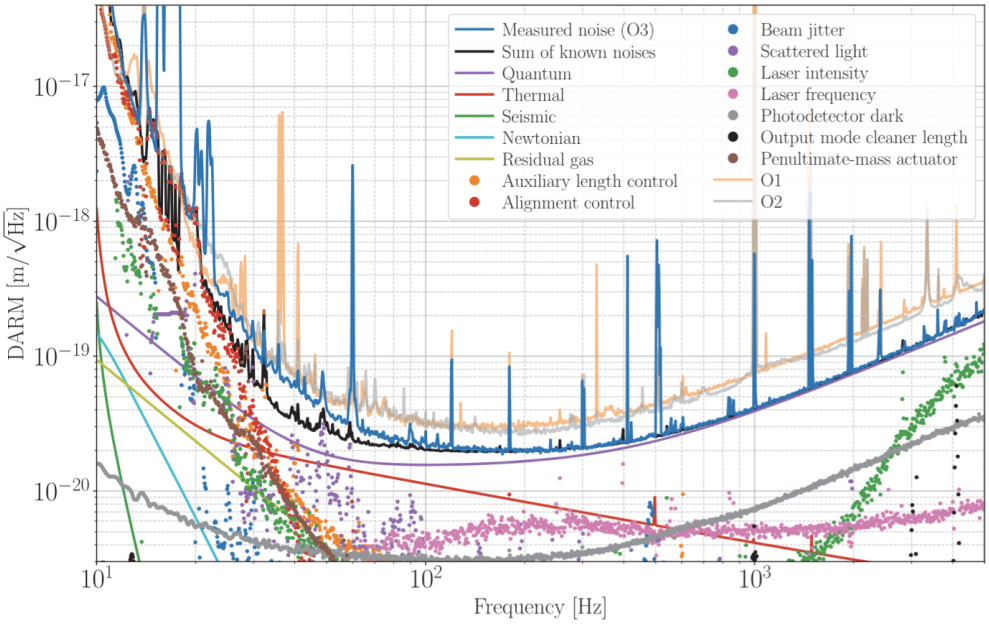

Figure 1.4 – Noise budget for the LIGO detector during O3[25]

1.3.1 Seismic noise and seismic isolation

A first example of displacement noise is the seismic noise, due to seismic motion, wind and human activity that causes noise at lower frequencies. To reduce its influence, the interferometer mirrors are suspended with multi-pendulum chains, acting as horizontal filters above their resonance frequency (about 0.5 Hz). The

chain is suspended using a pre-isolator: an inverted pendulum that guarantees isolation below 1 Hz and damping of the resonances of the chain [13]. The residual seismic noise, after filtering by this “super-attenuator" system (shown in Figure 1.5), is shown in the dark blue curve of Figure 1.3. Because the seismic noise is basically filtered passively, by seismic filters, whose resonance frequency changes smoothly with the length of the chain, gravitational-wave detectors have a *seismic wall*, at around 1 Hz, which cannot be overcome to improve the suspensions. To reduce further the seismic noise, detectors should be built underground (as KAGRA), since this allows to reduce the surface seismic waves drastically. Einstein Telescope adopts the same concept. Another strategy to remove the seismic noise is to build the detector in space (as the space detector LISA, planned by ESA).

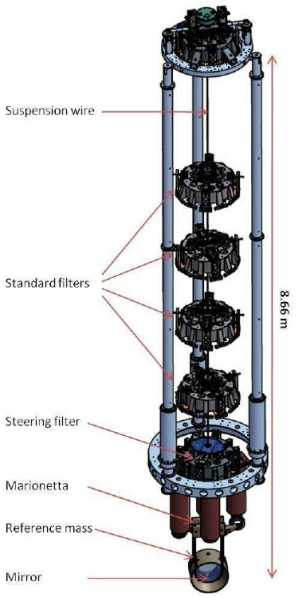

Figure 1.5 – Schematics of the Virgo super-attenuator[33]: the inverted pendulum, the Filter 0 and a chain of seismic filters and the mirror suspension.

To attenuate the effects of the seismic noise (for example, scattered light), all the sensitive optical components like the optical benches with the input-output auxiliary optics (i.e., input and output MC, mode-matching telescopes) are placed on suspended optical benches [13].

A consequence of the seismic noise is the Newtonian noise (or gravity gradient noise). This noise is due to the fluctuations of the local terrestrial gravity field due to seismic waves that change the mass density distribution of the ground. This noise acts directly on the mirrors and it cannot be shielded or filtered. To mitigate it in Advanced Virgo+, an off-line removal is planned using a network of seismometers around the test masses. Moreover, the Newtonian noise can be removed by building a future detector underground, since it is proportional to the seismic noise. Another type of Newtonian noise is generated by atmospheric fluctuations (for instance the *Infrasound Newtonian Noise* [41]).

1.3.2 Mirrors, monolithic suspensions and thermal noise

The thermal noise is the displacement noise created by the random fluctuations of atoms and molecules composing the interferometer apparatus and being at room temperature. In gravitational-wave detectors, the thermal noise has two main sources: the suspension wires and the mirrors. The thermal noise of the mirrors (coating and substrate) can be divided into thermo-elastic effects (thermal fluctuations coupling with a non-zero thermal expansion coefficient of the material), Brownian motion (kinetic energy of the mirrors atoms at temperature T), and thermo-refractive fluctuations (thermodynamical fluctuations coupled with variation of material refractive index with temperature) [13, 16]. The dominant source is the Brownian thermal noise of the multi-layer coatings used to set the reflectivities of the test masses (high reflectivity coatings are necessary to have Fabry-Perot cavities in the arms). The coating thermal noise scales as the square root of the temperature multiplied by the mechanical losses of the coating, and divided by the laser beam size [50].

In Advanced Virgo and Advanced LIGO the multi-layer coatings are made with fused silica (low index material) and Ti-doped Ta_2O_5 (high index material) which has the lowest mechanical losses [47]. Studies are ongoing to reduce further the mechanical losses of the material, and implement improved coating in *Advanced Virgo+ phase 2*. Moreover, in this phase, larger beams will be used to reduce the impact of the coating thermal noise.

The mirrors are suspended to *monolithic suspensions*, composed by 400 µm-

diameter SiO_2 fibers. Fused silica, a high-strength material with low mechanical losses whose intrinsic dissipation is about three orders of magnitude lower than steel [16], and allows to reduce the suspension thermal noise.

1.3.3 Quantum noise

As we will see in the following of this manuscript, Quantum Noise (QN) originates in the quantum nature of light, as a consequence of the Heisenberg Uncertainty Principle [27].

QN is composed of Shot Noise (SN), dominating above 100 Hz, and Radiation Pressure Noise (RPN), dominating below $\sim$ 100 Hz. The shot noise displacement Power Spectral Density (PSD) is written as [15]:

$$S_{SN}(f) = \frac{1}{(4\mathcal{F})^2}\frac{\pi\hbar\lambda c}{P_{bs}}\frac{1}{g(f)}, \tag{1.8}$$

Where P_{bs} is the input power on the BS and is equal to $P_{bs} = P_{in} \times G_{pr}$ with G_{pr} being the power recycling cavity gain and P_{in} the input laser power, and $g(f) = \left[1 + (f/f_p)^2\right]^{-1}$ is the frequency response of the Fabry-Perot arm cavity with the pole frequency $f_p = c/4\mathcal{F}L$, where $\mathcal{F}$ is the arm cavity finesse and L is the ITF arm length. The shot noise being the high-frequency component of the quantum noise, assuming $f >> f_p$ and thus $g(f) \sim f^{-2}$, the expression of the shot noise displacement PSD becomes:

$$S_{SN}(f) \propto \frac{f^2}{P_{in}}. \tag{1.9}$$

The radiation pressure noise displacement power spectral density is expressed as:

$$S_{RPN}(f) = \left(\frac{4\mathcal{F}}{M}\right)^2 \frac{\hbar P_{bs}}{\pi^5 \lambda c}\frac{g(f)}{f^4}. \tag{1.10}$$

The radiation pressure noise PSD is thus proportional to the laser input power. The displacement power spectral density of the quantum noise can be expressed as the sum of the PSD of the SN and the one of the RPN, where $S_{QN}(f) = S_{RPN}(f) + S_{SN}(f)$. Note that in Figure 1.3, the equivalent strain

sensitivity (or *amplitude spectral density*) for the quantum noise is represented, which is equal to $\sqrt{S_{QN}(f)}$ (in $1/\sqrt{\text{Hz}}$). As the SN equivalent strain sensitivity is inversely proportional to the squared of the laser input power, the natural solution to reduce this noise source is to increase the laser power. For instance, this has been done in Advanced Virgo, during the O3 data taking, and permitted to increase the sensitivity at high frequency. However, increasing the input laser power causes thermal effects in the mirrors and opto-mechanical instabilities, that make the interferometer difficult to control.

In 1981, Caves [27] proposed to inject *squeezed states* of vacuum to decrease shot noise without increasing laser power and *squeezing* is routinely used since O3 AdV [14] and Advanced LIGO (aLIGO) [80] with a reduction of the shot noise between 100 Hz and 3.2 kHz of about 3 dB, equivalent to an increase of the input power by a factor of 2. Figure 1.6 shows the strain sensitivity of the AdV without squeezing (black curve) and with squeezing (red curve).

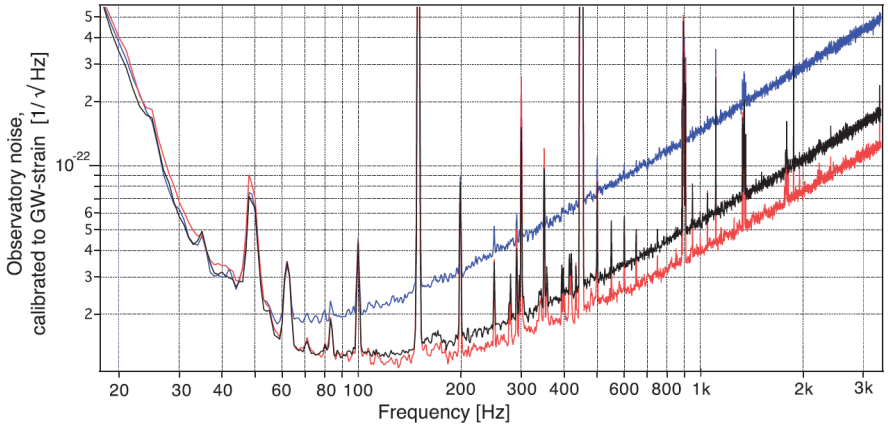

Figure 1.6 – AdV sensitivity curves in different conditions of squeezed light injection [14]. The black trace corresponds to the measured sensitivity without squeezing, the red and blue traces correspond to the measured sensitivity with *squeezing* and *anti-squeezing* respectively.

1.3.4 The gravitational-wave detection network

The development of the gravitational-wave detectors, over the last 50 years, brought to the development of the gravitational-wave detector network, formed

by the two LIGO detectors (Hanford and Livingston) in the US [4], the Virgo detector in Europe AdV and the KAGRA detector in Japan. The network performed already 3 data takings, whose results will be discussed in the next paragraphs. The first data taking (O1) was included only the two LIGO and led to the first gravitational-wave detection, the second and third data taking included 2 LIGOs and Virgo. The sensitivities of the detectors during O3 (April 2019 - March 2020) expressed in binary neutron star range are 50 Mpc for Virgo and 110-140 Mpc for the 2 LIGOs. The Binary Neutron Stars (BNS) range is a standard figure of merit for the sensitivity of the interferometer, which is the averaged distance at which it can detect a BNS merger composed of two 1.4 $M_{\odot}$ neutron stars, with a signal-to-noise ratio of 8, for sources uniformly distributed over the sky with random inclination and polarization angles.

Figure 1.7 shows the past and future LIGO-Virgo-KAGRA data takings, with sensitivities. The strategy adopted for the data takings is to alternate them with periods of upgrades. The data takings O1, O2 and O3 correspond to Advanced Virgo and Advanced LIGO detectors, while the O4 and O5 data takings (respectively planned for 2022 and 2025) correspond to Advanced Virgo+ and Advanced LIGO+. During the data taking O4, KAGRA (which is formally already part of the network but whose data were not yet used) will start to take data, and during O5 a third LIGO detector, LIGO India, will also join the network.

The network configuration allows to increase the significance of the detected events, localize them and to increase the overall duty cycle of the network.

Figure 1.8 depicts the antenna pattern of a single gravitational-wave detector, showing that a single instrument cannot localize the position of a GW transient. On the contrary, using the time of arrival of a GW at different detectors, and also the phase and the amplitude of the waves, a localization of tens of degrees can be obtained for 3 detectors, as demonstrated for GW170817. With 4 or more detectors the localization further improves, as discussed in[32], and also explained in Figure 1.9.

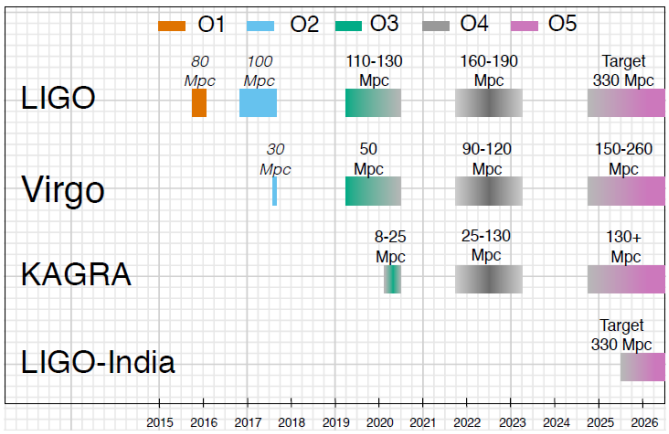

Figure 1.7 – Observing scenarios with targeted sensitivities for aLIGO, AdV, KAGRA and LIGO-India GW detectors for the coming years, from [32]

.

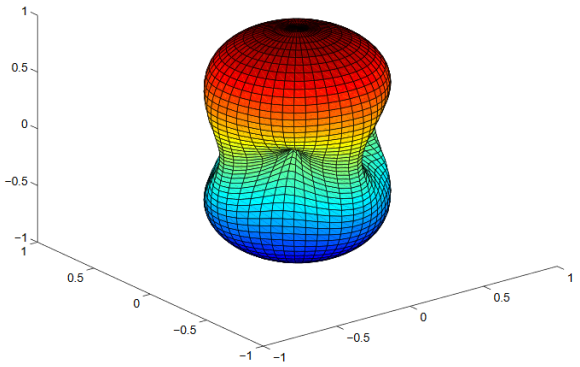

Figure 1.8 – The antenna pattern of a GW interferometric detector with the arms in the $x-y$ plane and oriented along the axes, from [67]. The response of the ITF for GW coming from a certain direction is proportional to the distance to the point on the antenna pattern, in that direction. The response is thus the best for GWs coming from the direction that is perpendicular to the plane formed by the two arms (the direction on the z-axis).

1.4 Gravitational-wave detections

In this section, I will summarize the LIGO-Virgo observational results made during the first data takings, between the first detection (September 14, 2015) to O3 (March 2020), and their consequences for test of general relativity and astro-

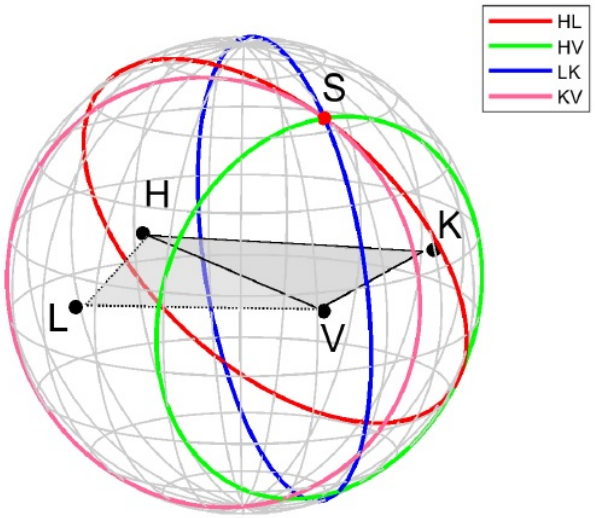

Figure 1.9 – Source localization for timing triangulation for the aLIGO-AdV-KAGRA GW detection network[32]. The location of each detector is indicated by black dots with H being LIGO Hanford, L being LIGO Livingston, V being Virgo and K being KAGRA. With two detectors, the locus of a GW event is an annulus on the sky. With four or more detectors, there is a unique intersection region, represented as the dot S.

physics. At the time of writing, the complete analysis of O3 is not performed.

1.4.1 GW150914

The first GW detection was performed by the two LIGO detectors on September 14, 2015. The data were analyzed jointly by the LIGO and Virgo Collaboration (which signed an agreement of data sharing and joint publication since 2007). The signal, called GW150914, was produced by the merger of two stellar-mass black holes, with masses of 29 and 36 solar masses ($M_\odot$). The event produced a final black-hole with 62 $M_\odot$, with 3 $M_\odot$ converted in GW energy, mainly during the fraction of second before the merger [10]. Although the existence of GW was proved using the data of the PSR1916+13 pulsar (Hulse and Taylor pulsar), GW150914 represented the first GW direct detection. Moreover, GW150914 also demonstrated the existence of binary black-hole and the fact that these binary systems can merge. Moreover, stellar-mass black-hole with masses higher than 20 $M_\odot$ were not observed yet with gravitational waves. The very good agreement

between the detected GW waveform and the GW prediction (before and during the merger) also allowed a first test of GR in the strong field regime and for relativistic speeds.

1.4.2 Detections during O1/O2

The two LIGO-Virgo observational runs (O1 and O2) resulted in the detection of GW from 10 Binary Black Holes (BBH) mergers and from one BNS merger, which is reported in the first catalog of gravitational-wave transient sources GWTC-1[7]. Among the catalog sources, important events are GW150914, already discussed, GW170814, the first triple detection, and GW170817, the first binary neutron star detection.

GW170814

On August 1, one month before the end of the O2 data taking, the Virgo detector started taking data with the 2 LIGOs. On August 14, the 3 detectors detected GW170814, a signal produced by the merger of two black holes. This first triple detection [9] allowed to localize the event with a much better precision (roughly a factor of 10) with respect to the 2 LIGO detections. Moreover, LIGO and Virgo not being aligned, GW170814 allowed a first test of the GW polarization. Previous tests were not possible, since the two LIGOs have been built to be aligned (to maximize their joint detection capability) and they cannot test, alone, different polarizations. This first test confirmed that GW have two tensor polarizations, as predicted by general relativity.

GW170817

The signal GW170817 was observed on August 17, in quasi-coincidence with a gamma-ray burst (GRB) detected by the Fermi and Integral satellites [6], confirming the hypothesis that at least some short-γ-ray bursts are linked to BNS mergers.

Figure 1.10 shows the GRB detection in different energy ranges and the spectrogram map of GW170817. The delay in the arrival times between GRB

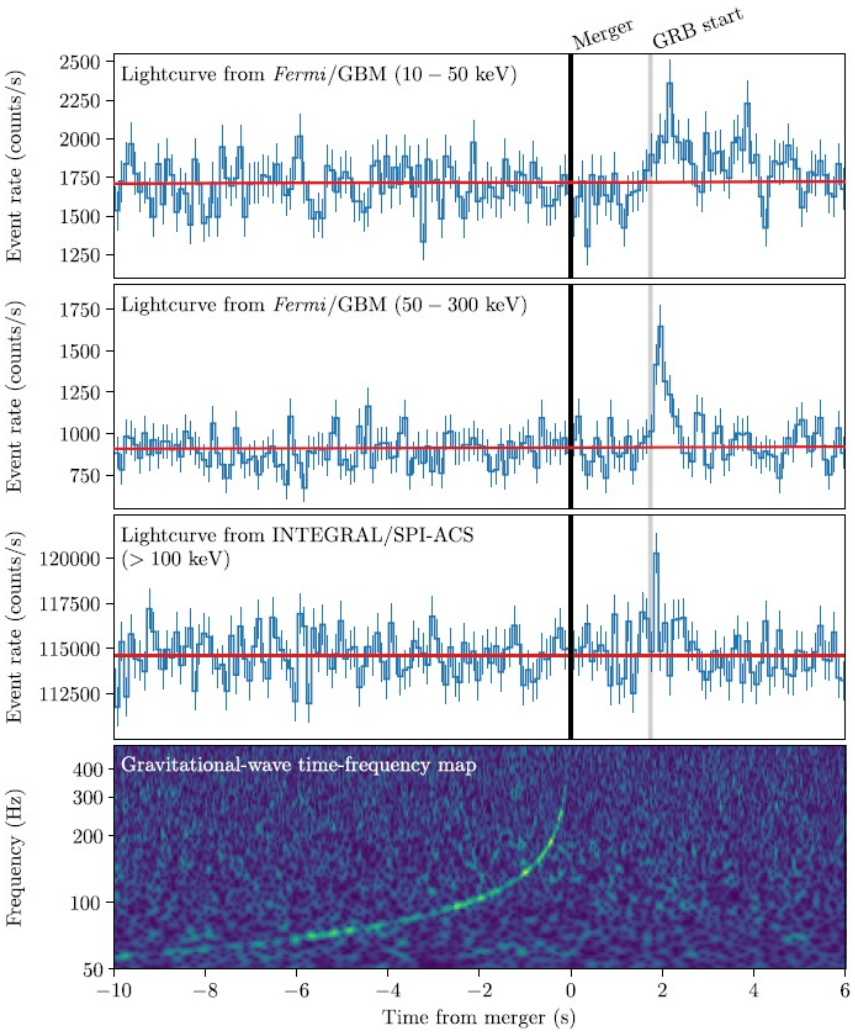

Figure 1.10 – Joint detection of GW170817 and GRB 170817A. Top/Second: the GRB lightcurve for GRB170817A between 10 and 50 eV (top figure) and in 50-300 keV the energy range (second figure). Bottom: the time-frequency map of GW170817.

and GW was used to measure the GW speed [5] are found in agreement with the speed of light with a precision of $\sim 10^{-15}$. The GW was produced by a merger of two neutron stars, located at about 40 Mpc from us. With respect to the previous detections, the signal produced by these two objects, lighter with respect to black holes, produced a much longer signal in the detector bandwidth, observable for tens of seconds (instead of a fraction of a second).

Even if a BNS system was already observed (i.e., Hulse and Taylor pulsar), GW170817 demonstrated the fact that a BNS system can merge within the Hubble time and gave the first measurement of their merging rate.

In addition to the detection of GRB 170817A, the LIGO-Virgo localization of the source allowed a follow-up by about 70 electromagnetic and neutrino observatories, identifying the host galaxy (NGC4993) and an electromagnetic transient called *kilonova* [8]. Among the various results of this observation, the multi-band electromagnetic observations of the kilonova revealed that BNS mergers are one formation site of some of the heaviest chemical elements (for example gold) through *r-process nucleosynthesis*.

Moreover, a joint measurement of redshift of the host galaxy and of the luminosity distance using gravitational waves enabled an alternative measurement of the Hubble constant [6], compatible with previous measurements (Planck satellite measurements using the CMB and supernovae).

1.4.3 Detections during O3 run

The third observation run (O3) started on April 1, 2019, after a series of detector upgrades and it continued until March 27, 2020, a month before the official closing time, due to the COVID pandemic. As already mentioned, the sensitivity of the three instruments, in terms of BNS range was 50-60 for Virgo, 110-140 for the two LIGOs. The 3-detectors *duty cycle* (the fraction of time in which 3 detectors were taking data together) was 47.4%, 2 detectors were online 36% of the time, only one detector was online 13.3% of the time (see Figure 1.11). The duty cycle of AdV was nearly 76%. The combination of the sensitivity increase and the high duty cycle, allowed the identification of about one GW every $\sim$ six days. The plot 1.12 shows the cumulative number of candidates during the three

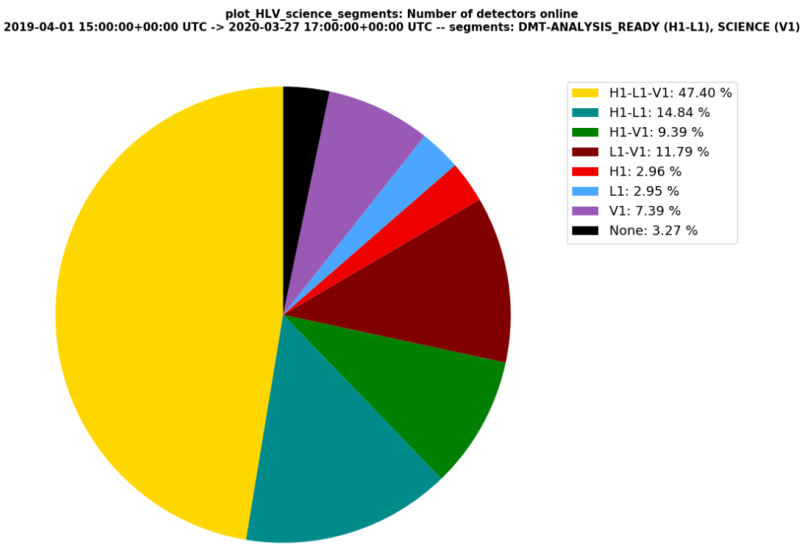

Figure 1.11 – Network duty cycle for LIGO Hanford, LIGO Livingston and Advanced Virgo

data takings. In the following, I will provide a summary of the published results. The last part of the data taking (O3b) is still under analysis.

GW190412

On April 12, 2019, two weeks after the beginning of the O3 run, GW from a BBH with asymmetric masses ($\sim 30M_{\odot}$ and $\sim 8M_{\odot}$) were detected. The measured mass ratio was much larger than any previous detection, and GR predicts that such a source would show much stronger contributions from GW higher-order modes, with respect to the fundamental quadrupolar mode. GW190412 allowed to test that the high order GW mode emission was in agreement with general relativity [49]. Moreover, the presence of these high order modes allows to partially break the degeneracy between the inclination angle of the source and the luminosity distance, allowing a better measurement of the two quantities.

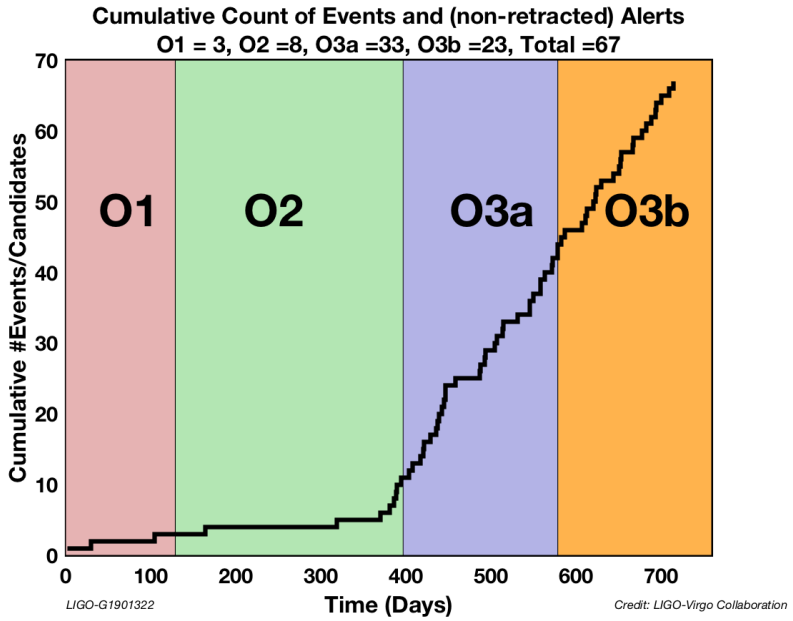

Figure 1.12 – Cumulative events (O1 and O2 runs) or candidates (O3 run) versus time for the three observing runs

GW190814

On August 14, 2019, AdV and aLIGO observed a compact binary coalescence between a 23 $M_\odot$ black hole and a compact object with mass of 2.50-2.67 $M_\odot$ [12]. The nature of the secondary component is under debate: it can be either the lightest black hole or the heaviest neutron star ever observed. Moreover, this compact binary system has the most unequal mass ratio ever detected with GW. Its existence is interesting from an astrophysical point of view, since it should be compatible with population synthesis models.

GW190521

On May 21, 2019, LIGO and Virgo observed a GW from a merger of two black holes (BH) of 66 $M_\odot$ and 85 $M_\odot$, that merged to a final black hole of mass 142 $M_\odot$. The final black hole is the heavier black hole detected so far using gravitational waves and the first firm evidence of an *intermediate-mass black-hole* (IMBH), a black hole with a mass higher than 100 $M_\odot$ [11]. Intermediate mass black holes are of great importance in studying the origin of supermassive black holes,

present in the center of big galaxies and whose formation may be explained by mergers of IMBH. This event is also interesting because the primary black holes, with a mass of 85 $M_\odot$, lies in the so-called *pair-instability mass gap*, a region between 60 $M_\odot$ to 120 $M_\odot$, where black holes are not expected to form by stellar collapse. In fact, astrophysical models show that stars with enough mass to produce a black hole in this range are completely disrupted by the supernova explosion.

GWTC-2

During the first part of O3 (between April 2019 and October 2019), 39 sources were observed and their properties have been published in the second gravitational-wave transient source catalog (GWTC-2). The sources include 37 BBH, whose statistical properties, for instance the mass distribution has been analyzed statistically. This opens the possibility to compare the observations with stellar evolution models.

GW200105 and GW200115

In January 2020 (formally part of O3b data taking), GW from two mergers from mixed NS-BH systems were observed, on January 5 and January 15. These were the first observation of mixed compact object systems. Even though the presence of tides or an electromagnetic counterpart has not been observed, the secondary components lie in the region of neutron star already detected, and in the mass range expected for mixed NS-BH systems.

All these detections allowed several tests of GR, by comparison of the GW observed with waveforms predicted by analytical and numerical GR templates. Other possible sources detectable in the future LIGO-Virgo-KAGRA data takings are spinning neutron stars and an astrophysical background of GW. Other possible GW sources include supernovae and a cosmological background of GW, which will not likely be detected during the timelife of the second generation gravitational-wave detectors.

1.5 Einstein Telescope

The plans of LIGO-Virgo-KAGRA extend to 2027 (end of O5). Discussions are ongoing to propose another upgrade of Virgo, for the period after 2027. Similar discussions are ongoing in LIGO. Even if current detectors can still be improved, at some point they will be limited by infrastructures and, to increase the sensitivity, longer arms will be necessary. Moreover, an underground site would also offer the possibility to enlarge the bandwidth towards lower frequencies.

Third-generation (3G) GW detectors, as Einstein Telescope or Cosmic Explorer are designed to have an order of magnitude better sensitivity and a wider band, compared to 2G detectors [57].

Einstein Telescope is designed to have 10-km arm length (compared to 3 km for AdV and 4 km for aLIGO) and to be built a few hundred meters underground to reduce gravity gradient noise and seismic noise. Moreover, Einstein Telescope (ET) will have a triangular shape, formed by three ITF which will allow to measure the two polarizations of a source. The detector is designed as a "xylophone" concept, in which there are two instruments with one optimized for low frequencies (cold, at 20 K) and one for high frequencies (at room temperature). Cosmic explorer is a project to build two instruments with 20 km and 40 km arm length, on the surface, extrapolating the technologies used for Virgo and LIGO (room temperature instrument).

With ET, coalescences of compact binaries with total mass 20-100 $M_{\odot}$, will be visible up to redshift $z \sim 20$ and higher. These redshifts correspond to an epoch before the formation of the first stars and a detection of a source would lead to possible indication of existence of primordial black holes. Moreover, the accessible range of black holes masses will greatly increase, ET will be able to detect black holes with masses up to several times $10^3 M_{\odot}$. ET could also detect new astrophysical sources of GW (signals emitted during core-collapse supernovae, continuous signals from isolated spinning neutron stars) but also study the nature of dark energy. The list of ET possible contributions to astrophysics, fundamental physics and cosmology are not yet complete [58].

1.5.1 Space-based observatory: LISA

LISA (Laser Interferometry Space Antenna), a mission led by ESA, will be the first GW observatory in space. LISA comprises three spacecrafts in a triangle formation, each relaying laser beams back and forth to the other spacecrafts, forming three Michelson ITF. Each arm (or the distance between two spacecrafts) is 2.5 million km long, changing the detection band from 100 Hz to mHz. Consequently, LISA will focus on sources with much wider orbits and more massive objects, such as supermassive black holes [1], or galactic binaries well before the merger.

1.5.2 Summary

Gravitational waves, small vibrations of the space-time metrics predicted by Einstein in 1916, represent a new way to make astrophysics and tests of fundamental physics. After the first gravitational-wave detection in 2015, tens of detections of compact binary objects have been accumulated. At the time of writing, 52 detections have been published: 2 BNS, 2 NSBH (neutron star - black hole), a binary system with a black hole and a compact object, and 47 BBH. GW170817 was a breakthrough in multi-messenger astrophysics, with a follow-up in all the electromagnetic bandwidths and several results for astrophysics, cosmology and test of general relativity.

The LIGO and Virgo detectors are currently being upgraded, to Advanced Virgo+ and Advanced LIGO+. The detectors are limited by the quantum noise in a large fraction of the spectrum (at high frequency and down to about 100 Hz). The reduction of quantum noise is a crucial research direction to further increase the astrophysical reach of these detectors and prepare the 3G generation detectors. Squeezing techniques, will become more and more important in the future, since they allow to reduce the quantum noise in the whole bandwidth and without the problems related to power increase, as we will see in the future chapters.

Chapter 2

Quantum theory of light: an introduction to squeezing techniques

Outline of the current chapter

The previous chapter introduces quantum noise as one of the major noise sources for interferometric GW detectors, and that *squeezing* technique is used to reduce this noise. It arises from the quantum nature of light and, more precisely, originates from Heisenberg's uncertainty principle.

To overcome this fundamental limit, it is possible to use a non-invasive method with non-classical states of the *radiation* field (a radiation field is a free electromagnetic field, far from sources), also called *squeezed states of light*. Moreover, other "brute-force" methods can be used, for example by increasing the input laser power or the weight of the mirrors test mass. Both methods (brute-force ones one and squeezing) to reduce quantum noise.

In the 1980s, theorists shaped the theory of such intriguing states. Then, Dick Slusher and his team at Bell Labs were the firsts to observe such states [74], by non-degenerate four-wave mixing due to Na atoms in an optical cavity.

In this chapter, I will give a quantum description of all the elements needed to understand squeezing techniques. In Section 2.1 and Section 2.2, I will give a quantum-mechanical description of the light, explain the quantization of the electromagnetic field, the different interesting states, and I will illustrate the quantized electric field in a quasi-classical state and in a squeezed state, to portray the theory of the squeezing technique. I will explain how the generation of such squeezed states is realizable with nonlinear optics in Section 2.3. We will also see that squeezed states can be measured by the homodyne detection method in Section 2.4. In the last part, I will introduce the quantum-mechanical description of a GW interferometer, to be able to explain in the next chapter the different quantum noise reduction techniques for GW detectors.

2.1 Quantum description of light

To quantize the electric and magnetic fields, we need to start from the classical description of light, based on the description of electromagnetic waves, ruled by Maxwell's equations. This description will enable to demonstrate the link between light and the quantum harmonic oscillator at both the classical and quantum-mechanical level. Then, I will be able to describe the properties of some interesting quantum states, as *Fock states*, *vacuum state*, *quasi-classical states*, to finally discuss the properties of *squeezed states*. This description will lead to present Heisenberg's uncertainty principle and connect it with the quasi-classical states and squeezed states.

2.1.1 Quantization of the electromagnetic field

The classical description of light is governed by the Maxwell's equations that describes the electromagnetic field. The electric field can be expressed as, assuming that the light is polarized along the x-axis and the direction of propagation

is along the z-axis:

$$\mathcal{E}_x(z,t) = \mathcal{E}_0 \sin(kz) \sin(\omega t) \tag{2.1}$$

where $\mathcal{E}_0$ is the amplitude, $k = 2\pi/\lambda$ is the wave vector and ω is the angular frequency.

Considering the Maxwell's equations in vacuum, in the absence of charges and currents:

$$\begin{aligned} \nabla \cdot \mathbf{E}(\mathbf{r},t) &= 0 \\ \nabla \cdot \mathbf{B}(\mathbf{r},t) &= 0 \\ \nabla \times \mathbf{E}(\mathbf{r},t) &= -\frac{\partial}{\partial t}\mathbf{B}(\mathbf{r},t) \\ \nabla \times \mathbf{B}(\mathbf{r},t) &= \frac{1}{c^2}\frac{\partial}{\partial t}\mathbf{E}(\mathbf{r},t), \end{aligned} \tag{2.2}$$

and in particular, using the third equation (*Ampere-Maxwell* equation) from above, the magnetic field can be written as:

$$B_y(z,t) = B_0 \cos(kz) \cos(\omega t), \qquad \text{with } B_0 = \mathcal{E}_0/c \tag{2.3}$$

where B_0 is the magnetic field amplitude. As the electric field is polarized along the x-axis, the magnetic field is consequently along the y-axis, using the fourth Maxwell's equations in 2.2.

The energy density can thus be expressed as:

$$U = \frac{1}{2}\left(\epsilon_0 \mathcal{E}^2 + \frac{1}{\mu_0} B^2\right). \tag{2.4}$$

where ϵ_0 is the vacuum permittivity and μ_0 is the vacuum permeability. By integrating Eq. 2.4 over the mode volume V, the total energy is expressed as:

$$E = \frac{V}{4}\left(\epsilon_0 \mathcal{E}_0^2 \sin^2(\omega t) + \frac{B_0^2}{\mu_0} \cos^2(\omega t)\right), \tag{2.5}$$

which clearly showcases that the energy is oscillating between the electric and the magnetic fields.

Then, remembering $B_0 = \mathcal{E}_0/c$, Eq. 2.5 becomes:

$$E = \hbar\omega\left(X_1^2(t) + X_2^2(t)\right), \tag{2.6}$$

where the dimensionless *field quadratures*, corresponding to the sine and cosine parts of the time-dependent electric field, is expressed as:

$$X_1(t) = \sqrt{\frac{\varepsilon_0 V}{4\hbar\omega}}\mathcal{E}_0 \sin(\omega t) \tag{2.7}$$

$$X_2(t) = \sqrt{\frac{\varepsilon_0 V}{4\hbar\omega}}\mathcal{E}_0 \cos(\omega t). \tag{2.8}$$

Eq. 2.6 is formally equal to the Hamiltonian of the mechanical Harmonic Oscillator by setting:

$$X_1(t) = \sqrt{\frac{\omega}{2\hbar}}q(t) \tag{2.9}$$

$$X_2(t) = \sqrt{\frac{1}{2\hbar\omega}}p(t), \tag{2.10}$$

with $q(t)$ and $p(t)$ the harmonic oscillator position and momentum. This leads to the quantization of the electromagnetic field, following the same method as for the harmonic oscillator, i.e., applying the quantum theory of the simple harmonic oscillator to the electromagnetic wave.

We can then introduce the *annihilation* and *creation* operators, $\hat{a}$ and $\hat{a}^\dagger$, hermitian conjugate of each other,

$$\hat{a} = \hat{X_1} + i\hat{X_2} \tag{2.11}$$

$$\hat{a}^\dagger = \hat{X_1} - i\hat{X_2}, \tag{2.12}$$

where $\hat{X_1}$ and $\hat{X_2}$ are the *quadratures observables*. The quantization of the electromagnetic field gives the following expression for the electric field:

$$\hat{\mathbf{E}}(\mathbf{r}, t) = i\boldsymbol{\epsilon}E^{(1)}\left(\hat{a}e^{i(\mathbf{k}\cdot\mathbf{r}-\omega t)} - \hat{a}^\dagger e^{-i(\mathbf{k}\cdot\mathbf{r}-\omega t)}\right), \tag{2.13}$$

where ω and $\mathbf{k}$ are respectively the frequency and wave vector, $\boldsymbol{\epsilon}$ is the polariza-

tion vector, and the one-photon electric field amplitude is equal to:

$$E^{(1)} = \sqrt{\frac{\hbar\omega}{2\epsilon_0 L^3}}, \tag{2.14}$$

where L^3 is the volume of quantization.

The Hamiltonian of the electromagnetic field can be expressed as:

$$\hat{H} = \hbar\omega(\hat{a}^\dagger\hat{a} + \frac{1}{2}), \tag{2.15}$$

The description of physical systems in quantum optics is based on two mathematical tools. On one hand, the Hermitian *operators*, linked to measurable quantities called *observables* and satisfying well-defined commutation relations. On the other hand, the *state vectors*, from a Hilbert space, allow the description of the specific state of the system. These tools are described in the Appendix A, where a small compendium about quantum mechanics formalism is presented.

Properties of the annihilation and creation operators

The annihilation and creation operators, $\hat{a}^\dagger$ and $\hat{a}$, are not observables (see definition in Appendix A) and any observable can be expressed with these operators. One crucial property is that their commutator is equal to 1:

$$[\hat{a}, \hat{a}^\dagger] = 1. \tag{2.16}$$

Properties of the quadrature observables

$\hat{X_1}$ is called the *amplitude quadrature*, $\hat{X_2}$ the *phase quadrature* and are *observables*. These observables are canonically conjugate observables with a commutator equal to $i/2$:

$$[\hat{X_1}, \hat{X_2}] = \frac{i}{2} \tag{2.17}$$

2.1.2 Quantum states of light

Number states and vacuum

The Hamiltonian of the electromagnetic field can be written as:

$$\hat{H} = \hbar\omega\left(\hat{N} + \frac{1}{2}\right), \tag{2.18}$$

where the *Number operator* is defined as:

$$\hat{N} = \hat{a}^{\dagger}\hat{a}. \tag{2.19}$$

Note that a number state is an eigenstate of the Hamiltonian of the electromagnetic field, as clearly shown by Eq. 2.15.

With the commutation relation 2.16, the set of eigenvalues of $\hat{N}$ is precisely the set of non-negative integers and the eigenvectors $|n\rangle$ is defined as:

$$\hat{N}|n\rangle = n|n\rangle, \qquad with \quad n = 0, 1, 2, ... \tag{2.20}$$

These so-called *number states* or *Fock states* form a basis for the Hilbert space of the radiation state. These states represent a monochromatic quantized field with an angular frequency ω and containing n photons. Their main properties are:

$$\hat{a}|n\rangle = \sqrt{n}\,|n-1\rangle \tag{2.21}$$

$$\hat{a}|0\rangle = 0 \tag{2.22}$$

$$\hat{a}^{\dagger}|n\rangle = \sqrt{n+1}\,|n+1\rangle. \tag{2.23}$$

The creation and annihilation operators in a number state represent the creation and the annihilation of a photon at angular frequency ω.

The lowest energy state $|0\rangle$ in (2.22) is the *vacuum or ground state* described.

By applying 2.21 n times, we obtain the following relation:

$$|n\rangle = \frac{(\hat{a}^\dagger)^n}{\sqrt{n!}}|0\rangle. \tag{2.24}$$

We can thus produce all the possible number states $|n\rangle$ by applying the creation operator to the ground state successively. This implies that $|n\rangle$ can be representing a state in which n photons have been excited from the vacuum.

We can thus determine the energy spectrum of $\hat{H}$, assuming $|n\rangle$ is the eigenstate and E_n the eigenvalue or energy of the hamiltonian $\hat{H}$:

$$\hat{H}|n\rangle = E_n|n\rangle = \left(n + \frac{1}{2}\right)\hbar\omega|n\rangle, \tag{2.25}$$

with $E_n = \left(n + \frac{1}{2}\right)\hbar\omega$, with $n = \{0, 1, 2, ...\}$ and n being the number of photons in the state $|n\rangle$. This equation shows the quantization of the energy of a monochromatic (single mode) electromagnetic field, with discrete levels characterized by the number of photons they have.

The ground state of quantum radiation, denoted by $|0\rangle$ and called the vacuum, contains zero photon $n = 0$. As explained in [46], "[...] it might better be referred to as darkness. Indeed, we shall see that the vacuum is not in fact nothing. It has specific properties, like the ground state of any other quantum system". Hence a vacuum state is a quasi-classical state.

Its energy E_v is the minimal energy of the quantized electromagnetic field:

$$E_v = \frac{1}{2}\hbar\omega. \tag{2.26}$$

Finally, the variance of the photon number is equal to zero for a number state:

$$\left\langle \Delta n^2 \right\rangle = \langle n|\Delta\hat{N}^2|n\rangle = \langle n|\hat{N}^2|n\rangle - \langle n|\hat{N}|n\rangle^2 = 0. \tag{2.27}$$

Consequently, number states do not represent states produced directly by a laser, especially states inside an interferometer. These states are more likely a basis set and in the following, we will describe more realistic states.

Quasi-classical states of light

Quasi-classical states of radiation or Glauber coherent states have properties very similar to those of the classical radiation and obey Maxwell's equations.

By definition, a quasi-classical state $|\alpha\rangle$ is an eigenstate of the annihilation operator $\hat{a}$. The corresponding eigenvalue is a complex number:

$$\hat{a}|\alpha\rangle = \alpha|\alpha\rangle \qquad \alpha \in \mathbb{C}. \tag{2.28}$$

As the operator $\hat{a}$ is not Hermitian, we express the state $|\alpha\rangle$ in terms of the basis of the number states $|n\rangle$:

$$|\alpha\rangle = \sum_{n=0}^{\infty} c_n |n\rangle. \tag{2.29}$$

Using the adjoint of the relation 2.23 and the subsequent recurrence relation, we obtain:

$$|\alpha\rangle = e^{-\frac{|\alpha|^2}{2}} \sum_{n=0}^{\infty} \frac{\alpha_l^n}{\sqrt{n!}} |n\rangle. \tag{2.30}$$

This state does thus exist for any complex number α. Then, using the adjoint of Eq. 2.28, the expectation of the photon number operator defined previously with (2.19) is equal to:

$$\left\langle \hat{N} \right\rangle = \langle\alpha|\hat{a}^\dagger\hat{a}|\alpha\rangle = |\alpha|^2. \tag{2.31}$$

This result will be compared with another special set of states, the squeezed states.

In another hand, the probability $P(n)$ of finding n number of photons, using Eq. 2.30:

$$P(n) = |c_n|^2 = e^{-|\alpha|^2} \frac{(|\alpha|^2)^n}{n!}. \tag{2.32}$$

This is a Poisson distribution with an average equal to α. This photon distribution in the quasi-classical states is purely a particle-like picture, representing independent particles distributed randomly and is not complete because it does not take into account the wave aspects of the radiation field. However, it can be useful for many photon counting experiments.

Concerning time evolution, a quasi-classical state remains a quasi-classical

state when it evolves.

Moreover, we can define any quasi-classical state as a displaced vacuum by α so that any quasi-classical state can be expressed with the vacuum state:

$$|\alpha\rangle = e^{-\frac{|\alpha|^2}{2}} e^{\alpha \hat{a}^\dagger} |0\rangle = \hat{D}(\alpha)|0\rangle. \tag{2.33}$$

The displacement vector is a unitary operator, defined as [27]:

$$\hat{D}(\alpha) = e^{-\frac{|\alpha|^2}{2}} e^{\alpha \hat{a}^\dagger + \alpha^* \hat{a}}. \tag{2.34}$$

The most useful property of the displacement operator is its action on $\hat{a}$ and $\hat{a}^\dagger$:

$$\hat{D}^\dagger(\alpha)\hat{a}\hat{D}(\alpha) = \hat{a} + \alpha \tag{2.35}$$

$$\hat{D}^\dagger(\alpha)\hat{a}^\dagger\hat{D}(\alpha) = \hat{a}^\dagger + \alpha^*. \tag{2.36}$$

Squeezed states of light

I will expose two ways to define the squeezed states: first, the squeezed state as an eigenstate of a generalized annihilation operator and secondly, the squeezed state being the displacement of a squeezed vacuum.

As defined in Eq. 2.28 for a single-mode quasi-classical state, a single-mode squeezed state is defined as an eigenstate of a *generalized annihilation operator* [17] $\hat{A_R}$:

$$\begin{aligned} \hat{A}_R |\alpha, R\rangle &= \alpha |\alpha, R\rangle \qquad && \alpha \in \mathbb{R} \\ \hat{A}_R &= \hat{a}\cosh R + \hat{a}^\dagger \sinh R \qquad && R \in \mathbb{R} \\ \hat{A}_R^\dagger &= \hat{a}^\dagger \cosh R + \hat{a}^\dagger \sinh R \qquad && R \in \mathbb{R}. \end{aligned} \tag{2.37}$$

Similarly to the commutator of $\hat{a}_l$ (2.16), the commutator of the generalized creation and annihilation operators $\hat{A}_R\dagger$ and $\hat{A}_R$ is equal to 1. Also as for $\hat{a}$, $\hat{A}_R$ is not Hermitian.

To introduce the second way to describe the squeezed states, we need to

present the definition of the unitary squeeze operator [27]:

$$S(\xi) = \exp\left\{\frac{1}{2}\xi^* \hat{a}^2 - \frac{1}{2}\xi^* \hat{a}^{\dagger 2}\right\} \qquad \xi = re^{i2\theta}, \tag{2.38}$$

where ξ is an arbitrary complex number. Note that $S^\dagger(\xi) = S^{-1}(\xi) = S(-\xi)$. The most useful unitary transformation properties are the following:

$$\begin{aligned} S(\xi)^\dagger \hat{a} S(\xi) &= \hat{a}\cosh r - \hat{a}^\dagger e^{i2\theta}\sinh r \\ S(\xi)^\dagger \hat{a}^\dagger S(\xi) &= \hat{a}^\dagger \cosh r - \hat{a} e^{-i2\theta}\sinh r. \end{aligned} \tag{2.39}$$

With the freedom to make rotations in the complex-amplitude plane and using Eq. 2.12, a rotated amplitude can be expressed as:

$$\hat{X_1'} + i\hat{X_2'} = (\hat{X_1} + i\hat{X_2})e^{-i\theta}. \tag{2.40}$$

Then, we can add to Eq. 2.39 the following equation:

$$S(\xi)^\dagger(\hat{X_1'} + i\hat{X_2'})S(\xi) = \hat{X_1'}e^{-r} + i\hat{X_2'}e^{r}. \tag{2.41}$$

This equation exposes the effect of the squeezed operator: it attenuates one quadrature ($\hat{X_1'}$) and amplifies the other one ($\hat{X_2'}$). The *squeezing parameter* is the degree of attenuation and amplification, provided by $r = |\xi|$. θ is the orientation of the squeezing axis (the angle for which the variance is the lowest for the concerned operator) or also called the *squeezing angle* and α^2 is the intensity of the state. Then, for the field quadrature $\hat{X_\theta} = \hat{X_1}\cos\theta + \hat{X_2}\sin\theta$, we can also define the *squeeze factor*, often given on a decibel (dB) scale:

$$-10 \times \log_{10}\left(\frac{\Delta\hat{X_\theta}^2}{\Delta\hat{X}^2_{vac}}\right) = -10 \times \log_{10}(-2r) \tag{2.42}$$

Now, thanks to the introduction of the squeeze operator, we can give the second definition of the squeezed state $|\alpha, \xi\rangle$, it consists in defining it as the displacement of a squeezed vacuum:

$$|\alpha, \xi\rangle = D(\alpha)S(\xi)|0\rangle, \tag{2.43}$$

where the single-mode *squeezed vacuum state* is defined as:

$$|\xi\rangle = S(\xi)|0\rangle \tag{2.44}$$

By calculating the expectation value and variance of the number operator in the squeezed states basis, we obtain:

$$\begin{aligned} \langle\alpha,\xi|\hat{N}|\alpha,\xi\rangle &= |\alpha|^2 + \sinh r^2 \\ \langle\alpha,\xi|(\Delta N)^2|\alpha,\xi\rangle &= \left|\alpha\cosh r - \alpha^* e^{i2\theta}\sinh r\right|^2 + 2\cosh r^2 \sinh r^2. \end{aligned} \tag{2.45}$$

Even that the expectation value of the number operator is increased by $\sinh r^2$ compared to a quasi-classical state (see Eq 2.31), this quantity is negligible when the number of photons is high (when $|\alpha| >> 1$). Hence the average power of a squeezed state is almost the same as a quasi-classical state. Furthermore, for a squeezed vacuum state, where $|\alpha| = 0$, the average number of photons in a squeezed state is not null (shown by the term $\sinh r^2$).

The second definition for the squeezed states of light is more common; the first one does not make appear the squeezing angle θ, that is implicit, in the fact that R is real, whereas r is real positive. However, I will keep the first definition to calculate the electric field in a squeezed state, which is more convenient.

2.1.3 The Uncertainty principle and minimum uncertainty states

Described in the Appendix of Ref. [29], the ordinary uncertainty principle states that, for two Hermitian operators $\hat{B}$ and $\hat{C}$, the product of their uncertainties satisfies:

$$\sqrt{\left\langle\Delta\hat{B}^2\right\rangle}\sqrt{\left\langle\Delta\hat{C}^2\right\rangle} \geq \frac{1}{2}\left|\left\langle[\hat{B},\hat{C}]\right\rangle\right|. \tag{2.46}$$

Quasi-classical states

Using the result of the commutator of $\hat{X}_1$ and $\hat{X}_2$ (2.17), we notice that a quasi-classical state is a **minimum dispersion state** for these quadrature observables, as the squared product of their variances is equal to:

$$\sqrt{\left\langle\Delta\hat{X_1}^2\right\rangle} \times \sqrt{\left\langle\Delta\hat{X_2}^2\right\rangle} = \frac{1}{4}. \tag{2.47}$$

Squeezed states

Using the expressions of the quadrature observables (2.12) and the relations (2.39), we obtained the following standard deviation for the observables quadratures for a squeezed state, with $\theta = 0$:

$$\sqrt{\left\langle \Delta\hat{X}_1{}^2 \right\rangle} = \frac{e^{-r}}{2}$$
$$\sqrt{\left\langle \Delta\hat{X}_2{}^2 \right\rangle} = \frac{e^{r}}{2}, \tag{2.48}$$

where the state is squeezed in the $\hat{X}_1$ quadrature or *amplitude-squeezed*. With $\theta = \pi$, the state would be squeezed in the $\hat{X}_2$ quadrature or *phase-squeezed*.

Using Eq. 2.46 and Eq. 2.47, the uncertainty principle gives the inequality $\Delta\hat{X}_1 \Delta\hat{X}_2 \geq \frac{1}{4}$. Then, Eq. 2.48 shows that the squeezed state $|\alpha, \xi\rangle$ is also a **minimum dispersion state** for $\hat{X}_1$ and $\hat{X}_2$ as for the quasi-classical states but the difference lies in their inequal uncertainties for these observables.

Phasor diagram

It is possible to represent field states as a vector in which the real part corresponds to the x-axis and the imaginary part corresponds to the y-axis. The field

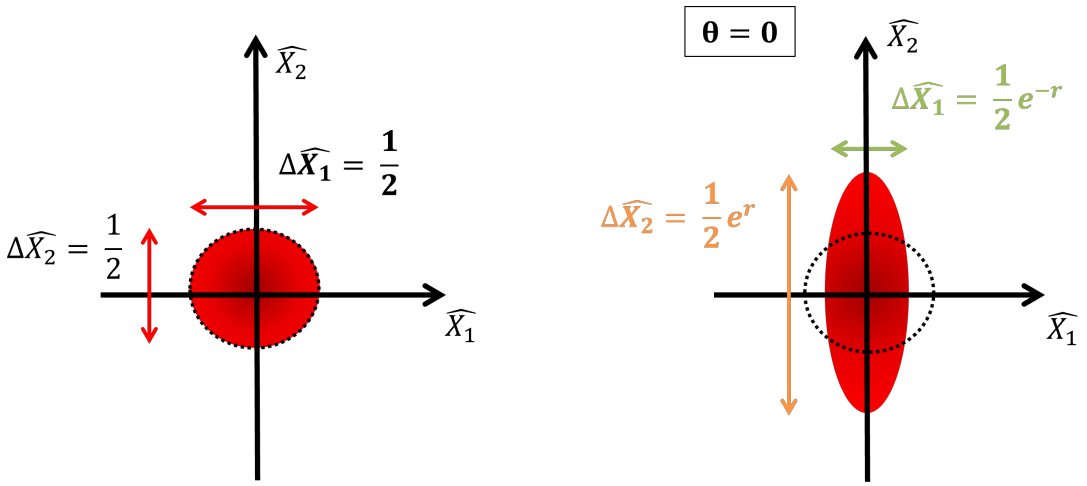

Figure 2.1 – Phasor diagram of the vacuum field: (left) in a quasi-classical state; (right) in a squeezed state (amplitude-squeezed, with $\theta = 0$).

amplitude (absolute value) is represented by the vector norm. This representation is called a *phasor diagram*. It is then convenient to choose the Cartesian coordinates as $\hat{X_1}$ and $\hat{X_2}$ to represent a quasi-classical state or a squeezed state. This representation does not show the evolution in time, while in a *complex-plane representation*, we can show the rotation of the vector during time, as shown later in Section 2.2. Consequently, we can represent the dispersion region as represented in red in Figure 2.1. For a vacuum quasi-classical state, a disk represents the fluctuations, whose radius is equal to the standard deviation: the dispersion is thus the same for all quadrature components. For a vacuum squeezed state with $\theta = 0$ (right figure), the dispersion region is "squeezed" into an ellipse of the same area as for the disk. It is then an *amplitude-squeezed* state with a smaller dispersion for the projection in $\hat{X_1}$ (amplitude quadrature).

2.2 Electric field representations

In this section, we will both represent the evolution in time of the electric field and in a *phasor diagram* when it is in a quasi-classical state and when it is in a squeezed state. These representations will illustrate the difference between these two states.

2.2.1 Electric field representation in a quasi-classical state

The quantization of the electric field is clear with the Hamiltonian of the electromagnetic field, shown in Eq. 2.15.

To represent the evolution in time of the electric field in a quasi-classical state, let's calculate its expectation value and variance.

First, the calculation of the electric field average of a quasi-classical state defined by α, considering only the time evolution with $\mathbf{r} = 0$ and the expression (2.13), leads to:

$$\langle\alpha|\hat{\mathbf{E}}(\mathbf{0},t)|\alpha\rangle = -2\mathcal{E}^{(1)}|\alpha|\sin(-\omega t+\phi). \tag{2.49}$$

Finally, we consider the conditions ($t = 0, \mathbf{r} = \mathbf{0}$) for the calculation of the

variance. Then, using the formula (2.27) and Eq. 2.13, we calculate first:

$$\begin{aligned}\langle\alpha|[\hat{\mathbf{E}}(0)]^2|\alpha\rangle &= -[\mathcal{E}^{(1)}]^2\langle\alpha|(\hat{a}-\hat{a}^\dagger)^2|\alpha\rangle = -[\mathcal{E}^{(1)}]^2[(\alpha-\alpha^*)+1] \\ &= [E_{class}(0)]^2 + [\mathcal{E}^{(1)}]^2,\end{aligned}$$

where $E_{class}(0)$ is the quantized classical electric field at $(t=0, \mathbf{r}=\mathbf{0})$. Finally, the last term to calculate $\left\langle\hat{\mathbf{E}}(0)\right\rangle^2$ is very simple, the variance is thus:

$$\left\langle\Delta\hat{\mathbf{E}}(0)^2\right\rangle = [\mathcal{E}^{(1)}]^2, \tag{2.50}$$

where the one-photon amplitude is also defined as the amplitude of a classical field whose total energy in the volume of quantization is $\hbar\omega$ (ie. the energy of one photon). For any $\mathbf{r}$ and t, the standard deviation of the electric field in a quasi-classical state is equal to the one of the vacuum: $\Delta\hat{\mathbf{E}}(\mathbf{r},t) = \mathcal{E}^{(1)}$.

The electric field evolution in time is depicted in Figure 2.2: the red line being the evolving average electric field while the fluctuations are represented with the green band whose half-width is equal to the standard deviation ($\frac{1}{2}\mathcal{E}^{(1)}$). The physical meaning of this band lies in the fact that almost all the measures (see Eq. 2.50) of the electric field at a given $(\mathbf{r},t)$ is comprised within this band. Then, at the left side of the figure, the complex plane represents the average and the dispersion of the field measurements using a green disk centered on the rotating complex number, this representation is more adapted for quadratures representation. The projection of the disk on the imaginary axis yields the green band in the right figure.

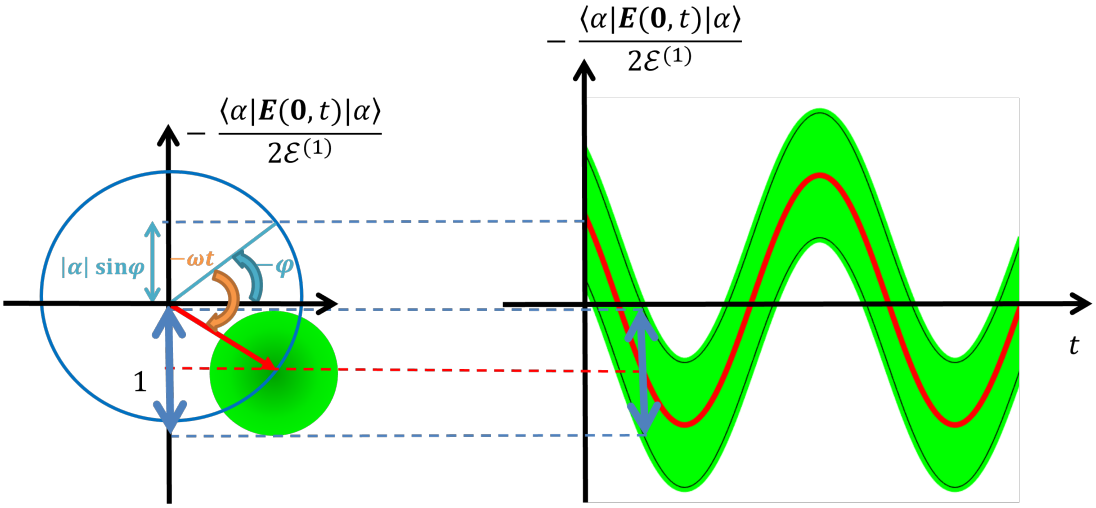

Figure 2.2 – Representation of the electric field in a quasi-classical state: (left) Complex plane representation; (right) graph of the electric field versus time with its average (red line) and fluctuations (green band).

2.2.2 Electric field representation in a squeezed state

As for the previous section, we first calculate the electric field variance in a squeezed state:

$$\left\langle \Delta\hat{\mathbf{E}}(0,t)^2 \right\rangle = \left\langle [\hat{\mathbf{E}}(0,t)]^2 \right\rangle - \left\langle \hat{\mathbf{E}}(0,t) \right\rangle^2 \tag{2.51}$$

Using the relation (2.37) to calculate the first term, we finally obtain the following result:

$$\left\langle \Delta\hat{\mathbf{E}}(0,t)^2 \right\rangle = [\mathcal{E}^{(1)}]^2 [e^{2R}\cos^2(-\omega t) + e^{-2R}\sin^2(-\omega t)] \tag{2.52}$$

The average of the electric field is then equal to, considering $\alpha' = \alpha e^{-R} \in \mathcal{R}^+$ and Eq. 2.37:

$$\left\langle \langle \alpha, R|\hat{\mathbf{E}}(\mathbf{0},t)|\alpha,R\rangle \right\rangle = -2\mathcal{E}^{(1)}\alpha' \sin(-wt) \tag{2.53}$$

Similarly to the variances calculated in Eq. 2.48:

- for the case of $R < 0$, we are in the case of a **phase-squeezed** state in $(\hat{X_1},\hat{X_2})$ coordinates, the projection of the ellipse on the $\hat{X_1}$ axis gives a standard deviation of $\frac{1}{2}e^R$ and for the other axis, a standard deviation of $\frac{1}{2}e^{-R}$.
- for the case of $R > 0$, we are in the case of an **amplitude-squeezed** state in $(\hat{X_1},\hat{X_2})$ coordinates, the projection of the ellipse on the $\hat{X_1}$ axis gives a

standard deviation of $\frac{1}{2}e^{-R}$ and for the other axis, a standard deviation of $\frac{1}{2}e^{R}$.

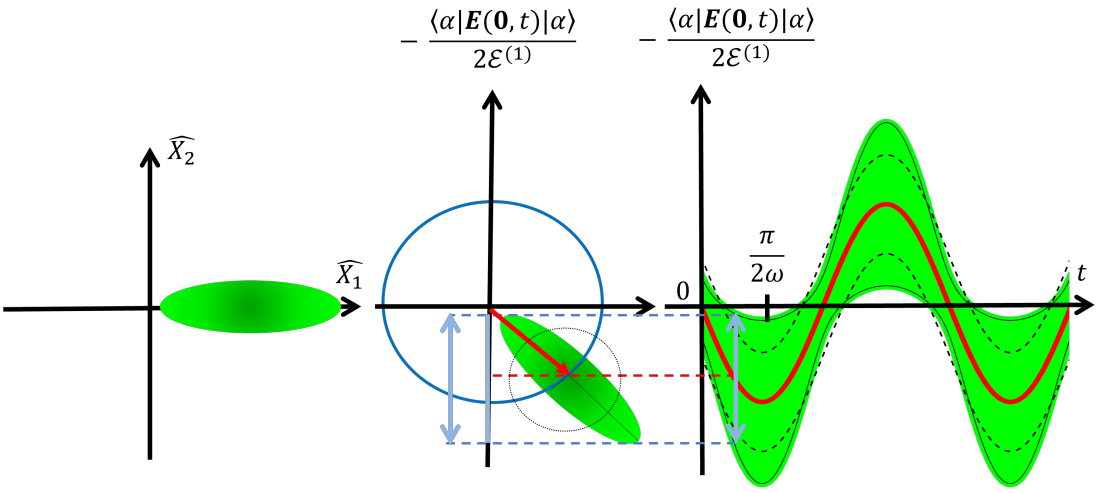

Figure 2.3 – Representation of the electric field in a squeezed stated with R<0: (left) Phasor diagram in ($\hat{X_1}$,$\hat{X_2}$) coordinates showing a phase-squeezed state; (middle) Complex-plane representation with minimum uncertainty when $t = \frac{m\pi}{\omega}$ ($m \in N$); (right) Graph of the electric field versus time with its average (red line) and fluctuations (green band), the fluctuations for an electric field in a quasi-classical state is shown as a comparison (black-dotted line).

The electric field evolution is depicted in the right side of Figure 2.3 for the first case and Figure 2.4 for the second case. The red lines still represent the evolving average electric field. The green band still represents the fluctuations. The black-dotted line represents the maximum and minimum fluctuations if the electric field would have been in a quasi-classical state. The phasor diagram is represented in the left side of these two figures and we use the quadrature observables, described in (2.12) for the axis ($\hat{X_1}$ and $\hat{X_2}$).

In these two last figures, the quadrature representation (phasor diagram in left figures) is static. It does not depict the time evolution of the electric field, which differs from Figure 2.2. These quadratures are unobservable with current techniques and their average and dispersion values are determined with series of measurements using the *balanced homodyne* technique.

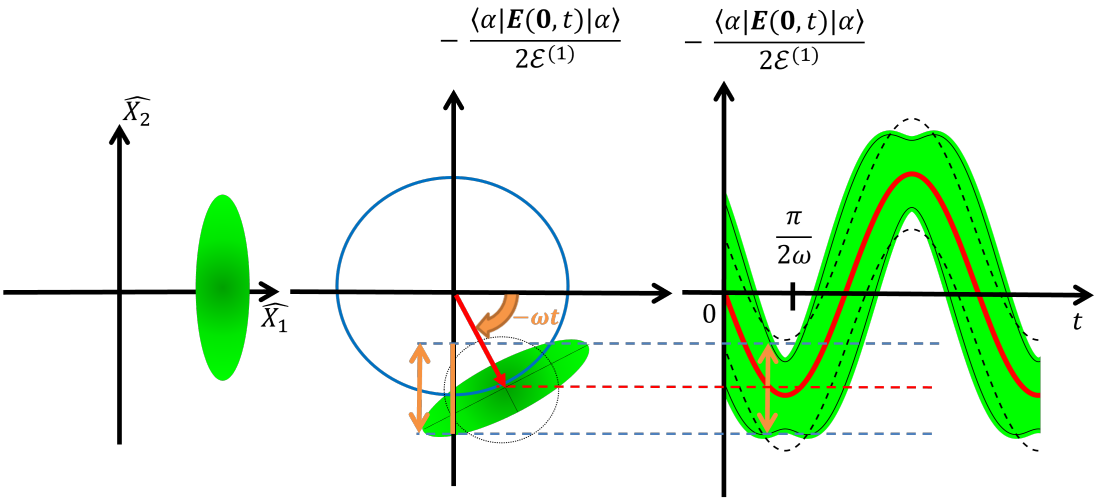

Figure 2.4 – Representation of the electric field in a squeezed stated with R>0: (left) Phasor diagram in $(\hat{X_1},\hat{X_2})$ coordinates showing an amplitude-squeezed state; (middle) Complex-plane representation with minimum uncertainty when $t = \frac{m\pi}{2\omega}$ $(m \in N)$; (right) Graph of the electric field versus time with its average (red line) and fluctuations (green band), the fluctuations for an electric field in a quasi-classical state is shown as a comparison (black-dotted line).

2.3 Generation of squeezed states of light

Squeezed states were experimentally produced in 1985 by Slusher *et al.* using four-wave mixing in a beam of Na atoms in an optical cavity [74]. Any nonlinear process can produce quadrature squeezing, but the most successful is the *parametric oscillation* inside a nonlinear crystal, placed in a resonant cavity (OPO). This process is also used to produce entangled beams, which is described further in the next chapter. I will first give a small compendium of nonlinear optics to explain the main features of nonlinear interactions and in particular, the second-harmonic generation (SHG), the optical parametric amplification (OPA) and the optical parametric oscillation (OPO). This will make easier the explanations about the generation of squeezed states.

2.3.1 A compendium of nonlinear optics

The origin of the optical nonlinear effects will be described through a standard model based on the classical anharmonic oscillator [39]. A dielectric material, composed of microscopic entities (atoms, molecules, ions...) is considered as a nonlinear medium, described as a collection of electric dipoles which is undergoing through an external electric field $\boldsymbol{\mathcal{E}}$. This medium then oscillates and radiates a source term called the *macroscopic polarization* $\boldsymbol{\mathcal{P}}$. This dielectric polarization comes from Maxwell's equations and the non-linearity arises when $\boldsymbol{\mathcal{P}}$ amplitude is no longer proportional to the applied electric field amplitude. We can then expand the dielectric polarization $\boldsymbol{\mathcal{P}}$ in function of $\boldsymbol{\mathcal{E}}$ [20], considering that the amplitude of the incident field (*pump field*) is much weaker than the atomic field strength:

$$\begin{aligned} \boldsymbol{\mathcal{P}}(\boldsymbol{\mathcal{E}}) &= \epsilon_0 \chi^{(1)} \boldsymbol{\mathcal{E}} + \epsilon_0 \chi^{(2)} \boldsymbol{\mathcal{E}}^2 + \chi^{(3)} \boldsymbol{\mathcal{E}}^3 ... \\ \boldsymbol{\mathcal{P}}(\boldsymbol{\mathcal{E}}) &= \boldsymbol{\mathcal{P}}^{(1)} + \boldsymbol{\mathcal{P}}^{(2)} + \boldsymbol{\mathcal{P}}^{(3)} ... \end{aligned} \tag{2.54}$$

where $\boldsymbol{\mathcal{P}}^i$ is the i-th order of polarization, ϵ_0 is the vacuum permittivity and χ is the susceptibility. Only the first and second-order susceptibilities are considered in the nonlinear interactions concerned by the generation of squeezing.

Nonlinear interactions

Considering only second-order nonlinearities, the nonlinear response arises from the fact that χ^2 is not a simple function but a tensor. The coefficients of this tensor, which translate an interaction of several waves inside the nonlinear crystal, depend on several parameters such as the propagation direction of the beams inside the crystal, the polarization of the beams, since the crystal is anisotropic, i.e., the susceptibility coefficients are not equal. We consider the propagation of three waves with angular frequency ω_1, ω_2 and ω_3, linked by the relation $\omega_1 + \omega_2 = \omega_3$ and interacting with a lossless second-order nonlinear medium, assuming that there is no energy exchange between the three waves and the material. The three coupled nonlinear equations at ω_1, ω_2 and ω_3 should satisfy two conditions which are the energy conservation and the momentum

conservation condition.

The **energy conservation** condition is expressed as:

$$\hbar\omega_3 = \hbar\omega_1 + \hbar\omega_2. \tag{2.55}$$

Another fundamental condition is **the momentum conservation**, a linear relation between the wavevectors of the various frequency components:

$$\Delta\mathbf{k} = \mathbf{k_3} - (\mathbf{k_1} + \mathbf{k_2}) = 0, \tag{2.56}$$

where $\mathbf{k_i}$ is the wavevector corresponding to the wave at frequency ω_i and $\Delta\mathbf{k}$ is the spatial *phase-mismatch*. The condition $\Delta k = 0$ is called the *phase-matching* condition. The efficiency of the nonlinear interaction between the propagating waves depends on the choice to fulfill (completely or almost) or not this condition.

The nonlinear processes described below are characterized by *parametric down-conversion* mechanism.

Second-Harmonic Generation

The Second-Harmonic Generation (SHG) is the process of frequency-doubling. It is the degenerate case of a *sum-frequency generation*, where two incident intense beams ω_1 and ω_2 generate a third beam $\omega_3 = \omega_1 + \omega_2$. In the case of a SHG, $\omega_1 = \omega_2$ thus one single intense (compared to the generated beam) incident beam at frequency ω (*pump beam*) will be then doubled in frequency to generate a beam at frequency $\omega_3 = \omega + \omega = 2\omega$, i.e., the generation of one photon at 2ω is sustained simultaneously by the annihilation of two incident photons at the same frequency ω, as illustrated in Figure 2.5. The crystal is placed inside a cavity to obtain a mode with high intensity at the frequency 2ω. This process will be used in the experiment described in Chapter 4. In particular, this cavity is used to produced the pump beam for the OPO cavity described immediately after.

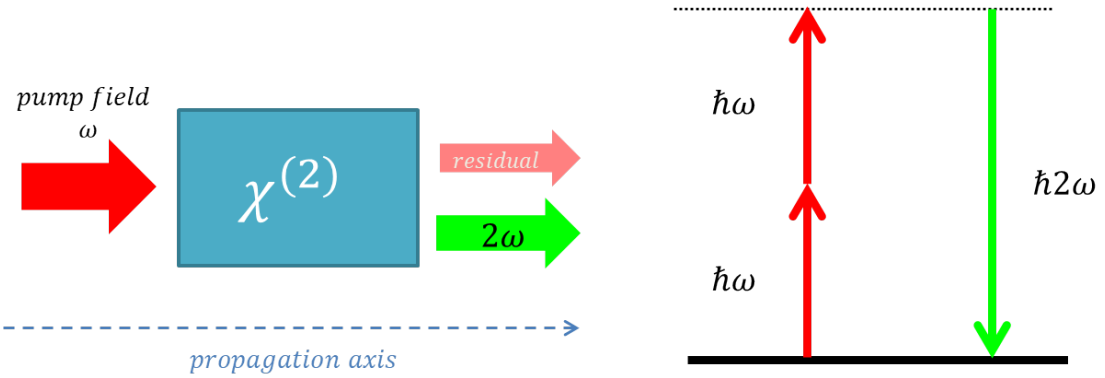

Figure 2.5 – Block diagram of a SHG interaction (left) and its energy diagram (right).

Optical Parametric Amplification (OPA) and Oscillation (OPO)

In the Optical Parametric Amplification (OPA), a beam with a very high intensity (compared to the fundamental beam) at ω_3 (*pump beam*) and a weak beam at ω_1 (fundamental field) is sent inside a lossless optical crystal with a high-order susceptibility. $\chi^{(2)}$ Through parametric fluorescence effect, photons at ω_1 (*signal beam*) and ω_2 (*idler beam*) are emitted, where the amplification of the incident ω_1 will be done at the expense of the pump beam ω_3. The idler beam is generated at $\omega_2 = \omega_3 - \omega_1$ (see the energy diagram in Figure 2.6).

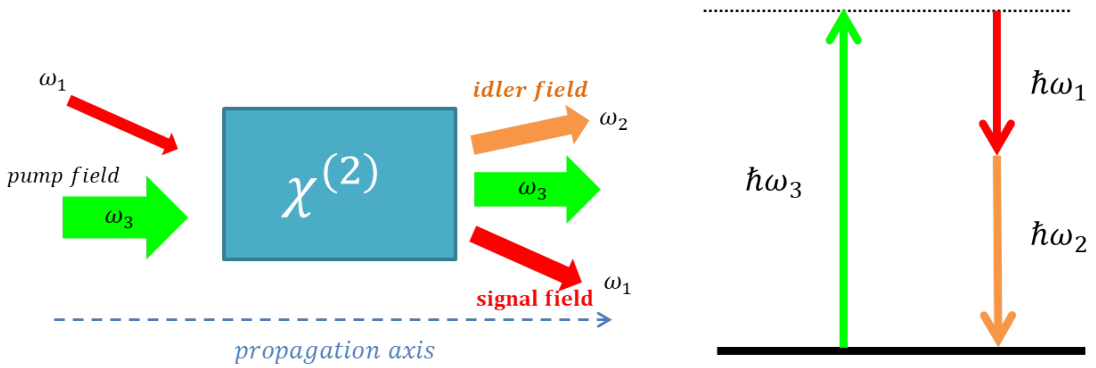

Figure 2.6 – Block diagram of an OPA interaction (left) and its energy diagram (right).

An Optical Parametric Oscillator (OPO) is an OPA placed into an optical resonator. The cavity oscillation condition is satisfied when the pump intensity reaches a threshold value, corresponding to when the parametric amplification gain experienced by either ω_1 or ω_2 perfectly compensates the optical cavity losses. In this configuration, the parametric gain is infinite when the pump power is above the threshold and only limited by the finite power (of the pump). Consequently, two coherent beams or bright laser fields (*signal* and *idler*) exit from the cavity.

Squeezing generation in GW detectors is made exclusively by this cavity but the pump power must be kept slightly *below the threshold*. The squeezing process requires a nonlinear crystal with negligible absorption losses at both concerned optical frequencies, especially at the wavelength of the squeezed mode. The highest squeeze factor achieved for the GW detectors was achieved by using periodically-poled KTP crystals. We will see in the next section that the expression of the hamiltonian of an optical down-conversion process has an expression analogical to the squeezing operator. Then, we will try to explain how squeezed states of light are generated.

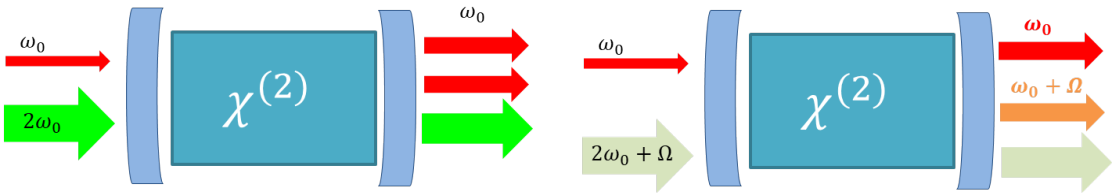

Figure 2.7 – Block diagram of an OPO interaction in a degenerate case where the signal and idler beams are identical (left) and in a non-degenerate case, where these two beams have different frequencies (right).

2.3.2 Generation of squeezed states with nonlinear optics

Squeezed states of light are generated by a *parametric down-conversion process*.

Quantum description of a parametric-down conversion

We pump a second-order nonlinear material (crystal) with a beam at frequency

ω_p into the production of two beams (*signal field*), at frequency $\omega_0 = \omega_p/2$ as for the *degenerate optical parametric amplification* (OPA) for instance. The hamiltonian of the process is described by [44]:

$$\hat{H} = \hbar\omega_0 \hat{a}^\dagger \hat{a} + \hbar\omega_p \hat{b}^\dagger \hat{b} + i\hbar\chi^{(2)}(\hat{a}\hat{a}\hat{b}^\dagger - \hat{a}^\dagger \hat{a}^\dagger \hat{b}),$$

where $\hat{a}^\dagger$ and $\hat{a}$ are respectively the creation and annihilation operators for the signal field at ω_0, similarly for the pump field with $\hat{b}^\dagger$ and $\hat{b}$ and $\chi^{(2)}$ is the second-order nonlinear susceptibility of the crystal. Moreover, the pump field is considered as a strong coherent classical field so that the parametric process does not impact its intensity significantly. We can thus replace the corresponding creation and annihilation operators with the classical expressions $\beta^* e^{i\omega_p t}$ and $\beta e^{-i\omega_p t}$. The hamiltonian becomes:

$$\hat{H} = i\hbar\chi^{(2)}\left(\beta^* \hat{a}\hat{a} e^{i(\omega_p - 2\omega_0 t)} - \beta \hat{a}^\dagger \hat{a}^\dagger e^{-i(\omega_p - 2\omega_0 t)}\right). \tag{2.57}$$

As $\omega_p = 2\omega_0$,

$$\hat{H} = i\hbar\chi^{(2)}(\beta^* \hat{a}\hat{a} - \beta \hat{a}^\dagger \hat{a}\dagger). \tag{2.58}$$

This hamiltonian shows that the two photons in the mode $\hat{a}$ are converted from the photon in the pump field mode, by a nonlinear process. We can clearly see the relation between this hamiltonian and the squeezing operator defined by Eq. 2.39. We thus demonstrate that a nonlinear optical down-conversion process generates squeezed states of light.

Generation of vacuum squeezed states

For the GW community, OPA and Optical Parametric Oscillation (OPO) are used as synonyms even if their definitions are different in nonlinear optics field. The optical component used in GW detection is the OPO cavity and the most successful process is the *degenerate optical parametric amplification below threshold* or also called *cavity-enhanced OPA* [69].

To generate squeezed vacuum states, only the pump field ($\omega_3 = \omega_p$) is injected as input field for the OPO cavity (thus, there is not another "bright" signal beam). Moreover, zero-point fluctuations at all frequencies and all directions

of propagation naturally enter the cavity as well. This explains the role of an optical resonator, which enables to only squeeze the concerned vacuum field. The optical resonator will be designed so that only the zero-point fluctuations at $\omega_s = \omega_p/2$, with a well-defined direction of propagation and transverse spatial mode constructively interferes with itself when reflected back and forth between the mirrors. This means that our OPO is degenerate as the idler and signal field (zero-point fluctuations in reality) have the same frequency ($\omega_1 = \omega_2 = \omega_p/2$), we will then called these zero-point fluctuations signal field at frequency $\omega_s = \omega_p/2$. Moreover, the pump beam needs to be aligned inside the cavity, matched with the signal field to maximize the spontaneous down-conversion probability. This means that the pump field and the signal field should have the same waist and direction of propagation. Finally, a nearly undepleted pump field and the down-converted field leave the crystal. In our case, a squeezed vacuum state leaves the crystal.

To understand better the amplification and deamplification of the vacuum field which occur in this process, let's consider a fundamental field at frequency ω_0, superimposed with a pump field at $2\omega_0$, the total field is thus:

$$\mathcal{E} = A\cos(\omega_0 t + \Phi) + B\cos(2\omega_0 t),$$

where A (respectively B) is the amplitude of the fundamental field (respectively pump field) and Φ is the relative phase between the two fields. Using the relation (2.54) to describe the interaction of this field with a nonlinear crystal, the expression of the second-order macroscopic polarization is expanded as:

$$\begin{aligned}\mathcal{P}^{(2)}(\boldsymbol{\mathcal{E}}) &= \epsilon_0\chi^{(2)}\left(\frac{1}{2}A^2[1+\cos(2\omega_0 t + 2\Phi)] + \frac{1}{2}B^2[1+\cos(4\omega_0 t)]\right.\\ &\quad \left. -AB[\cos(\omega_0 t - \Phi) + \cos(3\omega_0 t + \Phi)]\right)\end{aligned}$$

The second-order polarization contains a DC component and components at frequencies ω_0, $2\omega_0$, $3\omega_0$ and $4\omega_0$. Only the component at ω_0 interferes with the first-order polarization $\mathcal{P}^{(1)}(\mathcal{E}) = \epsilon_0\chi^{(1)}\mathcal{E}$ which generates the OPA effect. If all coefficients are positive, then values as $\Phi = 90°$ made the fundamental input field amplified (at ω_0) due to constructive interference and a $\Phi = 0°$ made it deam-

plified due to destructive interference. This optical parametric amplification process also applies to the quantum fluctuations of the field. For simplicity, the non-linearities above the second-order polarization are put at null. If the pump field intensity is high enough, the total field causes a nonlinear separation of charges inside the crystal (a nonlinear dielectric polarization of the crystal) due to the interaction of the two fields, resulting in a phase-dependent *amplification* and *deamplification* of the quantum fluctuations at the fundamental frequency ω. The quantum uncertainty at the fundamental wavelength is squeezed (deamplified) and anti-squeezed (amplified) twice per wavelength. The amplification factor and deamplification factor are usually quoted as e^r and e^{-r}, with $r > 0$ being the squeezing parameter. The product of amplified and deamplified uncertainties in an OPA process complies with Heisenberg's uncertainty principle. A graphical description of an optical parametric generation of vacuum squeezed states can be found in Ref. [69].

For the generation of squeezed states, the OPO is used below threshold which means that the pump field intensity is relatively low such that spontaneous emission dominates induced emission. This "operation mode", also called *spontaneous parametric down-conversion* (SPDC), enables not to degrade the squeezing produced. An SPDC also allows the production of entangled pairs, it will be discussed in the next chapter, for the squeezing using *Einstein-Podolsky-Rosen entanglement* technique.

2.4 Detection of squeezed states of light

We will see in this section how to measure squeezed states of light with a *homodyne detection* system. Indeed, we need a system able to access to the vacuum quadratures and thus to measure the effect of squeezing. First, I will briefly explain the *beam-splitter* in quantum optics. This will enable to introduce the use of the beam-splitter to materialize the effect of squeezing losses. Finally, I will explain the homodyne detection principle.

2.4.1 The *beam-splitter* in quantum optics

A beam-splitter, depicted in Figure 2.8, is a semi-reflecting mirror, assumed to be lossless (a suitable film has been deposited on the mirror face represented in black so that it has a reflection coefficient of 50% while an anti-reflecting coating has been deposited in the other face that plays no role), induces a transformation of type [17]:

$$|\Phi_{out}\rangle = U\,|\Phi_{in}\rangle, \tag{2.59}$$

where U is the transformation matrix yielding $U = \langle\Phi_{1,2}|\,U\,|\Phi_{3,4}\rangle$, (1) and (2) are input modes and (3) and (4) are output modes. For a lossless mirror where the reflected and transmitted beams have the same intensity, the complex field operators are expressed as:

$$\hat{E}_3^{(+)} = \frac{1}{\sqrt{2}}\left(\hat{E}_1^{(+)} + \hat{E}_2^{(+)}\right) \tag{2.60}$$

$$\hat{E}_4^{(+)} = \frac{1}{\sqrt{2}}\left(\hat{E}_1^{(+)} - \hat{E}_2^{(+)}\right) \tag{2.61}$$

The negative sign in the second equation ensures the conservation of energy. Using the relation (2.13), we can easily derive from these equations the relations between the destruction operators associated for each $\hat{E}_i^{(+)}$.

In reality, we can model any BS (with any split ratio) with the matrix U_η expressed as:

$$\begin{pmatrix} \Phi_3 \\ \Phi_4 \end{pmatrix} = U_\eta \begin{pmatrix} \Phi_1 \\ \Phi_2 \end{pmatrix} = \begin{pmatrix} \eta & \sqrt{1-\eta^2} \\ \sqrt{1-\eta^2} & -\eta \end{pmatrix} \begin{pmatrix} \Phi_1 \\ \Phi_2 \end{pmatrix}, \tag{2.62}$$

where $\eta = \frac{1}{2}$ for a lossless balanced 50/50 BS, η being the amplitude reflectivity of the mirror. This general definition will be used to model the degradation of squeezing due to losses.

2.4.2 Effect of losses

Losses can be due to absorption, straylight on an interface, a non-perfect efficiency of detection and can be modeled by a perfect BS. The BS's amplitude reflection and transmission coefficients are denoted by η and $\sqrt{1-\eta^2}$, as used in the matrix defined in Eq. 2.62. Assuming that a squeezed state $|\alpha, R\rangle$ (α positive and real) is incident at port (1) and vacuum $|0\rangle$ is entering by port (2) so that the input state is defined as :

$$|\Phi\rangle = |\alpha, R\rangle \otimes |0\rangle \tag{2.63}$$

The variance of the quadrature operators of port (4) is proportional to [46]:

$$(\Delta E_{Q4})^2 \propto \sqrt{1-\eta^2}e^{-2R} + \eta^2. \tag{2.64}$$

If $\sqrt{1-\eta^2}$ is small, η^2 is close to unity and thus, the fluctuations on the output field are proportional to η^2, which is caused by the vacuum fluctuations entering the unused input port. Finally, it is possible to represent any kind of losses between the squeezing source and the detection by this BS representation. Eq. 2.64 clearly shows that even very small losses can degrade the squeezing level. The objective is to reduce losses as much as possible, not to degrade this produced squeezing level.

2.4.3 Homodyne detection

In order to measure the squeezing level, it is necessary to use a device called a *homodyne detector*, described in Figure 2.9. For that, we need to measure the quadratures of the vacuum field and also of a squeezed vacuum field. In the homodyne detection scheme, the observed field $|\Phi\rangle_1$ (of mode 1), also called $|vac\rangle$ in the figure, beats with a reference field $|\Phi\rangle_2 = |\alpha_{LO}\rangle_2$, called the *local oscillator*.

The state $|\Phi\rangle_2$ is characterized by the complex number: $\alpha_{LO} = |\alpha_{LO}|e^{i\Phi_{LO}}$. The detection is homodyne because of the equality $\omega_1 = \omega_2$ (otherwise, it is *heterodyne*). Two photodetectors measure the photocurrents i_3 and i_4 and their averaged difference $\overline{i_3 - i_4}$, measured by a differential amplifier is proportional

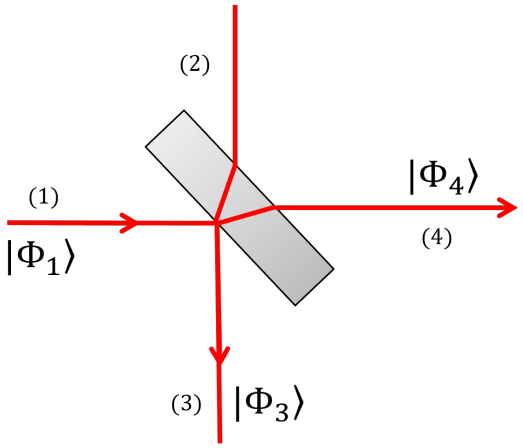

Figure 2.8 – Quantum description of a beam-splitter which couples the two fields entering at ports (1) and (2) with the fields leaving by ports (3) and (4). The semi-reflecting mirror is considered lossless.

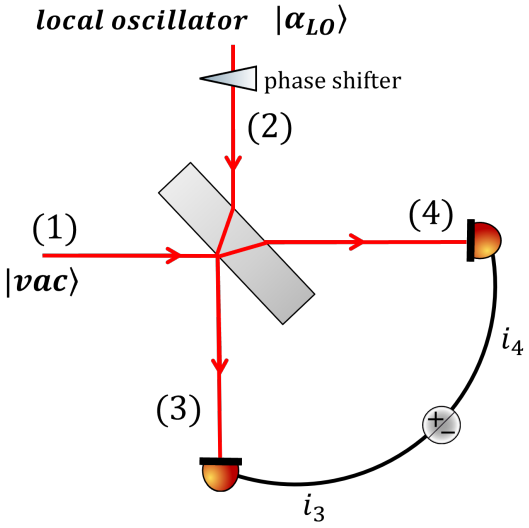

Figure 2.9 – Schematics of the homodyne detection where the field to measure is at (1), the vacuum denoted $|vac\rangle$, the phase shifter on the local oscillator beam stresses the importance of phase-locking. The measurement of the difference of output photocurrents will enable to measure each quadrature separately.

to:

$$\overline{d} = \langle\Phi|\hat{\boldsymbol{E}}^{(-)}(\mathbf{r_3})\hat{\boldsymbol{E}}^{(+)}(\mathbf{r_3})|\Phi\rangle - \langle\Phi|\hat{\boldsymbol{E}}^{(-)}(\mathbf{r_4})\hat{\boldsymbol{E}}^{(+)}(\mathbf{r_4})|\Phi\rangle. \tag{2.65}$$

Using the general expression of the electric field with the creation and annihilation operators in Eq. 2.13 (without the time variable because $\overline{d}$ is independent of time) and the relations (2.60)and (2.61), we can write the output fields as:

$$\begin{aligned}\hat{E}^{(+)}(\boldsymbol{r_3}) &= \frac{i}{\sqrt{2}}\mathcal{E}^{(1)}e^{ik_3\times\boldsymbol{r_3}}(\hat{a}_1+\hat{a}_2)\\ \hat{E}^{(+)}(\boldsymbol{r_4}) &= \frac{i}{\sqrt{2}}\mathcal{E}^{(1)}e^{ik_4\times\boldsymbol{r_4}}(\hat{a}_1-\hat{a}_2)\end{aligned} \tag{2.66}$$

$|\Phi\rangle$ is expressed in the input space and as the two incoming beams are indepen-

dent, $|\Phi\rangle$ can be expressed as a tensor product of:

$$|\Phi\rangle = |\Phi_1\rangle \otimes |\alpha_{LO}\rangle. \tag{2.67}$$

By substituting (2.66) into (2.65) and using the quadrature operators defined in (2.12), the difference signal is proportional to:

$$\overline{i_3 - i_4} \propto \cos\Phi_{LO} \langle\Phi_1| \hat{X}_1 |\Phi_1\rangle + \sin\Phi_{LO} \langle\Phi_1| \hat{X}_2 |\Phi_1\rangle. \tag{2.68}$$

Then, by taking the phase of the local oscillator equal to 0 or $\frac{\Pi}{2}$, we can obtain the expectation value of either the phase quadrature or the amplitude quadrature, respectively. Then, if $|\alpha_{LO}|$ is big enough, the variation of the difference signal becomes:

$$\overline{d}^2 \simeq [\mathcal{E}^{(1)}]^4 \Big(|\alpha_{LO}| \langle\Phi| (e^{-i\Phi_{LO}} \hat{a}_1 + e^{i\Phi_{LO}} \hat{a}_1^\dagger)^2 |\Phi\rangle \Big). \tag{2.69}$$

This expression shows that it is also possible to measure the quantum fluctuations of the phase and amplitude quadrature. Moreover, to measure the correct quadrature observables, it is essential to fix a common origin of time for the local oscillator and the input field (in our case, the squeezed field), i.e., to *phase-lock* the two light fields. Once the two light sources are phase-locked, we can easily choose the relative phase Φ_{LO} to select the observable to measure.

2.5 Quantum-mechanical description of GW interferometers

In Section 2.2, the quantization of the electromagnetic field was introduced with the expression of the electric Heisenberg field operator $\hat{E}(\boldsymbol{r}, t)$, as a function of the creation and annihilation operators (2.13). However, for ground-based GW detectors, a monochromatic laser with a carrier frequency at ω_0 is injected into the ITF and a GW signal around ω_0 creates a pair of modulation sidebands. The two-photon formalism is thus needed to express the outcoming light of the interferometer but above all, to describe the squeezing effect, characterized by the excitation of modes in pairs. Consequently, this formalism will enable to

calculate the power spectral density of the quantum noise with or without a squeezing injection.

2.5.1 Two-photon formalism

A freely propagating electromagnetic wave can be described in each spatial point by $\boldsymbol{r} = (x, y, z)$ and at the time t by the electric field Heisenberg operator. This operator of a light wave traveling along the z-axis (positive direction) can be expressed as a sum of positive-frequency and negative-frequency parts [36]:

$$\hat{E}(x, y, z; t) = u(x, y, z)\left(\hat{E}^{(+)}(t) + \hat{E}^{(-)}(t)\right), \tag{2.70}$$

where $u(x, y, z; t)$ is the spatial mode shape. To write the input and output fields at the BS, we will consider it to be infinitesimally thin so that these fields are only functions of time (and not of position), localized at the position where they hit the BS. The input field at the BS bright port (coming from the ITF laser) is a carrier, assumed to be in a perfect coherent state, with I_0 the light power arriving on the BS and with the angular frequency ω_0. The input field at the dark port of the BS is a quantized electromagnetic field described by (2.70) [54]:

$$\hat{E}^{(+)}(t) = \int_0^\infty \frac{d\omega}{2\pi}\sqrt{\frac{2\pi\hbar\omega}{\mathcal{A}c}}\hat{a}_\omega e^{-i\omega t}, \qquad \hat{E}^{(-)}(t) = \left[\hat{E}^{(+)}(t)\right]^\dagger, \tag{2.71}$$

where $\mathcal{A}$ is the effective cross-section area of the light beam, and $\hat{a}_\omega$ (respectively $\hat{a}_\omega^\dagger$) is the single-photon annihilation (respectively creation) operator in the mode of the field with frequency ω. Indeed, Eq. 2.71 implies that the free radiation can be expressed as an expansion over the continuum of harmonic oscillators.

Figure 2.10 represents the two input fields (from the bright port and the dark port) and the output field leaving the dark port. The *single-photon operators* are defined by the the following commutation relations:

$$\left[\hat{a}_\omega, \hat{a}_{\omega'}^\dagger\right] = 2\pi\delta(\omega - \omega'), \qquad \left[\hat{a}_\omega^\dagger, \hat{a}_{\omega'}^\dagger\right] = 0, \tag{2.72}$$

which are the same commutation relations as for the quadrature observables operators $\hat{X}_1$ and $\hat{X}_2$ (defined in Section 2.1.1). For ground-based GW detectors,

a monochromatic laser with a carrier frequency ω_0 is injected into the ITF. Due to modulation of the interferometer arms lengths, a GW signal around ω_0 creates a pair of modulation sidebands. The outcoming light of the interferometer cannot be expressed as the continuum of independent modes anymore. Indeed, the modes of light at frequencies $\omega_{1,2} = \omega_0 \pm \Omega$, that described the quantum field transformations inside a GW ITF, have correlated complex amplitudes and these sidebands, appearing in pairs, hints at the need for the *two-photon formalism*. This formalism is needed to describe the processes occurring in GW interferometers, but above all, to describe "two-photon devices" mechanism, these devices can produce squeezed states and excite modes in pairs. The sidebands frequencies Ω for the GW range is from about 10 to 1000 Hz. The *modulation sideband amplitudes* were first defined by Caves and Schumaker [29, 71], as:

$$\hat{a}_+ = \hat{a}_{\omega_0+\Omega}, \qquad \hat{a}_- = \hat{a}_{\omega_0-\Omega}. \tag{2.73}$$

By factoring Eq. 2.71 with the carrier frequency ω_0 and injecting the sideband amplitudes, we have:

$$\begin{aligned} \hat{E}^{(+)}(t) &\simeq \frac{\mathcal{C}_0 e^{-i\omega_0 t}}{\sqrt{2}} \int_0^\infty \frac{d\Omega}{2\pi} \lambda_+(\omega) \hat{a}_+ e^{-i\Omega t} \\ \hat{E}^{(-)}(t) &\simeq \frac{\mathcal{C}_0 e^{i\omega_0 t}}{\sqrt{2}} \int_0^\infty \frac{d\Omega}{2\pi} \lambda_+(\omega) \hat{a}_- e^{i\Omega t}, \end{aligned} \tag{2.74}$$

where $\mathcal{C}_0$ is the light quantization normalization constant and $\lambda_\pm(\Omega)$ are equal to:

$$\mathcal{C}_0 = \sqrt{\frac{4\pi\hbar\omega_0}{\mathcal{A}_c}}, \qquad \lambda_\pm(\Omega) = \sqrt{\frac{\omega_0 \pm \Omega}{\omega_0}}, \tag{2.75}$$

and $\omega_0 \gg \Omega_{GW}$ enables to expand the integral limits from ω_0 to ∞. We approximate $\lambda_\pm(\Omega) \sim 1$ as $\frac{\Omega}{\omega_0}$ is very small. The expression for the dark port input field is thus equal to:

$$\hat{E}_{in}^{dark} = \frac{\mathcal{C}_0 e^{-i\omega_0 t}}{\sqrt{2}} \int_0^\infty \frac{d\Omega}{2\pi} (\hat{a}_+ e^{-i\Omega t} + \hat{a}_- e^{i\Omega t}). \tag{2.76}$$

We then define the two-photon quadrature operators, the amplitude (or

cosine) and phase (or sine) quadrature operators as:

$$\begin{aligned}\hat{a}_1 &= \frac{\hat{a}_+ + \hat{a}_-^\dagger}{\sqrt{2}} \\ \hat{a}_2 &= \frac{\hat{a}_+ - \hat{a}_-^\dagger}{i\sqrt{2}}.\end{aligned} \tag{2.77}$$

These quadrature operators are Hermitian, implying that in the frequency domain, we have:

$$\hat{a}_{1,2}^\dagger(\Omega) = \hat{a}_{1,2}(-\Omega). \tag{2.78}$$

The commutation relations can be derived from Eq. 2.72:

$$\begin{aligned}\left[\hat{a}_{1,2}(\Omega), \hat{a}_{1,2}^\dagger(\Omega')\right] &= 2\pi\delta(\Omega - \Omega') \\ \left[\hat{a}_1(\Omega), \hat{a}_2^\dagger(\Omega')\right] = \left[\hat{a}_1(\Omega)^\dagger, \hat{a}_2^\dagger(\Omega')\right] &= 2i\pi\delta(\Omega - \Omega').\end{aligned} \tag{2.79}$$

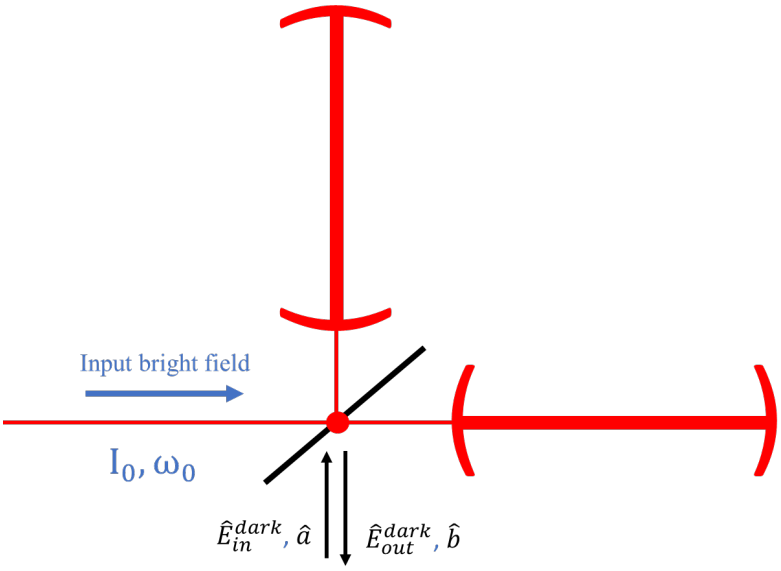

Figure 2.10 – Schematics of a GW interferometer with two inputs at the BS (the carrier field at the bright port and the input field at the dark port $\hat{E}_{in}^{dark}$) and one relevant output field, $\hat{E}_{out}^{dark}$.

Injecting these *two-photon quadrature operators* into (2.76), the input field at the dark port of the BS is then described as:

$$\hat{E}_{in}^{dark} = \frac{\mathcal{C}_0}{\sqrt{2}}\left[\cos(\omega_0 t)\int_0^\infty \frac{d\Omega}{2\pi}\left(\hat{a}_1 e^{-i\Omega t} + \hat{a}_1^\dagger e^{i\Omega t}\right) + \sin(\omega_0 t)\int_0^\infty \frac{d\Omega}{2\pi}\left(\hat{a}_2 e^{-i\Omega t} + \hat{a}_2^\dagger e^{i\Omega t}\right)\right]. \tag{2.80}$$

Hence $\hat{a}_1$ (respectively $\hat{a}_2$) is called the *cosine* (respectively *sine*) quadrature, being the field amplitude for photons in the $\cos(\omega_0 t)$ (respectively the field phase for photons in the $\sin(\omega_0 t)$) quadrature.

Similarly, the output field at the BS dark port $\hat{E}_{out}$ is described with the same form but with the operators $\hat{b}_i$ instead of the operators $\hat{a}_i$ (for $i = 1, 2$), with $\hat{b}_1$ being the amplitude quadrature and $\hat{b}_2$ being the phase quadrature. Then, we can write the output field as a function of the amplitude and phase quadratures $\hat{E}_1(t)$ and $\hat{E}_2(t)$, as:

$$\hat{E}_{out} = \hat{E}_1(t)\cos(\omega_0 t) + \hat{E}_2(t)\sin(\omega_0 t)$$
$$\hat{E}_i(t) = \frac{\mathcal{C}_0}{\sqrt{2}}\int_0^\infty \frac{d\Omega}{2\pi}\left(\hat{b}_i e^{-i\Omega t} + \hat{b}_i^\dagger e^{i\Omega t}\right).$$

2.5.2 Input/output relations

Let $\hat{a}_1(\Omega)$ and $\hat{a}_2(\Omega)$ be the amplitude and phase quadrature, respectively, of the vacuum mode entering the dark port of the ITF, defined according with 2.77, $\hat{b}_1(\Omega)$ and $\hat{b}_2(\Omega)$ the corresponding quadratures of the outgoing vacuum mode and h the dependent Fourier transform of the GW field $h(t)$, defined by:

$$h(t) = \int_{-\infty}^{+\infty} h e^{-i\Omega t}\frac{d\Omega}{2\pi}. \tag{2.81}$$

The fluctuations of the input light pressure amplitude produce the test mass motion via the radiation pressure on it, thereby inducing a phase shift in the light inside the arm cavities and thus in the output field. Hence the optomechanical response of the ITF produce the coupling by which this radiation-pressure back-action converts the input field quadrature $\hat{a}_1$ into the noise of the output phase quadrature Δb_2.

Consequently, the input/output relation can be written as:

$$\begin{bmatrix}\hat{b}_1(\Omega)\\ \hat{b}_2(\Omega)\end{bmatrix} = e^{2i\beta}\begin{bmatrix}1 & 0\\ -\mathcal{K}(\Omega) & 1\end{bmatrix}\begin{bmatrix}\hat{a}_1(\Omega)\\ \hat{a}_2(\Omega)\end{bmatrix} + e^{i\beta}\begin{bmatrix}0\\ \sqrt{2\mathcal{K}(\Omega)}\end{bmatrix}\frac{h(\Omega)}{h_{SQL}}. \tag{2.82}$$

The optomechanical coupling factor or so-called *Kimble factor* [54] defined as:

$$\mathcal{K}(\Omega) \equiv \frac{(I_0/I_{SQL})2\gamma^4}{\Omega^2(\gamma^2+\Omega^2)}, \tag{2.83}$$

where

$$I_{SQL} = \frac{mL^2\gamma^4}{4\omega_0}, \tag{2.84}$$

being m the mirrors mass, and where

$$\gamma = \frac{Tc}{4L}, \tag{2.85}$$

is the ITF arm cavities half-bandwidths (or *cavity pole*), L the ITF cavities arm-length and T the input mirrors transmissivities.

I_{SQL} is the input laser power required for *a power-recycled Michelson interferometer* (a GW detector without a signal recycling mirror) to reach the so-called Standard Quantum Limit (SQL) h_{SQL}, that we will define in the next chapter.

Eq 2.82 leads to the the linear *input-output relations* for the ITF:

$$\begin{aligned}\hat{b}_1 &= \Delta\hat{b}_1 = \hat{a}_1 e^{2i\beta}\\ \hat{b}_2 &= \Delta\hat{b}_2 + \sqrt{2\mathcal{K}}\frac{h}{h_{SQL}}e^{-\beta}\\ \Delta\hat{b}_2 &= (\hat{a}_2 - \mathcal{K}\hat{a}_1)e^{2i\beta}.\end{aligned} \tag{2.86}$$

The quantities $\Delta\hat{b}_i$[1] are the parts that remain when there is no GW signal and is thus the noise source of $\hat{b}_i$. The $\hat{a}_i$ quadratures impinge on the arm cavities at a frequency $\omega_0+\Omega$, that is consequently off-resonant compared to the carrier frequency, so these operators gained a phase shift, after exiting the cavities, equal

[1] the notation $\Delta\hat{A}$ for any operator $\hat{A}$ corresponds to $\Delta\hat{A} \equiv \hat{A} - \langle\hat{A}\rangle$

to:

$$\beta = \arctan(\Omega/\gamma). \tag{2.87}$$

Chapter 3

Quantum noise reduction in GW Detectors

Outline of the current chapter

It is possible to beat the SQL and then, circumvent the limitations imposed by the uncertainty relations while not violating them, by injecting non-classical states of light, described in Section 2.1.2 and particularly squeezed vacuum states. This technique was originally proposed by Caves in 1981, who first demonstrated [28] that the quantum noise in an interferometer originates from the vacuum (zero-point) fluctuations that enters from the unused port (the so-called *dark port*) of

the BS of the interferometer. As explained in Section 1.3.3 (Chapter 1), there are two components of QN. The *quantum shot noise* arises from the quantum fluctuations of the phase, comes from the photon-counting noise and dominates at the high-frequency part of the ground-based GW detectors. The latter, the *quantum radiation pressure noise* (or quantum back-action noise), arising from the fluctuations of the amplitude, manifests itself from the differential radiation pressure noise on the suspended mirrors, due to the beating between the strong carrier field circulating in the arm cavities with the vacuum quantum fields that enter from the detection port and manifests as the low-frequency component of the quantum noise. There is no quantum noise due to the ITF laser thanks to the symmetry of the two arms so that the quantum fluctuations of the fields from each cavity are canceling each other out.

The squeezed vacuum state, generated by non-linear optical processes, as described in Section 2.3, enters the interferometer from the dark port. This technique, called *frequency-independent squeezing* lies in the phase-squeezed vacuum injection, i.e. squeezed vacuum states where the minimal fluctuation is found in the phase quadrature while the maximal one is found in the amplitude quadrature, implying the reduction of SN at the expense of increasing the RPN (the so-called *anti-squeezing*) because the fluctuations in the amplitude and phase quadratures contribute separately to the quantum noise at different frequencies of the detection band. This technique is thus frequency-independent because the relative phase between the main carrier of the ITF and the pump field that produces the squeezed light is fixed, meaning that the squeezing angle does not change accordingly with the detection frequency band. Since up to the O3 science run, the quantum radiation pressure noise is just below the residual technical noise sources at GW detection frequencies so that a broadband sensitivity improvement can be achieved by reducing the shot noise component with an injection of frequency-independent squeezed vacuum states. This enables to reduce the quadrature of the light aligned with the GW signal, which is equivalent to increasing the circulating optical power in the interferometer, without the disadvantages of increasing thermal effects inside the ITF's optics. However, the FIS technique is currently not sufficient for the next upgrades of ground-based GW detectors. Between O3 and O4 science run, due to the reduction of technical

noise contributions, an increased level of RPN (due to the anti-squeezing) will be detrimental for the low-frequency band of GW detectors as it will not be covered anymore by the technical noises. A frequency-dependent squeezing angle is required to induce a broadband reduction of quantum noise without disturbing the low frequencies.

I will first give a description of the quantum noise power spectral density in Section 3.1. Then, I will illustrate the effect of the squeezing injection in the case of a frequency-independent squeezing and the case of a frequency-dependent squeezing and describe a technique of FDS using a filter cavity in Section 3.2. In a second time, I will describe the experimental demonstrations of FIS and FDS using a filter cavity in Section 3.3. Finally, in Section 3.4, I will describe the main subject of my thesis, i.e. the theory and state-of-the-art of the FDS technique using EPR entangled states.

3.1 Quantum noise power spectral density: *Radiation Pressure Noise* and *Shot Noise*

The single-sided spectrum density $S_h(f)$ associated with the quantum noise, is described by:

$$\frac{1}{2}2\pi\delta(\Omega-\Omega')S_h(\Omega) = \langle\Phi_{in}|\, h_n(\Omega)h_n^\dagger(\Omega')\,|\Phi_{in}\rangle_{sym}\,^1 \tag{3.2}$$

where $|\Phi_{in}\rangle$ is the quantum state of the input light field.

For a GW interferometer (without squeezing injection), the dark-port input field is in its vacuum state, described in Section 2.5.1 and is denoted as:

$$|\Phi\rangle_{dark}^{in} = |0_a\rangle \tag{3.3}$$

[1] the subscript *sym* means "symmetrize the operators whose expectation value is being computed", as replacing $h_n(\Omega)h_n(\Omega')^\dagger$ by:

$$\frac{1}{2}(h_n(\Omega)h_n^\dagger(\Omega') + h_n^\dagger(\Omega')h_n(\Omega)) \tag{3.2}$$

Using the relations/output relation (2.86), we have:

$$\langle 0_a | a_i a^{\dagger}_{j'} | 0_a \rangle_{sym} = \frac{1}{2} 2\pi\delta(\Omega - \Omega')\delta_{ij}. \tag{3.4}$$

In a power-recycled Michelson ITF, we can use the input/output relation (2.86) to compute the noise of the Fourier transform of the GW signal $h(\Omega)$:

$$h_n(\Omega) = \frac{h_{SQL}}{\sqrt{2\mathcal{K}}} \Delta\hat{b}_2. \tag{3.5}$$

Using Eqs. 3.1 and 3.4, we can compute the noise spectral density for a GW interferometer:

$$S_h = \frac{h^2_{SQL}}{2}\left(\frac{1}{\mathcal{K}(\Omega)} + \mathcal{K}(\Omega)\right), \tag{3.6}$$

The Kimble factor $\mathcal{K}(\Omega)$ is defined in Eq. 2.83 and is proportional to the input laser power I_0. This equation shows the contribution of the two components of the quantum noise. The *shot noise*:

$$S_{SN} = \frac{h^2_{SQL}}{2}\frac{1}{\mathcal{K}(\Omega)} = \frac{h^2_{SQL}}{2}\frac{\Omega^2(\gamma^2 + \Omega^2)}{(I_0/I_{SQL})2\gamma^4}, \tag{3.7}$$

is proportional to the inverse of the laser input power I_0 and dominant for $\Omega \gg \gamma$, where it becomes flat (does not depend on Ω; we remember that γ is the cavity pole).

The *radiation pressure noise*:

$$S_{RPN} = \frac{h^2_{SQL}}{2}\mathcal{K}(\Omega) = \frac{h^2_{SQL}}{2}\frac{(I_0/I_{SQL})2\gamma^4}{\Omega^2(\gamma^2 + \Omega^2)}, \tag{3.8}$$

is proportional to the laser input power and dominant for $\Omega \ll \gamma$, where it goes as the inverse of Ω^2. This explains why one has to compromise when increasing the input laser power of the GW interferometer as it reduces the SN while increasing the RPN.

The *standard quantum limit* (SQL), equal to h^2_{SQL} limits the laser interfero-

metric GW detectors sensitivity and comes from the trade-off between the SN, which is inversely proportional to the optical power, and the RPN, which is proportional to this optical power. It is not possible to beat the SQL only using the laser power as a parameter. For a dual-recycled Michelson interferometer or in general for a free-mass for GW strain, it is equal to [37]:

$$h_{SQL} = \sqrt{\frac{8\hbar}{m\Omega^2 L^2}}, \tag{3.9}$$

where m is the mass of the mirror (test mass), Ω is the modulation sideband frequency equal to $\Omega = \omega - \omega_p$, ω_p being the laser frequency and ω the optical frequencies. The relation between the SQL and the laser power shows that the optimal laser power to achieve the desired sensitivity in the whole detection band for a GW detector is determined by the SQL.

3.2 Squeezing injection

As mention earlier, the dark-port input field is in its vacuum state as described by Eq. 3.3. A *squeezed-input interferometer* is an interferometer where the vacuum fluctuations (defined by $\hat{a}_1$ and $\hat{a}_2$) at the dark port are replaced by a squeezed state [54]. In this configuration, the dark-port input field is:

$$|\Phi\rangle_{dark}^{in} = S(r,\theta)|0_a\rangle, \tag{3.10}$$

where r is the squeeze factor and $\theta = \theta(\Omega)$ is the squeeze angle depending on sideband frequency and one can adjust it to minimize the noise in one fixed quadrature for the FIS technique. $S(r,\theta)$ is the squeezing operator in two-photon formalism and is defined by:

$$S(r,\theta) = \exp\left\{\left[r\left(\hat{a}_+\hat{a}_- e^{-2i\theta} - \hat{a}_+^\dagger \hat{a}_-^\dagger e^{2i\theta}\right)\right]\right\}. \tag{3.11}$$

This operator is unitary as for the same operator in one-photon formalism and the effect on the annihilation operators is:

$$S(r,\theta)\hat{a}_{\pm}S^{\dagger}(r,\theta) = \hat{a}_{\pm}\cosh r + \hat{a}_{\mp}^{\dagger}e^{2i\theta}\sinh r. \tag{3.12}$$

3.2.1 Frequency-independent squeezing

By setting a frequency-independent squeezed angle to $\theta = \pi/2$, it gives the following single-sided amplitude spectral density noise [54]:

$$S_h = \frac{h_{SQL}^2}{2}\left(\frac{1}{e^{2r}\mathcal{K}(\Omega)} + e^{2r}\mathcal{K}(\Omega)\right). \tag{3.13}$$

This equation differs from the relation of the spectral density of the quantum noise (3.6) by the factor e^{-2r} in the shot noise term and the factor e^{2r} in the radiation pressure noise term. This is the well-known consequence of the FIS technique which increases the SN at the expense of the RPN.

We use a convenient mathematical formalism, described in [55], where vacuum fields are proportional to the identity matrix ($\sqrt{2\hbar\omega_0}$) and their interaction with an optical element or system is described by the multiplication with a 2 x 2 transmission matrix $\mathbf{T}$, giving $v_{out} = \mathbf{T}v_{in}$, where v is a vacuum field [55]. The transfer matrices can model the propagation of the vacuum field through the squeezer and injection optics. They can also describe the modification of this field by a filter cavity, which will be developed in Section 3.2.2. Concerning the squeezed field injection, the squeezer is represented by the operator $\mathbf{S}(r,\theta)$, which can be decomposed with rotation matrices:

$$\mathbf{S}(r,\theta) = \mathbf{R}(\theta)\mathbf{S}(r,0)\mathbf{R}(-\theta) = \mathbf{R}_{\theta}\mathbf{S}_r\mathbf{R}_{\theta}^{\dagger} \tag{3.14}$$

$$= \begin{pmatrix} \cos\theta & -\sin\theta \\ \sin\theta & \cos\theta \end{pmatrix}\begin{pmatrix} e^{r} & 0 \\ 0 & e^{-r} \end{pmatrix}\begin{pmatrix} \cos\theta & \sin\theta \\ -\sin\theta & \cos\theta \end{pmatrix}, \tag{3.15}$$

where the term e^{-r} refers to the squeezing effect at angle θ and e^{r} refers to the anti-squeezing effect at angle $\theta + \pi/2$. The squeezing magnitudes are expressed in decibels (dB), described by (2.42). Note that the rotation operator $R(\theta)$ is

defined by:

$$R(\theta) = \exp\left\{\left[-i\theta\left(\hat{a}_+^\dagger \hat{a}_+ + \hat{a}_-^\dagger \hat{a}_-\right)\right]\right\}. \tag{3.16}$$

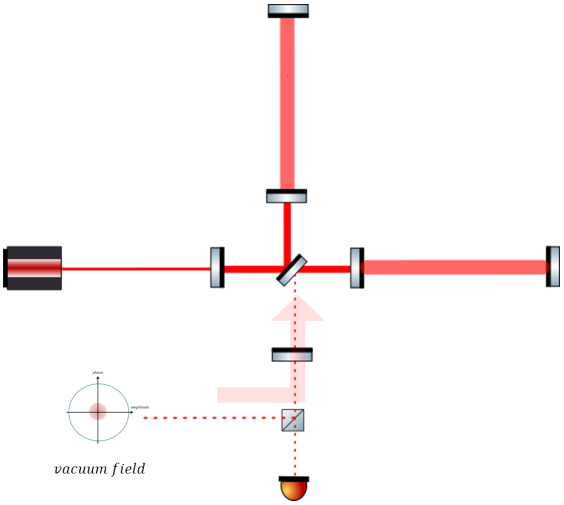

Figure 3.1 – Schematics of the origin of quantum noise in a GW detector where there are vacuum fluctuations entering from the dark port of the BS (see red transparent arrow).

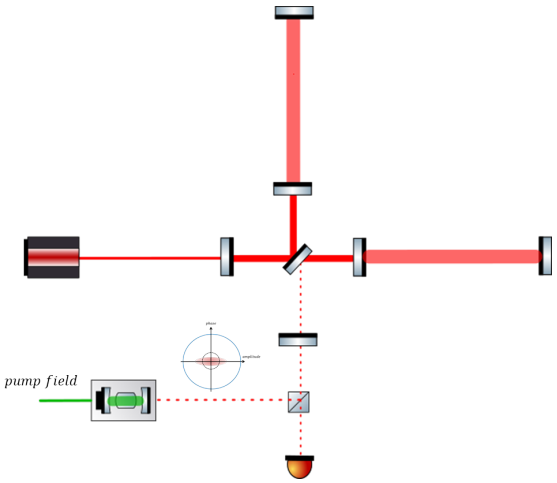

Figure 3.2 – Schematics of the frequency-independent squeezing technique with the injection of phase-squeezed vacuum into the dark port of a tuned dual-recycled Michelson ITF.

Figure 3.2(left) shows with and red arrow where the vacuum fluctuations is entering from the dark port the interferometer's BS and illustrates in the right figure the frequency-independent squeezing technique with the injection of phase-squeezed vacuum.

3.2.2 Frequency-dependent squeezing using a filter cavity

In this technique, a standard frequency-independent squeezed vacuum is reflected off from a detuned low-loss high-finesse Fabry-Perot cavity and this method was first suggested by Kimble and coworkers [54], 20 years ago. The filter cavity resonance is chosen detuned compared to the carrier frequency so that, when frequency-independent squeezed states are injected into this cavity, their upper and lower sidebands undergo a differential phase. Indeed, the spectral components that lie within the cavity linewidth experience a phase

shift before being reflected off the cavity while those outside of the linewidth do not. This spectral selectivity is the key to rotate the squeezing quadrature angle in a frequency-dependent way as the squeezing angle for each sideband frequency depends on the relative phase between the upper and lower sidebands. Consequently, the rotation induced by the filter cavity will compensate for the rotation induced by the optomechanical coupling of the ITF. In the following I will explicit the parameters at stake which characterize this technique.

The *Kimble factor*, defined in (2.83), can also be expressed as:

$$\mathcal{K} = \left(\frac{\Omega_{SQL}}{\Omega}\right)^2 \frac{\gamma^2}{\Omega^2 + \gamma^2}, \tag{3.17}$$

where γ is the interferometer signal bandwidth and Ω_{SQL} is the approximate frequency at which, for a given interferometer configuration, the RPN is switched to the SN and also the ITF quantum noise equals the SQL. For second-generation GW detectors (Advanced Virgo and Advanced LIGO), $\Omega_{SQL} \sim 2\pi \times 70\,Hz$.

Moreover, the interferometer transfer matrix can be expressed with the squeeze and rotation operators as:

$$\mathbf{T_{ifo}} = \mathbf{S}(r_{ifo}, \theta_{ifo})\mathbf{R}(\Phi_{ifo}), \tag{3.18}$$

with

$$\begin{aligned} r_{ifo} &= -(\mathcal{K}/2) \\ \theta_{ifo} = \frac{1}{2}\operatorname{arccot}(\mathcal{K}/2), \qquad \Phi_{ifo} &= -\arctan(\mathcal{K}/2). \end{aligned} \tag{3.19}$$

The filter cavity has to rotate the input squeezed quadrature in function of frequency to have the input quadrature always aligned with the signal quadrature at the output of the ITF, also considering the rotation induced by Φ_{ifo} and the one due to squeezing θ_{ifo}. The rotation required by the action of the filter cavity is:

$$\theta_{fc} = \arctan(\mathcal{K}), \tag{3.20}$$

The frequency range where the rotation of the squeezing ellipse takes place

is set by the filter cavity storage time, as:

$$\tau_{storage} = \frac{1}{\gamma_{fc}}, \tag{3.21}$$

where the half-width-half-maximum (HWHM)-power linewidth of the filter cavity γ_{fc} can be expressed as:

$$\gamma_{fc} = \frac{\pi c}{2L_{fc}\mathcal{F}} \tag{3.22}$$

where L_{fc} is the cavity length, $\mathcal{F}$ the finesse and c the speed of light. Hence to obtain a rotation around 30 Hz-70 Hz, this required either a very long cavity or a very high-finesse cavity.

However, in reality, the level of squeezing can be degraded by losses such as internal losses of the filter cavity, propagation losses, mode mismatch, squeezed quadrature fluctuations (phase noise), hence the need for a low-loss filter cavity. Finally, the spectral density of the quantum noise when choosing the right angle for the filter cavity to counteract the ITF rotation is then described by [54]:

$$S_h = \frac{h_{SQL}^2}{2}\left(\frac{1}{\mathcal{K}(\Omega)} + \mathcal{K}(\Omega)\right)e^{-2r} \tag{3.23}$$

Compared to the spectral density noise of a power-recycled Michelson ITF, the only difference is an overall reduction by a factor e^{-2r}, where r is the squeeze factor.

3.3 Experimental demonstrations of quantum noise reduction: beating the standard quantum limit with non-classical light

As shown in the previous section and in Figure 1.6, the frequency-independent squeezing, i.e., the injection of a phase-squeezed vacuum (fixed squeezing angle) only improves the sensitivity for the higher frequencies and, particularly, only

the high-frequency part of the GW interferometer detection band, where the shot noise dominates. Indeed, the optomechanical coupling between the momentum of the TM and the amplitude of the ITF's optical field leads to a rotation of the squeezing ellipse by 90° at low frequencies so that the ellipse is no longer aligned with the signal quadrature. Up to previous science run O3, the side effect of the injection of FIS vacuum, which is the increase of the RPN (anti-squeezing), was not detrimental for the low-frequency band of GW detectors. Indeed, the radiation pressure noise was not dominating at these frequencies and was covered by technical noises, as shown by Figure 1.3.

However, for the next upgrade of the GW detectors, called *Advanced Virgo+* and *Advanced LIGO+*, the RPN will dominate at low frequencies because of the reduction of technical noises. Consequently, a frequency-dependent squeezing (FDS) technique is required, by impressing a frequency-dependent rotation upon the squeezing ellipse to counteract the rotation induced by the ITF, allowing to reduce each component of the quantum noise. The rotation of the ellipse should be performed at the crossover frequency between the RPN-dominated frequency-band and the SN-dominated frequency-band, which is around 30 Hz-70 Hz for the advanced GW detectors.

In Section 3.3.1, I will detail the achieved performance of the shot noise reduction during O3 and present the performance records in achieved squeezing level. In Section 3.3.2 are presented the experimental demonstrations of FDS using a filter cavity by two different teams and the status of the installation of the filter cavity for Advanced Virgo+.

3.3.1 FIS injection in GW detectors

The German-British GEO600 team members are squeezed light pioneers. Squeezing enhancement has been routinely used since 2010 and GEO600 have been the only instrument in the world to do so until the start of O3 in April 2019. Recently, a squeezing level of 6 dB was reached, which is the strongest level ever seen in a GW detector [3, 48]. Then, FIS technique was routinely used by AdV [14] and aLIGO [80] during the last observation run O3. The sensitivities enhancement for Advanced Virgo was reported in Section 1.3.3. A shot noise reduction of

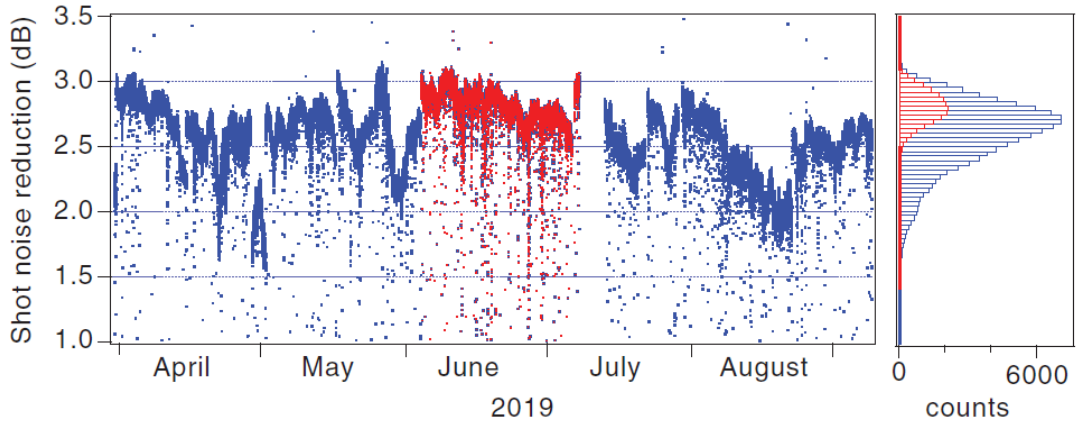

Figure 3.3 – Long-term performance of the shot noise reduction during the first 5 months of the O3 science run for AdV, from [14]. Data in red correspond to a certain time interval (5 June - 8 July 2019). Data gaps are due to non-science mode periods. Right: histogram of the shot noise reduction value with a bin width of 0.036 dB.

up to $3.2 \pm 0.1\,dB$ has been observed [14] at frequencies between 100 Hz and 3.2 kHz, leading to a 5 – 8% improvement in BNS range, which corresponds to a 16 – 26% increase of detection rate. During the first 5 months of the 03 science run, a duty cycle of more than 99% was achieved for the injection of squeezing. We can visualize the long-term performance of the shot noise reduction and the duty-cycle during this period in the Figure 3.3.

For the Advanced LIGO detectors [80]: the squeezing enhancement for the L1 detector (detector at Livingston) was up to 2.7 dB above 50 Hz leading to a 14 % increase in BNS range and 50 % increase in expected detection rate, L1 achieved then the highest BNS range ever reported, up to 140 Mpc; for the H1 detector (Hanford), squeezing enhances the sensitivity by 2.0 dB ± 0.1 dB, leading to a 12 % increase in BNS range. The duty cycle reached 98 % for L1 and 100 % for H1.

Achieved squeezing level

In general, the squeezing technology for the reduction of quantum noise is limited by optical loss and phase noise [78, 79] but since the first observation of squeezed light in 1985 [74], squeezed light sources have constantly been

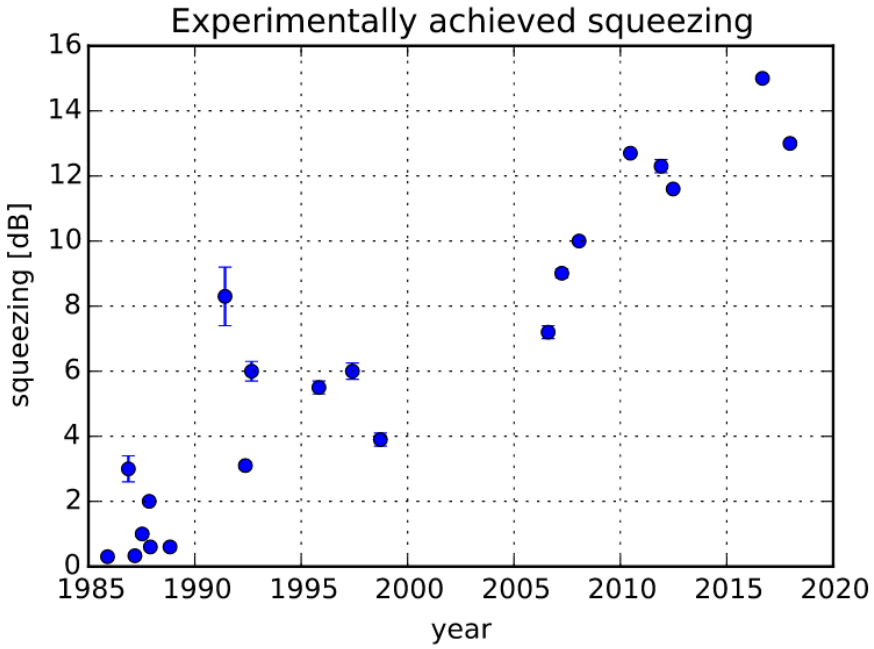

Figure 3.4 – Timeline of experimentally achieved light squeezed (dB) in published laboratory experiments, from [2].

improved, as shown by Figure 3.4 which shows the level of achieved squeezing through the years. An observed squeezing level up to 12 dB in the frequency band from 10 Hz to 100 kHz, is the strongest non-classical noise suppression reported to date in this detection band. Based on simulations, a maximum level of 14 dB can be inferred for a downstream application [61]. Ref. [82] presents a low-loss squeezed-light experiment, allowing for the first direct measure of up to 15 dB squeezing, which is the strongest quantum noise reduction demonstrated to date. This novel approach was used for the precise calibration of absolute external quantum efficiencies of PIN photodiodes based on a continuous wave squeezed-light source. The generation of a high squeezing factor, together with a low anti-squeezing factor is of high relevance for the application in GW detectors.

3.3.2 FDS in LIGO, TAMA and AdV+

The **experimental demonstration** of FDS with a filter cavity was realized by the MIT team [60] and the TAMA team [87].

For the first one, a 16-m filter cavity produces a frequency-dependent rotation at 30 Hz, which meets the requirement for the upgrade of Advanced LIGO detectors (to achieve a rotation frequency of the squeezed states <40 Hz). When improving certain optical elements, it is possible to obtain a broadband reduction of noise of a factor 2 in the detection band of Advanced LIGO, which corresponds to an increase of the volume of the detectable universe by a factor of 8. The low-loss filter cavity was placed in ultrahigh vacuum chambers, identical to those in LIGO detectors and the seismic isolation platforms was designed to look like those of Advanced LIGO. The cavity has a finesse of ~ 80000 for 1064 nm.

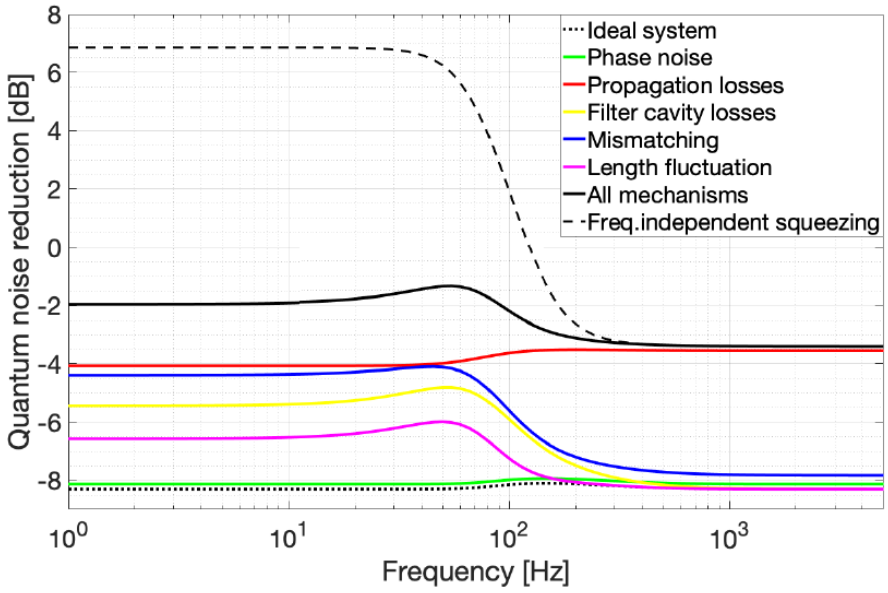

Figure 3.5 – Estimation of the degradation budget for the frequency-dependent squeezing source, from [87]. The black curve shows the improvement of the quantum noise with all the losses combined, expected for a GW detector as KAGRA. The dashed line shows the level of quantum noise reduction from the injection of a frequency-independent squeezed source (using the same magnitude as the frequency-dependent case). The dotted line shows the overall quantum reduction induced by an ideal system.

The second experiment is the first demonstration of FDS reducing quantum noise of advanced GW detectors in their whole observation bandwidth, using a suspended 300 m-long filter cavity, similar to the one planned for the detectors KAGRA, Advanced Virgo and Advanced LIGO. The finesse of the cavity (at 1064 nm) is 4425 so that a squeeze ellipse rotation at about 75 Hz can be achieved. Figure 3.5 shows a degradation analysis for the measured frequency-dependent squeezing, with the modelization of the effect of each degradation source (phase noise, propagation losses, filter cavity losses, mismatching, etc.). The losses used for the modelization were overestimated compared to the effective degradation that is expected for advanced detectors in the next science runs. Therefore, the quantum noise reduction expected is higher than what is shown in this figure. Moreover, the limitations, as for the one due to propagation losses are well understood and can be further reduced. The rotation of the squeezing ellipse was below 100 Hz, which is the region where it is needed to rotate the ellipse for optimal broadband reduction of quantum noise, for GW detectors. By mitigating the limitations, at least 4 dB of broadband quantum noise reduction would be possible.

Advanced Virgo+ filter cavity

The filter cavity (285 m-long) is already installed (suspended mirrors, vacuum chamber pipe) for Advanced Virgo +, as shown by Figure 3.6. This cavity was successfully locked for the first time on June 2021.

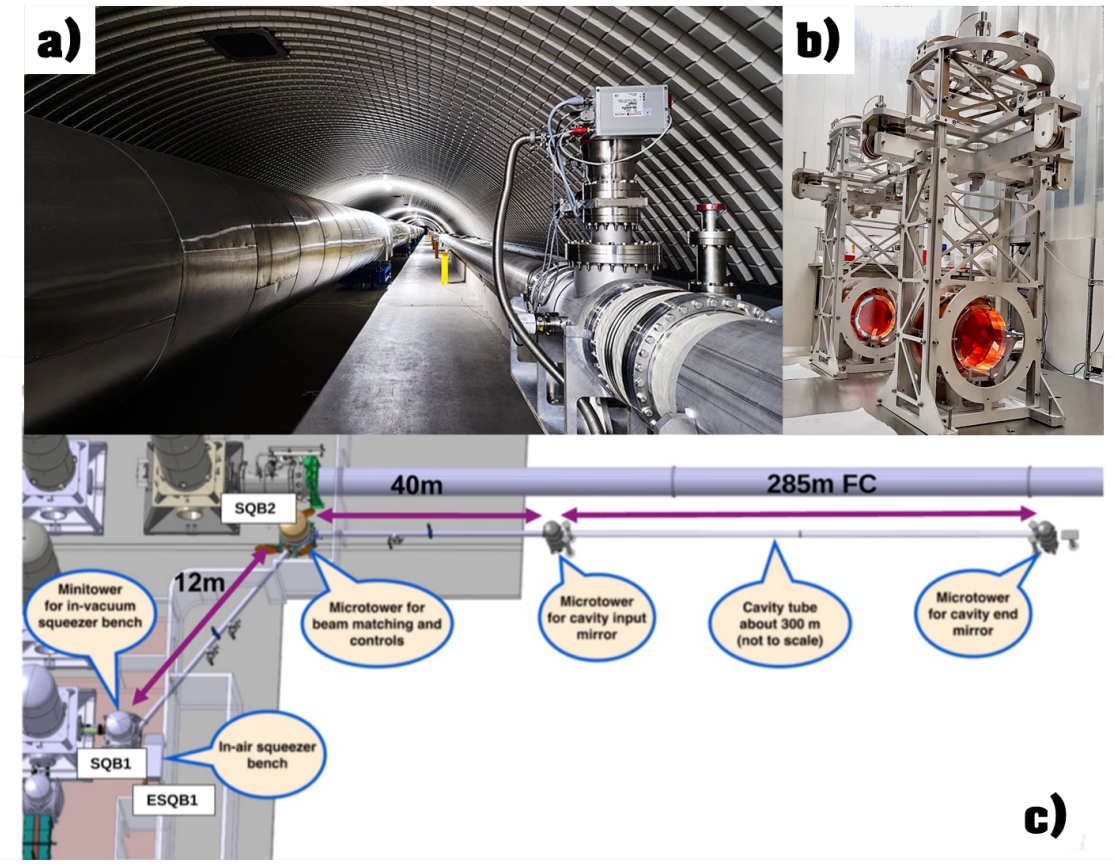

Figure 3.6 – Scheme and photographs (Credit: Virgo Collaboration) of the filter cavity of Advanced Virgo+ (a) Photograph of the filter cavity (in right side) along with the west arm of AdV. (b) Photograph of the input and output suspended mirrors of the 285-m optical filter cavity. (c) Schematics of the filter cavity beam along with the Advanced Virgo infrastructure [34]. FC means filter cavity, SQB1/SQB2 and ESQB1 are the name of the benches (respectively squeezing bench and external squeezer bench).

3.4 EPR entanglement technique

The description of the theory and features of a filter cavity shows its complexity: it requires a very long low-loss filter cavity. In 2017, Ma *et al.* proposed an alternative technique using EPR entangled states, without the need for a cost-intensive external filter cavity [56]. This is very compelling for future detectors as Einstein Telescope [57, 21] because of the reduced cost by not building a long cavity, the flexibility, as having another cavity requires more controls within all the other existing cavities (e.g., with the recycling cavity), and less complex because we do not need to lock this cavity with other auxiliary beams.

This proposal relies on using the interferometer itself as a filter cavity and has been experimentally demonstrated with proof-of-principle experiments [77, 85]. With this technique, two EPR-entangled fields (at different frequencies) are generated by the same OPO which also generates frequency-independent squeezed states (see the right part of Figure 2.7). These two fields are then separated before being measured by two separate homodyne detectors. Once the two entangled fields are detected, the rotation of the squeezed vacuum states is achieved when each measurement is combined. The figure 3.7 depicts the optical configuration for FDS with EPR entanglement. I will describe the theory in Section 3.4.1. In Section 3.4.2, I will present the results of the two proof-of-principles experiments. Then, I will explain two applications of the EPR technique: one for GEO in Section 3.4.3 and the other one for the future long-baseline interferometers in Section 3.4.4.

3.4.1 Principles of the EPR technique

The squeezed-light source is a non-degenerate OPO (the idler and the signal fields do not have the same frequency) which produces two modes: the *signal beam* at frequency ω_0 (described by the quadratures $\hat{a}_1$ and $\hat{a}_2$) and the *idler beam* at frequency $\omega_0 + \Delta$ (described by the quadratures $\hat{b}_1$ and $\hat{b}_2$) by pumping this OPO, at frequency $\omega_p = 2\omega_0 + \Delta$. Note that the name of the quadratures refers to the two-photon operators already described in relations (2.77). The pump field is thus detuned of a quantity Δ (generally of the order of MHz),

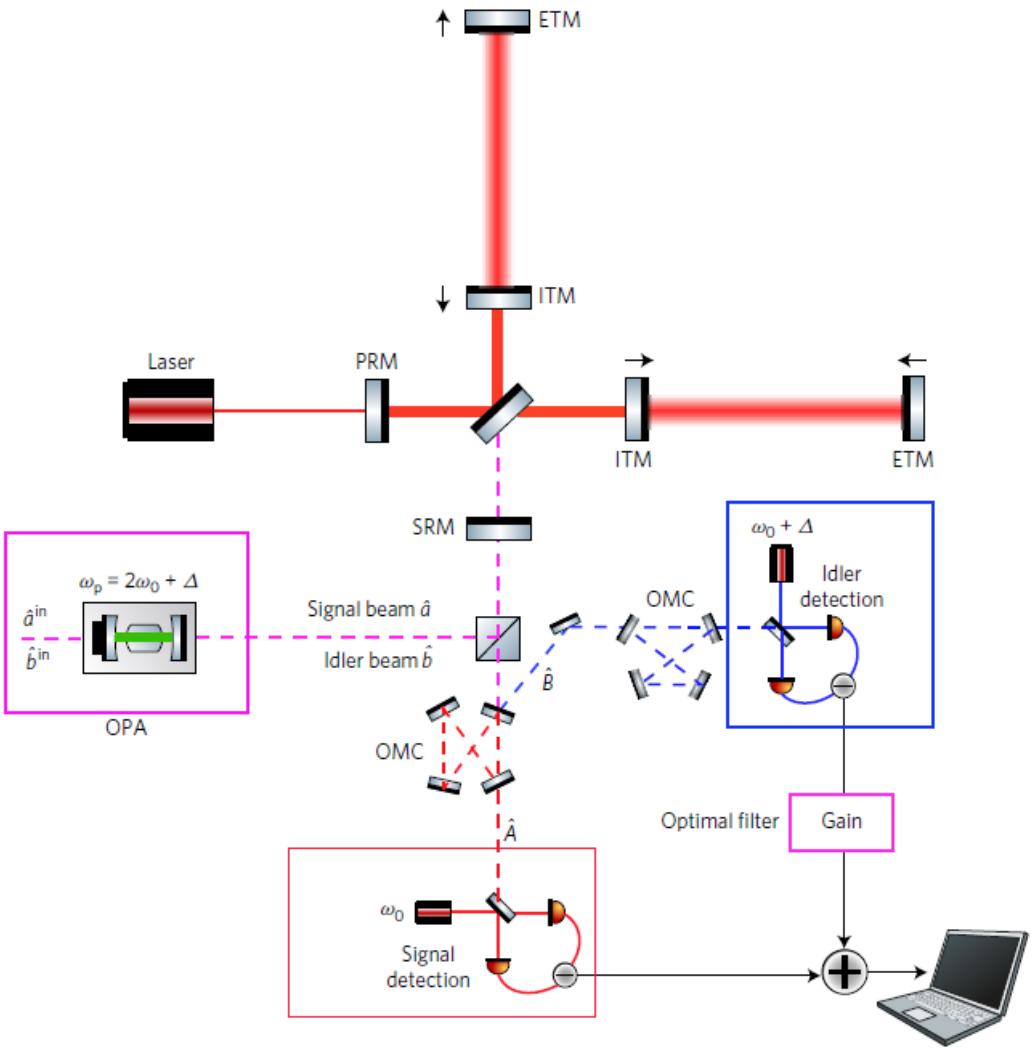

Figure 3.7 – Schematics from [56] for the optical configuration of EPR scheme. The pump field of the OPA (in reality, OPO) is detuned by Δ, generating the signal and idler beam $\hat{a}$ and $\hat{b}$. These fields are injected into the dark port of the ITF and the output beams, reflected back by the ITF arm, $\hat{A}$ and $\hat{B}$, are separated and filtered by the Output Mode Cleaner (OMC) of the ITF. Each field is detected via two separated homodyne detectors and the two measurements are combined with an optimal filter to achieve squeezing on the signal channel. The abbreviations PRM, ITM, ETM and SRM stand for power recycling mirror, input test mass mirror, end test mass mirror and signal recycling mirror, respectively.

and the ω_0 still represents the carrier field of the ITF. In frequency space, the action of the optical parametric amplifier can be visualized as a device that takes

uncorrelated sidebands and entangles or correlates them. Indeed, any frequency modes ω_s and ω_i that verify $\omega_p = \omega_s + \omega_i$ within the squeezing bandwidth, will be entangled with each other. This led to the creation of correlated sidebands around the frequency of the idler and signal beams: we have entanglement between $\omega_0 + \Omega$ and $\omega_0 + \Delta - \Omega$, as well as between $\omega_0 - \Omega$ and $\omega_0 + \Delta + \Omega$, as depicted in the Figure 3.8.

Using the two-photon formalism described in Section 2.5.1, the amplitude and phase quadratures for the signal beam $\hat{a}_1$ and $\hat{a}_2$, are described as:

$$\begin{aligned} \hat{a}_1(\Omega) &= \frac{\hat{a}_+ + \hat{a}_-^\dagger}{\sqrt{2}} \\ \hat{a}_2(\Omega) &= \frac{\hat{a}_+ - \hat{a}_-^\dagger}{\sqrt{2}}, \end{aligned} \tag{3.24}$$

and for the idler beam $\hat{b}_1$ and $\hat{b}_2$:

$$\begin{aligned} \hat{b}_1(\Omega) &= \frac{\hat{b}(\omega_0 + \Delta + \Omega) + \hat{b}(\omega_0 + \Delta - \Omega)^\dagger}{\sqrt{2}} \\ \hat{b}_2(\Omega) &= \frac{\hat{b}(\omega_0 + \Delta + \Omega) - \hat{b}(\omega_0 + \Delta - \Omega)^\dagger}{\sqrt{2}}, \end{aligned} \tag{3.25}$$

These equations can be written in another form, as (Supplementary Info of [56]):

$$\begin{aligned} \hat{a}_1 + \hat{b}_1 = e^r(\hat{a}_{in,1} + \hat{b}_{in,1}), \quad \hat{a}_1 - \hat{b}_1 = e^{-r}(\hat{a}_{in,1} - \hat{b}_{in,1}); \\ \hat{a}_2 + \hat{b}_2 = e^{-r}(\hat{a}_{in,2} + \hat{b}_{in,2}), \quad \hat{a}_2 - \hat{b}_2 = e^r(\hat{a}_{in,2} - \hat{b}_{in,2}); \end{aligned} \tag{3.26}$$

where $\hat{a}_{in}$ and $\hat{b}_{in}$ represents the vacuum fields entering into the squeezer and r is the squeezing degree of the OPO. These quadratures verify an EPR-type commutation relation $\left[\hat{a}_1 - \hat{b}_1\right] = 0$, enabling the existence of the state in which the fluctuations of the linear combinations of quadrature $(\hat{a}_1 - \hat{b}_1)/\sqrt{2}$ and $(\hat{a}_2 + \hat{b}_2)/\sqrt{2}$ are much below the SQL. Indeed, their spectra $S_{\hat{a}_1 - \hat{b}_1} = S_{\hat{a}_2 + \hat{b}_2} = e^{-2r}$. Consequently, $\hat{b}_1$ is correlated with $\hat{a}_1$ while $\hat{b}_2$ is correlated with $-\hat{a}_2$.

Moreover, the general quadratures for these two beams, seen at a random

angle θ is written as:

$$\begin{aligned} \hat{a}_\theta &= \hat{a}_1 \cos\theta + \hat{a}_2 \sin\theta \\ \hat{b}_\theta &= \hat{b}_1 \cos\theta + \hat{b}_2 \sin\theta. \end{aligned} \tag{3.27}$$

Then, $\hat{a}_{-\theta}$ is correlated with $-\hat{b}_\theta$. This means that if we detect $\hat{b}_\theta$, we can predict $\hat{a}_{-\theta}$ with a very good accuracy, while not having any information about $\hat{a}_{\pi/2-\theta}$. In other words, the conditional spectrum of $\hat{a}_{-\theta}$, given the measurement data of the idler quadrature $\hat{b}_\theta$:

$$S^{|\hat{b}_\theta}_{\hat{a}_{-\theta}\hat{a}_{-\theta}} = \frac{1}{\cosh 2r}, \qquad S^{|\hat{b}_\theta}_{\hat{a}_{\pi/2-\theta}\hat{a}_{\pi/2-\theta}} = \cosh 2r, \tag{3.28}$$

the signal beam is thus conditionally squeezed at the quadrature $\hat{a}_{-\theta}$, the squeeze angle being $-\theta$ and the squeeze factor $\frac{\log(\cosh 2r)}{2}$. This squeeze factor is different from the one when using filter cavity, which is r and when $e^{2r} >> 1$, there is $3\,dB$ less squeezing with the EPR squeezing technique.

Note that our notation has changed and the quadratures $\hat{b}_j$ does not represent the quadratures after being injected into the ITF. Instead, the quadratures for each beam, after entering the dark port is written with the same alphabet letter but in upper case. The signal $\hat{a}_{1,2}$ and idler beams $\hat{b}_{1,2}$ enter the ITF dark port and couple with the arm of the ITF. The phase quadratures of the signal and idler beams, after exciting the ITF, $\hat{A}_2$ and $\hat{B}_2$, are detected. The signal beam sees the ITF as a resonant cavity and using the same input-output relations defined in Eq. 2.86, the phase quadrature of the signal beam is:

$$\hat{A}_2 = e^{2i\beta}\,(\hat{a}_2 - \mathcal{K}(\Omega)\hat{a_1}) + \sqrt{2\mathcal{K}(\Omega)}\frac{h}{h_{SQL}}e^{i\beta} = \hat{A}_2^{QN} + \hat{A}_2^{GW}, \tag{3.29}$$

where h is the GW signal, β is the phase shift resulting from the signal beam quadratures inpinging on the arm cavities and defined by Eq. 2.87, h_{SQL} is defined by Eq. 3.9 and $\mathcal{K}$ is the Kimble factor described by Eq. 2.83. $\hat{A}_2$ thus contains shot noise, radiation-pressure noise and GW signal. The first term,

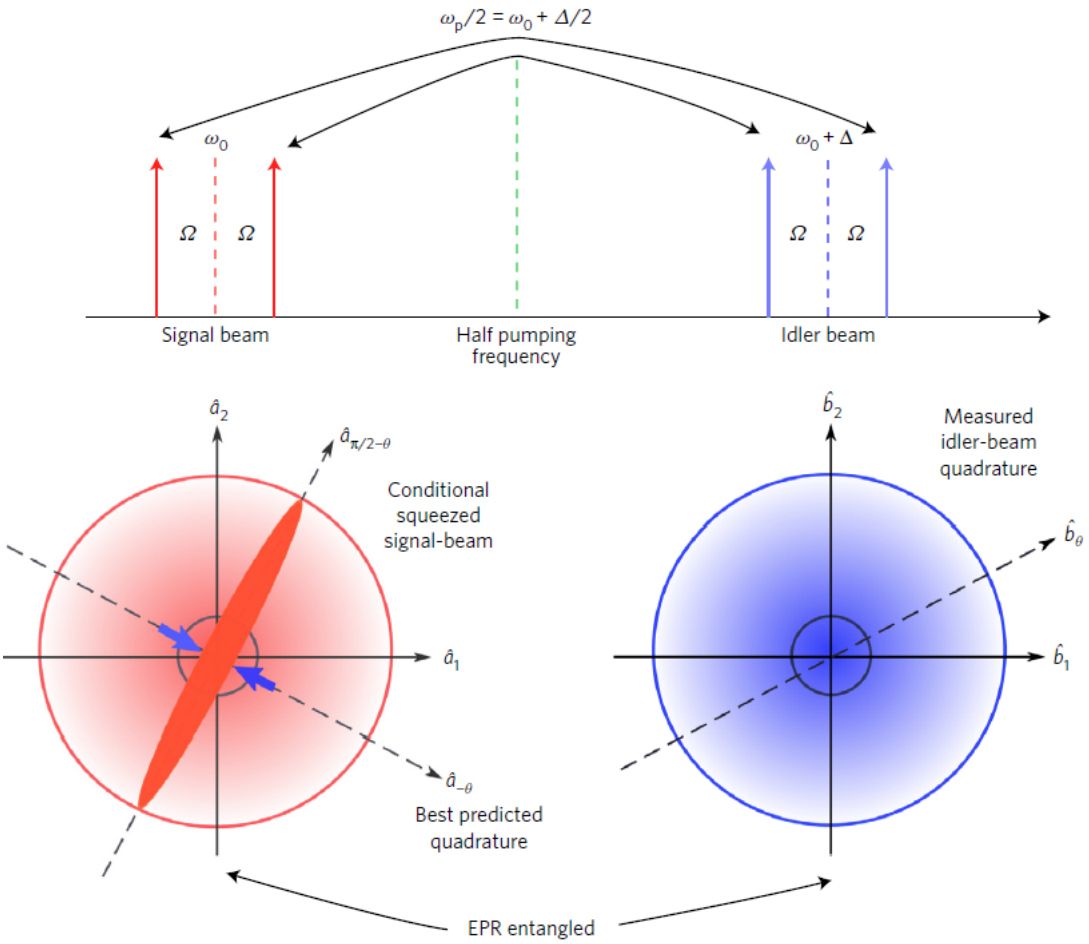

Figure 3.8 – Schematics from [56], visualizing the conditional squeezing related to $\hat{a}_{-\theta}$ and $\hat{b}_\theta$ quadratures. (upper panel) Frequency spacing diagram of the pump field along with the idler, signal fields and their sidebands.(lower panel) Quantum statistics of the signal and idler beams

$\hat{A}_2^{QN}$, representing the quantum noise field, can be written as:

$$\hat{A}_2^{QN} = e^{2i\beta}(\hat{a}_2 - \mathcal{K}\hat{a}_1) = e^{2i\beta}\left(\sqrt{1+\mathcal{K}^2}\right)(\hat{a}_1 \cos\xi - \hat{a}_2 \sin\xi), \tag{3.30}$$

where $\xi = \arctan 1/\mathcal{K}$. However, the idler beam, is far detuned from the carrier frequency of the ITF and thus, does not produce any noticeable back-action noise on the ITF test masses. The idler beam then sees the ITF as a simple detuned cavity, then simply experiences a frequency-dependent ellipse rotation, such

that the quadrature phase of the idler beam is equal to:

$$\hat{B}_2 = e^{i\alpha}(-\hat{b}_1 \sin\Phi_{rot} + \hat{b}_2 \cos\Phi_{rot}), \tag{3.31}$$

where α is an unimportant phase factor accumulated by sidebands of the idler field during its propagation inside the ITF and the rotation angle Φ_{rot} must be equal to $\arctan\mathcal{K}$ so that $\hat{B}_2 = \hat{b}_{\arctan(1/\mathcal{K})}$ is maximally correlated with $\hat{A}_2$, as we need to squeeze the $\hat{a}_{[-\arctan(1/\mathcal{K})]}$ quadrature. The Φ_{rot} can be obtained by detuning Δ and the recycling cavity and arm cavity length. Considering $\hat{A}_2^{GW}$ and having a perfect required Φ_{rot}, the noise spectral density can be expressed as:

$$S_h = \frac{h_{SQL}^2}{2\cosh 2r}\left(\mathcal{K} + \frac{1}{\mathcal{K}}\right). \tag{3.32}$$

Hence the conditional squeezing, if we compare with Eq. 3.6, gives a noise suppression of $\cosh 2r$.

Concerning the detection stage, the reflected fields from the interferometer arm are then separated and filtered by the interferometer OMC and then measured by two separate homodyne detectors. The idler photocurrent undergoes an optimal filtering (called *Wiener filtering*) to counteract the quantum RPN and is subtracted from the photocurrent. Indeed, when combining the two homodyne detection results electronically, we assume that the measurement of the idler field quadrature $\hat{B}_2$ is filtered with a filtering gain factor g and then combining with the signal field quadrature $\hat{A}_2$ as:

$$\hat{A}_2^g = \hat{A}_2 - g\hat{B}_2. \tag{3.33}$$

The variation with respect to the g leads to the Wiener filter, with g_{opt} that give a minimum variance for $S_{\hat{A}_2\hat{A}_2}^{cond}$.

This combination of the measurement of the idler field and the signal field results in a conditional squeezing in a frequency-dependent way, achieving a broadband reduction of quantum noise.

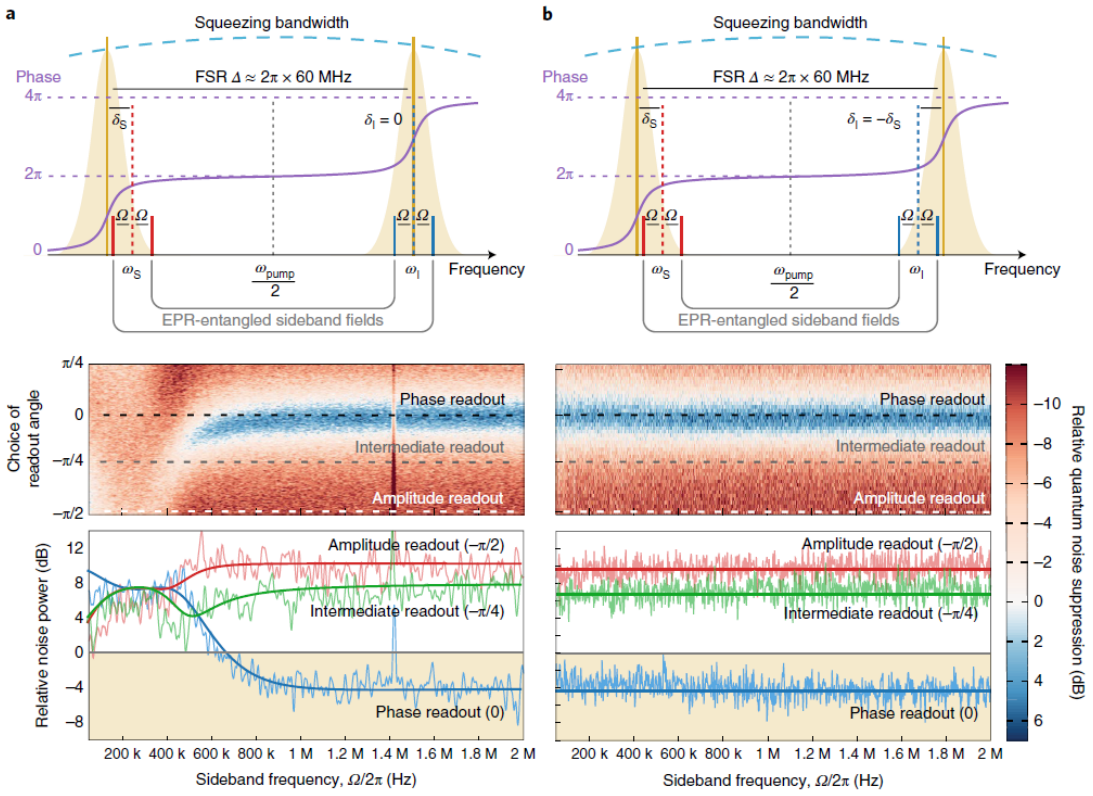

Figure 3.9 – Schematics from [77] showing on top, the relative positions of the signal and idler bands around their frequencies ω_S and ω_I. The EPR entangled fields are shown. The bichromatic homodyne readout enables to have the total quantum noise directly. The spectrograms in the middle show the measured quantum noise variances when scanning continuously the readout angle. The plots in the bottom show cuts of the spectrogram at phase, intermediate and amplitude readout quadratures with the light traces representing experimental data and the dark traces the theoretical fits. (a) The signal band around ω_S is detuned from the cavity resonance by an offset frequency $\delta_S = 2\pi \times 460\,kHz$ while the idler band around ω_I is exactly and the next resonance. The spectrogram shows a frequency-dependent squeezing phase below $\sim 1\,MHz$ but around the detuned cavity resonances, sidebands of idler and signal fields experience different phase shifts, degrading the EPR correlations and leading to increased noise. (b) When the signal and idler field frequencies are detuned by the same amount but opposite phase shift $\delta_S = -\delta_I$, the EPR entangled fields for all sidebands Ω experiences the same frequency-dependent phase shift, resulting on a frequency-dependent squeezing scheme.

3.4.2 Proof-of-principle experiments

There are two proof-of-principles experiments, realized by the University of Hamburg team and the Australian National University. In the first one, Ref. [77] used a 2.4 m-long standing wave cavity to mimic the Signal Recycling Cavity (SRC) of a GW detector and the detection for the two entangled beams at ω_S and ω_I is simplified to a bichromatical homodyne detection. Two bright fields, $LO_{S,I}$ are overlapped with the output entangled fields at a 50:50 BS and the difference in photo-currents is detected at the two BS outputs.

The figure 3.9 depicted the schematics with: on top, the relative positions of the signal and idler bands around their frequencies ω_S and ω_I; in the middle, the spectrograms showing the measured quantum noise variances when scanning the readout angle continuously and at the bottom, the plots in the bottom showing cuts of the spectrogram at phase, intermediate and amplitude readout quadratures with the light traces representing experimental data and the dark traces the theoretical fits. The photo-current variance, in the middle, is normalized to the vacuum noise of both LO. Then, a noise power below 0 dB demonstrates an effective noise reduction with EPR entangled states. First, in figure 3.9(a), the signal and idler fields are adjusted such that the signal frequency ω_S is slightly detuned by a quantity δ_S from one resonance of the linear cavity to have the idler field in the next resonance peak. The measurement sidebands $\pm\Omega$ around ω_S experience a different (unequal and opposite) phase shift which generates a frequency-dependent quadrature rotation, as shown on the spectrogram at the bottom. This is only valid for sideband frequencies Ω much larger than the linewidth of the cavity, because it was not possible to apply an optimal Wiener filter in the readout scheme of the experiment, as proposed by [56]. In the second case, portrayed by figure 3.9(b), the entangled fields have the same but opposite phase-shifts $\delta_S = -\delta_I$ compared to the resonance peak of the cavity, then the noise sidebands of ω_I experience the same but opposite phase shifts to the ones of ω_S, leading to a frequency-independent squeezing, with no quadrature rotation. Indeed, the two measurement bases were optimally aligned at all frequencies, which cancels the frequency-dependent rotation for all of them.

In the second experiment [85], as depicted in Figure 3.11, a pump field, as explained previously, at $2\omega_0 + \Delta$ is injected into an OPO, generating two entangled fields: the signal field (in red) at ω_0 and the idler field (in blue) at $\omega_0 + \Delta$. Then, these two beams are injected into a test cavity, where the signal beam is on the resonance peak while the idler beam sees it as a detuned cavity. Finally, the reflected beams from the cavity arrived to the detection stage where the separation of the idler and signal beams is done by a triangular OMC cavity and detected by two separate homodyne detectors. There is also an auxiliary phase modulated Coherent Locking Field (CLF), injected into the OPO, to control the squeezing angle (readout angle). The measurement is done by recording a spectrogram of the combined ouput (from the two homodyne detectors) while a linear ramp is placed on the idler LO phase. The Figure 3.10 stresses the importance of the detuning of the signal and idler, wrt. the test cavity response. For the first case where $\delta_{sig} = \delta_{idl} = \gamma_{tc}$(left), with γ_{tc} being the linewidth of the test cavity, the same quadrature rotation is imparted onto both the entangled fields, leading to a shot noise reduction. This is equivalent to a squeezed state reflecting off the test cavity with a detuning γ_{tc} so that the spectrum is rotated to the orthogonal quadrature about γ_{tc}. In the second case where $\delta_{sig} = 0$; $\delta_{idl} = \gamma_{tc}$ (middle), the situation is the one propose in [56]. The idler field sees the test cavity as a detuned cavity and is rotated in a frequency-dependent way. Its measurement by the homodyne detector is conditioned onto the signal field measurement (combined electronically), leading to the generation of FDS. Finally, for the last case where the entangled fields are detuned at opposite sides of the test cavity by the same amount, it is the same as the right part of Figure 3.9, the quadrature rotation experienced by the entangled fields cancels one another.

3.4.3 Application to GEO600

Ref. [24] stresses the importance of testing EPR squeezing for the GEO600 detector which is the only GW detector that is taking science data for an extended length of time while using squeezed light. The results are based on the theory applied to the dual-recycled Fabry-Perot Michelson topology (LIGO, Virgo) to adapt to a dual-recycled Michelson without arm cavities, topology used by GEO.

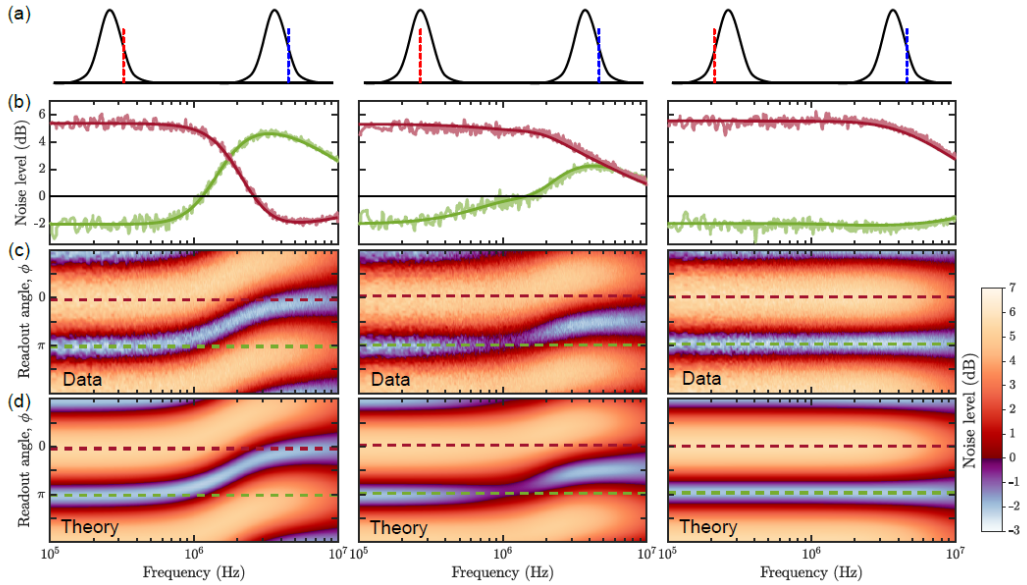

Figure 3.10 – Noise spectrum from Ref. [85] with 3 different test cavity detuning. (**a**) Frequency diagram of the signal (red) and idler (blue) fields wrt. test cavity resonances: $\delta_{sig} = \delta_{idl} = \gamma_{tc}$(left), $\delta_{sig} = 0$,$\delta_{idl} = \gamma_{tc}$ (middle) and $\delta_{sig} = -\delta_{idl}$(right). (**b**) Noise spectrum of the combined measurements at the homodyne stage, for the readout angle 0 (maroon) and π (green). The dark colours line are the theoretical fits. (**c** and **d**) Measured and associated modeled noise spectrum respectively, as a function of readout angle.

The motivation is to "use squeezing effectively in a detuned mode, in which the signal recycling cavity (SRC) and thus the peak sensitivity of the detector is tuned to a particular offset frequency". The paper presents the modelization of different sources of squeezing degradation and concludes that the implementation of EPR squeezing into GEO600 will offer minimal benefits for the sensitivity but is crucial in the purpose of experimental verification in an active detector. First, it is shown that with an optimal parameter for EPR squeezing and using the already used DC readout technique, there is an intrinsic 3 dB loss. The first limiting parameter is the Schnupp asymmetry (macroscopic differential arm length ensuring that RF sidebands to couple at the output port, enabling to detect the SRC for control purposes, when the main carrier light is still near a dark fringe). The choice of this is linked with the detuning frequency Δ for the EPR technique and the conclusion is to use the smallest Schnupp asymmetry possible

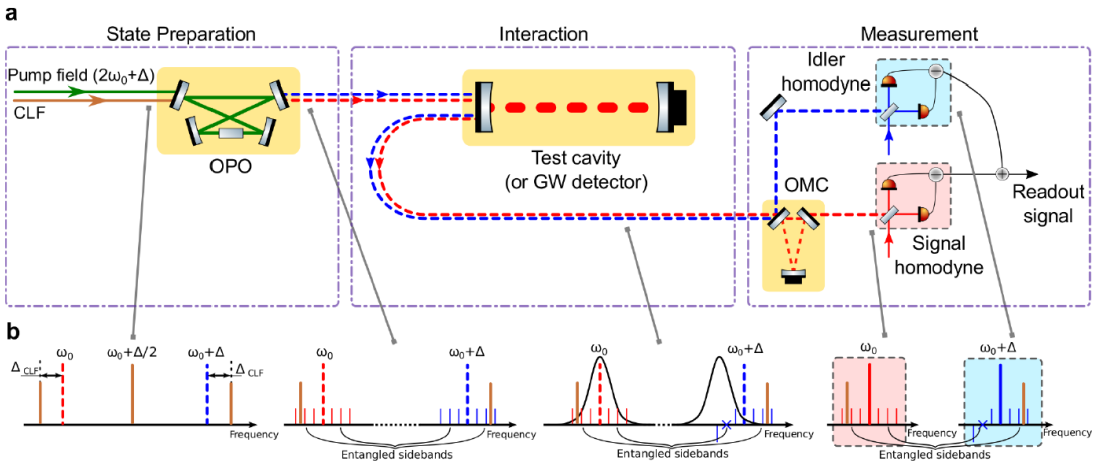

Figure 3.11 – Scheme from Ref. [85] for the generation of FDS with EPR entangled states. (a) Schematic of the experiment where in the left panel, the OPO generates the entangled fields: signal (red) and idler (blue). These fields are injected in the middle panel to a test cavity and reflected back. In the right panel, the reflected beams are sent towards the measurement stage, where they are spatially separated by an OMC cavity and measured with two homodyne detectors and are electronically recombined for the final readout measurement. An auxiliary phase-modulated Coherent Locking Field (CLF) is injected into the OPO, to control the angle of the squeezing ellipse. (b) Frequency diagram of the signal, idler and control fields. In the middle panel, the entangled sidebands between signal and idler fields are represented. The idler field, being detuned from the resonance of the test cavity so that its sidebands experience a differential phase shift when reflected off the cavity.

because it quickly degrades the broadband sensitivity when the SRC FSRs are higher. The second limiting parameter is the imperfect separation of the signal and idler fields when taking into account a realistic OMC model. The noise reduction depends on the Δ quantity, which depends on the number of ω_{SRC} (= FSR of SRC). Finally, the last limiting parameter is the optical losses which are composed of two types: input and output losses (any loss on the squeezing input path and those on the output path after the SRM up to the photodiodes) and the internal loss in the ITF (clipping, surface scattering, absorption) that can be separated into symmetric and asymmetric losses. The first type shows a resonance peak in sensitivity due to Schnupp asymmetry and the last one shows in addition, at the detuning frequency that EPR squeezing is way more affected

by losses, due to the resonance of the SRC.

3.4.4 Application to future Long-Baseline Interferometers

Ref. [21] explains how EPR scheme can be applied to future Long Baseline Interferometers (10-km Einstein Telescope and the 40-km Cosmic Explorer) with a systematic way of finding the working points and achieving nearly perfect ellipse rotation and that the optomechanical coupling constant $\mathcal{K}$ that was described for the 4-km case ([56]) can break down for longer baselines. Indeed, the definition of the optomechanical $\mathcal{K}$ is given, in comparison with the ones from Kimble *et al.*, the difference being the SRC length which is longer, and that the signal recycling mirror transmission becomes comparable to that of the input TM. Then, it is shown that the rotation angle Φ_{rot} depends on the effective detuning and bandwidth of the ITF. The limit on the error in the rotation angle, to keep the degradation in noise reduction to 10% is easily achievable with the LBIs broadband detection mode. Finally, the results from the systematic approach to finding working points for the Einstein Telescope are presented. The tunable parameters are the detuning frequency of the squeezing pump, the small change of the arm length, and SRC length, all scale similarly with the Einstein Telescope. It seems that there is always a working point for the EPR scheme to achieve almost the ideal frequency-dependent rotation of the squeezing quadrature and the area where there are no working points is likely due to inefficient computational parametrization.

3.5 Sources of losses

In a real experiment, it is not possible to only describe the interferometer with the I/O-relations (2.86). In a lossy system, there are always additional channels through which a part of the carrier field leaves the ITF unobserved, while the incoherent vacuum fields from the environment enter and can mix with the squeezed light traveling through the ITF, thus increasing noise. The sources of optical loss are:

- scattering and absorption on the mirrors and finite transmissivity through

end mirrors for the light inside the ITF arm cavities.

- concerning the squeezed vacuum injected into the dark port: fractional photon losses in the circulator (a four-port optical device that separates spatially the injected input and the returning output from the ITF; in our case, a Faraday isolator) used for the injection of FDS, in the BS and in mode-matching into the ITF.

- concerning the ITF signal that leaves, unobserved: fractional photon losses in the BS, in the circulator, in mode-matching into each of mode cleaner (MC), in mode-matching with the local-oscillator light used for homodyne detection and in the photodiode inefficiency.

3.5.1 Loss analysis for the EPR scheme

Compared to a filter cavity scheme, we suffer less from loss in the filter cavity, since the ITF arm have less loss. However, the input and detection losses are doubled because the two entangled fields experience the same amount of loss during their propagation inside the ITF, in addition to the intrinsic penalty on the noise reduction that is equal to $1/\cosh 2r$ instead of e^{-2r} for the filter cavity. There are other losses: the loss due to the arm cavity and the SRM, the phase fluctuation on the two LO to measure the entangled fields. In the following, I will only develop more about the input and readout losses as it concerns the etalon design presented in Chapter 6.

Input and readout losses

The Supplementary information of [56] gives the approximated formula for the degradation of the strain sensitivity as a sum of input loss contribution $\Delta S_{hh}^{\epsilon_{in},cond}$ and the readout loss contribution $\Delta S_{hh}^{\epsilon_r,cond}$:

$$\Delta S_{hh}^{cond} = S_{hh}^{\epsilon_{in}cond} + \Delta S_{hh}^{\epsilon_r cond}, \tag{3.34}$$

where ϵ_{in} and ϵ_r are respectively, the input and readout losses (in terms of power) of the entangled fields. Assuming that $\epsilon_{in} = \epsilon_r = \epsilon$, the noise spectrum for the

traditional broadband squeezing (using an external filter cavity) $\Delta S_{hh}^{\epsilon,trad}$ and the EPR squeezing $\Delta S_{hh}^{\epsilon,cond}$, under the approximation that the squeezing degree is large:

$$\Delta S_{hh}^{\epsilon,cond} \simeq \frac{h_{SQL}^2}{2}\left(\frac{2}{\mathcal{K}}+\frac{3}{2}\mathcal{K}\right)2\epsilon, \qquad \Delta S_{hh}^{\epsilon,trad} \simeq \frac{h_{SQL}^2}{2}\left(\frac{2}{\mathcal{K}}+\mathcal{K}\right)\epsilon, \tag{3.35}$$

We have clearly $\Delta S_{hh}^{\epsilon,cond} \sim 2\Delta S_{hh}^{\epsilon,trad}$, which is coherent with what was explained earlier, that both signal and idler fields experience the same loss during their propagation.

3.6 Summary

In 1981, Caves demonstrated that quantum noise originates from the zero-point fluctuations entering from the dark port of the GW interferometer beam-splitter. A solution to beat the standard quantum limit is to inject squeezed vacuum states into this dark port.

The frequency-independent squeezing technique was routinely used during the O3 data-taking. This technique consists in the injection of phase-squeezed vacuum: the minimal fluctuation is found in the phase quadrature while the maximal one is found in the amplitude quadrature. The side effect of this technique was the increase of the radiation pressure noise. This was not detrimental for the GW low-frequency sensitivities as this noise was just below the residual technical noise sources up to the O3 science run. The frequency-independent squeezing technique enables for the LIGO detectors to have up to a 50% increase in the expected detection rate (around 14% increase in the BNS range with the highest BNS range achieved for the L1 detector) and for the Advanced Virgo detector, a 16-26% increase in the detection rate was observed.

Between O3 and O4 science run, the technical noise contributions will be reduced below the RPN level so that an increase of RPN will degrade the GW detectors sensitivity. Consequently, arises the need of a technique where the squeezing angle is frequency-dependent to achieve a broadband reduction of

quantum noise. For Advanced Virgo+ and Advanced LIGO+, a frequency-independent squeezing technique using an external filter cavity is adopted. The strategy is to inject a frequency-independent squeezed vacuum inside this filter cavity, whose upper and lower sidebands will undergo a differential phase. This will leads to a rotation of the squeezing quadrature angle in a frequency-dependent way. Several experimental demonstrations proved the feasibility of this technique and the filter cavity of Advanced Virgo+ was successfully locked for the first time on June 2021.

The use of an external filter cavity raises logistical and financial problems. The filter cavity required must be very long (285 m for Advanced Virgo+), which is cost-intensive, requires more controls within all other existing cavities as the recycling cavity and thus making the detector more complex and less flexible. In 2017, Ma and coworkers proposed an alternative technique using EPR-entangled states, eliminating the need of an external filter cavity. In this technique, two EPR-entangled fields are generated by the same OPO cavity which is used to generate frequency-independent squeezed states. These two fields are then injected inside the ITF where one of the arms will act as a filter cavity. Then, these fields are reflected off from the ITF, separated by the ITF output mode-cleaner. Finally, they are detected separately by two different homodyne detectors: the outcome of the detection of one of the fields will condition the outcome of the detection of the other field, leading to a frequency-dependent squeezing. Two proof-of-principles experiments demonstrated the feasibility of the technique. This technique is promising, in particular for 3G detectors as Einstein Telescope. The next chapters will describe the preliminary work to build the EPR demonstrator, compatible for a direct injection inside a GW detector and which will test the radiation pressure noise reduction with EPR squeezing in a small suspended interferometer, this noise being present in the same frequency band as the current GW detectors.

Chapter 4

Development of a frequency-independent automated squeezed vacuum source for GW detectors

Outline of the current chapter

In Chapter 2, I explained that it is possible to beat the Standard Quantum Limit, which limits interferometric GW detectors, with the injection of non-classical quantum states of light, called squeezed states. The frequency-independent squeezing (FIS) technique, enables to reduce quantum noise at high frequencies

(the shot noise) while increasing the noise at low frequency (the quantum radiation pressure noise). Both LIGO and Virgo routinely used squeezing injection during the last observing run O3 and it allowed to significantly increase their detection rate.

In this chapter, I will present the frequency-independent squeezing experiment performed in the *1500 W lab*, a laboratory located on the Virgo site, in a cleanroom along the Virgo 3 km west tube. The experiment was designed in the first place, to build the vacuum squeezer source for Advanced Virgo. Fortunately, with the enlargement of the Virgo collaboration, it was decided that the Hannover Max-Plank institute team (pioneer for the injection of squeezing in a GW detector) provided the squeezer. Then, the purpose of the experiment changed and it has been to develop and test advanced methods for quantum noise reduction. In this framework, I participated in the implementation of coherent-control technique, in the improvement and characterization of the overall bench needed for the implementation of its automation. This work was published in [62].

The chapter is organized as follows. The main optical features of our experiment are described in Section 4.1, encompassing the three lasers (one main laser and two auxiliary lasers), the non-linear cavities (SHG and OPO cavities), the Mach-Zehnder interferometer, the mode-cleaner cavities, the homodyne detector and the description of the auxiliary beams needed for the experiment. Then, the description of the different steps and experimental methods to measure the squeezing performances is given in Section 4.2. In Section 4.4, the software-based FSM used to automatize some parts of the bench is described. These techniques can be used for other experiments and designed to be compatible with Virgo. In particular, we will use them for the EPR-based squeezing experiment described in Chapter 5.

4.1 Experimental setup

The optical layout of the frequency-independent squeezing generation experiment is shown in Figure 4.1.

The Main Laser, a 1 W continuous laser at 1064 nm, generates the pump

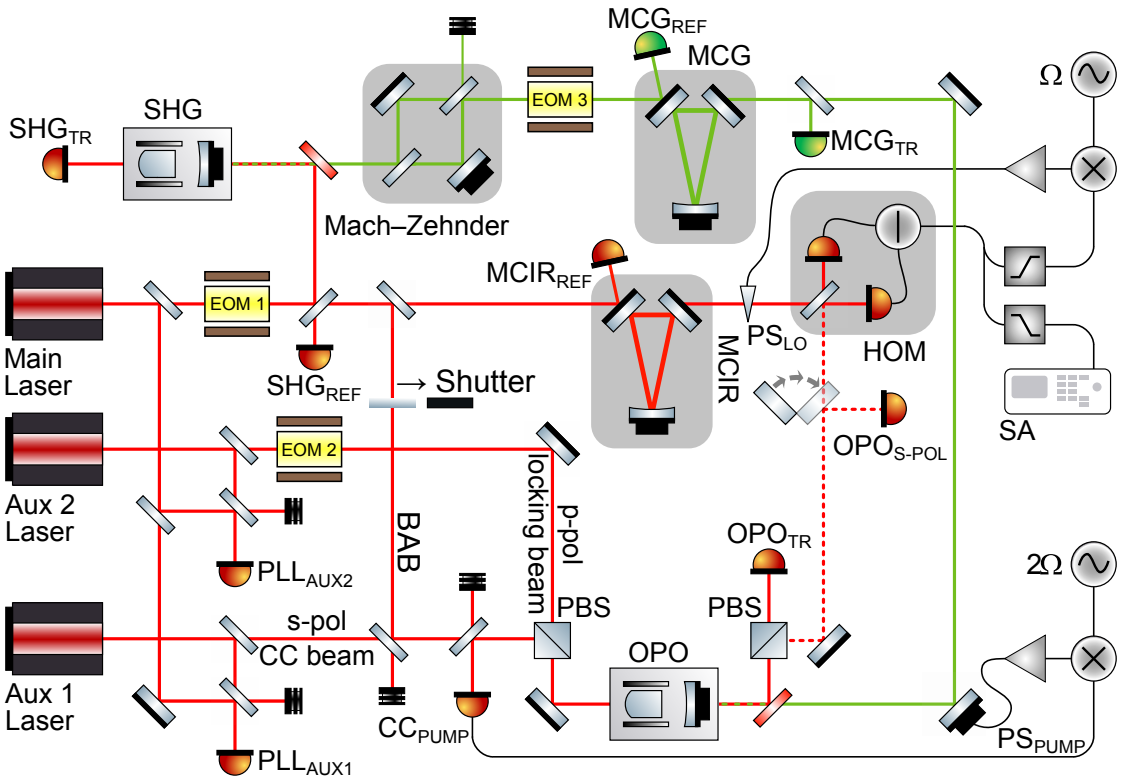

Figure 4.1 – Schematics of the optical layout of our FIS experiment, from [62].

field for SHG cavity, the Bright Alignment Beam (BAB) and the main carrier frequency for the local oscillator field (LO) for the homodyne detection (HOM). The two auxiliary lasers AUX 1 and AUX 2, with a nominal power of 200 mW, are phase-locked to the main laser employing an optical phase-locked loop (OPLL). The beat note of each of them and the Main Laser is obtained respectively with the photodiodes PLL_{AUX1} and PLL_{AUX2}. AUX 1 provides the Coherent Control (CC) beam and AUX 2 provides the OPO locking beam (Length Control Beam (LCB)). The triangular cavities Mode-Cleaner Green (MCG) and Mode-Cleaner Infrared (MCIR) are respectively used for the spatial mode-cleaning of the green pump field generated by the SHG and the LO while the Mach-Zehnder (MZ) interferometer's goal is to stabilize the power of the pump beam. Phase shifter PS_{LO} and PS_{PUMP} are mirrors with piezoelectric actuators for the coherent-control technique, described in Section 4.1.2. The measurement of the squeezing level is done with a homodyne detector coupled with a spectrum analyzer (SA).

The suffixes REF and TR respectively stand for "reflection" and "transmission," and they are used for the names of all the photodiode (PD)s for cavities' locking which are presented here.

In the following subsections, I will describe the different optical components and auxiliary beams. A further description of the experiment can be also found in [73, 38, 53, 83].

4.1.1 Laser sources

Three solid-state continuous-wave NPRO (Non-Planar Ring Oscillator) Nd:YAG laser sources with a wavelength at 1064 nm) are used in the experiment.

The main laser (ML), whose output power is 1 W, is a Mephisto model (from COHERENT company) and produces an s-polarized beam at a wavelength of 1064 nm (correspondent to a frequency ω_0 in the following of the chapter). This laser is characterized by a frequency linewidth of about 1 kHz, and a relative intensity noise (RIN) of -140 dB/Hz. This laser generates the pump field for SHG cavity, an auxiliary beam called BAB (described in Section 4.1.2), and the local oscillator field (LO) for the homodyne detection. In order to lock the cavities as SHG and Mode-Cleaner InfraRed (MCIR) with the Pound-Drever-Hall technique (whose principle is explained in Section 4.4.2), the laser is phase-modulated with the resonant electro-optic modulator (EOM) EOM 1 at 80 MHz.

The auxiliary lasers AUX 1 and AUX 2 are Mephisto S model. Each of them is phase-locked with the ML via a PLL (phase locked loop) feedback control system. This makes their frequency to be $\omega_0 + \Omega_{AUX1/AUX2}$.

AUX 1 generates an s-polarized beam for the CCB, described in Section 4.1.2 to stabilize the phase of the generated squeezing, i.e., to fix the angle of the squeezing ellipse. For the PLL, the beat note between a pick-off beam from the ML and one from AUX 1 is detected by the photodiode PLL_{AUX1} and the constant frequency detuning is kept at $\Omega_{AUX1} = 7$ MHz.

AUX 2 is used in p-polarization for the active length control of the OPO cavity, the LCB, described in Section 4.1.2 and its detuning with respect to ML is $\Omega_{AUX1} = 150$ MHz. Its phase is modulated, at a frequency of 78 MHz by the resonant EOM 2 to generate the Pound-Drever-Hall signal (explained in Sec 4.4

to lock the OPO cavity. The beat note of this laser with the ML is detected by the photodiode PLL_{AUX2}.

4.1.2 Auxiliary beams

There are three auxiliary beams needed to run the experiment: the Bright Alignment Beam (BAB), used to align the squeezed vacuum into the homodyne detector, the Locking Beam (or Length Control Beam/LCB), to lock the OPO cavity and, finally, the Coherent Control Beam (CCB), to control the phase of the squeezing ellipse (CCB_{pump}) with respect to the phase of the LO field (CCB_{LO}).

Bright Alignment Beam (BAB)

Since the squeezed field is a vacuum field, it cannot be used for control and alignment purposes. We then need a *bright* beam (beam with a non null power) to align the squeezed beam from the OPO to the homodyne detector. The BAB is a pick-off from the main laser and it is s-polarized. As shown in Figure 4.2 and 4.3, after being transmitted into the OPO, the BAB is reflected by a dichroic mirror and then, reflected by the PBS_{OPO}. Two steering mirrors STR_{B1} and STR_{B2} are used to align the BAB to the BS of the Homodyne Detector (HD). Since the BAB, as the squeezed beam is resonant inside the OPO, it is always co-aligned with it. To achieve the measurement of squeezing, as explained in Section 4.2, we need to superimpose perfectly the BAB and the LO field. When the alignment is done, the BAB path can be blocked with a shutter as depicted in Figure 4.1, to let only the squeezing field reach the homodyne detector.

Length Control Beam (LCB)

As explained previously, we use AUX 2 which provides a p-polarized beam for the LCB. This beam is phase-modulated with a resonant EOM to lock the OPO cavity with the Pound-Drever Hall (PDH) technique. The polarization of LCB is perpendicular to the one of the squeezed field so that any coupling between the two is avoided. Due to the birefringence of the OPO crystal, the resonance conditions for p and s-fields are frequency offset with respect to each other.

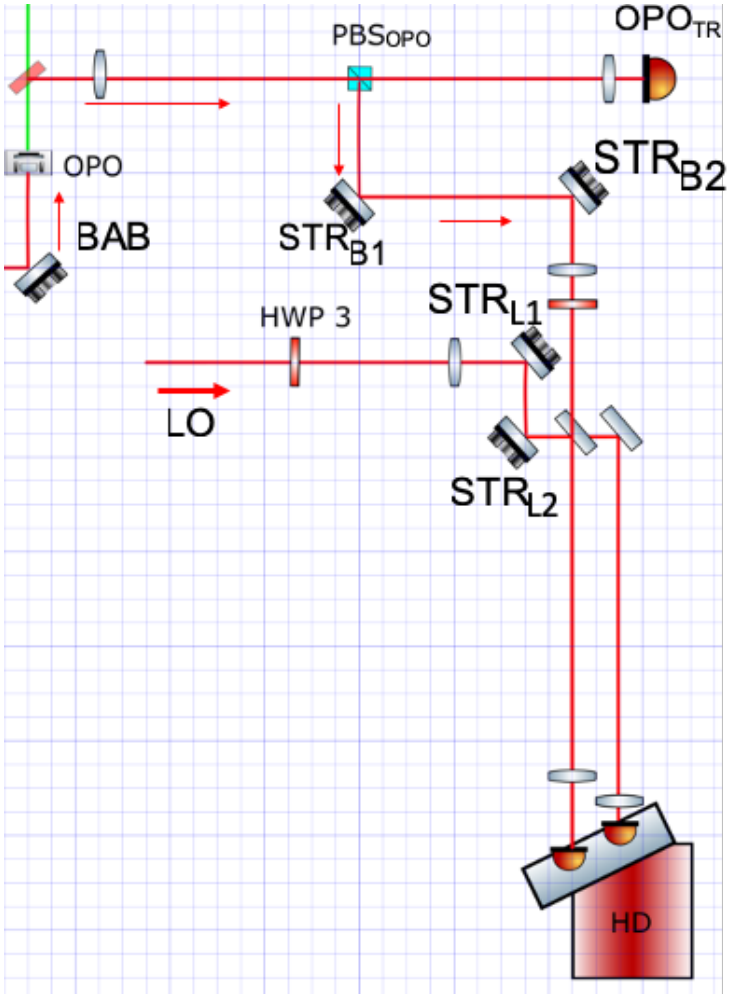

Figure 4.2 – Path of the BAB from the OPO to the homodyne detection represented in an in-scale optical layout.

Consequently, the frequency of the LCB is constantly detuned (with an optical phase-locked loop) from the one of ML (and thus the squeezed field and BAB) of 150 MHz. The temperature of the OPO crystal should be tuned to have LCB and BAB both resonant inside the cavity.

Coherent Control Beam (CCB)

To observe squeezing in the audio-band, we have to actively control the squeezing angle, which is usually affected by large fluctuations, especially at low frequency.

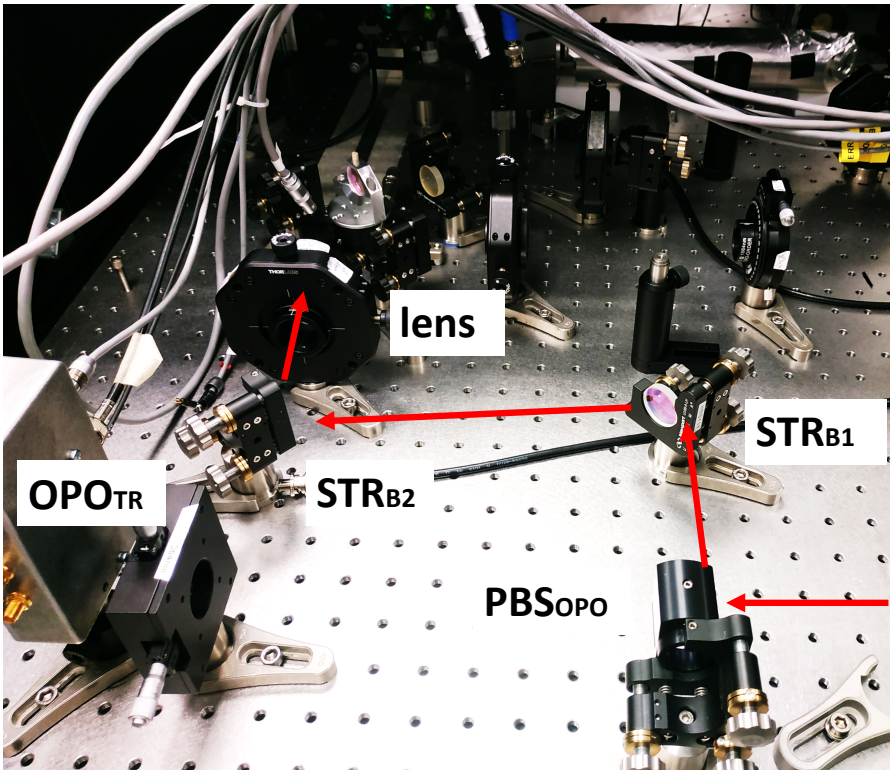

Figure 4.3 – Path of the BAB from the OPO to the homodyne detection represented in an in-scale optical layout.

The stability of the squeezing angle is strictly related to the stability of the phase of the pump beam and of the LO that is taken as a reference for the measurement. The method used to achieve this, is called the *coherent-control* technique [81]. This makes use of a beam with the same polarization as the squeezed beam (s-polarized) injected in the OPO, with a shift in frequency done by an OPLL of Ω_{AUX1} = 7 MHz [62] with respect to the frequency of the ML. The frequency shift being lower than the OPO linewidth (25 MHz), this beam is thus still resonant inside the OPO. Hence the OPO non-linear process (see parametric gain explanation in Section 4.3.2) generates a symmetric sideband, with respect to the carrier, at -7 MHz (-Ω_{AUX1}).

In order to control the phase between the OPO pump field and CC_{pump}, an error signal is generated using the back-reflected CCB from the OPO acquired by the photodiode CC_{pump} whose photo-current is demodulated at 2 Ω_{AUX1}

crystal dimensions	1 x 1.5 x 9.3 mm
curved face RoC	8 mm
curved face reflectivity	> 99.975 % (both frequencies)
distance coupling mirror-flat face	22 mm
coupling mirror inner RoC	25 mm
coupling mirror outer RoC (only for SHG)	20 mm
coupling mirror outer face	AR coated at both wavelengths
Reflectivity inner face @1064 nm	90 % (SHG)
	92 % (OPO)
Reflectivity outer face	< 0.2 % (@1064 nm)
	< 0.3 % (@532 nm)

Table 4.1 – Parameters of SHG and OPO's crystal and mirrors. The RoC is the ray of curvature.

(14 MHz). The feedback loop is made using a piezoelectric (PZT)-mounted mirror PS_{pump} along the green pump beam path (see Figure 4.1).

The transmitted CCB, through the OPO cavity, is used to lock the squeezed field phase to that of the LO, which is the reference for the measurement. To fix the phase between the squeezed beam and the LO, the error signal is derived from the radio frequency (RF) difference signal provided by the HD, demodulated at Ω_{AUX1} (7 MHz). This signal is again fed back to another phase-shifting PZT-mounted mirror PS_{LO}.

4.1.3 Nonlinear cavities: SHG and OPO

The two nonlinear cavities, SHG and OPO, described in Section 2.3, are hemilithic cavities both made with a Periodically Poled Potassium Titanyl Phosphate (PPKTP) crystal with a high reflectivity (HR)-coated (R = 99.975% at both 1064 nm and 532 nm) curved face and an in-coupling mirror. The choice of a periodically-poled material enables to reach the phase-matching condition with a loose condition on the crystal temperature. The flat surface of the crystal is anti-reflection coated ($R < 0.2\%$ for 1064 nm and $R < 0.3\%$ for 532 nm). This compact configuration enables to have low intracavity losses and ensures a good conversion efficiency even with a pump beam that is not perfectly aligned on the crystal. The coupling mirror is linked to a PZT actuator enabling to scan the

SHG and OPO cavity length, to be able to lock with the PDH technique.

Table 4.1 summarises the parameters of the OPO and the SHG cavities, whose design and characterization are described in [73, 38]. The OPO scheme with its geometrical parameters is presented in Figure 4.4.

SHG

As described in Section 2.3.1, the SHG process is based on three-wave mixing. The pump field for the SHG is provided by ML, at ω_0 (1064 nm) and the output beam is at $2\omega_0$ (532 nm). This output field is used as a pump field for the OPO cavity. The SHG design was inspired by [70], presented in [38], where the characterization was also done. The SHG finesse is $\mathcal{F}_{SHG} = 54$ with a Free Spectral Range (FSR) of about 3.8 GHz, which corresponds to a full-width at half maximum (FWHM) of about 71 MHz. The achieved SHG conversion efficiency is more than 69 % at the optimal phase-matching temperature of 31.6 °C.

The beam from ML is separated with a 50:50 BS, then phase-modulated by *EOM* 1 at 80 MHz for the active length control of the SHG cavity. It enters the SHG cavity through a dichroic mirror, where the second harmonic beam is transmitted. The cascaded dichroic mirrors are used to filter out the residual IR beam at 1064 nm and the Faraday isolator at 532 nm is placed to remove the back-reflected beams towards the SHG cavity, as shown in Figure 4.5.

Degenerate OPO

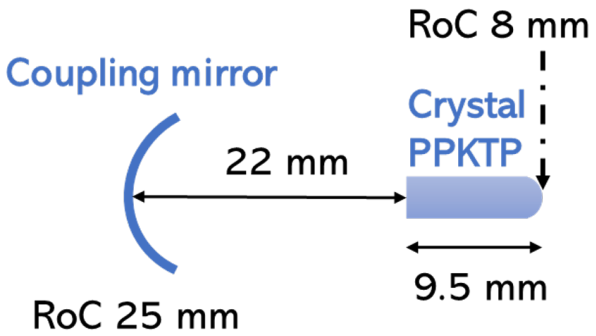

Figure 4.4 – Geometrical parameters of the OPO cavity.

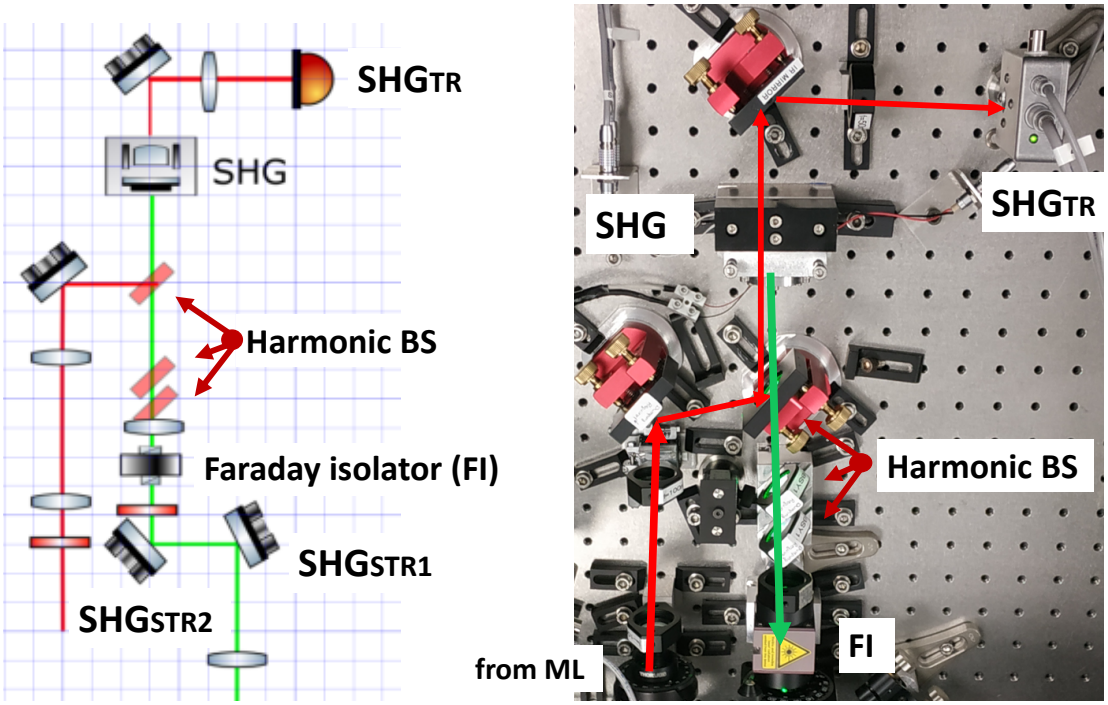

Figure 4.5 – (Left) Optical layout of the SHG path. (Right) Photo of the SHG path.

The Optical Parametric Amplification process, described in Section **??** is a three-wave mixing interaction with $\hbar\omega_3 = \hbar\omega_1 + \hbar\omega_2$, the OPO being degenerate, $\omega_1 = \omega_2$. The input field at ω_3, with a very high intensity compared to the beam at ω_0, is the pump field, corresponding in our case, to the green beam at $2\omega_0$, generated by the SHG cavity, the weak field (also called fundamental field or signal field) at ω_1 is the vacuum field at ω_0. Our OPO cavity is chosen to be singly-resonant, i.e., it is only resonant on the signal field, enabling to avoid the phase compensation (an offset between pump and signal beam's resonance frequencies) required in a doubly resonant cavity. As shown by Figure 4.2, the OPO is pumped by the green beam that enters through the incoupling mirror on the other side, and a BAB can be injected instead of the vacuum, to align the squeezed beam to the homodyne detector (HD). There are also two other auxiliary beams entering from the same side: the locking beam (LCB) and the coherent-control beam (CCB). The finesse of the OPO is equal to $\mathcal{F} = 75$ at 1064 nm (and the FSR is 3.8 GHz and thus the FWHM is 50 MHz), while at 532 nm,

the parameter is $\mathcal{F} = 3.5$ (FSR = 3.74 GHz and a FWHM =1.01 MHz). These parameters were chosen and measured in [73]. A general scheme of the OPO cavity with its geometrical parameters is presented in Figure 4.4. The mechanical design is similar to the one of the GEO600 team [51].

4.1.4 Pump beam power stabilization

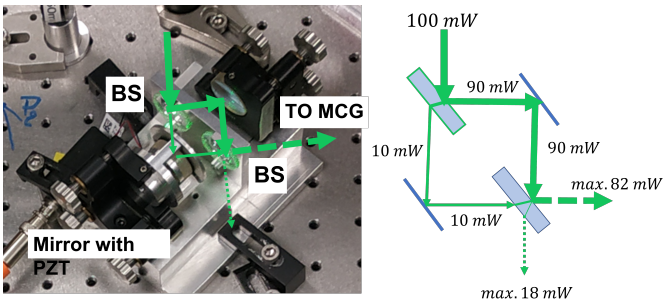

Figure 4.6 – (Left) Photo of our MZ interferometer with the green path drawn. (Right) Scheme of the power distribution for an incident beam of 100 mW.

The pump beam at 532 nm generated by the SHG cavity is power-stabilized by a Mach-Zehnder (MZ) interferometer, before being sent to the OPO cavity. In fact, the fluctuations of the OPO pump power result in fluctuations of the squeezing level [52]. The interferometer, depicted in Figure 4.6, is composed of two mirrors ($R > 99.99\%$) and two BS with unbalanced arm power to keep a maximum and stable power for the pump field before entering the Mode-Cleaner Green (MCG) (see right figure for the power distribution of each beam). Indeed, as the pump beam is divided in two twice (topology of a MZ interferometer), by two BS, we chose a transmission ratio of 90% for the BS so that the final transmitted beam will not lose too much power, compared to the beam before entering the MZ interferometer. The two BS have a reflectivity of $R = 10\%$ for p-polarized beam and 1 % for s-polarized beam. The MZ is locked with a Proportional Integrative Derivative (PID) loop using the photodiode MCG_{REF}. The procedure is to scan the MZ interferometer with one piezo-actuated mirror (indicated in the figure) to see fringes due to the unbalanced optical path along each MZ interferometer arm, on the MCG_{TR}, to choose a voltage level on these

fringes and lock the MZ on this level. The MZ interferometer output is thus constant in time and the OPO green pump field is power-stabilized.

4.1.5 Mode-cleaner triangular cavities

The mode-cleaner cavities in our experiment are triangular cavities, which have the role of cleaning the beam mode spatially, suppressing the higher-order modes and transmitting only the fundamental TEM_{00} mode. These cavities are composed of two plane mirrors (input and output couplers) and a curved mirror with a radius of curvature (RoC) of 1 m. The optical elements are mechanically mounted on an INVAR spacer with a thermal expansion coefficient of $\alpha = 1.2 \times 10^{-6} K^{-1}$, ensuring good thermo-mechanical stability. The control on the cavity length is obtained with a PZT actuator attached to the rear surface of the curved mirror. There are two mode-cleaner cavities in our experiment: the MCG, which cleans the green pump beam before injecting it inside the OPO and the MCIR, which cleans the LO field, before overlapping it with the squeezed beam and ensuring a good overlap integral between them. The spectral properties of these two mode-cleaner cavities are presented in Table **??**. These cavities were characterized in [53].

	FSR	FWHM	$\mathcal{F}$	λ
MCG	$515 MHz$	$5 MHz$	101	532 nm
MCIR	$550 MHz$	$7.7 MHz$	71.3	1064 nm

Table 4.2 – Spectral properties of the two mode-cleaner cavities.

4.1.6 Homodyne detector

As explained in Section 2.4, the homodyne detection system [76] is needed to measure the squeezing level, produced by our setup. The squeezed field beats with a strong coherent field, the LO, used as a phase reference. The detector electronics design is based on a self-subtraction scheme: two PD, which have a high quantum efficiency ($\sim$ 99 %) and a photosensitive area of 500 x 500 m, provide photo-currents that are first subtracted and then amplified. The

homodyne detector provides, among others, the DC readout of each PD (used for power balance and alignment), an AC readout of the difference and sum of the photo-currents in the audio-band (10 Hz-10 kHz), a RF channel for the *coherent-control technique*. The design is detailed in [86].

4.2 A typical squeezing measurement

In this Section, we will give an exhaustive description of all the steps needed to measure the squeezing. The locking of the PLLs, the MZ interferometer and cavities (SHG, MCG, OPO, MCIR) is done using a Finite-State Machines (FSM)-based software, which will be developed in Section 4.4. The squeezed vacuum generated by the OPO cavity, is sent to the homodyne detector. By acquiring and comparing the signal with and without a squeezing beam with a spectrum analyzer, it is possible to measure the squeezing level. An example of squeezing measurement is shown in Figure 4.10, where the squeezing level is at -1.6 dB and the antisqueezing at 2.3 dB. The measurement is performed in time domain by setting the spectrum analyzer in the zero-span mode with a central frequency of 1.1 MHz. The dark noise of the detection system is measured before, by blocking all the beams arriving on HD (BAB and LO) and is around -89.0 dBm. The coherent vacuum noise (i.e the shot noise) was recorded when only the LO is reaching the homodyne, and it is around -78.1 dBm, giving a clearance between the electronic detection dark noise and the vacuum noise reference of up to 10.9 dB at 1.1 MHz. The clearance is limiting the maximum squeezing level that can be measured with the setup.

Before performing the squeezing measurement, we must also optimize the Common-Mode Rejection Ratio (CMRR) for the homodyne detector and the contrast between the LO and the squeezed beam. The alignment procedures needed to measure these two parameters will be described in the next subsections.

4.2.1 Laser sources

The first step is to lock the two PLLs, PLL_{AUX1} and PLL_{AUX2}. The PLL is described in Section 4.1.1 and the control system is described in Section 4.4. This

enables to have a stable frequency shift with respect to the ML beam, respectively for CCB and LCB.

4.2.2 Green pump injection

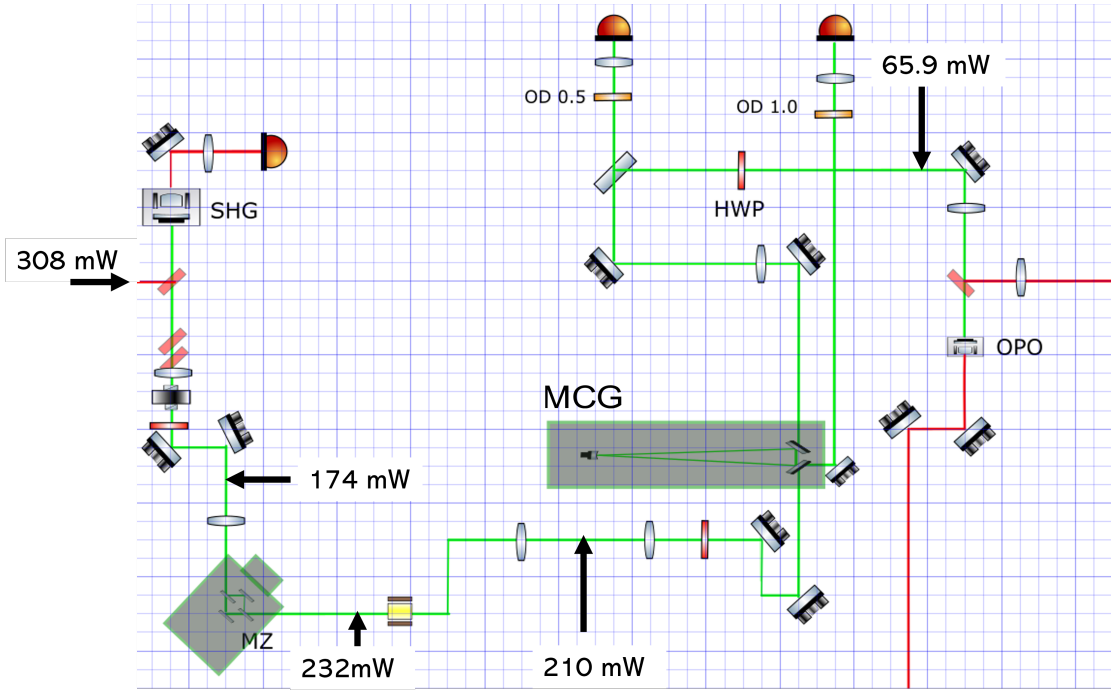

Figure 4.7 – Power budget of the path of the green beam, from the IR pump injection to the green pump injection inside the OPO.

The beam from the ML should be aligned inside the SHG and the mode-matching of the SHG was calculated. To do so, we scan the cavity (by injecting a ramp in the PZT-mounted mirror of the cavity) to see all the spatial modes of the incoming light (IR pump beam) inside the cavity, as shown in Figure 4.15. We improve the alignment with two steering mirrors before the cavity, to maximize the TEM_{00} mode. The mode-matching is then calculated as:

$$\text{mode-matching} = \frac{\text{height of the } TEM_{00} mode}{\sum \text{height higher order modes}} \tag{4.1}$$

The mode-matching measured was equal to 91%. SHG being locked, the green

pump beam is then aligned inside the MZ and then, inside the MCG. Then, we ramp the MCG cavity, align better the green pump inside it, measured a mode-matching of 81%, lock the MZ and then the MCG. The green pump is finally sent to the OPO with a power of 65.9 mW. Figure 4.7 shows the budget power along this path. We can see a loss of 9.5% due mainly to the EOM between the MZ and the MCG. Around 25% of green power is lost after the injection inside the MZ interferometer. 68.7% of green power is lost between the EOM and before injecting inside the OPO. We will discuss this losses in Section 4.3.1.

4.2.3 LO alignment

The LO is a pick-off from the ML. Before being injected inside the MCIR, this beam is at 7.8 mW and the transmitted LO from the MCIR has a power of 4.5 mW. As for the other cavities, the alignment inside the MCIR is optimized. The LO beam will be then aligned to the HD to measure the CMRR described immediately after.

4.2.4 CMRR measurement

Ideally, a balanced homodyne detection can completely cancel the fluctuations of the LO after the subtraction. In practice, there could be several differences in the two PDs (quantum efficiencies, temporal responses and the subsequent electronic amplification), limiting the capability to appreciate the common mode noise rejection. However, these differences can be partially compensated by well-balancing the optical power of beams reaching each homodyne PD [30]. The common-mode rejection ratio (CMRR) of a homodyne detector measures its ability to reject the signals common to both PD, in order to have the possibility to measure only the random fluctuations due to the interaction of the beam with the coherent vacuum (shot-noise measurement) and with the squeezed vacuum produced by the OPO (squeezing measurement). It is defined as

$$CMRR_{dB} = 20\log_{10}\left(\frac{GAIN * SUM}{DIFF}\right) \tag{4.2}$$

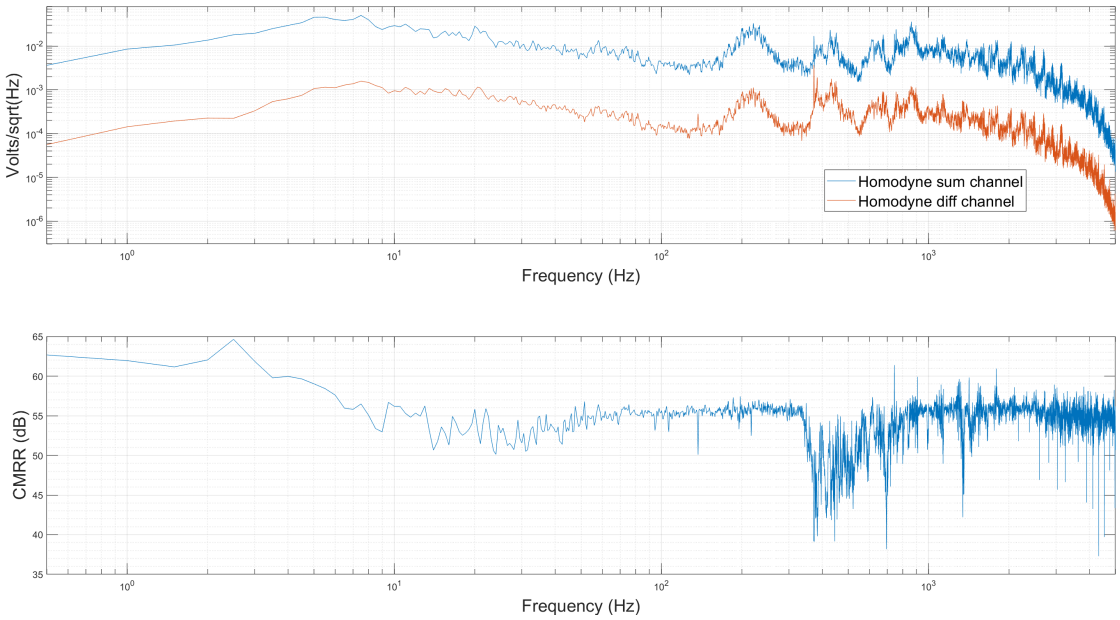

Figure 4.8 – (top) Graph of the FFT of the audio channel SUM and DIFF vs frequency. (bottom) CMRR value in dB for each frequency.

where SUM and DIFF are the power spectra of the sum and difference channels and GAIN corresponds to the differential gain of the amplifier between them. In our detector GAIN is equal to 21. Figure 4.8 (top) shows the FFT of SUM and DIFF signals and the spectrum of the CMRR (bottom), from 100 Hz to 5 kHz. The mean value of CMRR shown in the plot is about 55 dB. As we did not record the CMRR plots for the concerned squeezing measurement (we had 39 dB), we show another measurement, as the logic is the same. Anyway, with the same detector, better values (between 80 and 90 dB) have been obtained (See Chap. 5 of [53]).

To perform this measurement, we need only the LO beam arriving at the HD, so the beams coming from the OPO are stopped. We then use the LO at its maximum power. In our experiment it was around 4.5 mW and was obtained by tuning the dedicated half-wave plate (HWP). Before performing the measurement, we checked first that the shot noise spectra scale linearly with the square root of the input power, as expected from a shot noise-limited signal. The voltages of the two PD (called PD 1 and PD 2) are visualized with an oscilloscope. Using the two steering mirrors (STR_{L1} and STR_{L2}, cf. Figure 4.2),

a rough alignment of the BS output beams towards the two PD was done. We then combine the use of these steering mirrors with the HD screws (for vertical, horizontal and vertical alignment) to do a precise alignment.

Translation stages for HD's lenses

In order to avoid any clipping due to the dimensions of the photodiode sensitive areas (500 µm × 500 µm), two lenses are used to adapt the beam waist size. We placed one of them in a translation stage, as depicted in Figure 4.18. We can thus act on the translation of the global HD or on the translation of one lens. Indeed, the photodiode efficiency depends on the geometrical overlap of laser beam profile and PD sensitive area. If the tails of the beam fall outside of the sensitive area, the detection efficiency is reduced. Even a few % optical losses would spoil the squeezing measurement. Moreover, any asymmetry in the beam clipping would couple angular beam jitter into detection noise in the differential channel, thus reducing the shot noise clearance.

Once the HD is balanced, the CMRR can be improved by directly looking at the FFT of the audio-band sum and difference channels, also playing with the beams' polarization.

4.2.5 BAB/LO contrast measurement

As it will be shown in Section 4.2.6, a sub-optimal visibility is a source of optical losses, strongly impacting the measured squeezing level. For this reason it is crucial to optimize the overlap between squeezed vacuum field and LO. As shown in Figure 4.9, two steering mirrors (STR_{B1} and STR_{B2}) are used to superpose BAB (and thus the vacuum field) to LO field once it is aligned on the HD photodiodes. The two beams should be matched and, to make easier the measurement of their contrast, they should have the same power. For this reason, the LO oscillator power must be reduced, in our case from $\sim 4.5\,mW$ to $\sim 90\,\mu W$, using the HWP_1 (in the scheme) located before the MCIR. Then, we put a beam profiler on the path from the BS to the first photodiode (PD 1 in the scheme) of the HD, at two locations: in "near-field" and in "far-field". With the beam profiler, we can save the position of the LO beam and then, superpose the

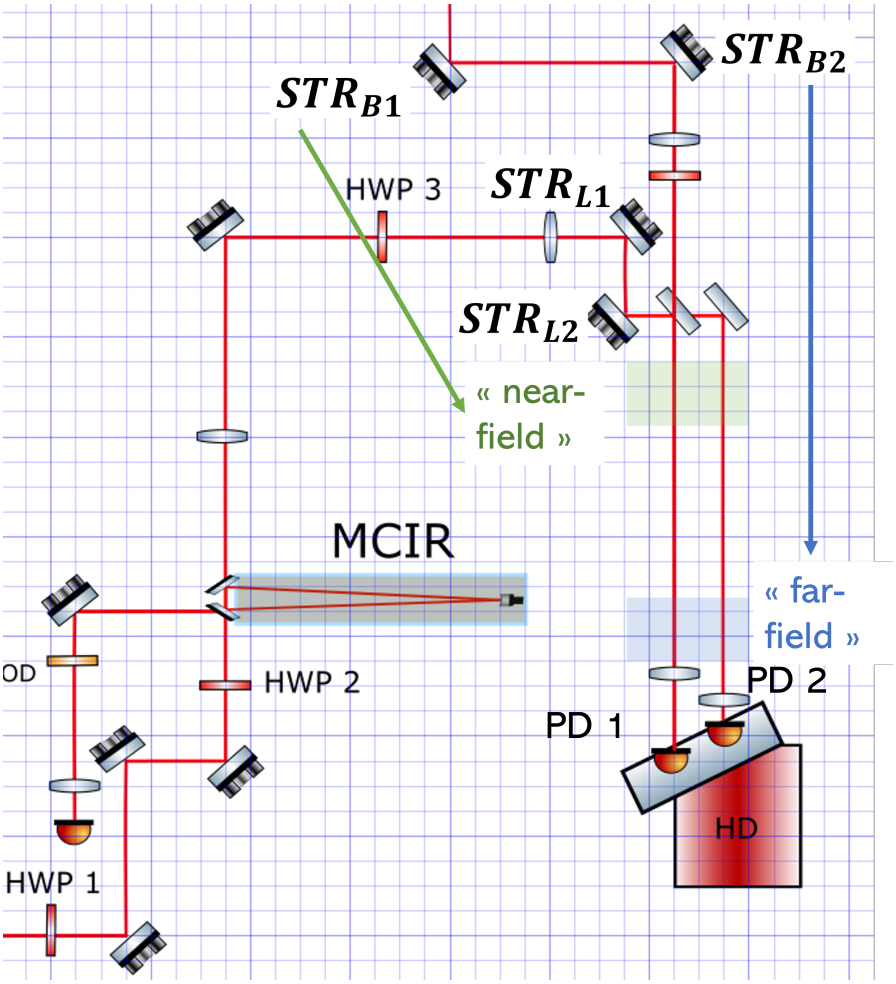

Figure 4.9 – Alignment of the BAB inside the HD. "near-field" and "far-field" are the names given to indicate the relative position in the beams path (BAB and LO) with respect to the homodyne detector. At this position, we can put a beam profiler and acts with the corresponding steering mirror to superimpose BAB with LO field.

BAB acting on its steering mirror (STR_{B1} for near-field and STR_{B2} for far-field). When the two beams are overlapped, we change the position of the beam profiler, switching from near-field to far-field position in an iterative way, until the two beams are always overlapped. The size of BAB can be adapted by acting on the lens in the BAB path (see Figure 4.2). The beam profiler is thus used for coarse matching while the visibility, described below, is used for fine tuning.

The contrast can be evaluated, measuring the fringe visibility, which is a

criterion for the quality of the interference between BAB and LO fields when they have equal intensities (so that the maximum value could reach 100%):

$$\mathcal{V} = \frac{I_{max} - I_{min}}{I_{max} + I_{min} - 2 * I_{dark}} = \frac{V_{max} - V_{min}}{V_{max} + V_{min} - 2 * V_{dark}} \tag{4.3}$$

where V_{max} and V_{min} are respectively the maximum and the minimum voltages of every single homodyne photodiode while the relative phase between the LO beam and the BAB is changing, sending a modulation to a PZT-mounted mirror along the local oscillator path and V_{dark} is the PD dark voltages. The contrast achievable in our experiment was 99% but for our squeezing measurement, we only reached 94%. $\mathcal{V}^2$ is one of the factors in the degradation losses calculated further in Section 4.2.6, which implies the importance of having a high overlap between both input fields (squeezed vacuum field and LO field) to detect strong squeezed states.

After having optimized the CMRR and the homodyne visibility, we stop the injection of the BAB into the OPO so that only the LO and the squeezed vacuum arrive at the homodyne detector. Then, the squeezing measurement can be performed. Using PS_{PUMP}, we can change the relative phase between the vacuum field and the LO and observe, as shown in the following section, squeezing and anti-squeezing at different phases of the pump field.

4.2.6 Squeezing level and degradation losses

In Section 2.1.2, paragraph "Squeezed states of light", is defined the squeezed factor, usually measured in decibels. Figure 4.10 depicts the measurement of SN reduction using squeezed vacuum, performed at 1.1 MHz of detection frequency. In this figure, LO shot noise and the measured squeezing and anti-squeezing are plotted in green and blue, respectively. The purple line represents the estimated level of squeezing that the OPO cavity can produce, calculated from the measured level of squeezing and taking into account the squeezing degradation due to optical losses. The measured squeezing level is −1.6 dB and the anti-squeezing level is 2.3 dB. The squeezing measurement has been performed following the steps explained below. The pump power for the OPO

in our measurement is 65.4 mW and the LO power is 4.5 mW. The parametric gain amplification is equal to 2.28. The CMRR was equal to 39 dB, the shot noise level was equal to -78.1 dBm and the dark noise level was equal to -89.0 dBm.

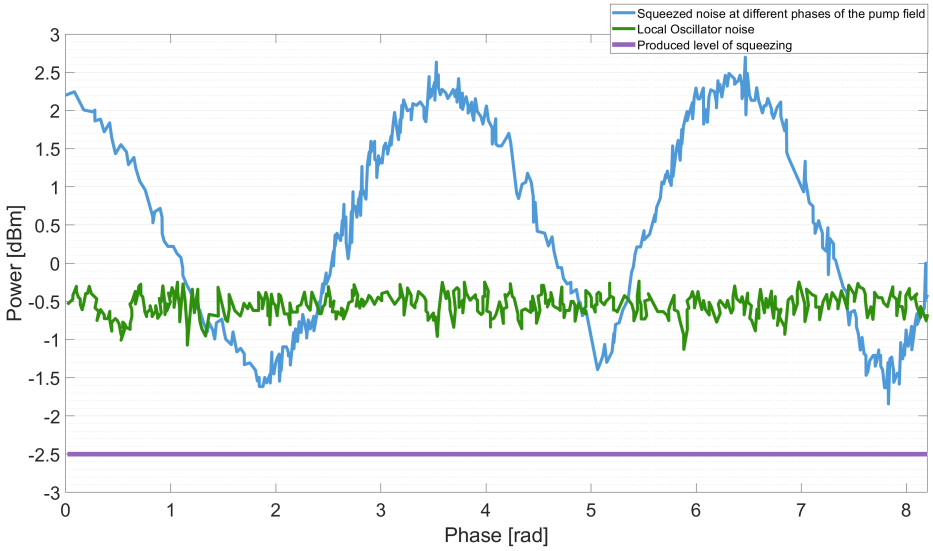

Figure 4.10 – Preliminary squeezing measurement in the radio frequency band. The characterization is performed at 1.1 MHz of Fourier frequency. The two plotted curves represent: the LO shot noise (green curve) and the injected squeezing at different phases of the pump field (blue curve). The dark level noise was -89.0 dBm (it is not represented for clarity reasons)

Starting from the squeezing and anti-squeezing variance measurement, it is easy to find the OPO achievable squeezing variance (or produced squeezing and anti-squeezing level) by using the following relationship:

$$V_{\pm}^{\text{meas}} = \eta_{\text{tot}} V_{\pm}^{\text{prod}} + (1 - \eta_{\text{tot}}), \tag{4.4}$$

where V_+ and V_- are, respectively, the anti-squeezing and squeezing variances with V^{prod} the achievable variance and V^{meas} the measured variance. η_{tot} is the total optical efficiency that includes all the losses L from the generation to the detection of squeezed light and these follows the relation $\eta_{tot} = 1 - L$.

The calculation of the optical losses L includes the propagation efficiency η_{prop}, the PD quantum efficiency η_q, the OPO escape efficiency η_{esc} and the homodyne mismatch measured with the fringe visibility ν. Thus, the overall

	η_{prop}	η_{esc}	v^2	η_q	η_{tot}
budget (%)	84.7	94.9	88.4	99	74.8

Table 4.3 – Optical efficiency budget for the calculation of produced squeezing.

optical losses can be computed given the total efficiency η_{total}:

$$\eta_{total} = v^2 \eta_q \eta_{esc} \eta_{prop}. \tag{4.5}$$

Each efficiency and the total efficiency are shown in table 4.3. In the following, we will describe the computation of each contribution to the total optical efficiency.

Propagation losses

The propagation losses include those of the infrared light transmission of the harmonic BS (equal to 0.5 %), those of the PBS (equal to 0.5 %), and the ones from other optics including lenses, mirrors, half-wave plate (experimentally equal to 3.8 %). To measure the loss budget, due to the optics between the generation of the squeezed beam and its injection into the HD system, we measure the power of the BAB, on the path shown in Figure 4.2: we measure the power just after STR_{B1} and the powers in DC1 and DC2 paths, before each photodiode' lens. We use the same 2-inch lens to focalize into our powermeter because the beam is bigger than the sensitive area of the powermeter after the PBS_{OPO}. To do this measurement, we tried to keep the same spot size arriving on the powermeter and we repeated the three power measurements nine times and sixteen times using the CCB beam instead. We realized it was better to do the measure in the dark and do the zeroing of the powermeter before each measurement. The dark powers of DC1 and DC2 was also checked with the same powermeter to know if they are similar and not too high ($P_{DC1}^{dark} = 196\,mW$ and $P_{DC2}^{dark} = 173\,mW$). We repeated the measurement many times because there were power fluctuations due to several reasons, such as the fluctuations in the room temperature, in the temperature of the OPO crystal, straylight arriving at the powermeter.
Moreover, the beam diameter for the two beams arriving in the two photo-diodes of the homodyne detector, has been over-sized compared to the adapted beam

waist for the homodyne detector (31 µm) and the waist position of each beam falls at the middle distance between the two photo-detectors. Hence a fraction of the beam power is clipped by the two detectors and by estimating this loss with a Gaussian probability distribution function, the results obtained is 94.3% for the fraction of power collected by each detector. This calculation is more described in [83].

The total propagation losses are equal to 15.3%.

Escape efficiency

The escape efficiency of a squeezed light source is defined as:

$$\eta_{esc} = \frac{T}{T+L}, \tag{4.6}$$

where $T = 0.08$ is the transmission of the output coupling mirror and L the intra-cavity Round-Trip Losses (RTL). These include the PPKTP losses due to the residual transmission through the HR-coated backside (0.025%); the negligible absorption within the crystal which is $12\,ppm/cm$ and the residual reflection of the AR-coated frontside (0.2%), which must be taken in account two times. Thus, RTL ~0.43%, hence $\eta_{esc} = 0.949$. A high escape efficiency is suggested to generate strong squeezing.

Homodyne mode mismatch

As described in Section 4.2.5, to perform the squeezing measurement, it is necessary to overlap the LO with the BAB. To evaluate the imperfect spatial mode-matching between the squeezed field and the LO field, which results in losses in the squeezing measurement, the *fringe visibility* $\mathcal{V}$ is evaluated and was equal to 94%. The homodyne efficiency is then $\mathcal{V}^2 = 88.4\%$.

Photodiode quantum efficiency

The conversion efficiency of a photodiode, i.e., the capacity to convert a photon into a photo-electron, is not perfect. The quantum efficiency of our photodiodes is equal to 99%.

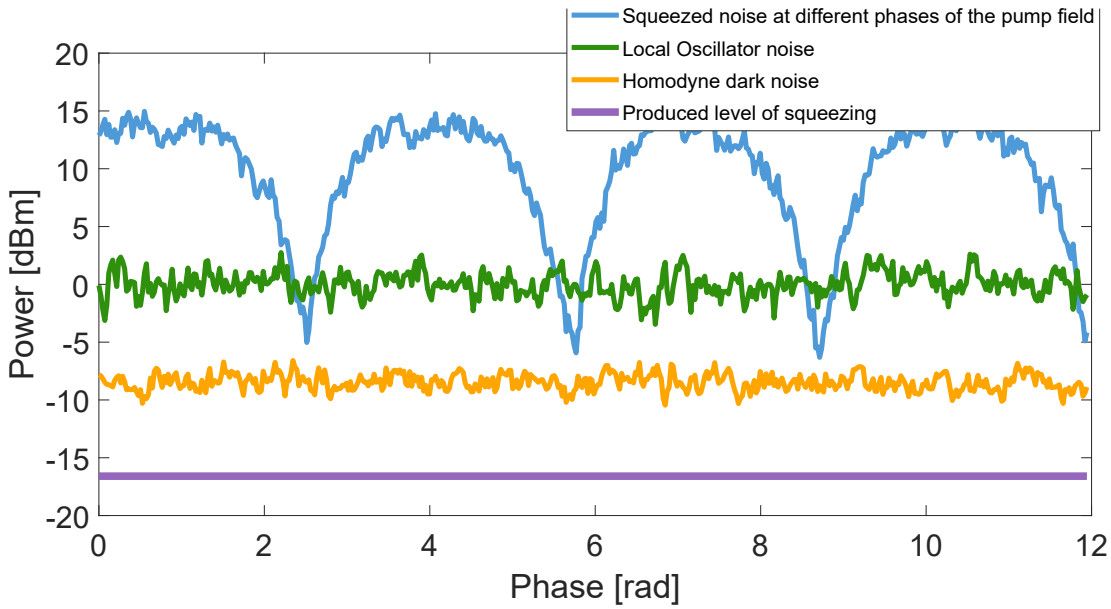

Figure 4.11 – Squeezing measurement in the radio frequency band done nearly three years before the measurement presented above. The characterization is performed at 1 MHz of Fourier frequency. The three plotted curves represent: the homodyne dark noise (orange curve), the LO shot noise (green curve), the injected squeezing at different phases of the pump field (blue curve) and our OPO produced squeezing (purple curve).

Produced squeezing level

According to Equation 4.4, with $\eta_{tot} = 0.703$, the produced squeezing level of our OPO is $-2.5\,dB$, this value does not take into account the dark noise of the homodyne detector and the effect of phase noise.

Comparison with older measurement

Figure 4.11 shows a measurement done nearly 3 years before the previous measurement. Dark noise, LO shot noise and the measured squeezing and anti-squeezing are plotted in orange, green and blue, respectively. The purple line represents the estimated level of squeezing that the OPO cavity can produce, calculated from the measured level of squeezing and taking into account the squeezing degradation due to optical losses. The measured squeezing level is –5.7 dB and the anti-squeezing level is 14.7 dB. The pump power for the OPO

in our measurement is 69 mW and the LO power is 4 mW. The CMRR was between 60 and 80 dB, the parametric amplification was equal to 4.35. Doing the calculation again with Eq. 4.4, with $\eta_{tot} = 0.748$, the produced squeezing level of our OPO was $-16.4\,dB$, this value does not take into account the dark noise of the homodyne detector and the effect of phase noise.

For the losses estimation, the only difference between the two squeezing measurements is the value for $\mathcal{V}^2$ which is higher and equal to 0.94. The parametric gain was higher than our new measurement (4.35 instead of 2.28), this can explain the low measured squeezing level, compared to this old measurement. We can improve this gain with the alignment, as explained in Section 4.3.2. Moreover, another problem can be the decrease of the performances due to OPO aging.

4.3 Optical characterization

In this section, I will describe the optical measurements and modifications I contributed to and will enumerate some experimental methods to have a better measured squeezing level.

4.3.1 Power budget

It is essential to keep track of the power budget of each beam and these measurements should be done regularly. This allows following the performances of components during time. This power budget also enables to have a reference for the design of the EPR experiment presented in Chapter 5, as we will keep most of the components already used for this FIS experiment. It is also very useful to have in mind the power budget so that we can have hints about malfunctions. For example, when the BAB power, after the OPO was less than 30 µW (instead of $\sim$ 90), we realized that the PLL for the AUX 2 laser was unlocked, so the co-resonance between LCB and BAB was fluctuating a lot (as the frequency shift between BAB and LCB was not stabilized anymore).

Concerning the green pump beam, we know that we can reach at least 69 mW before injecting inside the OPO so we should pay attention to do a good align-

ment in SHG, MZ and MCG to reach at least this power. In particular, we can see in Figure 4.7 that the path from SHG to OPO is too long, involving several optics (mirrors and lenses) and can explain the losses observed. In the chapter 5, we will reduce this path drastically, to avoid losses due to alignment and optical components. Moreover, the MCG transmission is quite low ($\sim$ 60%), suggesting extra intra-cavity losses, which could be probably improved with better cleaning of cavity mirrors.

Alignment and mode-matching

Table 4.4 shows the mode-matching achieved these last years (between 2018 and 2020) for each cavity when optimizing the alignment. These values can then be used as a reference of what we can reach by doing the best alignment possible.

SHG	MCG	OPO	MCIR
91%	90%	93%	93%

Table 4.4 – Fundamental mode content for the transmitted power of each cavity.

4.3.2 Layout modification: modification of CCB/BAB paths

In the former design shown in Figure 4.12 (left), the design made it impossible to both block the BAB (and not send it to the OPO) and keep the PLL_{AUX1} locked as while blocking the BAB, the pick-off from it, used to beat with the CCB (or also called COH) does not reach the PLL_{AUX1}. In this design, having the CCB and the BAB in the same path, we chose to send to the OPO, whether BAB or CCB using a HWP before a polarizing beam splitter (PBS). When choosing only to send CCB and thus produce vacuum squeezing, this method does not completely extinguish the BAB. The constraints in changing the layout are:

- the matching (size and alignment) should be kept between BAB and CCB on the path where they are coincident, before arriving on the photodiode PLL_{AUX1};
- the matching between BAB and CCB should be kept where they started to travel together to go to the OPO.

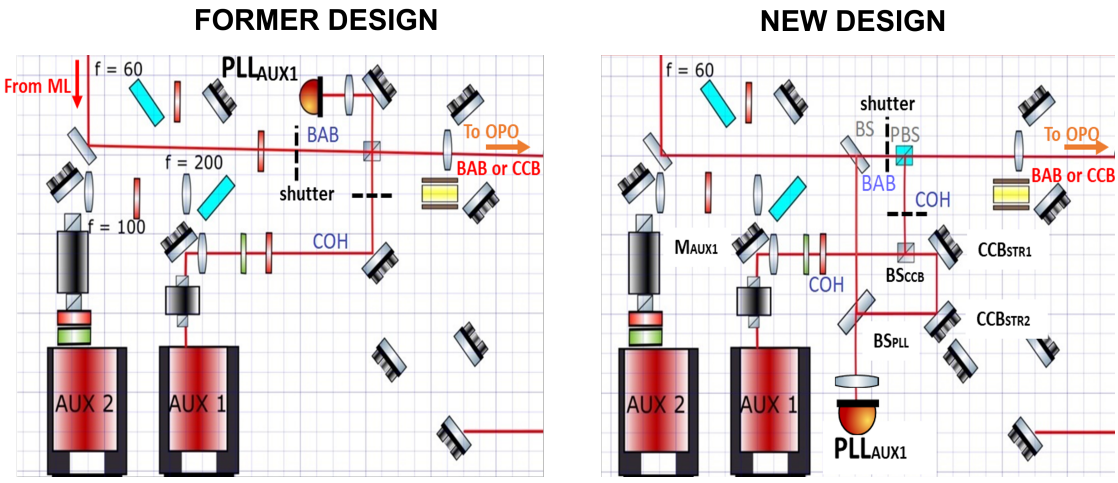

Figure 4.12 – Left figure represents the optical layout before modifications on the BAB and CCB path while the right figure shows the layout with the modifications.

The new design presented in Figure 4.12 (right) uses additional elements as: a BS which enables to block only the BAB part which is sent to the OPO and not the BAB part used for the PLL_{AUX1}, a PBS to combine the CCB and BAB path and a BS to send one part of the CCB to the OPO. After placing the optical elements according to the layout, the alignment must be done in this order:

1. align CCB and BAB in the path going to OPO with the steering mirror M_{AUX1} and BS_{CCB}
2. align CCB and BAB in the path where they recombine for the PLL, using CCB_{STR1} and CCB_{STR2}

Parametric gain

The method to evaluate the parametric gain of the squeezing cavity, consists of the measurement of the amplification and deamplification of a seed beam (signal beam), the BAB in our case. Before injecting this beam, we must ensure that the green pump beam is well aligned into the OPO. A way to check this alignment is to look for the green back-reflected beam's spot on one of the two steering mirrors used to align the beam from MCG to OPO (see Figure4.7). The

back-reflected beam should coincide with the green transmitted beam's spot, meaning the green beam is better aligned.

The OPO should be locked using the LCB (injected from the same side as BAB) and the temperature of the OPO crystal should be tuned, so that there is a co-resonance between BAB and LCB. Indeed, the two beams having orthogonal polarization and the crystal being birefringent, the matching condition for each polarization is different. While scanning the OPO cavity, if we acquire the transmitted power of the BAB, using an oscilloscope, we should see all the modes with the TEM_{00} mode, which is the highest peak (see MCIR scanning in Figure 4.15) and, by tuning the crystal temperature, we must overlap the highest peak from BAB and the one from LCB should. The OPO cavity being locked, the level of the BAB transmitted power should be improved by slightly tuning the OPO crystal temperature and noted down (acquired with an oscilloscope, for example, at the output of the harmonic mirror, before the PBS). Then, the green beam is injected from the other side of the OPO and the temperature of the OPO should be decreased. In fact, the injection of the green will heat the crystal and the co-resonance between BAB and LCB should be rechecked.

The next step is to switch on the PS_{PUMP} to slightly change the phase of the green path and observe interference fringes on the oscilloscope. The amplification/deamplification is the ratio between the highest level/lowest of BAB and the level of BAB without the injection of the green.

4.4 Automation and controls

The development of a highly automated setup where all the required control loops are supervised by a finite-state machine (FSM) was reported in [62]. The software based on FSM was realized by Mateusz Bawaj (INFN and Perugia University), who also dealt with the electronics and control system. Control theory is about maintaining measurable parameter of a process at a given value (setpoint). I contributed to the realization of the optical setup, to the optical characterization and the performances tests of the FSM-based software.

The objective to have a high level of automation in our experiment is for the various scientists working on the experiment and having different expertise, to

use the control system easily. This step towards a fully automated control system aims to minimize human intervention and dead time, which is required by a running GW detector in *science mode*. Indeed, during this data-taking period, a high-duty cycle for the squeezing source is required and was reported to be above 99% for the last observing run O3 [14]. In this section, I will first describe the two types of control techniques that are driven by the FSM-based software before presenting the structure of the logic and the performances.

4.4.1 Control techniques

- with *PID controllers*
  In our system, we control several devices. The temperature stabilization and the MZ interferometer's working point are driven by feedback controllers, called later *PID*. I will describe three loops using PID controllers: MZ length control, CC_{PUMP} and CC_{PUMP}. The left part of Figure 4.13 and Figure 4.14 show respectively the error signal (top) along with the corresponding piezoelectric signal (bottom). To obtain the fringes and have the highest range (between the minimum and the maximum voltages), we should well-align the signal into the photodiodes CC_{PUMP} and CC_{LO}, to be able to find a setpoint.

  The same kind of control is also used for the OPLLs and temperature control of SHG and OPO crystals.

- *with PDH technique loops*

  We also control a particular device called *optical oscillator*, whose length must be tuned to match a co-resonance with the incoming light. In this particular application, obtaining the setpoint is called *locking*. Pound-Drever-Hall (PDH) technique [22] is a clever way to obtain a linear error signal (which can be used in a feedback controller) in the vicinity of the resonance. However, when being far from the resonance, it is not enough for a successful lock. The length control of all the cavities involved in the experiment is ensured by PDH technique. The SHG and the MCIR are locked using the fundamental beam, the MCG using the second-harmonic

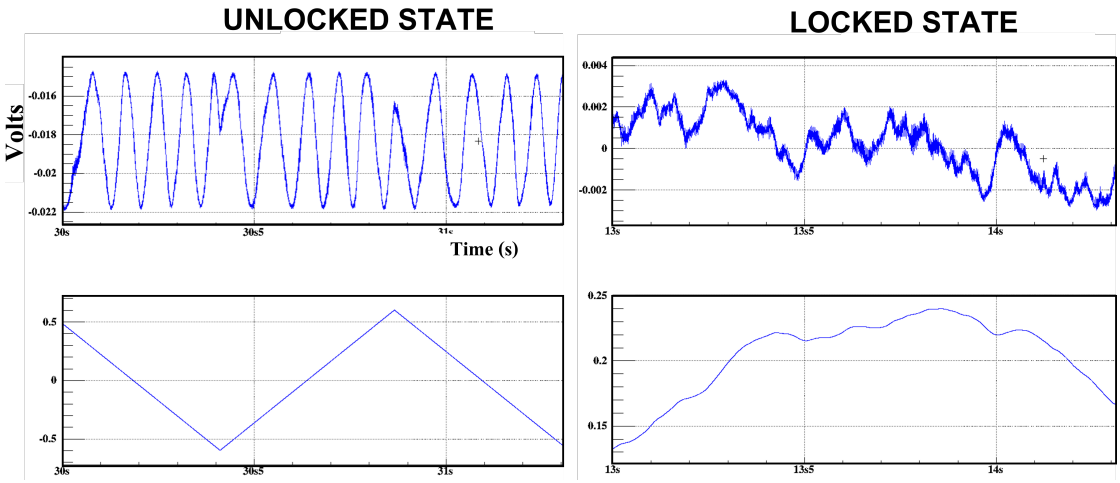

Figure 4.13 – Upper panel represents the error signal for the squeezing angle control loop along with the signal (triangular waveform) injected into the PZT-actuated mirror PS_{PUMP} represented in the lower panel, in the unlocked state (left) and the locked state (right).

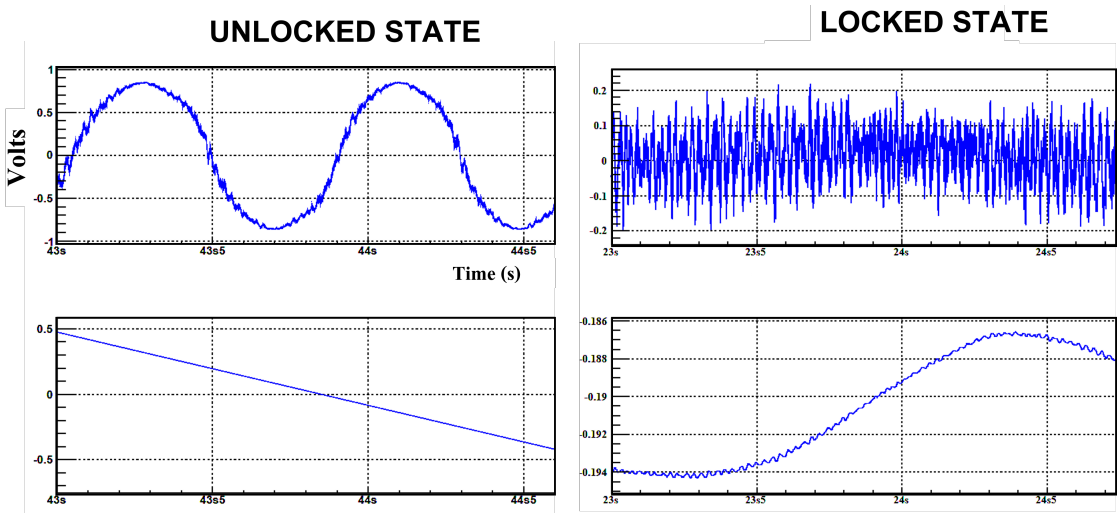

Figure 4.14 – Upper panel represents the error signal for the LO phase control along with the signal (triangular waveform) injected into the PZT-actuated mirror PS_{LO} represented in the lower panel, in the unlocked state (left) and the locked state (right).

beam and the MCIR the LO beam, all modulated at a frequency of 80 MHz, while the OPO is locked using the LCB modulated at 78 MHz. Each beam is reflected back from each corresponding cavity (except for the OPO cavity

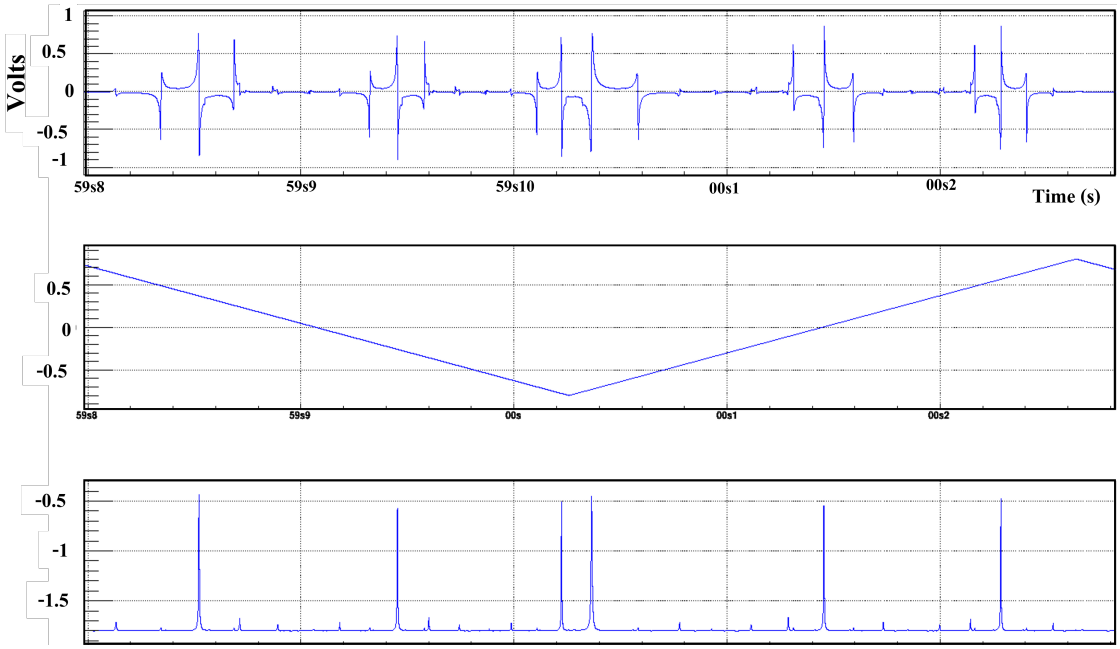

Figure 4.15 – Upper panel shows the error signal of the MCIR cavity; middle panel depicts the ramp signal which is sent to the PZT-actuated MCIR's mirror; bottom panel represents the signal detected by $MCIR_{TR}$ while scanning the MCIR cavity. It is possible to measure the mode-matching by measuring the ratio between the highest peak (which was chosen to be TEM_{00}) and the smaller peaks which are the higher-order modes).

where it is transmitted) and detected by the respective RF photodetectors SHG_{REF},MCG_{REF},OPO_{TR} or $MCIR_{REF}$ (cf. Figure 4.1). Each signal is demodulated by a RF local oscillator signal at the modulation frequency and then low-pass filtered. This is the error signal which fed back to the PZT-actuator of the concerned mirror's cavity, to control and stabilize the corresponding cavity length. Figure 4.15 shows the error signal, the triangular ramp sent to the PZT-actuated mirror and the transmitted signal while scanning the MCIR cavity.

4.4.2 Control using finite state machine (FSM)

We have implemented and tested a new technique to improve the control strategies for a squeezed vacuum source, using a software based on Finite-State Machine (FSM), which is "a mathematical concept used in automata theory to

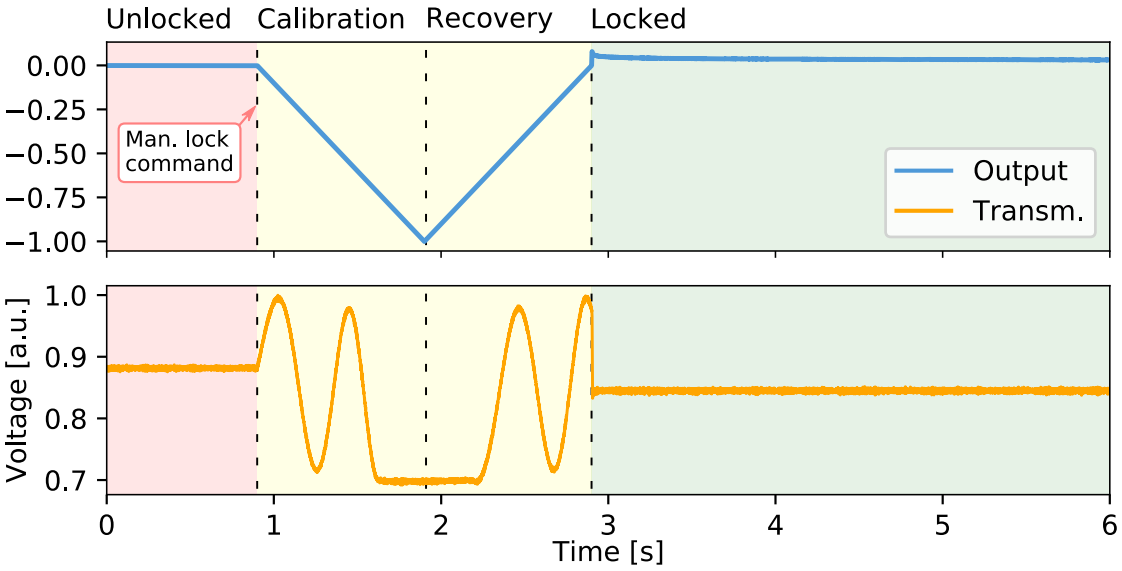

Figure 4.16 – PID (Proportional Derivative Integral) loop lock sequence using finite state machine, from [62]. The upper panel represents the controller output electric signal (the piezoelectric signal), while the lower panel depicts the error signal, which is the signal acquired by the MCG_{REF}. Three colored sections are representing the lock phases: unlocked (background in red), locking (in yellow) and locked (in green). The locking phase is divided into calibration and recovery phases, as indicated in the figure. The moment where the manual lock command occurs is also indicated.

describe an automation mechanism which can change from one state to another in response to input signals. An FSM is defined by a list of states and the inputs that trigger transitions" [62]. Our working proof-of-principle is evaluated in terms of Quality of Service (QoS), which is the ratio of the working time requested from each control loop and the real-time working conditions.

For the two topologies of feedback controllers described above, two different FSMs were developed. Those FSMs are implemented inside the digital signal processing units and the algorithm is executed between consecutive ADC samples, i.e. in real-time. The slow logic algorithm of the FSM is executed in one second interval and in each iteration, it checks the transition conditions and acts accordingly. MZ and CC loop (locking with a PID controller) are managed by a dedicated FSM, which has two stable states: UNLOCKED and LOCKED. At the beginning of each lock procedure (a manual lock while clicking the button

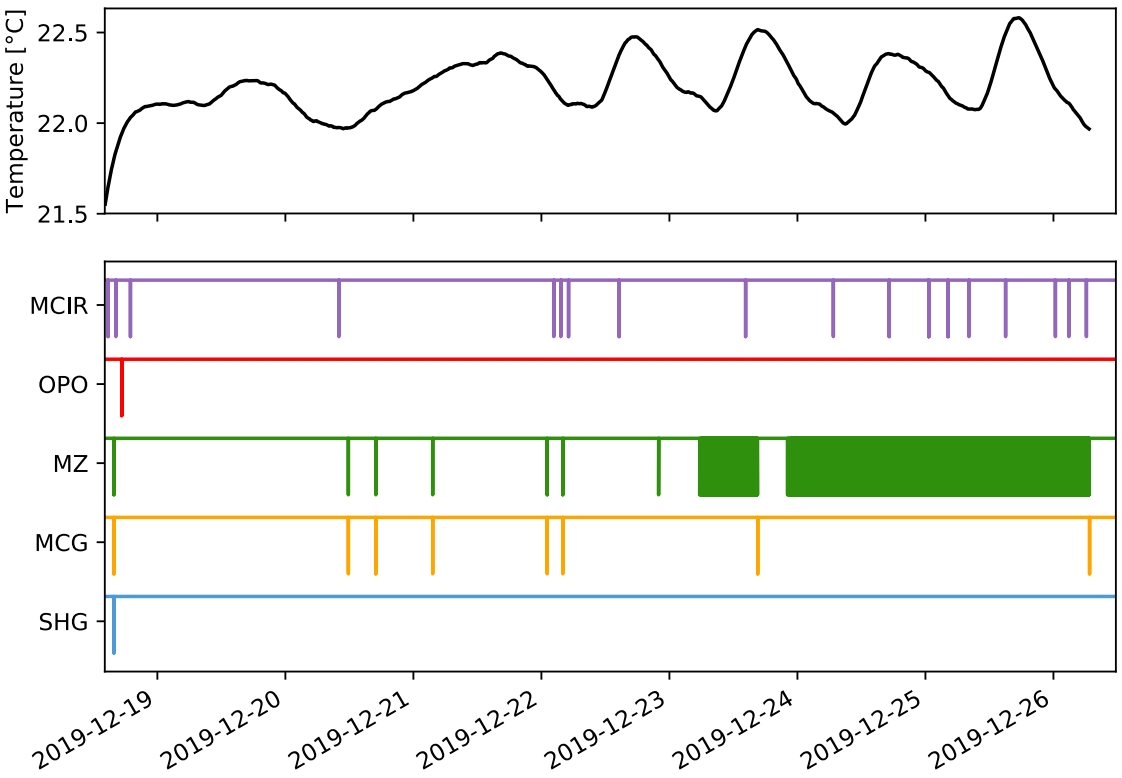

Figure 4.17 – Visualisation of data characterizing QoS in time, from [62]. Upper panel shows the temperature trend of the optical setup. In the lower panel each row indicates binary state of monitored loop.

"LOCK" on the board, after achieving a good error signal), the FSM performs calibration and manages automatic re-locking during this operation. The algorithm acquires the outermost values of the transmission signal and mean value of the error signal during the calibration step.

This logic is shown for the MZ length control in Figure 4.16. Three colored sections represent the lock phases: unlocked (background in red), locking (in yellow) and locked (in green). The locking phase is divided into calibration and recovery phases, as indicated in the figure. The moment where the manual lock command occurs is also indicated. This manual lock is explained in Section 4.4.1. The other locking loops, MCIR, OPO, SHG and MCG, are also driven by a similar logic. Even if the locking technique is different (PDH), it follows the same logic.

Finally, the QoS is evaluated with two parameters: lock acquisition time

of an uncalibrated loop, measured separately for each loop and statistics of uptime during a test period, also calculated for each loop. Figure 4.17 represents the transition of all FSM for MZ interferometer, MCIR, OPO, MCG and SHG cavities' locking, along with the temperature evolution during a period of almost eight consecutive days (189.5 h). In the upper panel, the temperature is stable during the first half of the test but in the second half, there are fluctuations corresponding with day and night changes. Indeed, the laboratory is localized in a non-thermalized building, the fluctuations are likely due to the increased daily change of the environment temperature, caused by weather conditions. In the bottom panel, the status of each loop is represented as a binary value where high state (respectively low state) corresponds to *Locked* state (respectively *Unlocked* state).

Table 4.5 shows the measured lock acquisition time (with the calibration step included). The recovery of the green light path takes 12 s. We observe a low QoS for the MZ, compared to the other loops. This is due to the small dynamic range of the actuation due to the slightly too low visibility of the MZ interferometer during the measurement period. Increasing this visibility will lead to an improvement of the MZ QoS while not choosing too high values to avoid MZ unlocks for the MCG. Doing so, we should reach a QoS of 99.9%.

It is the first time this real-time FSM is used and it can potentially be used for Virgo from now. Another FSM is used to control the status of all feedback controllers for the squeezing implementation of Advanced Virgo. It is much slower (each execution lasts 1 s) and is implemented in a PC which manages the experiment. *squeeze_loops* is a Graphical User Interface developed to interact with this slow FSM. This FSM in Virgo are implemented using *Metatron* (a system for slow control) and we will also use it for the EPR demonstrator, so that our demonstrator will be compatible with Virgo control system.

The QoS enables us to conclude that the performance of this software is compatible with the very high-duty cycle required for GW detectors, as mentioned at the beginning of the section. The very feasible improvement of the MZ will allow to easily exceed a duty cycle of 99.9%.

	Lock acquisition mean [s]	QoS [%]	Out of service total time [s]
SHG	2.7(1)	99.9995	2
MCG	2.4(2)	99.9964	23
MZ	2.0	81.53	238 477
OPO	3.1(2)	99.9995	2
MCIR	4.0(4)	99.9726	185

Table 4.5 – Characterization of quality of locking, from [62]. In the first column there is time necessary to acquire lock of the longitudinal degree of freedom with corresponding uncertainty. Column titled QoS shows the amount of time in which the loop remained locked with respect to the total time of the measurement. In the last column we report the total time the loop was out of service during the testing period. MZ loop is the only PID loop characterized in the set. Its locking sequence comprises only the arbitrary calibration and recovery time thus its variance is not reported.

4.5 Lessons learned for the next experiment

In this section, I will describe problems encountered when we were working on the experiment and the improvements for next experiments. It is then important to tackle these issues before installing the new bench, so that the working conditions would be more optimal.

4.5.1 Room temperature and air fluctuations

The temperature monitoring of the setup is essential for the stability of the experiment. There are thermometers on the room and the bench to keep track of fluctuations. We can see the importance of isolating the bench from the air fluctuations and the temperature, using a cover, by looking at the transmission signal of the MCG in Figure 4.19. Indeed, the signal is more stabilized when the bench is "closed" (a cover is put on). We observe that with fluctuations of amplitude higher than 3 °C, in tens of minute-scale, for the room temperature, the alignments inside the cavities are all lost, even by covering the bench.

In the left photo of Figure 4.18, we decided to cover the MCIR cavity, which has a temporary mechanical case, with an aluminum foil because the locking

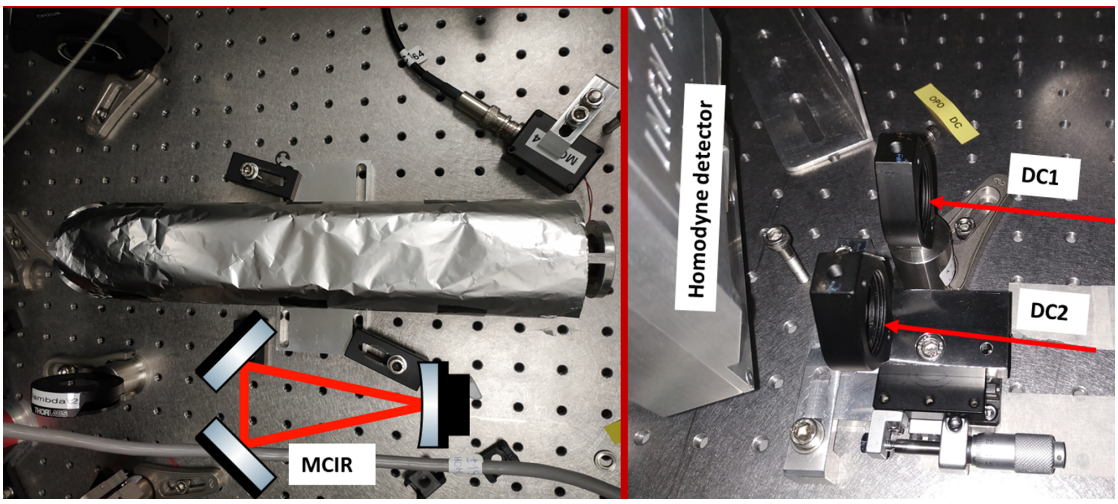

Figure 4.18 – Left photo shows the top of the MCIR which is covered with aluminium foil to reduce the impact of air fluctuations and right photo depicts the lens in DC2 path (homodyne detector) mounted on a translation stage.

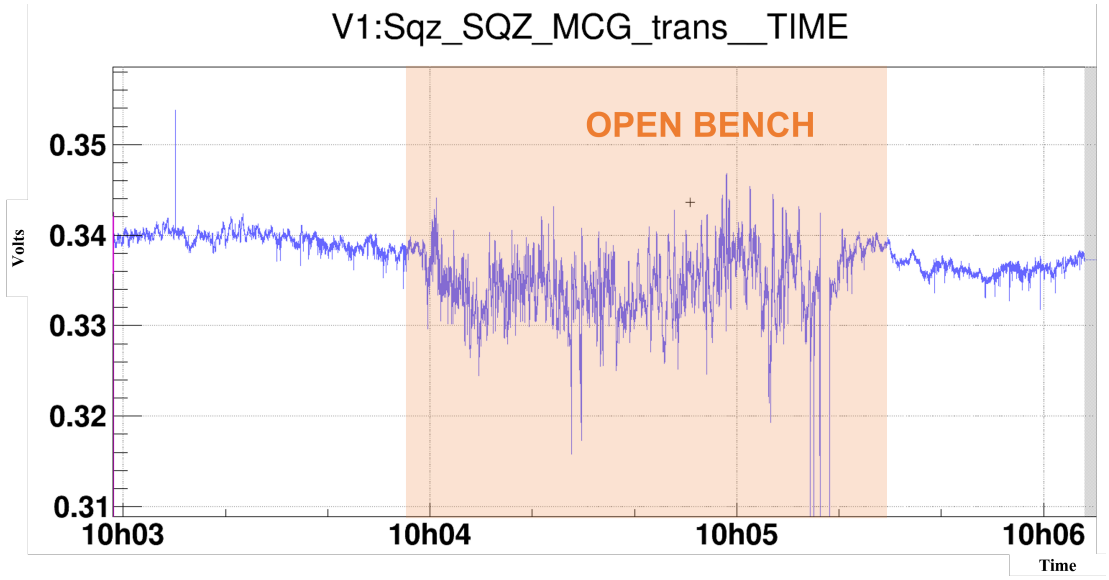

Figure 4.19 – Evolution of the MCG transmitted pump beam signal when MCG and MZ are locked. The bench is "opened" and "closed" (covered) alternatively.

is less stable with the cavity open. It is thus better to protect the mode-cleaner cavity with an insulation box. In general, it is better to cover as many optical components as possible. In the chapter 6, a similar cover will be machined for the etalon.

4.5.2 Mitigation of straylight

A big amount of straylight was observed coming from the direction of the MCIR and towards the DC1/DC2 paths (from left to right if we look at Figure 4.2 and arriving on the homodyne detection path (from the BS to the photodiodes). While trying to dump light from this region, a reduction in the power measured by PD1 and PD2 was observed.

4.5.3 Alignment

To perform precise alignment, we observe that in this experiment, there was sometimes not enough space to place a powermeter, a beam profiler or an external photodiode, between optical elements. When designing, we have to pay attention to let enough space for these measurement devices, so that we can keep track of the power budget and to find misaligned beams, when there is a big power loss between two optical elements for example. Moreover, some steering mirrors will be automatized so the alignment will be easier, as we will have quantitative values to know how much did we turn each screw (on the mirrors). Finally, some alignment problems were linked to loose optics on the table. We should check carefully that each optics are well-fixed, to avoid losing time to align again.

4.5.4 Cavities aging

One of the reasons explaining that the recent measurement of squeezing is lower than the older one (-1.6 dB instead of -5.7 dB) can be explained by the aging of cavities. This can be explained by the fact that the experiment has been running without interruption for more than four years and thus lasers are hitting concerned birefringent crystal for that long. We will switch off the

lasers as much as possible to avoid deteriorating the performances of our cavities (especially SHG and OPO cavity).

4.6 Conclusion of the chapter

In this chapter, I present my experimental contribution on a robust and stable optical setup for frequency-independent squeezed vacuum generation, with a high degree of automation.

This is a preliminary work with the goal to test techniques and optical components for a table-top experiment to produce frequency-dependent squeezing using Einstein-Podolsky-Rosen (EPR) entanglement, whose design and tests are described in Chapters 5 and 6. This work allows me to have a global point-of-view of the production of a squeezed vacuum and understand all the measurements and alignments needed to achieve a squeezing measurement. The current optical bench on which the FIS experiment is carried out, is being transformed into an EPR optical bench.

As most of the optical components from the FIS experiment (lasers, SHG, OPO, MZ interferometer, MCG, MCIR) will be used for the EPR experiment, their characterization was an important preliminary activity. It is also true for auxiliary beams and coherent control technique. I have also detailed some alignment procedures to illustrate the required level of precision and the complexity of the experimental work to produce squeezing. I measured a level of squeezing of 1.6 dB, which was not very high. Consequently, the optical characterization, such as the evaluation of the losses that degrade the squeezing level, is useful to understand the limitations of our experiment.

Then, I described the finite state machines-based software realized to automate the control of the cavities locking, with the goal to simplify the operation and optimize the duty-cycle of the squeezing. Reducing the downtime of the squeezed light source has a direct impact on the detection rate of a GW detectors. My work was dedicated to the optical measurements and alignments needed to run this software. This real-time FSM-based software was implemented for the first time for the generation of vacuum squeezed and the QoS evaluated enables to conclude about its robustness and compatibility with the duty-cycle required

for Virgo.

Finally, with this fruitful experimental work, I identified some technical problems and proposed solutions for next experiments. This was the first time that a collaboration of laboratories from the Virgo collaboration build a complete frequency-independent squeezed vacuum source.

Chapter 5

Demonstrator of a squeezed vacuum source through EPR entanglement

Outline of the current chapter

The theory of the frequency-dependent squeezing technique through EPR has been described in Chapter 3, along with the results of two table-top experiments. In this chapter I present the design of an EPR table-top experiment [72] developed within the Virgo community, by a Collaboration of INFN groups and the APC laboratory. The goal of the experiment is to have the first EPR squeezing experiment compatible with a GW detector (Virgo) as the two proof-of-principle experiments only demonstrates the feasibility of the technique with a simplified setup. This experiment will test the technique first in a test cavity and then in a small-scale interferometer with suspended test masses (SIPS). The SIPS is RPN-limited in the same frequency band of AdV+. Testing the reduction of

radiation pressure noise into the SIPS with EPR squeezing is a step forward the implementation into the Virgo detector. In order to have EPR squeezing, the optical bench for the FIS experiment, detailed in Chapter 4 and [62], will be modified. First, I will explain the main features to build a table-top experiment and I hereby list each needed auxiliary beam and show how we can shape the proposal of the EPR technique into a demonstrator, compatible for the injection into Virgo. Then, in Section 5.2, I will describe the first optical design and the need to do a second design, described in Section 5.3. I will then discuss the trade-off between them. Subsequently, I expose the most updated optical design realized with the new elements with respect to the FIS experiment in Section 5.4. In addition to that, I will detail the new components and how we design mode-matching telescopes for all the needed beams for the final step.

5.1 Conceptual design of the table-top demonstrator

The EPR entangled technique was proposed in [56] and the scheme in Figure 3.7 shows how to implement the technique into a GW detector. In the next subsections, I will summarize the main features to build a demonstrator to produce squeezing using EPR entanglement. Finally, I will detail in subsection 5.1.5 the different auxiliary beams needed to run this EPR experiment.

5.1.1 Generation of a pair of entangled photons

As explained in Section 3.4.1 and shown in Figure 5.1(left), the generation of a pair of entangled photons uses the same optical elements as a usual frequency-independent squeezed vacuum source. The difference consists in the use of the OPO in a non-degenerate configuration: the signal being at frequency ω_0 and the idler being at frequency $\omega_0 + \Delta$, both frequencies resonating inside the OPO. This is obtained by detuning the pump field by a quantity Δ, which is obtained by detuning the main laser by $\omega_0 + \Delta/2$. For our experiment, we chose a detuning equal to the OPO FSR (3.8 GHz).

As for the degenerate frequency-independent squeezed vacuum source, described in the previous chapter, the pump beam is power-stabilized by a MZ interferometer and the outcome is spatially filtered by a green Mode-Cleaner (GMC) cavity (calledMCGin the previous experiment) before being used as a pump beam for the OPO. The seed beam is still a vacuum field so that the signal and the idler field are entangled-vacuum fields (but having different frequencies).

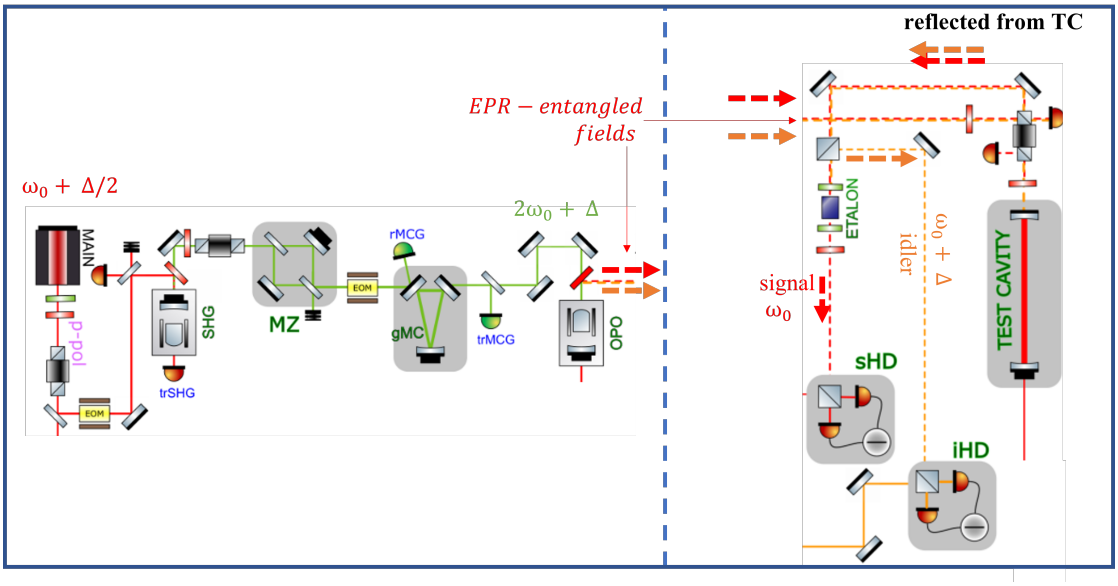

Figure 5.1 – (Left) Schematics of the generation of a pair of entangled photons. (Right) Schematics of the separation of the entangled beams with an etalon.

5.1.2 Test cavity

In the technique proposed by Ma *et al.* [56], the two entangled fields are injected into the dark port of the GW detector and will be filtered by the ITF arm (the signal is resonant inside the cavity while the idler is not), which then, reflects them back. The two beams thus experience a differential phase shift, which leads to a frequency-dependent ellipse rotation. In our experiment, a test cavity was designed to mimic the ITF arm. The requirements are the followings: only the TEM_{00} mode resonates inside this Fabry-Pérot cavity, the total length of

the cavity is around 1 m (we are limited by our optical bench space) and the FSR of this cavity should be adjusted compared to the frequencies of idler and signal beams (the signal beam should be resonating while the idler beam sees the cavity as a detuned cavity but stay inside the linewidth of the cavity). The final parameters were calculated in [23]and the resulting parameters for the test cavity is a plano-concave configuration with a total length of 0.394 m, a FSR of 401 MHz and a finesse of 92.8.

5.1.3 Test on a small-scale suspended interferometer (SIPS)

In our EPR experiment, the goal is also to inject the EPR-entangled beams inside the small-scale Suspended Interferometer for Pondemorotive Squeezing (SIPS) [63, 64, 45] to test the EPR squeezing technique, after successfully testing the technique with the filter cavity. SIPS is a table-top interferometer with macroscopic mirrors opto-mechanically coupled by radiation pressure and the goal was to generate squeezing through ponderomotive technique in the GW detectors detection band. As SIPS is RPN-limited in the same frequency band of Advanced Virgo+ (AdV+) (10 Hz-1 kHz), it is a suitable demonstrator for FDS using EPR entanglement and this will be the first demonstration of the reduction of the quantum RPN by EPR squeezing technique. The suspended interferometer will be in a vacuum chamber and placed next to the EPR optical bench. Consequently, the injection of EPR squeezing into the SIPS enables to test the radiation pressure noise reduction, which has never been tested before and is another step towards the injection of FDS using EPR entanglement inside Virgo.

5.1.4 Separation of the entangled beams and detection

Figure 5.1 (right) depicts the injection of the entangled beams inside the test cavity until the final separate detection. In order to detect the idler and signal fields, once they come back from the test cavity or from the suspended interferometer, we need a Fabry-Perot cavity, reflecting the idler beam and transmitting the signal beam. For our experience, in order to separate the fields, we have decided to use a thin solid etalon, a thermally-controlled optical resonator (a

Fabry-Perot cavity especially designed for this purpose). The description of this choice and the characterization of the cavity are developed in the next chapter.

Being separated, the idler and signal fields are being detected separately with a homodyne detector each. Then, the combination of the measurement of the idler field and the signal field leads to a conditional squeezing, as the outcome of the idler field measurement will determine the outcome of the signal field measurement.

5.1.5 Auxiliary beams

As the experience involves the same optical cavities for the generation of entangled fields, the same homodyne detection system, then the same type of auxiliary beams will be needed. In addition to that, as there is a new component, the test cavity, we need a supplementary locking beam for this cavity. As the OPO is in a non-degenerate configuration in this experiment, this will increase the number of auxiliary beams needed. Another BAB is needed to align the idler field, another CCB is needed to phase-lock the second LO field with the squeezing ellipse and a second LO is needed for the second homodyne detection system. The notation of the auxiliary beams is composed of the acronym in capital letters with a prefix in lowercase which indicates to which cavity or type of beam the auxiliary beams are linked. The different auxiliary beams are:

- LO: Local Oscillator
- CCB: Coherent Control Beam
- BAB: Bright Alignment Beam
- LCB: Locking Control Beam

For example, sLO designates the local oscillator for the detection of the signal beam. For the locking control beams, the prefix is different from the other auxiliary beams. We distinguish two kinds: opoLCB, which is the locking beam for the OPO cavity, identical to the one used in the FIS experiment and tcLCB, which is the locking beam for the test cavity. The table 5.1 describes the frequency and the polarization for each auxiliary beam.

Local oscillators

After being reflected back from the test cavity, the idler and signal fields are separated by the etalon and being detected separately with two homodyne detection systems. For each detection system, we thus need two LO fields, one for the signal homodyne detector at $\omega_s = \omega_0$ and one for the idler homodyne detector at $\omega_i = \omega_0 + \Delta$. Each LO can be generated by different lasers, the signal laser and the idler laser, as shown in Figure 5.5 but this is not the only way, as shown by the second optical layout. Prior to couple with the corresponding entangled field, each LO is spatially filtered by the corresponding mode-cleaner for each beam. sLO and iLO are thus filtered by, respectively, the sMC (signal mode-cleaner) and iMC (idler mode-cleaner).

Coherent control beams

As for the FIS technique (see Section 4.1.2), the coherent-control technique is essential to have a stable squeezing angle. Each CCB has the same polarization as the squeezed beam (s-polarized) and has a small frequency shift (for example, a shift of $\Phi = 7\,\mathrm{MHz}$).

The transmitted CCBs, through the OPO cavity, are used to lock each entangled field to their corresponding LO field, while the reflected CCBs is used to lock the pump phase.

Bright alignment beams

Similarly to the FIS technique, described in Chapter 4, BABs are needed for the idler and signal beam. A bright alignment beam can be used for several purposes: OPO cavity alignment, matching with the pump beam, to verify the co-resonance between the p-polarized locking beam (opoLCB) and the s-polarized entangled fields, alignment for the path from the OPO to the test cavity, for the path from the test cavity to the etalon and, finally, for the separate paths towards each homodyne detector, where sBAB and iBAB will be overlapped with sLO and iLO, respectively. Each BAB beam is an s-polarized beam that is mode-matched with the OPO cavity. Then, sBAB and iBAB are perfectly overlapped to generated signal and idler beams.

Locking beams

To monitor the length of the OPO cavity and of the test cavity and thus to lock them, a locking beam with an orthogonal polarization (with respect to the resonant beam), is needed. Concerning the test cavity case, according to the EPR technique described in Section 3.4.1, the signal field is resonant inside the cavity while the idler field sees it as a detuned cavity.

OPO locking beam

The OPO locking beam, which is a p-polarized beam, is shifted from the main carrier frequency of a quantity Ω, as for the FIS technique. Due to the birefringence of the OPO crystal, the resonance condition is different for two beams with orthogonal polarization and the same frequency. The OPO locking beam has an orthogonal polarization compared to the pump field to avoid the OPO seeing the opoLCB as a seed and, consequently, generating a bright squeezed beam. The opoLCB can be obtained by frequency-shifting the pick-off of the sLO beam. We will do it using an acousto-optic modulator (AOM). A brief description of this method is given in Section 5.2.3.

Test cavity locking beam

The test cavity locking beam tcLCB is an s-polarized beam, with a frequency shift of γ with respect to the frequency of the signal beam. It can be obtained with the same method used for opoLCB.

Auxiliary beams	Polarization	Frequency
sLO	s-pol	ω_0
iLO		$\omega_0 + \Delta$
sBAB	s-pol	ω_0
iBAB		$\omega_0 + \Delta$
sCCB	s-pol	$\omega_0 + \Phi$
iCCB		$\omega_0 + \Delta + \Phi$
opoLCB	p-pol	$\omega_0 + \Omega$
tcLCB	s-pol	$\omega_0 + \gamma$

Table 5.1 – Sum-up of the characteristics (polarization and frequency) of the different auxiliary beams.

5.2 First optical design

In the previous section, I described the main features of a table-top EPR proof-of-principle experiment, explaining all the characteristics that the different auxiliary beams needed to run the experiment. In this section, I will describe the first optical design we propose and expose the reason for the need of a second design.

5.2.1 Conceptual design

The conceptual design, depicted in Figure 5.5 shows the strategy adopted for the design of the EPR experiment. We want to keep the three lasers from the previous experiment so that we also don't have to place them and the PLL of the two auxiliary lasers are already installed. The ML will produce the pump beam (colored in pink on the scheme) for the SHG at $\omega + \Delta/2$ and only a small fraction are taken for the two PLLs. Then, the pump beam for the SHG will have even more power than the pump beam of the previous experiment, which will enable to produce a more powerful green pump beam for the OPO.

In addition to the main beam which pumps the SHG, there are now eight different beams to generate, with six different frequencies, as shown in Table 5.1. We can divide these beams into two categories: beams shifted with respect to ω_0 or equal to ω_0 (sLO, sBAB, sCCB, tcLCB and tcOPO) and beams shifted with respect to $\omega_0 + \Delta$ or equal to $\omega_0 + \Delta$ (iLO, iBAB and iCCB). The two auxiliary lasers will produce these eight beams, the first laser (called *IDLER* laser), with the beams in yellow, will allow to produce beams shifted with respect to $\omega_0 + \Delta$ or equal to $\omega_0 + \Delta$ (iLO, iBAB and iCCB) and the second laser (*SIGNAL* laser), with the beams in red, will allow to produce beams shifted with respect to ω_0 or equal to ω_0 (sLO, sBAB, sCCB, tcLCB and tcOPO). As there is a lot of different beams with different frequencies, it is not possible, as for the FIS experiment, to shift each laser frequency to produce them and we have only two auxiliary lasers to generate six different frequencies. sLO, iLO, iBAB, sBAB have the same frequency as the laser associated to each of them. sCCB/iCCB required a small shift from their respective laser (to stay inside the OPO linewidth equal

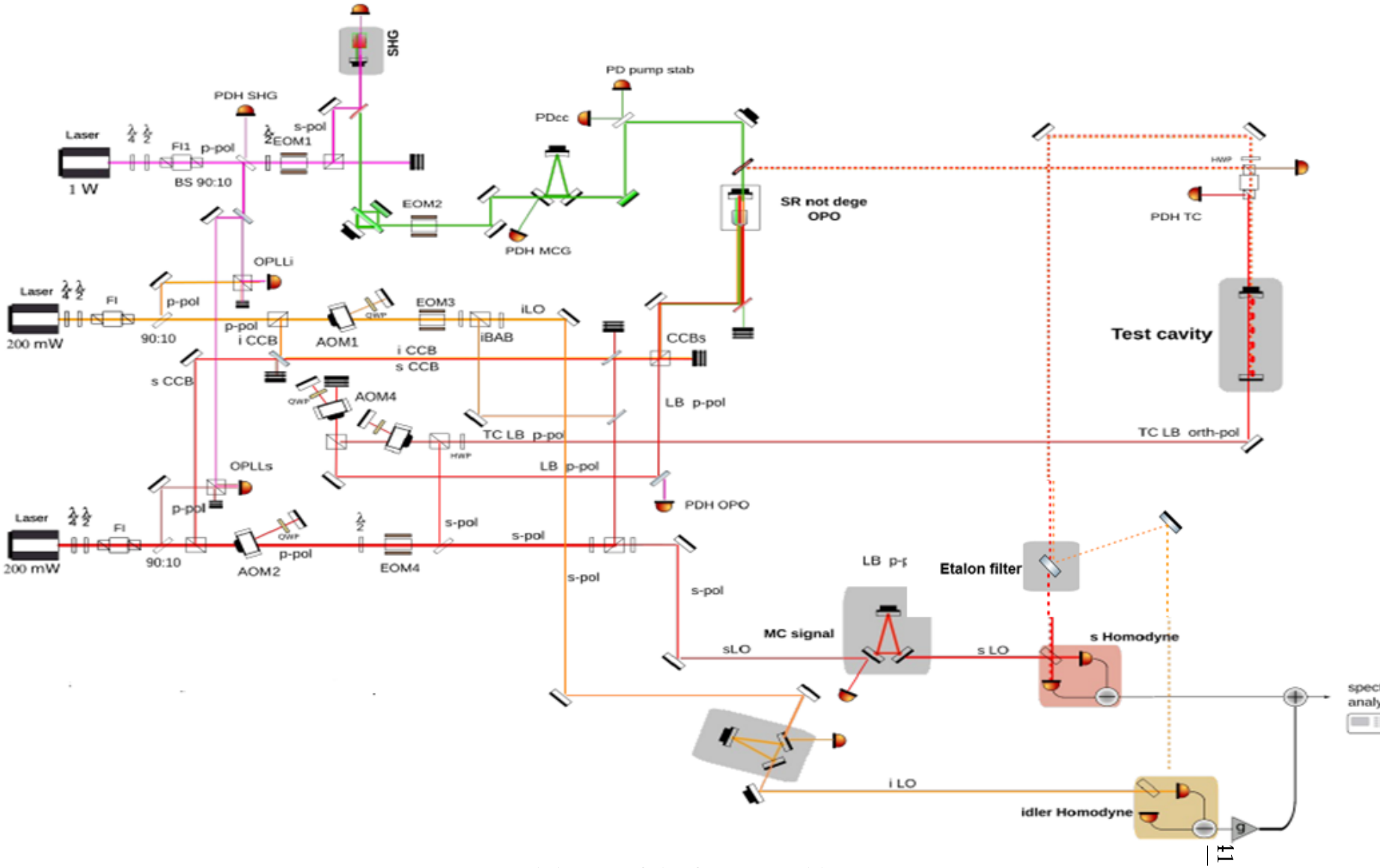

Figure 5.2 – Conceptual design of the first optical layout.

to 25 MHz) so we chose to use two acousto-optic modulators (AOM) in cat's eye configuration [59]. This device will be described in Section 5.2.3, the cat's eye configuration is required as the minimum shift produced by an AOM is around 200 MHz, which is too high for the small shift needed. Concerning the LCBs, the use of one AOM is enough as the frequency shifts required are not too small compared to 200 MHz. These beams have a perpendicular polarization with respect to the beam resonating inside the OPO or the filter cavity.

Five auxiliary beams are injected inside the OPO and as they are produced separately (they are not spatially overlapped), they have to be recombined before being injected inside the OPO all together. For each couple, sBAB/iBAB and sCCB/iCCB are recombined with a beam-splitter (as shown in the scheme) and thus 50% of each beam power is lost. Each recombined couple will be recombined again with a BS so that these four auxiliary beams (s-polarized) are injected inside a PBS, the opoLCB are also recombined with this PBS and having a perpendicular polarization with respect to the other four beams (p-polarized), there is no loss in this recombination.

5.2.2 Strategy and specifications

I will explain the strategy and specifications to realize the final optical layout.

Topology of the bench

The first constraint for the complete optical design is the space we have. I have drawn the complete FIS experiment in an in-scale optical scheme, reporting all the structures of the optical bench (walls, holes). The structure of the bench is presented in Figure 5.3, where we can see three areas separated by walls and holes were made to pass the beams through each area. Another constraint is these holes. We will try not to create a lot of new holes and design the beams so that they pass through these existing holes.

Thanks to the lessons learned in Section 4.5, we decided to adopt the following strategy: to have the smallest green path possible. To do so, we choose to put the main laser, the SHG, the MZ and the MCG on the top part of the first area. The ML, the SHG and the MZ were already located there, we will only change

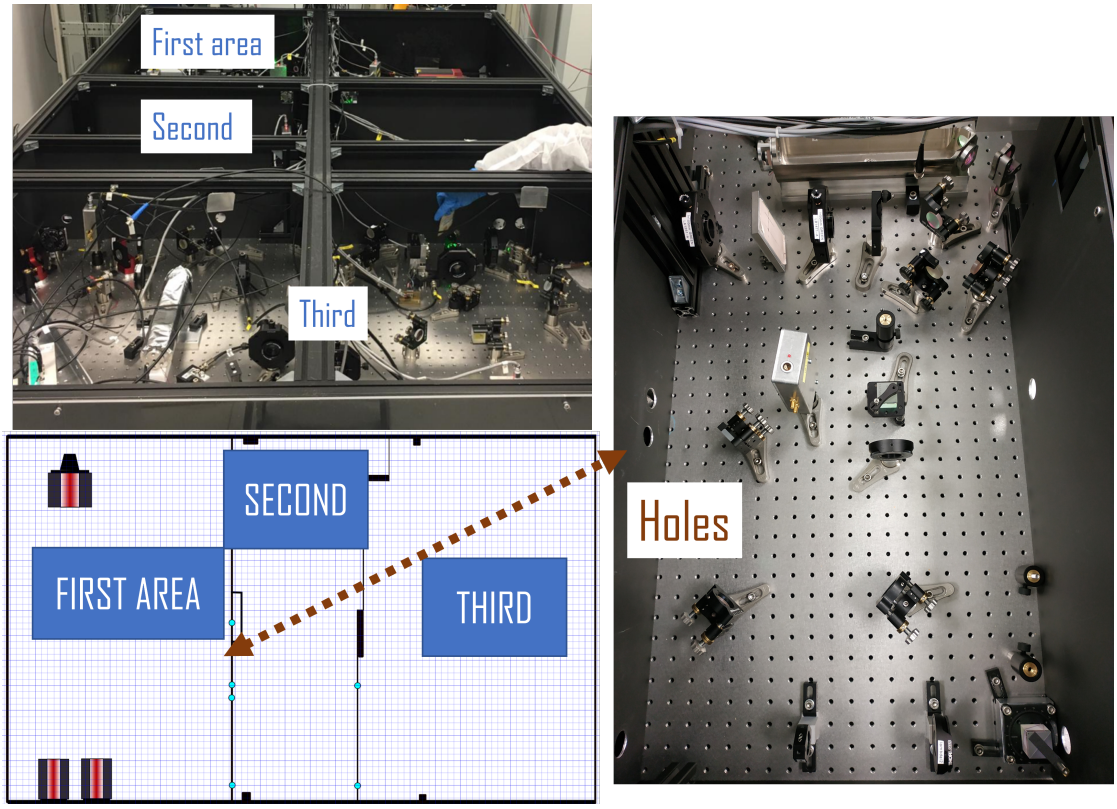

Figure 5.3 – Topology of the bench where the experiment will be installed. Top figure: the bench with its three areas, separated by walls (separator). Bottom figure: in-scale scheme of the bench without optical elements, the grid pattern represents a basic optical bench with its holes represented by grid corners. The black lines represent the small walls separating the benches, the blue light dots on the wall are the holes to pass beams. Right figure: zoom on an area of the bench with the holes and walls.

the path from the SHG to the MZ, for these elements. The two auxiliary lasers, the PLL with the ML are chosen to stay at their previous location, at the bottom of the first area. Indeed, for the FIS experiment, the MCG was in the second area and the OPO was in the third area, making the green path too long and increasing the losses in optical power. Consequently, the OPO is chosen to be in the top part of the second area. We also chose to put the two MCs in the second area, so that the etalon, the test cavity, the MOPA laser (for the SIPS) and the two HDs are located in the third area.

Injection specifications

After choosing the position of each optical element, it is important to represent all the beams. In the optical design of Figure 5.5, the red beams have a frequency of ω_0 or $\omega_0+\Delta/2$. The green beams are at frequency $2\omega_0+\Delta$ and the orange beams are at the idler frequency. While drawing the beams, we have to keep in mind to use a couple of two steering mirrors for precise alignment for critical elements as cavities (SHG, MCG, OPO, sMC, iMC, Test cavity, etalon), MZ interferometer, AOMs and for the Optical Phase-Locked Loop (OPLL). Finally, the waist required by each cavity, each optical components (AOMs, EOMs) and homodyne photodiodes are the specifications to design the mode-matching telescopes (optical system with lenses). At 1064 nm, the waist required to couple inside the OPO cavity is $\sim$ 33 µm and inside the MC is 392 µm [53]. At 532 nm, the waist required for the SHG/OPO and the MCG cavities are respectively 23 µm and 277 µm. The waist required for the test cavity (for tcLCB) is 406.8 µm. For the etalon, the waist is required to be at least 338.7 µm (see in Chapter 6), the divergence angle should be higher than a limit to not decrease the performances of the etalon. Otherwise, the transmission and reflection efficiency will drop. For the homodyne detection system, the radius of the beam has to be smaller than 50 µm, as the photodiode area is a square $500 \times 500\,\mu m$. The waist for a beam entering the AOMs that are tested in this experiment is chosen to be $\sim$ 80 µm. The EOMs that were already in the FIS experiment have an aperture of 1 cm. The specifications are summarized in Table 5.2

Frequency and polarization check

The last step for the design is to check the frequency of each beam, according to Table 5.1 and put HWP to correct beam polarization.

5.2.3 Complete design

In Figure 5.4, the legend for some components used in the optical design drawings and a sum-up of the used acronym and prefix are shown.

Optical cavity/component	Waist (µm)
SHG (@532 nm)	23
SHG (@1064 nm)	*not needed*
MCG	277
OPO (@532 nm)	23
OPO (@1064)	33
sMC/iMC	392
TC (plane mirror)	406.8
etalon	min. 339
homodyne PD	max. 50
AOM	~ 80
EOM clear aperture	~ 10000

Table 5.2 – Specifications about waist values for some critical optical elements.

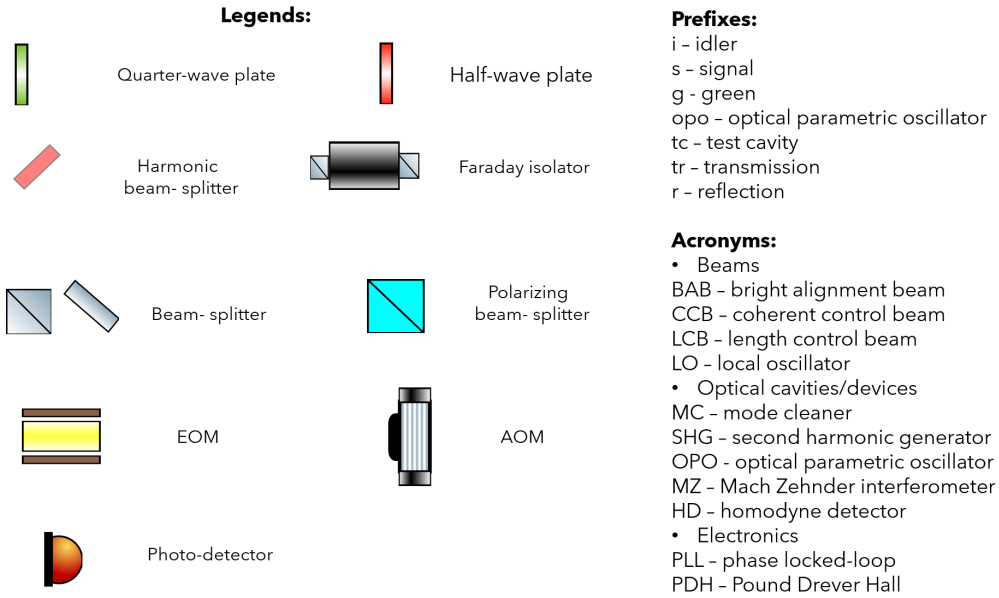

Figure 5.4 – Legend of some optical components and sum-up of the acronyms and prefixes used in the schemes.

The first optical scheme is depicted in Figure 5.5 and is based on the conceptual design presented above. The three Nd:YAG lasers at 1064 nm are kept on the bench, along with the Phase-Locked-Loop (PLL) loops. The main laser (on the upper left corner), with an output power of 1 W still provides the frequency doubling for the SHG cavity. The two former auxiliary lasers AUX 1 and AUX 2 (two Mephisto S200 Nd:YAG laser from Coherent), with a nominal output power

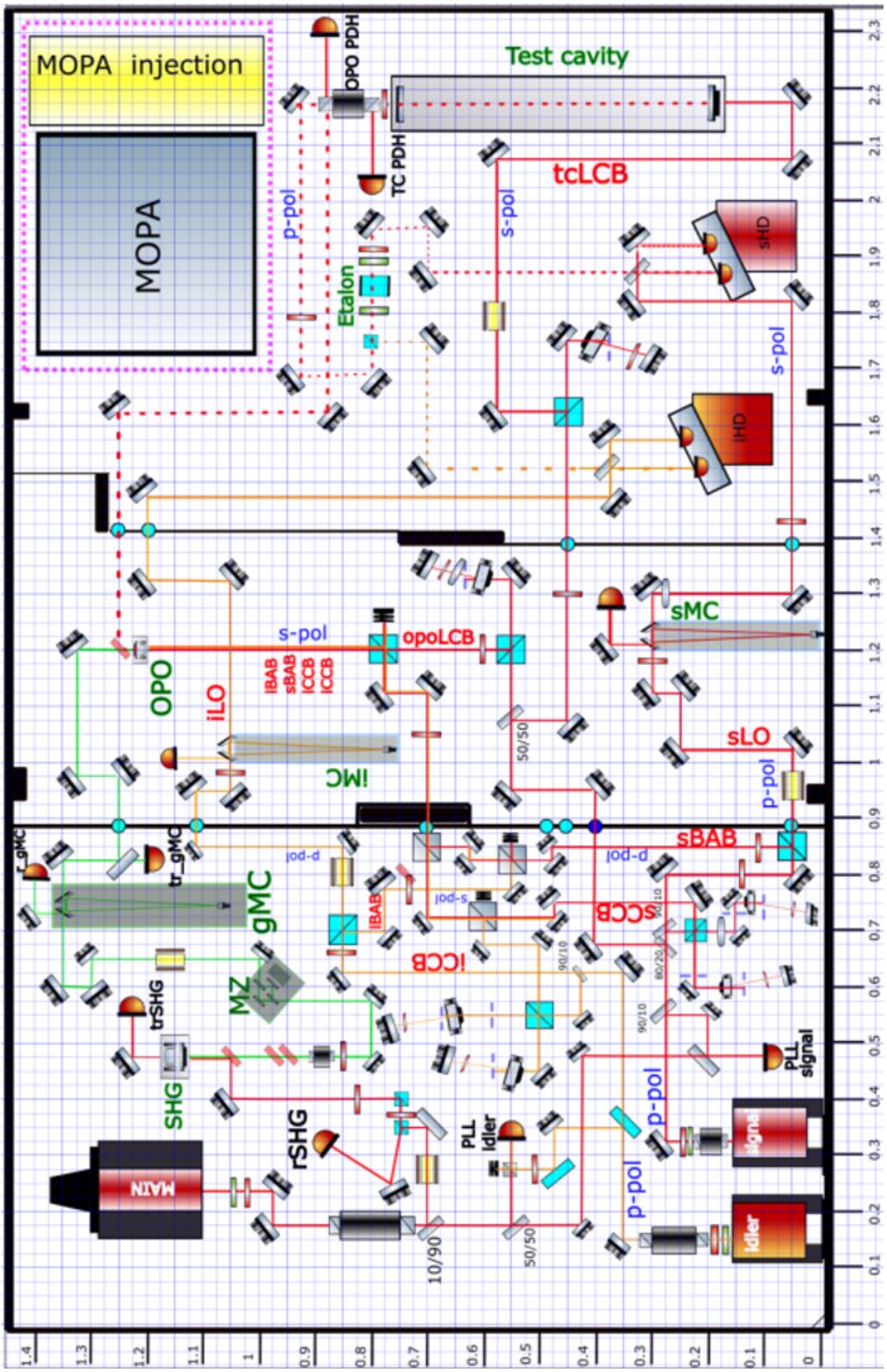

Figure 5.5 – First complete optical layout (without the mode-matching telescopes). The unity is in meters. The black lines represent the small walls separating the benches, the blue light dots on the wall are the existing holes to pass the beam and the dark blue hole is a new hole needed. The acronym of each cavity is in bold green and the name of each auxiliary beam is in red (see the convention in Section 5.1.5). "PDH" means Pound-Drever-Hall. The ratio of each BS is indicated near the symbol. The polarization of each beam is indicated in blue. The MOPA is the name of the laser source for the SIPS and is placed in the scheme (in the purple-dotted frame).

of 200 mW (currently 170 mW due to aging), are now called *idler* (in orange in the figure) and *signal* (in red in the figure) and the phase-lock of each auxiliary laser to the main laser is kept. The former SHG, MZ, GMC and OPO cavities, from the FIS experiment are still used in a similar way, as well as the detection system (the MC for a LO beam and the homodyne detector).

AOM

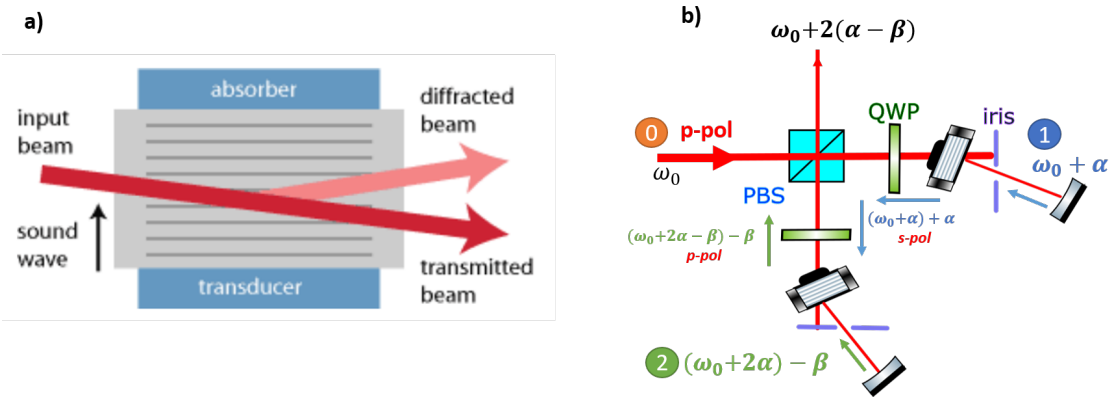

Figure 5.6 – a) Schematics of an AOM from [65] b) Simplified optical scheme of double-pass AOMs in cat's eye configuration.

An AOM or Bragg cell is used to modulate a laser beam in frequency, intensity, and direction and is composed of a crystal where a piezoelectric transducer is attached. Sound waves are created inside the material when an oscillating electric signal drives the transducer to vibrate (see Figure 5.6 a)). The interaction can be interpreted as in non-linear optics described in Section 2.3 and can be assimilated with a three-wave mixing process (Sum-frequency generation or Difference-frequency generation). The modulation is achieved by varying the amplitude and frequency of the acoustic waves traveling through the crystal.

The model of the AOM we will use is AOMO 3200-1113 from Crystal Technology (with an active aperture of 0.1 mm). These devices have been tested and it was found that the deviated beam power is maximized while sending a 217 MHz RF signal to the AOM and the diffraction efficiency obtained is $\sim 40\%$. In a double-pass configuration, the minimum shift is ~ 200 MHz [42].

The cat's eye configuration, illustrated in Figure 5.10, uses the polarization discrimination: for the CCB beams, the beam from the AUX laser is s-polarized and is reflected by the PBS, goes through a quarter-wave plate (QWP) and the first AOM, where the deviated beam is selected spatially (the iris is filtering spatially) and reflected back inside the AOM, going through again the QWP and is then p-polarized and is transmitted through the PBS. After being transmitted, the same scheme is reproduced with another QWP and AOM. The output beam is then s-polarized and then goes to the OPO. The deviated beam from the first AOM is at frequency $\omega_0 + 2\alpha$ (double-pass) and the deviated beam from the second AOM is at frequency $(\omega_0 + 2\alpha) - 2\beta$: the cat's eye configuration enables to have a small phase shift equal to $2(\alpha - \beta)$, as the CCB beams need to be inside the OPO linewidth (25 MHz), which is not achievable with a single AOM in single-pass or double-pass, as schematically represented in Figure 5.6 b).

5.2.4 Limitation: power budget

Thanks to the similarities with the previous experiment, it is possible to take some experimental numbers as references. In our case, the measure of power for some beams can be used as a reference in order of magnitude for the EPR experiment. In particular, we know that with these levels of power, it is possible to run the experiment. In the case of the FIS experiment:

- the IR pump beam for the SHG is around 330 mW;
- the green pump beam before entering the OPO is around 70 mW;
- the IR beam injected into the MCIR is around 8 mW;
- the LO at its maximum power, for CMRR measurement, is around 4.5 mW;
- the BAB and CCB beams, injected to the OPO cavity are around 200 mW.

The power budget is analyzed for each auxiliary beam shown in the schematics of Figure 5.7. We can observe that there is not enough power for the auxiliary beams (the optical power allocated to sBAB is clearly not enough). Indeed, in the FIS experiment, with around 200 mW of BAB, the BAB transmitted by the OPO

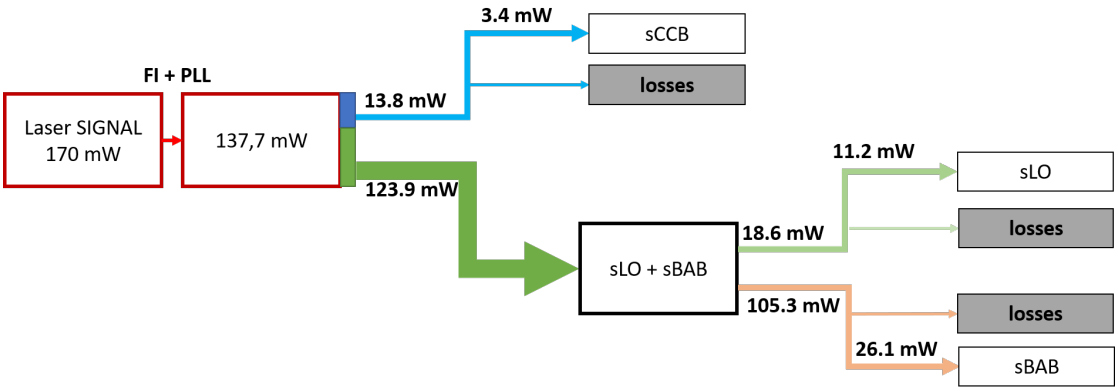

Figure 5.7 – Simplified power budget for the beams from laser SIGNAL. The opoLCB and tcLCB should be included in this budget but the conclusion is the same. Indeed, even without these two beams, the optical power allocating to each auxiliary beam is not sufficient. The losses from the Faraday isolator (FI) is assumed to be 10 % and another 10% is used for the phase-locked loop (PLL).

is at around 90 µW and it is already a little bit difficult to follow the beam with an IR card to align. With only 26 mW of BAB, it will not be even possible to see the BAB with an IR card to align into the HD, which makes the BAB useless.

The schematics only focuses on the beams generated by the laser SIGNAL but the power budget is similar for the beams generated by the laser IDLER, as we will produce the same type of auxiliary beams. The beam from the laser SIGNAL undergoes the losses from the Faraday isolator (FI), assumed to be 10 % and 10% are used for the PLL to the main laser. Then, there is a BS that sends 90% of the power for the sLO and sBAB and 10% for the sCCB. The losses of the CCB part are composed of the 50% losses due to the recombination of the sCCB and iCCB into one BS and of another 50% due to the recombination of the four auxiliary beams (BABs and CCBs). The losses in the sBAB part, similar to the losses in the sMC part, are due to the MC with 40% of losses (see Chapter 4). I chose to separate the power in 15% for the sLO part and 85% for the BAB part (and not 50/50 as in the optical scheme). In fact, in the FIS experiment, we have around 4.5 mW for the LO (after going through the MCIR), so even by minimizing the LO power, the sBAB is still not powerful enough.

5.3 Second design and trade-off

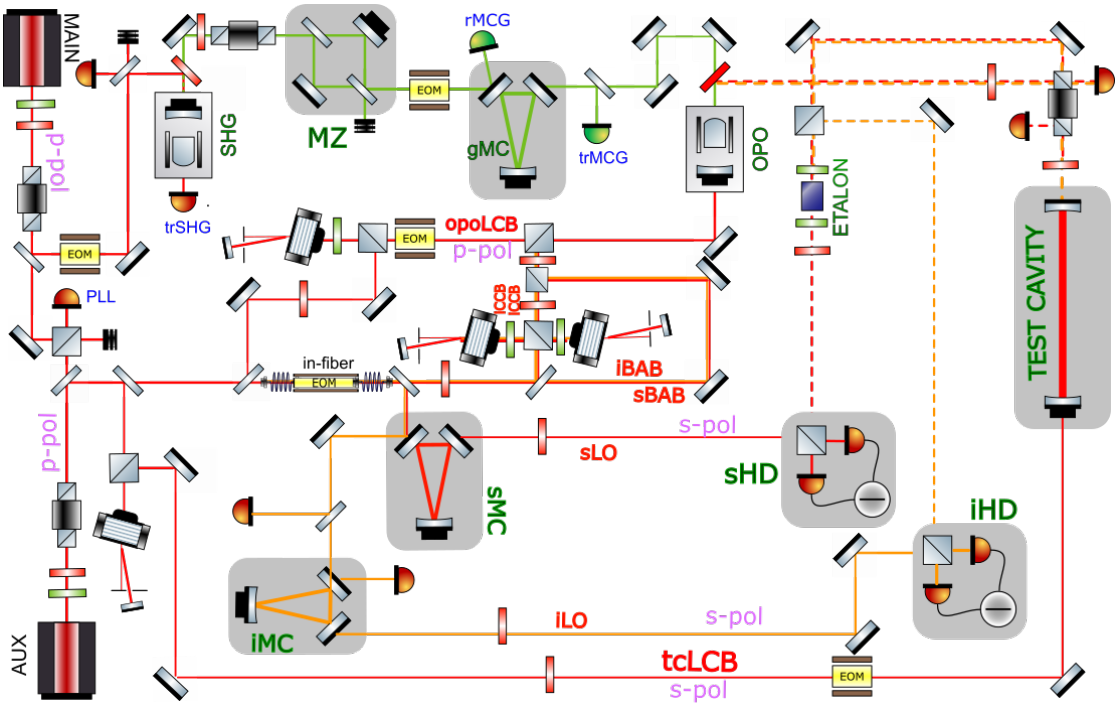

Figure 5.8 – Conceptual scheme for the second optical design. The orange beams are the beams at idler frequency, $\omega_0 + \Delta$, the cube BS represents PBS. The coupled-fiber EOM will generate two sidebands, in addition to the carrier frequency (input field at ω_0).

I will explain in this section the second optical design, depicted in Figure 5.8. This design will imply the use of two laser sources instead of three, still one main laser (called "MAIN") and only one auxiliary laser (called "AUX"). The beam from the auxiliary laser, at ω_0, is divided into three auxiliary beams: two of them are used to generate the two locking beams with a double-pass AOM. The third one is sent to an EOM in-fiber, which is briefly explained in Section 5.3.1, tuned so that it will produce two sidebands around ω_0: $\omega_0 + \Delta$ and $\omega_0 - \Delta$. Then, one part of the sideband at $\omega_0 + \Delta$ is sent to OPO for sBAB and iBAB The other part is sent to two AOMs in cascade (cat's eye configuration) to produce the two CCBs. In the simplified scheme, the cube BS represents a PBS. The advantage using a fiber-coupled EOM is that the main beam at ω_0 and the sideband at $\omega_0 + \Delta$ are

spatially overlapped, we will see later why it is crucial for the power budget. In the conceptual design, the switch from the BAB to the CCB, the two having orthogonal polarizations, is done using a HWP and a PBS. But, to avoid the BAB contamination when we want to produce a squeezed vacuum, we will avoid this solution as we did for the FIS experiment. Indeed, as for the FIS experiment, we send first the bright alignment beams to align, and then we only send the coherent control beams.
Another part of the carrier with the sidebands is used to generate the local oscillators: first, they are sent to the sMC, which is locked on the same frequency of the signal. The cavity is designed to filter the beams so that the beam at the frequency of $\omega_0 + \Delta$, which corresponds to one of the sidebands produced by the EOM, is reflected and arrives inside the iMC, that is locked at this frequency.

5.3.1 Fiber-coupled EOM

A fiber-coupled integrated EOM can be used to have high modulation frequencies in the gigahertz range and have high optical power stability. The principle of this device lies in the linear electro-optic effect or the *Pockels effect*, which is based on the variation of the refractive index of a nonlinear crystal by applying an electric field. In the fiber-coupled modulators, the Pockels cell is placed between two fiber collimators. The typical insertion loss value is around 4 dB and generally, these modulators accept an incident beam with a maximum power of 50 mW [66]. These devices have the advantage of having a high optical power stability, low modulation voltages and high extinction ratios.

5.3.2 Trade-off

In this section, I will justify why the first optical design is hardly usable in our case and explain why we chose our last design with a trade-off based on several criteria: space, structure and power budget.

- *Space*

As the bench is divided into three different areas, we chose where to place each optical cavity and the choice is the same for the two designs. The first area (left)

contains the laser sources, the elements to produce and stabilize the green pump for OPO (the SHG cavity, the MZ interferometer and the GMC cavity) and the optical elements to generate the auxiliary beams (sCCB/iCCB and sBAB/iBAB). The central area is dedicated to the mode-cleaners for the signal and idler beams (sMC and iMC), the OPO locking beam, and the EPR-entangled beams generation with the pump beam injected into the OPO. The last area comprises the test cavity, the etalon, the two separate homodyne detectors and the part inside the purple-dotted frame in Figure 5.5 which is the MOPA laser. For the second design, there is one couple of AOMs in cat's eye configuration less, compared to the first design but one fiber-coupled EOM more. As we can see in Figure 5.5, one couple of AOMs takes a lot of place. Moreover, for the second design, as the BABs and the CCBs are overlapped with each other, there is two auxiliary beam recombinations (with a BS) less in the second design, which is a consequent gain of space. Consequently, the second design is more complex than the first design, in terms of space.

- *Structure*

The first optical design enables to keep the three laser sources (one main laser/master laser and two auxiliary lasers) and the two PLLs, from the FIS experiment. The second version has one auxiliary laser less.

For the first design, each type (in frequency) of auxiliary beams are produced by two different lasers (one for the signal auxiliary beams and one for the idler auxiliary beams) so, to recombine all the different beams, we need one BS (with 50% loss for each) to recombine the two BABs, one BS for the two CCBs and one final BS for the four previous BABs and CCBs. Then, the production of CCBs requires 4 AOMs (2 couples of AOMs in cat's eye configuration). For the second optical scheme, the coupled-fiber EOM produced the beams at the two frequencies needed, which are spatially overlapped, so we only need 2 AOMs and only one PBS to recombine BABs and CCBs.

- *Power budget*

In order to compare the power budget of the two designs, we will confront them in a Sankey diagram representation, as shown in Figure 5.9. That enables

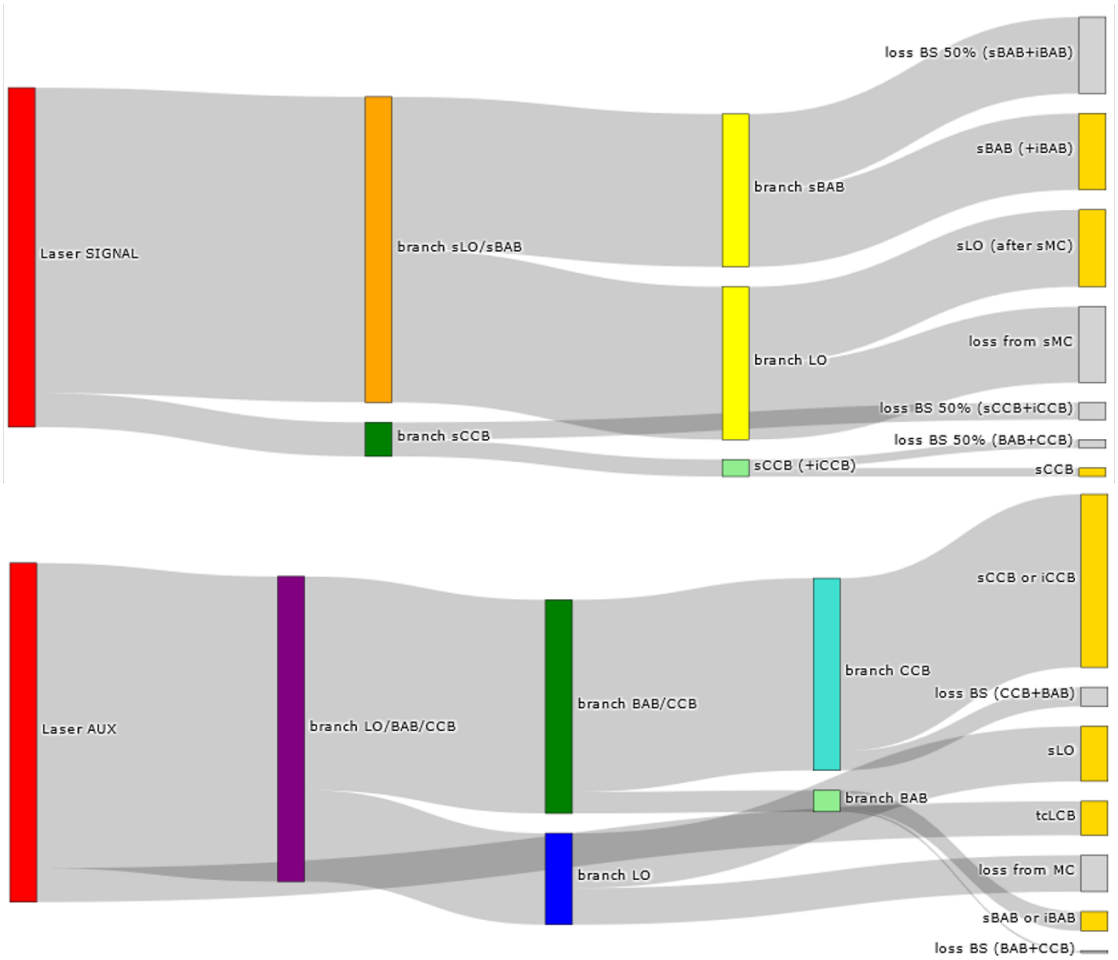

Figure 5.9 – Representation in a Sankey diagram for: (top) the power budget for the sBAB and the iCCB in the first optical design; (bottom) the power budget for the tcLCB, sBAB/iBAB and the sCCB/iCCB in the second optical design. The two diagrams are in the same scale and the power of each laser source is 137.7 mW. This is the power obtained after a 10% loss from a Faraday isolator and 10% is taken for the PLL with the master laser. Generally, the separation of one "flow" in two "flows" is done by a BS whose ratio is tunable.

to compare the differences between the power distribution for each design. In this figure, the fiber-coupled EOM losses were not considered. As we can see, for the second design, the losses are reduced because for each couple of auxiliary beams sCCB, iCCB and sBAB, iBAB, they are not generated separately, as for the first design, so there is no need to combine them again with a BS and loose half

of their power at each combination.

5.4 Last version of the optical design

The previous budget power reveals that the first conceptual design is not optimal to have enough optical power for the auxiliary beams and limit the optical losses. We then chose to keep the second optical scheme, also for the reduced complexity in terms of space, even if the first optical design was convenient in terms of minimizing the change with respect to the previous experiment (keeping three laser sources, the already installed OPLLs). Using the simplified scheme in Figure 5.8, a more complete optical layout is presented in Figure 5.10.

5.4.1 New components and differences

After rechecking the power budget with this complete design, we made a list of new components needed, compared to our FIS experiment:

- 4 AOMs (two double-pass AOMs and a couple of two double-pass AOMs in a cat's eye configuration) which are tested at Genova University [42];
- a second homodyne detector, designed and tested at the Università di Roma "La Sapienza";
- an etalon into its mechanical holder and its thermal control system, developed and tested at AstroParticule and Cosmologie laboratory and described in Chapter 6;
- a fiber-coupled EOM, the choice of a commercial model is under study;
- a second triangular MC to filter one of the two local oscillators, which will be designed and tested in collaboration with KASI (Korea Astronomy and Space Science Institute);
- a Test Cavity;

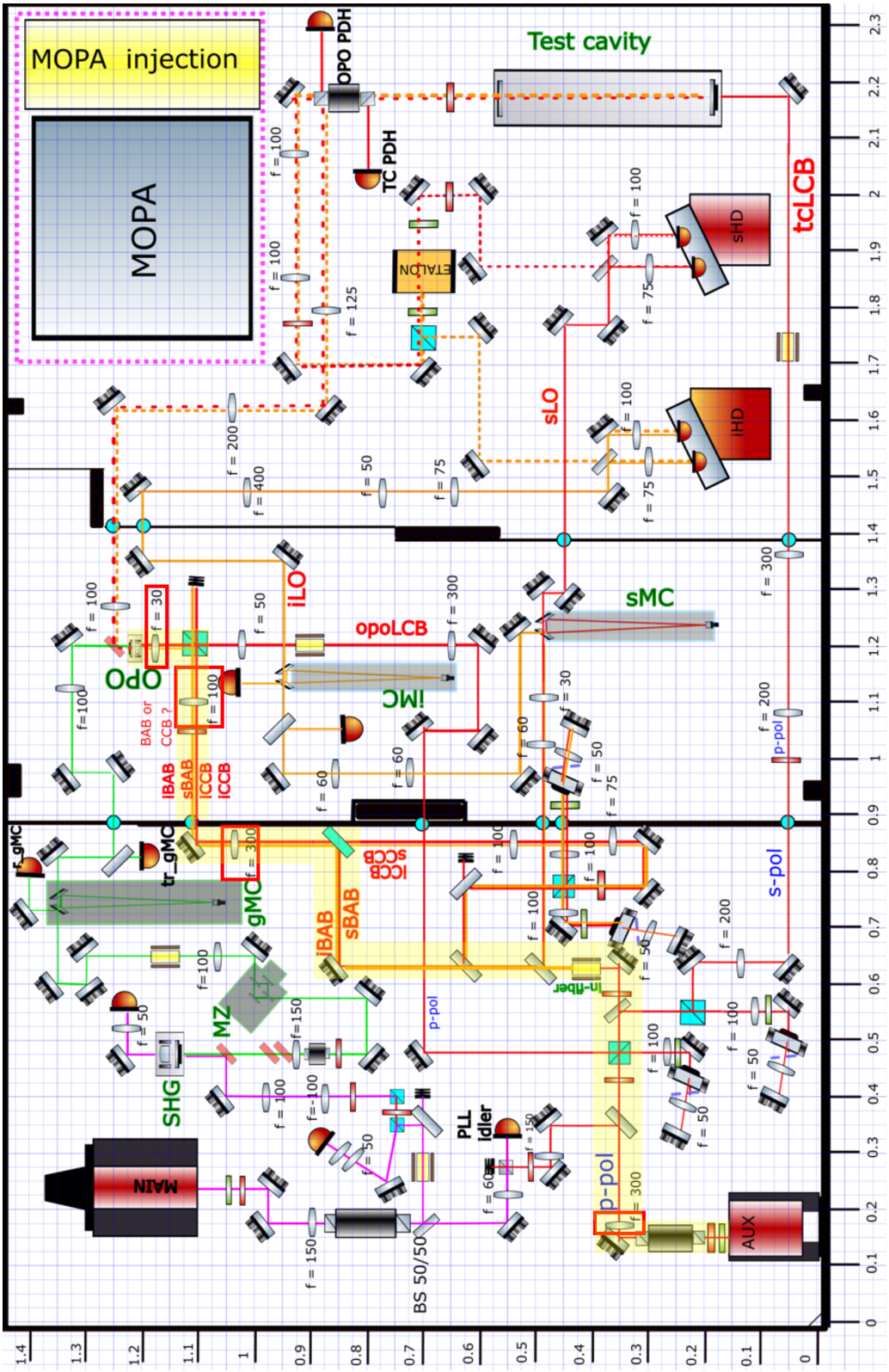

Figure 5.10 – Second complete optical design with the mode-matching telescopes using the conceptual design of Valeria Sequino. The BAB path is colored in yellow and the mode-matching telescopes in this path are in a red frame.

- the SIPS, its laser source (MOPA), mode-matching telescope to inject the laser into the ITF, a vacuum chamber and mechanics required to inject beams into this chamber.

There is one auxiliary laser less, compared to the previous experiment.

5.4.2 Design of mode-matching telescopes

Optics	Position (mm)	Relative position (mm)	Properties	Waist (µm)	Waist position (mm)	Rayleigh range (mm)	Divergence (mrad)	Sensitivity (%/mm²)	Name	Lock
Input beam	-90		n = 1, M² = 1	132	-90	51.4465	2.56576	0.00944556	laser AUX	absolute
Lens	210	300	f = 300 mm	769.731	510	1749.39	0.44	0.0100093	L1	none
Flat mirror	387.5	177.5		769.731	510	1749.39	0.44	0	BS PLL	none
Flat mirror	512.5	125		769.731	510	1749.39	0.44	0	PBS	none
Flat mirror	937.5	425		769.731	510	1749.39	0.44	0	BS CCB	none
Flat mirror	1162.5	225		769.731	510	1749.39	0.44	0	mirror	none
Flat mirror	1387.5	225		769.731	510	1749.39	0.44	0	PBS CCB+BAB	none
Lens	1567.5	180	f = 300 mm	121.132	1886.26	43.3235	2.79597	0.0137792	L2	none
Flat mirror	1637.5	70		121.132	1886.26	43.3235	2.79597	0	M4	none
Lens	1887.5	250	f = 100 mm	112.321	1902.58	37.2504	3.01529	0.010354	L3	none
Flat mirror	1987.5	100		112.321	1902.58	37.2504	3.01529	0	PBS OPO	none
Lens	2062.5	75	f = 30 mm	24.9325	2098.9	1.83544	13.5831	6.81877	L4	none
Flat mirror	2100	37.5		24.9325	2098.9	1.83544	13.5831	0	OPO	none

Figure 5.11 – Data editor from GaussianBeam of the BABs simulation from the AUX laser to the OPO.

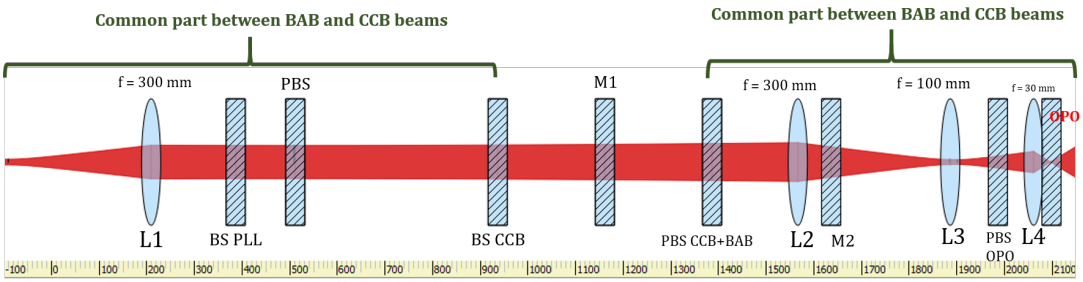

Figure 5.12 – Graphical interface from GaussianBeam of the BABs simulation from the AUX laser to the OPO. The name given for each element in the data editor is reported. The parts of the BABs which are common with the CCBs are indicated. At the bottom, the ruler is in millimeter and indicate the position for each optical element.

Mode-matching telescopes are mandatory for each beam to enter a cavity or optical component with the correct waist. Their design was done with *Gaussian-Beam* [43], a Gaussian optics simulator. This software has a graphical interface and an optical data editor where we can put the parameters of the input beam (position, properties as refractive index, M^2 factor, waist size,...), insert some lenses at the wanted position and the focal length or flat interface (to represent the final target).

During the step where we design the mode-matching telescopes, all the beams and optical elements are already present in the optical scheme. The starting point is thus to enter the input beam parameters, in GaussianBeam which are:

- for the main laser, ω =152 µm at the position -106 mm from the laser shutter;
- for the auxiliary laser, ω =132 µm at the position -90 mm from the laser shutter.

Then, we report each relevant optical element in the design, for example, mirrors, PBS and BS, and represent them with a "Flat mirror" which will not change the beam size. This step is useful to understand the space where we can put lenses and to have in mind, for example, that a PBS (cube) or a mirror take some amount of space and we should place lenses accordingly. For the position of each optical element, the scheme is in scale with the grid equal to the space between two holes in a metric optical bench (25 mm). We have to simulate the optical path linearly, with the input beam as a starting point and the concerned cavity for the arrival. It is still possible to modify the optical path in the design a little bit, if there is enough space. The focal length values are chosen by looking at the existing focal length values for 1-inch lenses among the commercially available lenses. We also try to make the beams collimated as long as possible.

Concerning the green path, as the path from the SHG to the MCG and the path from the MCG to the OPO are symmetrical, i.e., the waist required inside the SHG and the OPO is identical, we chose the put the same lens and the same optical path length for these two symmetrical paths.

In the design of mode-matching telescopes, the most difficult step is to design the ones for the four auxiliary beams that have some common paths, just before being injected into the PBS (sBAB, iBAB, iCCB, sCCB).

Figures 5.11 and 5.12 show the data editor and the graphical representation of the BABs simulation. In the data editor, the different optical elements listed are:

- the "BS PLL" is the 90/10 BS where 10% of the beam is used for the PLL between the AUX laser and the MAIN laser;
- the "PBS" is the one in the path of opoLCB;
- the "BS CCB" is used to separate the CCB beams that need to undergo a particular frequency shift (through AOMs in a cat's eye configuration);
- the "PBS CCB+BAB" is where the CCBs and BABs recombine;
- M3 and M4 are mirrors;
- "PBS OPO" is the PBS where the five auxiliary beams recombined before being injected into the OPO.

We can see that the waist is equal to 24.9 µm at 1.1 mm from the OPO cavity. The optical scheme (with the grid) is not precise enough to have such precision. The position of each laser shutter and the position of the waist inside each cavity cannot be more precise than about ± 12.5 mm. The BAB path is highlighted in yellow in the complete optical scheme in Figure 5.10, the mode-matching telescopes from GaussianBeam simulation are in a red frame.

When using GaussianBeam, one has to analyze each optical path, whether there are numerous beams in the same optical path or whether there is only one type of auxiliary beam in the optical path considered. Moreover, the complexity is higher when there is an AOM in the optical path because one has to simulate the double-pass and simulate twice some elements, as the deviated beam is reflected back to the AOM (double-pass).

5.5 Conclusion of the chapter

This chapter is dedicated to the design of our EPR demonstrator. As two proof-of-principles experiments demonstrated the feasibility of the technique with simplified setups, our table-top experiment is a step towards implementing EPR squeezing into second-generation and future GW detectors. The produced EPR squeezing will be injected in a test cavity (which mimics the ITF arm) and then in a small-scale suspended interferometer, which is RPN-limited in the same frequency band of AdV+. This will be the first radiation pressure noise reduction by the injection of frequency-dependent squeezing using EPR entanglement.

As we will transform our previous bench (described in Chapter 4) into an optical bench to test the EPR squeezing, the two optical designs we made take into account the space constraints. Moreover, one of the advantages of the technique is that it does not require many new components, so we tried to make a design with the least possible change compared to the previous bench. In our approach, we also took into account the power budget of the different beams. The first design aims to keep the lasers and the PLLs unchanged, from the previous experiment but the power budget reveals poor powers allocated to auxiliary beams, which will make them useless. For that reason, we have chosen to opt for the second design presented in Figure 5.8, which is also less complex in terms of space. In this work, the experiences learned from the FIS experiment allow me to contribute to the realization of the two complete optical designs and understand all the critical points.

Currently, the optical design with the mode-matching telescopes is being finalized and the first third of the bench (with the lasers and the PLL) is being installed. The next step is the complete installation of the bench, with the integration of the etalon, whose design and tests are described in Chapter 6.

Chapter 6

Thermally controlled Fabry-Perot cavity for entangled beam separation

Outline of the current chapter

The previous chapter describes the optical design (shown by Figure 5.8) adopted for the EPR experiment. In this design, a Fabry-Perot cavity is used to separate the two entangled squeezing fields, the signal field at ω_0 and the idler field at $\omega_0 + \Delta$ (with $\Delta = 3.8\,\mathrm{GHz}$), tuning the length of the cavity in order to allow the transmission of the signal field and the reflection of the idler field. This chapter aims to describe the design of this Fabry-Perot cavity, the choice of the main parameters, its construction and tests.

In the two proof-of-principle experiments [77, 85], the separation of the entangled fields is made with a triangular stable cavity, similar to the other *mode-cleaner cavities* used in the squeezing experiment. In our experiment, as separation cavity, we have chosen to use a solid Fabry-Perot etalon, consisting of two parallel planar highly-reflective coated surfaces with a fixed spacing made by a solid transparent material, fused silica in our case.

The reason to choose an etalon cavity for this experiment is the possibility of simplifying its alignment and control as much as possible. First, choosing a very thin cavity makes it less sensitive to the frequency changes of a free-running laser. Moreover, the possibility to stabilize the cavity temperature with a simple thermal control system, makes also - at least in a first step - possible to keep the cavity at its working point without an error signal made with a bright beam, which will greatly simplify the optical scheme of the experiment. Of course, a bright beam can be added, if needed. A final reason to use the etalon, is to acquire experience with a different method with respect to the $\sim 20cm$ triangular cavities used in the squeezing experiment for other purposes.

The chapter is structured in the following way. In Section 6.1 I will explain the choice of the cavity parameters. In Section 6.2.1 and 6.2.2, I will define the mechanical holder design and the thermal control system, ensuring a good thermal stabilization. Finally, the performances of the thermal control system, the optical characterization of the etalon and the stabilization tests are presented.

This work has been done in collaboration with APC laboratory engineers, technicians and researchers.

6.1 Optical resonator design

6.1.1 Thickness

The first optical parameter to be defined is the etalon thickness. Since the etalon purpose is to separate the two entangled fields (at frequency ω_0 for the signal beam, in blue in the following of the chapter, and $\omega_0 + \Delta$ for the idler beam, in red in the following of the chapter), the etalon FSR is chosen as the double of the entangled beam separation. The signal field will be kept at the cavity resonance

while the idler field will be at the cavity anti-resonance (see fig.6.1). Since in our experiment, $\Delta = 3.8\,GHz$, equal to the OPO FSR, we have:

$$FSR_{etalon} = \frac{c}{2nL_{et}} = 7.6\,GHz \qquad L_{etalon} = 13.6\,mm,$$

where L_{et} is the physical length of the etalon and n = 1.4496 (for the fused silica), c is the speed of light.

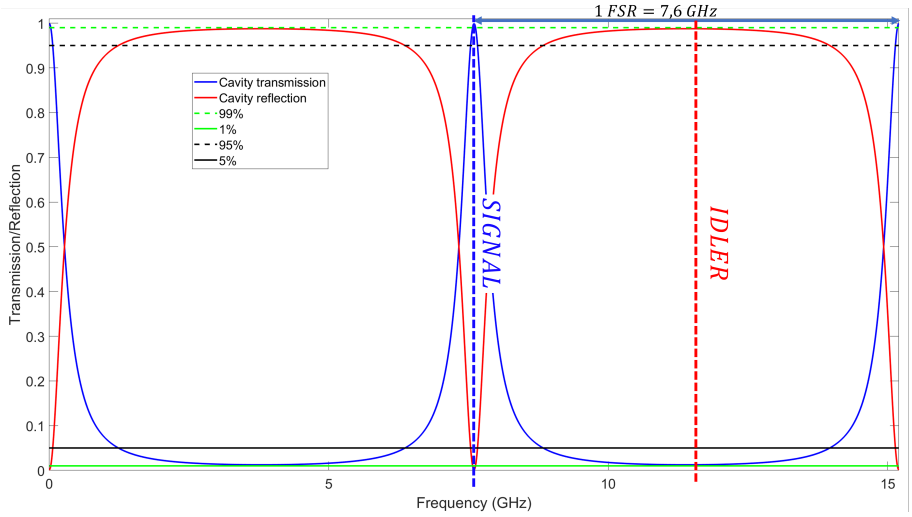

Figure 6.1 – Transmission and reflection of the etalon, the signal (dotted-blue) and idler (dotted-red) frequencies with respect to the resonance and anti-resonance of the cavity are indicated. The curves at 1%, 5%, 95% and 99% are also indicated.

6.1.2 Choice of the finesse: transmitted and reflected fields

The choice of the finesse (and then of the reflectivity of the two etalon surfaces) is dictated by two constraints: the first one is to correctly separate the two beams with the minimum optical losses (as they highly impact the squeezing), and the second one is to allow the simplest possible control of the cavity (and then, have the lowest possible finesse).

The first constraint translates in having the maximum transmission for the signal beam (ω_0), kept at the resonance, and the maximum reflection for the idler beam ($\omega_0 + \Delta$), kept at the anti-resonance.

The expression for the transmitted and reflected field of the cavity (normalized with respect to the input beam), are:

$$T_{cav}(\Phi) = \frac{I_{trans}}{I_{inc}} = \left(\frac{t_1 t_2 e^{i\phi}}{1 - r_1 r_2 e^{i\phi}}\right)^2 \tag{6.1}$$

$$R_{cav}(\Phi) = \frac{I_{ref}}{I_{inc}} = \left(\frac{r_1 - r_2(1-A)e^{i\phi}}{1 - r_1 r_2 e^{i\phi}}\right)^2, \tag{6.2}$$

where r_1 and r_2 are the two surface reflectivities and the round-trip phase inside the etalon is:

$$\phi(f) = \frac{4\pi n L_{et} f}{c} \tag{6.3}$$

For $r_1 = r_2 = r$ the transmission becomes:

$$T_{cav}(\Phi) = \left(1 - \frac{A}{1-\mathcal{R}}\right)^2 \frac{1}{1 + (2\mathcal{F}/\pi)^2 \sin^2(\phi(f)/2)} \tag{6.4}$$

$$\tag{6.5}$$

where $\mathcal{R} = r^2$ and $\mathcal{A}$ are the round trip losses. When the finesse is high enough, the previous formula can be approximated as:

$$T_{cav}(\Phi) \simeq \left(1 - \frac{A\mathcal{F}}{\pi}\right)^2 \frac{1}{1 + (2\mathcal{F}/\pi)^2 \sin^2(\phi(f)/2)}, \tag{6.6}$$

with the finesse $\mathcal{F}$ is defined as:

$$\mathcal{F} = \frac{\pi\sqrt{\mathcal{R}}}{1-\mathcal{R}} \simeq \frac{\pi}{1-\mathcal{R}}. \tag{6.7}$$

The roundtrip losses A can be estimated from the surface roughness (making a reasonable assumption that the scattering dominates on the absorption), with:

$$A = 2 \times \left(\frac{2\pi\sigma}{\lambda}\right) = 144\left(\frac{\sigma}{1\,nm}\right)^2 ppm, \tag{6.8}$$

where we have considered two surfaces. The total losses are:

$$A_{tot} \simeq \frac{2A}{1-\mathcal{R}} \simeq \frac{2A\mathcal{F}}{\pi}. \tag{6.9}$$

For the following estimations, we will consider a roughness of 0.5 nm (hypothesis to be checked with respect to the measured etalon properties), giving a total round trip losses of $\simeq 70$ ppm, which for the design phase will be approximated, in a conservative way, to 100 ppm.

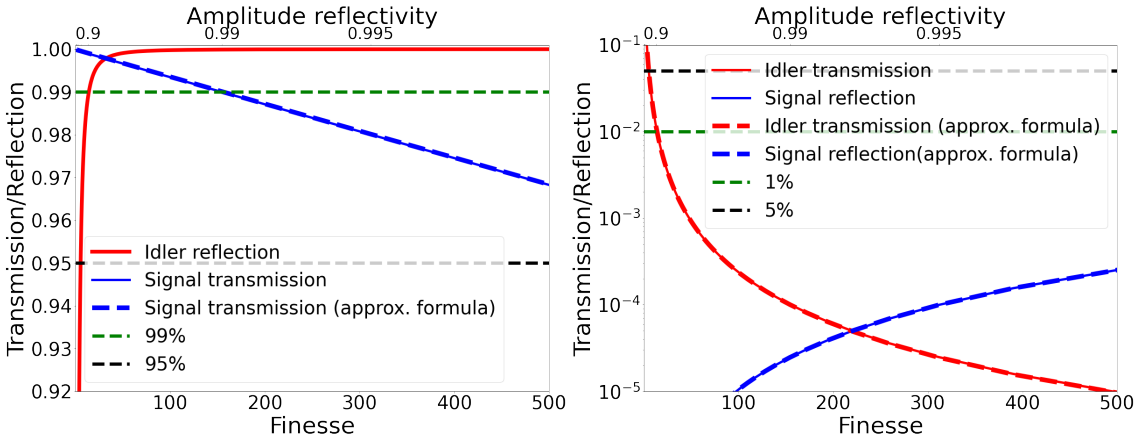

Figure 6.2 – Transmission and reflection of the idler and signal fields as a function of the finesse and the amplitude reflectivity r. (Left) Idler reflection (in red) and signal transmission (in blue) along with the requirement curves at 95% (in black-dotted) and 99 % (in green-dotted). (Right) Idler transmission (in red) and signal reflection (in blue) along with the requirement curves at 5% (in black-dotted) and 1 % (in green-dotted).

The transmission and reflection at resonance ($\phi(f) = 0$) and anti-resonance ($\phi(f) = \pi$) can be expressed as:

$$R_{cav}^{res} = \left(\frac{Ar}{1-r^2}\right)^2 \tag{6.10}$$

$$T_{cav}^{res} = \left(1 - \frac{A}{1-r^2}\right)^2 \tag{6.11}$$

$$R_{cav}^{anti} = \frac{4r^2}{(1+r^2)^2} \tag{6.12}$$

$$T_{cav}^{anti} = \frac{1 - \frac{A}{1-r^2}}{1 + \frac{4r^2}{(1-r^2)^2}}, \tag{6.13}$$

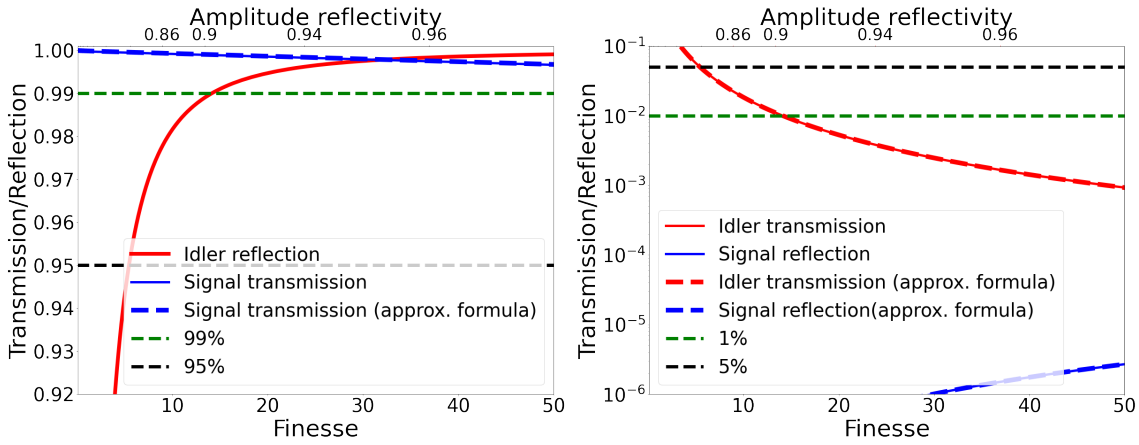

Figure 6.3 – zoom of Figure 6.2 for finesses from 0 to 30.

which can be approximated as:

$$R_{cav}^{res} \simeq \left(\frac{A\mathcal{F}}{\pi}\right)^2 \tag{6.14}$$

$$T_{cav}^{res} \simeq \left(1 - \frac{A\mathcal{F}}{\pi}\right)^2 \tag{6.15}$$

$$T_{cav}^{anti} \simeq \frac{(\pi - \mathcal{F}A)^2}{\pi^2 + 4\mathcal{F}^2}. \tag{6.16}$$

Figures 6.2 and 6.3 give the transmitted and reflected idler and signal fields as a function of the finesse and the amplitude reflectivity r. We see that to have a signal field transmitted at more than 99% the finesse should be less than 150. For finesses higher than 150, the round-trip losses start to have a non-negligible impact on the transmission. Moreover, in order to have an idler field reflected at more than 99%, the finesse should be higher than ~ 14.

The conclusion is that, in order to have less than 1% of losses for the signal and idler beam, the possible range for the finesse is between 14 and 150.

Considering this range, we chose the lowest possible finesse (14), in order to release as much as possible the requirements on the cavity control, then to have a less stringent constraint in the stability of the temperature and less sensitivity with respect to the frequency noise and drifts. For this choice, we also notice that the signal beam reflection is lower than 1% and the idler beam transmission is lower than 1%.

A higher value of the finesse would help to increase the signal for the cavity control, and then the shot noise limited sensitivity of a signal used for the cavity control. However, since we have decided not to use a bright beam for the cavity control at least in a first stage, we don't consider the shot noise limited sensitivity as a parameter for the choice of the finesse.

Let's also remark that the requirements of 95% for the signal transmission and 5% for the idler reflection are preliminary requirements, aiming to minimize the readout losses, defined in Section 4.2.6, which can degrade the squeezing level.

6.1.3 Etalon production

Based on the previous considerations, four quotations were asked (Light Machinery, SLS Optics, ARDoP Industrie, VM Optics) and based on the price, the delivery time, the quality of the quotations and the specifications ensured by each company, we chose the one from SLS Optics.

Table 6.1 describes the etalon properties provided by SLS Optics. Figure 6.4 shows two photographs of the etalon without its holder.

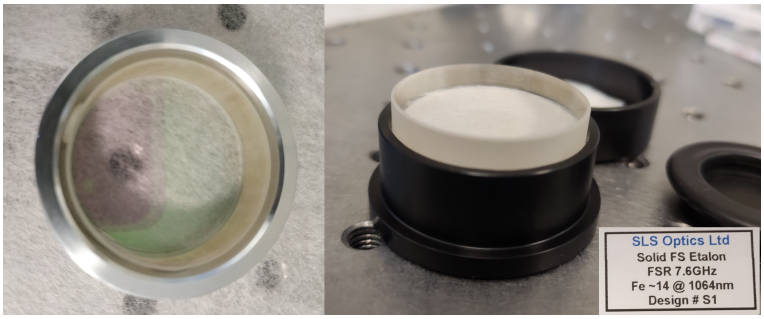

Figure 6.4 – (Left) Top view of the etalon in a ring. (Right) Side view of the etalon in its protection box.

We observe that the finesse, FSR and roughness measured by the manufacturer are compatible with the specifications of our experiment.

Manufacturer	SLS Optics Ltd.
Etalon thickness	13.604 mm
Clear aperture	28.0 mm
FSR	7.6 GHz
Finesse	14
Reflector coating	80.0 %
Parallelism error over clear aperture. @ operational wav.	$\lambda \setminus 420$
Sphericity error over clear aperture. @ operational wav.	$\lambda \setminus 4204$
Surface roughness	0.44 nm RMS

Table 6.1 – Design parameters provided by the manufacturer

6.1.4 Cavity control: Temperature stability

In order to study the control of the cavity, we have considered two main perturbations: the temperature variations of the etalon and the frequency drift of the laser.

The temperature affects the transmission and reflection of the etalon as follows:

$$\phi(f, \Delta T) = \frac{4\pi n f L_{et}}{c}(1 + \frac{dn}{dT}\Delta T)(1 + \alpha \Delta T), \tag{6.17}$$

where $\alpha = 0.55 \times 10^{-6}\ °C^{-1}$ is the fused silica thermal expansion coefficient (for Suprasil fused silica) and $\frac{dn}{dT} = 0.87\times\ 10^{-5}$ the change in the refractive index with temperature [84].

The previous expression can be approximated as :

$$\phi(f, \Delta T) \simeq \frac{4\pi n f L_{et}}{c}\left(\frac{dn}{dT}\Delta T + \alpha \Delta T\right), \tag{6.18}$$

where we have neglected the term $O(\Delta T^2)$ and considered that the etalon is at resonance for $\Delta T = 0$.

Figure 6.5 (left) shows the transmission of the signal beam as a function of the temperature variation of the etalon and the finesse, for 100 ppm round trip losses. As expected, the sensitivity to the temperature variations increases with the finesse. A similar calculation was done with the idler field reflection at the anti-resonance condition, but the resulting tolerance is much looser than the one for signal transmission.

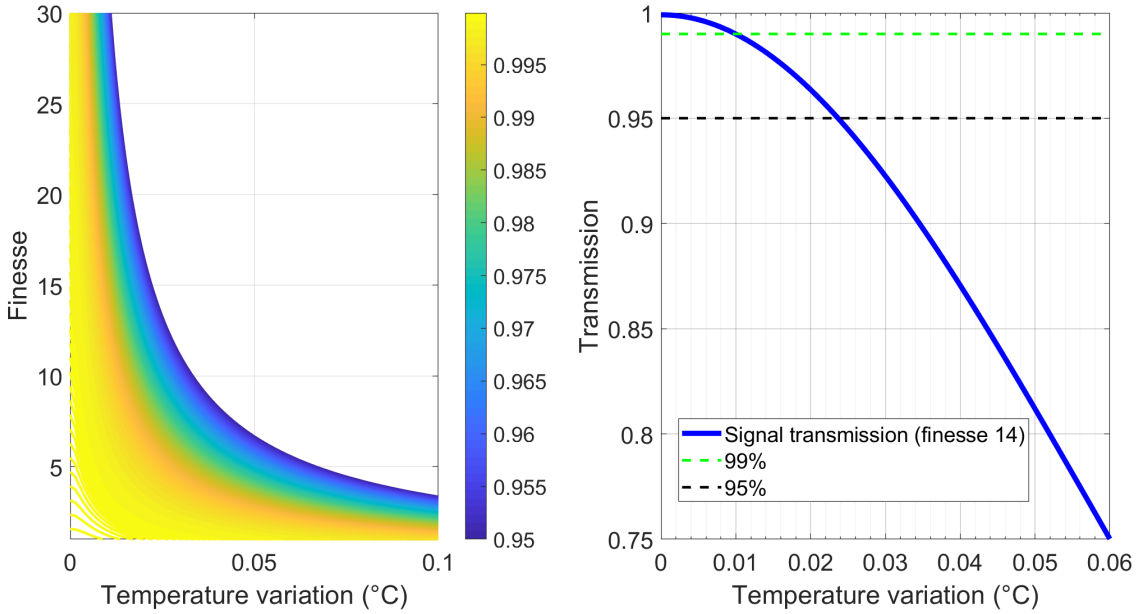

Figure 6.5 – (Left) Transmission of the signal field at the resonance condition in function of the temperature variation and the finesse. (Right) Signal transmission as a function of temperature variation for a finesse of 14 along with the requirement level at 95% (black-dotted) and 99 % (green-dotted).

Figure 6.5 (right) shows the transmission of the signal field for a finesse of 14. We see that in order to guarantee a transmission of 99% we need a stability of $\sim 0.01\,°C$ and for a transmission of 95% we need a stability of $0.025\,°C$. Consequently, for the thermal control system described in 6.2.2, the specification taking into account is that the temperature fluctuations have to be smaller than $\pm 0.01\,°C$. Considering variations of the room temperature of the order of a fraction of degree, this means that we need a temperature stabilization to keep the etalon in resonance with the laser light.

6.1.5 Frequency noise

Figure 6.6 shows the influence of the frequency drift on the cavity transmission. In order to have a transmission higher than 95% the frequency should not change more than 60 MHz, and not more than 25 MHz for a transmission higher than 99%. The lasers Mephisto and Mephisto S from Coherent company [31] used in this experiment (see their description in Section 4.1.1), have a long-term drift of

the order of 5 MHz, then the laser drifts, due to the cavity small thickness, will not put the cavity out of resonance.

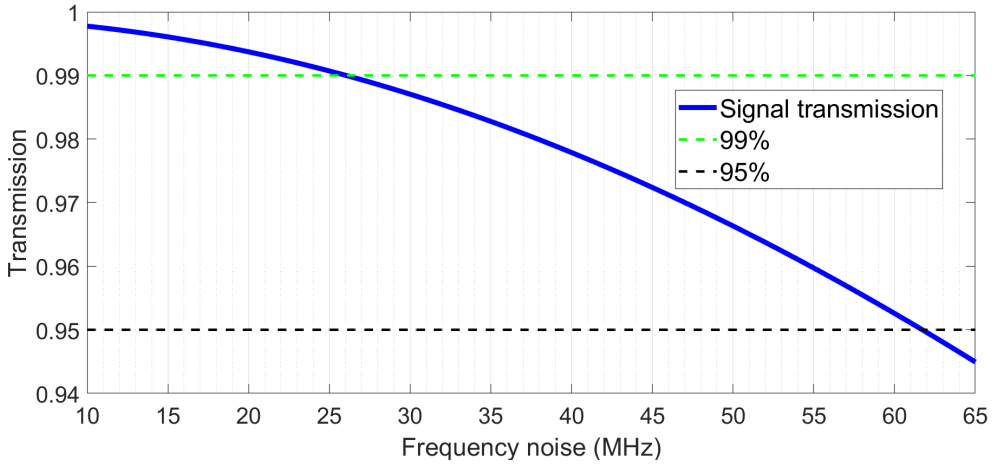

Figure 6.6 – Signal transmission in function of frequency noise for a finesse of 14.

6.2 Holder design and thermal stabilization elements

The previous study on temperature stability gave the tolerances to design the thermal control system.

6.2.1 Mechanical holder design

Here we describe the etalon mechanical design and realization, performed with the help of the APC mechanical department. The strategy for scanning and stabilizing the etalon temperature to find the working condition is to use a Peltier element (thermoelectric cooler). We decided to design a mechanical holder with the Peltier element glued at its top. The topology of the holder should ensure good thermal contact with the etalon. Indeed, when a temperature change is dictated by the Peltier element, the heat from the Peltier element should be transferred homogeneously to the whole etalon.

As shown in Figure 6.7, the holder's main part (in grey) in contact with the etalon is designed so that the holder compresses all the lateral parts of the etalon. The position of the screws secures a good thermal contact between the etalon and the holder.

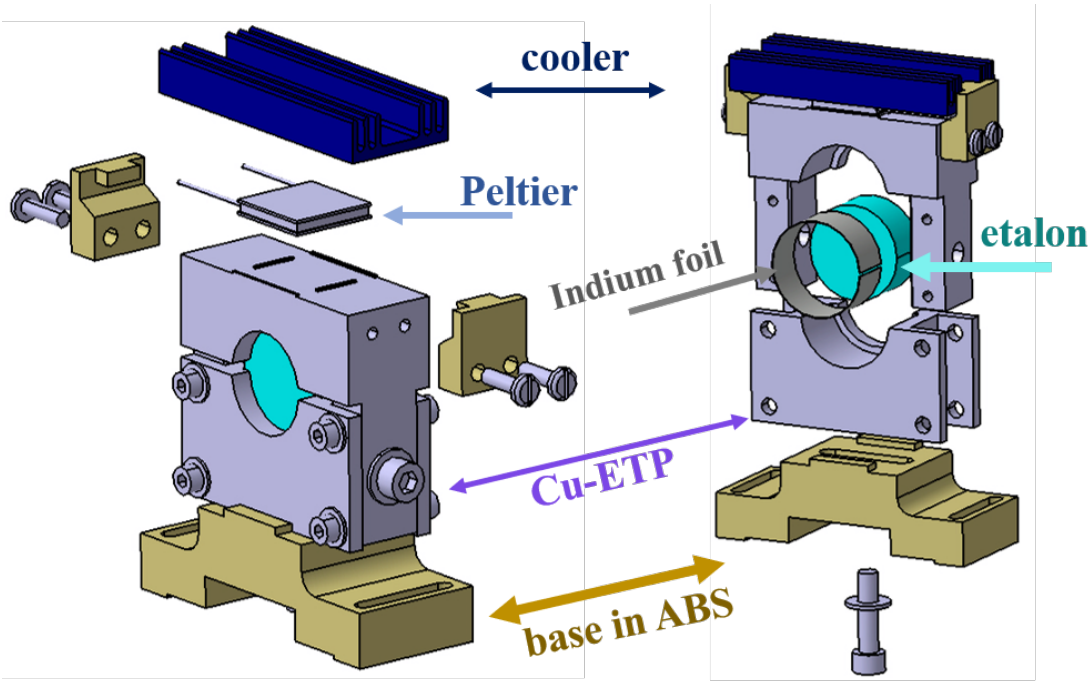

Figure 6.7 – Two exploded views of the mechanical design of the etalon holder. (Left) A Peltier element is glued on the top of the holder and a cooler is on top of it. (Right) An indium foil covers the etalon lateral side and then enables a good thermal contact between the etalon and the holder. The bottom part of the holder is in ABS to ensure no thermal cut-off between the optical table and the holder. Design of Jean-Pierre Baronick.

The holder main part is made with Copper Cu-a1 (French AFNOR norm) or Cu-ETP (European-equivalent norm), which is a copper containing oxygen (electrolytic copper) with a very high thermal conductivity of about $388\,\mathrm{WK^{-1}m^{-1}}$. An indium foil wraps the etalon lateral side, to ensure a good thermal contact with the holder. The bottom part of the holder (in yellow in the drawing) is in acrylonitrile butadiene styrene (ABS), a durable plastic for printing machines with good mechanical properties and which will prevent from thermal cut-off with the optical table where the etalon will be fixed. The technical drawing of

the mechanical holder is presented in Appendix B.

The requirements for the dimensioning of the etalon holder are the following:

- diameter of the etalon : 28 mm
- thickness of the indium foil : 0.2 mm
- height of the beam with respect to the bench : 62 mm
- size of the Peltier: 23×23 mm
- holes spacing on the bench: 25 mm

The grey part (the base, linking the grey part with the optical bench) was machined at the APC mechanical workshop and the part in yellow was machined with the APC printing machine.

A sensor (a thermistor) is glued on the holder main part with a thermal tape, to ensure that the holder's temperature is well representative of the one of the etalon, to guarantee a precise operation of the feedback loop.

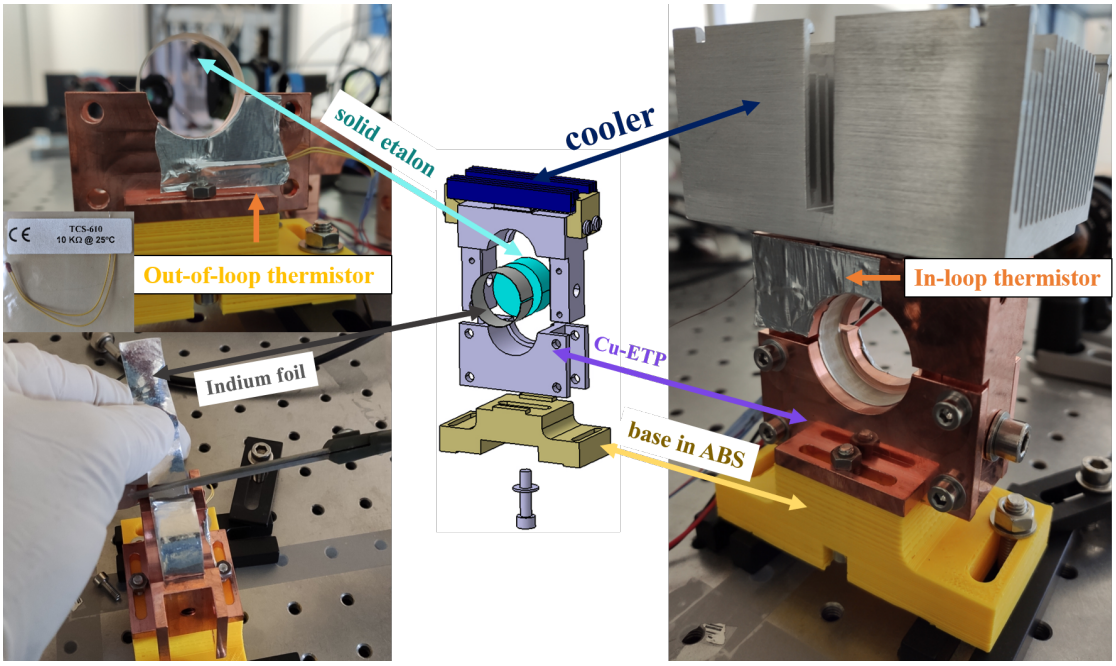

Figure 6.8 – Schematics of the mechanical design and photographs of the etalon in its holder, with the thermistor glued on the holder with thermal tape.

Figure 6.8 shows how the thermistors are fixed to the holder and the mechanical design corresponding to the real etalon with its machined holder. Two thermistors are used: an *in-loop thermistor* used in the PID control and an *out-of-loop thermistor* used as a temperature witness.

6.2.2 Temperature controlled system design

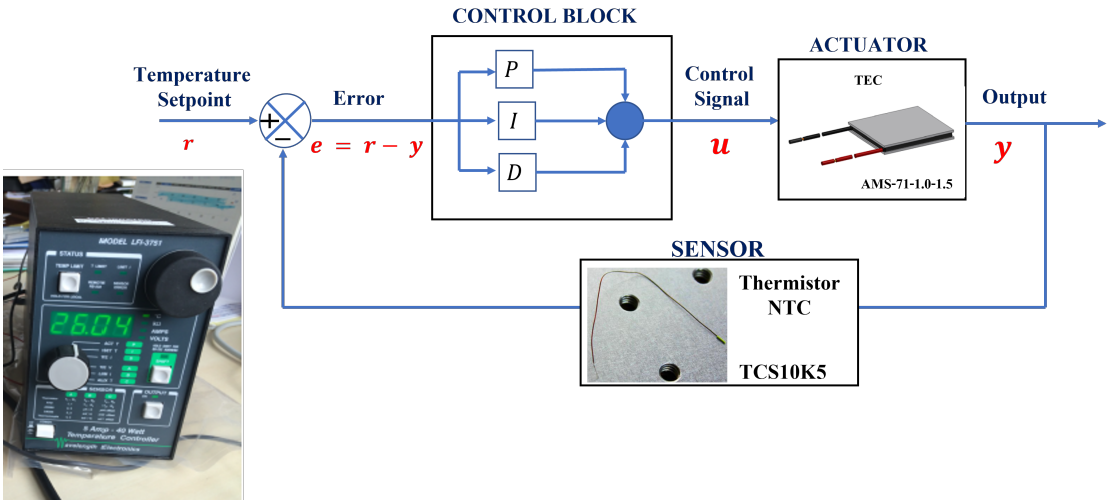

Figure 6.9 – Representation of the temperature feedback control system and photo of the temperature controller.

The temperature controlled system needed have to enable to scan enough range of temperature to find the working point and then, stabilize in a long-term duration (the duration needed to measure the squeezing first and then, to have a good duty-cycle) at this temperature with a maximum range of temperature fluctuations of $\pm 0.01\,°C$. Since the room temperature can change by a fraction of a degree or more, we need a feedback system, to keep the temperature of the etalon constant. The feedback system is represented in Figure 6.9, in a block diagram. $e = r - y$ is the *control error*, equal to the difference between the reference signal (or command signal or also called the *setpoint*) r and the output of the system y, u is the actuation command. There are three main components in such a system: the temperature sensor (we chose to use a thermistor, described in Section 6.2.2), the temperature controller (model LFI-3751 from Wavelength Electronics, described

Thermoelectric parameters	Value
I_{max} (Amps)	3,1
U_{max} (Volts)	8,8
ΔT_{max} (K)	69
Q_{max} (Watts)	16,7
Max. operating temperature (Â°C)	120
Ceramic material	Al_2O_3

Table 6.2 – Some parameters of the TEC AMS-71-1.0-1.5 from [75]

in Section 6.2.2) and a Peltier device (so-called thermoelectric cooler (TEC), described in Section 6.2.2).

Thermistor

A thermistor is a resistance thermometer, i.e. a resistance whose value proportionally depends on the temperature. Thermistors are ideal for our case, because they are very precise for temperature measurement (we need at least a precision of ± 0.01 °C), respond very well to changes in temperature (we need to scan a range of temperature equal to an etalon FSR) and when the temperature changes are not extreme. Indeed, a thermistor gives a high precision within a limited temperature range of about 50 °C [40] around the target temperature. The two model chosen are TCS10K5 (in-loop, for the PID system) and TCS610 (out-of-loop). Their resistance at 25 °C is equal to 10 kΩ.

Temperature controller

We chose the high-performance temperature controller *LFI-3751 with Autotune PID*, from Wavelength Electronics, as temperature controller. It can drive up to ±5 A and it ensures a linear stability of ± 0.001°C (which is ten times smaller than our requirement). We can implement heat and cool current limits and also high and low-temperature limits. These limits are useful for not damaging the Peltier during long-term utilization, which is our case and avoiding big temperature drifts.

Peltier device

A thermoelectric cooler (TEC) or Peltier device is a solid-state active heat pump, which, driven by an adapted current, transfers heat from one side of the device to the other side. Depending on the current direction, a TEC can be used for heating or cooling. The model AMS-71-1.0-1.5 from AMS Technologies is compliant with the requirements, some parameters are presented in Table 6.2. For example, I_{max} is under the maximum current that can drive the chosen thermal controller.

6.3 Thermal control system: PID description

6.3.1 Basics of PID Control

The proportional-integral-derivative or PID control is a very common type of control loop. The control law is described as follows [18]:

$$u = k_p e + k_i \int_0^1 e(\tau) d\tau + k_d \frac{de}{dt} = k_p \left(e + \frac{1}{T_i} \int_0^1 e(\tau) d\tau + T_d \frac{de}{dt} \right) \tag{6.19}$$

where $e = r - y$ is the *control error*, equal to the difference between the reference signal (or command signal or also *setpoint*) r and the output of the system y, u is the actuation command, k_p is the proportional gain, k_d is the derivative gain and T_i is the integral time constant.

6.3.2 PID description

Here below are explained the experimental meaning of each parameter, the tuning of them, as shown in Figure 6.9, will condition the resulting control signal. This control signal is a voltage (or intensity) sent to the TEC, to correct the temperature of the etalon.

The Proportional Gain P, in Amps Output Current per Volt Error Voltage, commands an output power which is proportional to the error voltage (difference between the LFI-3751's Setpoint and the measured voltage feedback from the

in-loop thermistor). However, when this Error Voltage drops to zero, this output power also is null. Consequently, the larger the P values, the closer the load to the set temperature will be settled but the greater the tendency to have temperature overshoot.

The Integrator Time Constant I, in seconds, "integrates" the error voltage over time. When the error voltage is high, i.e., the actual temperature is far from the setpoint temperature, the integrator charges more quickly while when the error voltages decrease to zero, the integrator charges less quickly. Finally, when the temperature is equal to the setpoint, the integrator only controls the output current at the necessary level to achieve a constant load temperature equal to the desired temperature. This enables to have less static error.

The Differentiator Time Constant D, also in seconds, compensates the tendency of P and I to cause the temperature overshoot, by using the derivative of the error voltage versus time. When the error voltage drops to zero, the proportional gain ("P") stops driving the output current to the TEC, leading the load's thermal inertia to overshoot the setpoint temperature. As the differentiator is proportional to the slope of the error voltage, it will force more the output current to reduce the changes in the error voltage when a load responds faster. Then, this enables to maintain a stable temperature, i.e. a zero slope even if the load's temperature is not at the setpoint. The differentiator's value should not be too high because it will likely counteract the proportional gain and integrator's action to move the load's temperature to the setpoint.

6.4 Experimental setup

The characterization of the whole etalon system (etalon installed in its mechanical holder with its thermal control system) has been done in a cleanroom of Class ISO 08 at the APC laboratory.

As depicted in Figure 6.10, a Nd:YAG at 1064 nm (a Mephisto S laser [31]) provides a p-polarized beam which is injected through the etalon. Before being injected, the beam is going through a PBS, then a QWP. If the beam is reflected back by the etalon, it will undergo a second time through the same QWP and become s-polarized. This beam will arrive back to the PBS reflecting this beam

in the "reflection detection arm." If the beam is transmitted by the etalon, it will go through a second QWP that will turn the polarization from circular to linear. For each detection arm, the beam is detected by a photodiode and also imaged by a camera.

6.4.1 Alignment and beam size adjustment procedure

The beam parameter was checked with a GaussianBeam simulation, depicted in Figure 6.11, to place the lens at the adapted position, so that the beam is collimated when arriving on the etalon. GaussianBeam is described in Section 5.4.2. The size of the beam is chosen, to be higher than the minimum waist equal to $\sim 340\,\mu m$. Indeed, the manufacturer ensures a reflectivity higher than 95% if the incident beam has a full beam divergence smaller ≤ 1 mrad, which gives the specification on the minimum beam waist. The simulation on GaussianBeam gives a waist of $\sim 600\,\mu m$ at the etalon position, this waist is also chosen to be smaller than the 1-inch optics, photodiode sensitive area and camera that are used on the bench.

The procedure for the alignment of the etalon is the following. First, the beam should be roughly aligned on the etalon path (parallel to the optical bench and no big incidence angle with respect to the etalon). We then send a ramp to the laser controller (this step will be described in the next section), to scan the laser frequency and be able to visualize on the oscilloscope, the transmission and reflection curves, acquired by the two photodiodes (PD_{trans} and PD_{refl}). Our goal is to achieve the highest transmission peak and the highest level for the reflection curve when being off-resonant.

The iris (shown on the scheme of the experimental setup) should be opened very slightly, so the beam can pass and the reflected beam from the etalon, if not perfectly aligned, can be seen on the mount of the iris (near the aperture of the iris). Then, with an IR viewer to better visualize the two spots (incident and reflected beam) on the iris, we search for this reflected beam and:

1. we use the steering mirror STR_2 (the closest to the etalon) to overlap the incident beam with this reflected beam, so that the transmitted beam and

the reflected beam only pass through the iris small aperture.

2. when doing so, the transmitted peak power will drop and we will retrieve it (and increase it) by acting on the steering mirror STR_1 (the farthest from the etalon).

After doing that, we check again by looking with the IR viewer, at the iris holder if the two beams are still overlapped and we can repeat steps 1 and 2 until the transmitted beam is overlapped with the reflected beam. Note that one should check the alignment of the transmitted beam, on PD_trans and PD_refl at each step 1 and 2, to visualize the transmission and reflection curves correctly (on the oscilloscope) at every time that we are moving the steering mirrors. Indeed, by moving them, the transmitted beam will no longer be well-aligned inside the corresponding photodiode. We have to ensure that, when being at a resonance frequency (respectively at anti-resonance frequency), the transmitted beam (respectively the reflected beam) is in fundamental mode, by looking at the corresponding camera. When the alignment is done, placing an external photodiode before and after the etalon, we then checked the transmitted power (with respect to the incident power) and the reflected power. This measure is described in the next section.

6.5 Experimental results: optical characterization

The experimental results will be divided into two categories: optical characterization and thermal stabilization. The optical characterization aims are to evaluate the separation power of the etalon and the conservation of the TEM_{00} mode for both transmitted and reflected beams. The thermal stabilization part aims to evaluate the thermal stabilization efficiency to keep the cavity in resonance with the laser light.

The optical characterization is separated into two parts. The first is the determination of the etalon finesse and the evaluation of the transmission (at the resonance) and reflection (at the anti-resonance). As already mentioned, the two EPR-entangled beams, separated by the etalon will be separately detected by two different homodyne detectors, as depicted in Figure 5.8.

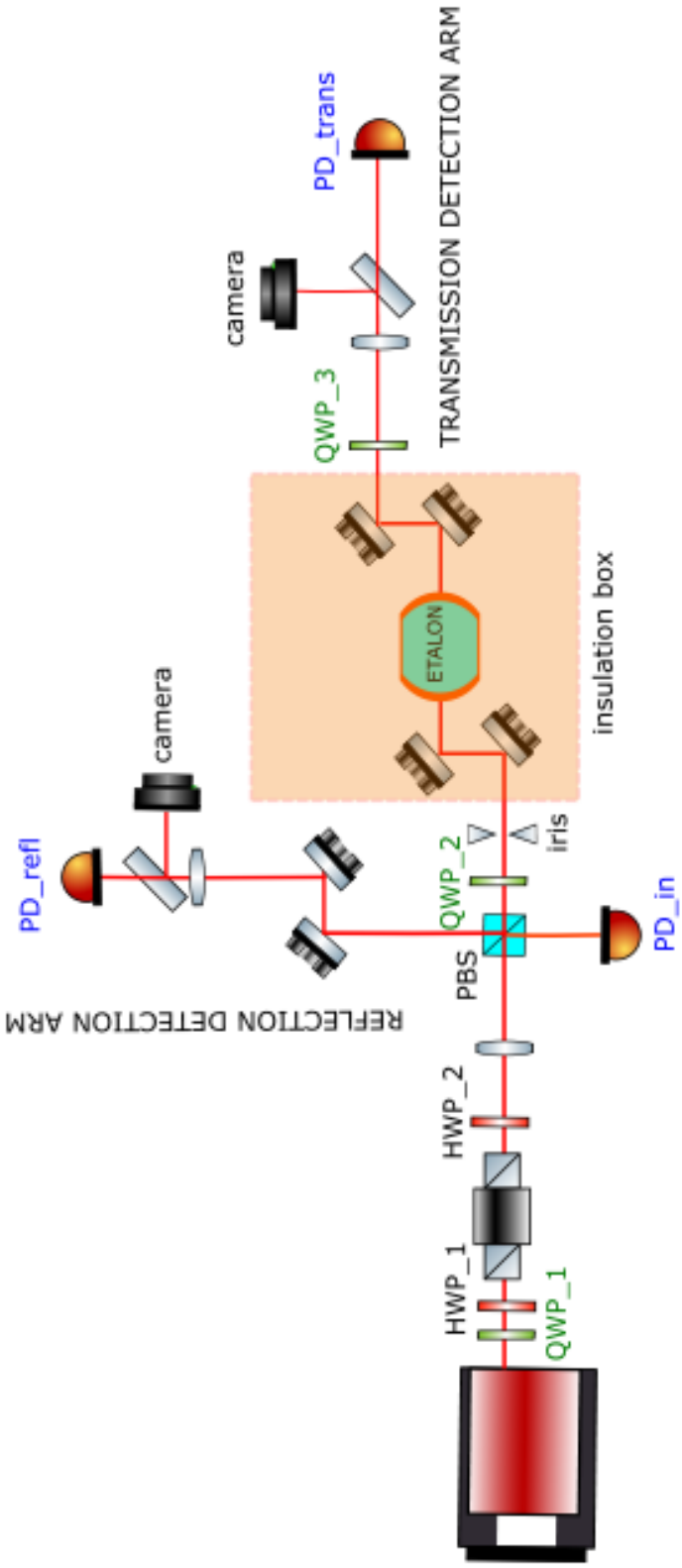

Figure 6.10 – Schematics of the characterization bench for etalon tests.

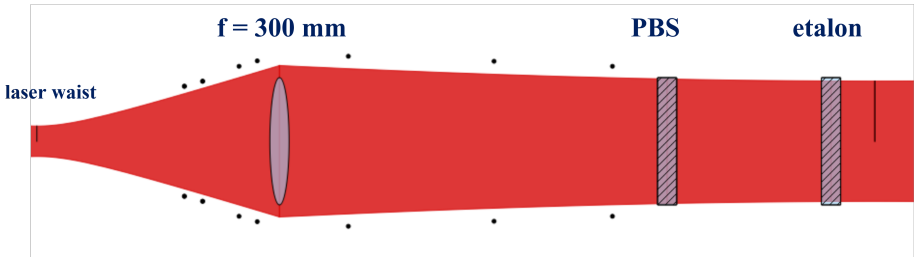

Figure 6.11 – GaussianBeam simulation of the laser beam parameter from the laser to the etalon. The black dots are the measures taken from the beam profiler at the corresponding position.

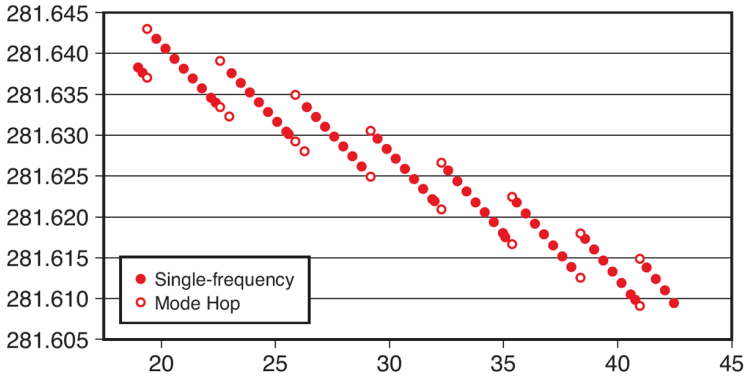

Figure 6.12 – Frequency of the Mephisto laser in function of its temperature, from [31].

The second part of the optical characterization is the measurement of the overlap integral between the measured transmitted and reflected mode and a Gaussian beam. In fact, in the homodyne detection, the signal and idler beams should overlap with the LO and the detection is degraded if the beams separated by the etalon are no longer TEM_{00} modes.

6.5.1 Finesse and efficiency

To measure the finesse of the etalon experimentally, we acquire PD_trans and PD_refl while scanning the laser frequency in a range where the etalon is resonant and off-resonant, through a scan in temperature of the laser crystal and then we perform a fit of the transmitted power.

The data of the curve, provided by the Coherent team, in Figure 6.12 enables

to convert laser temperature value into laser frequency.

To scan the laser temperature a ramp is sent to the laser controller. Preliminary measurements were done to verify the conversion between the voltage sent to the laser controller and the temperature change of the laser. The conversion was found equal to 0.92 °C per volt, similar to what indicated by the datasheet of the laser (1 °C per volt).

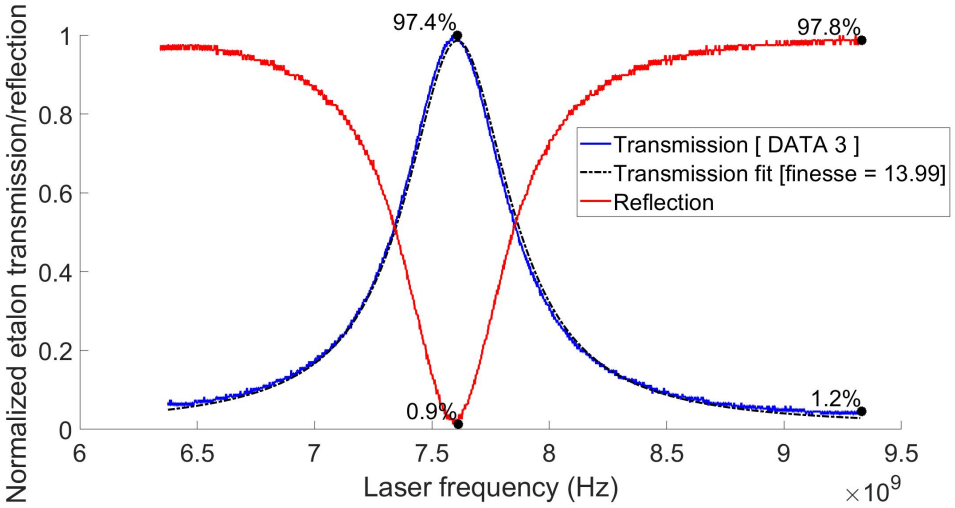

Figure 6.13 – Normalized transmission and reflection vs. frequency from DATA 3: etalon transmission curve (blue) along with its fit curve (black-dotted), etalon reflection curve (red) and the transmission and reflection values at resonance and anti-resonance.

A typical curve obtained during the scan is shown by Figure 6.13, where the y-axis is normalized to 1 (the maximum transmission and reflection) and the laser temperature is converted into frequency. The normalization of the transmission beam is done by measuring several times, with the same external photodiodes, the amplitude of the beam just before the etalon and the one of the beam right after the etalon. For the reflection part, the reflected beam power can only be measured after the PBS (in the reflection arm). To subtract the losses of the path from the etalon to the PBS (losses from the steering mirrors, QWP_2 and the PBS), a mirror is placed just before the etalon, so that the propagation losses can be estimated. Then, it is possible to normalize the reflected beam power. At the resonance condition, the transmission is equal to 97.4% while the reflection is

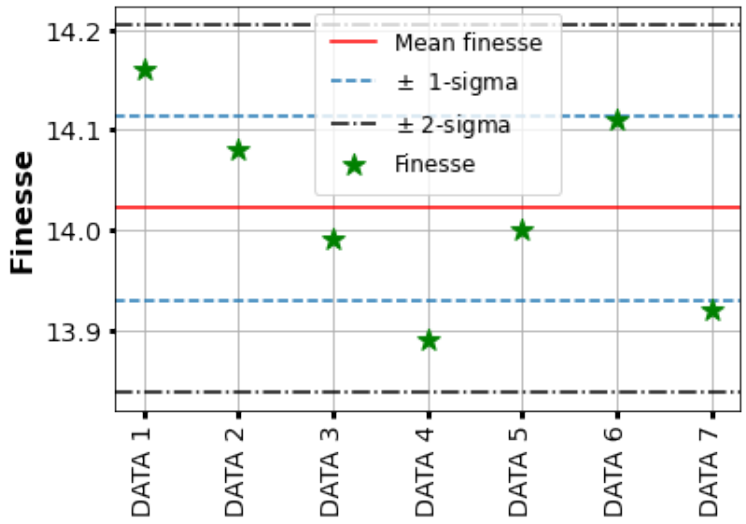

Figure 6.14 – Plot of 7 different fits of finesse along with its statistic mean equal to 14.02, its 1-sigma and 2-sigma intervals.

equal to 0.9%. At the anti-resonance condition, the transmission is equal to 1.2% while the reflection is equal to 97.8%. These values meet our specifications of having more than 95% for signal transmission and idler reflection.

According to Figure 6.14, the measured finesse is 14.02 with a standard deviation (calculated from the 7 data) of ±0.08, the finesse quoted by the manufacturer being inside this interval.

6.5.2 Overlap integral

Figures 6.15, 6.16 and 6.17 (left) show the images of the input, transmitted and reflected field from the etalon. We notice some interference fringes, probably made by some optical components on the beam path. It was not possible to remove these fringes optically for lack of time. However, it was possible to remove offline these fringes by applying a low-pass filter to the FFT of each image but we notice that the calculated overlap integral (explained later) are the same, with or without these fringes. The figures at the right side are the corresponding fit of each image with a TEM_{00} intensity profile.

We use an *intensity overlap integral* to measure the purity of the transmitted and reflected modes. The overlap integral is made with a perfect TEM_{00} beam

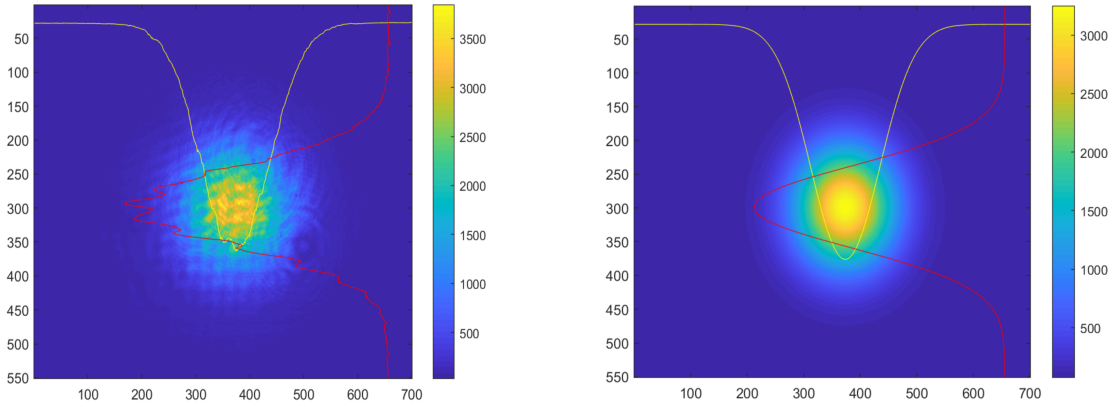

Figure 6.15 – (Left) Image of the input beam captured by the beam profiler at about 75 mm before the etalon, plotted along with its averaged horizontal and vertical profiles (scaled to fit in the picture). (Right) Fit of the input beam with a TEM_{00} intensity profile, plotted along with the averaged horizontal and vertical profiles.

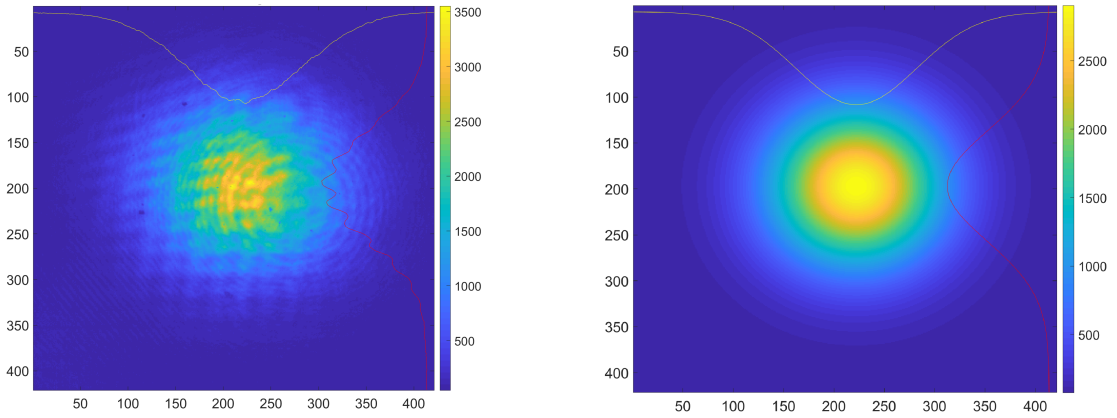

Figure 6.16 – (Left) Image of the transmitted beam captured by the beam profiler at about 75 mm after the etalon, plotted along with its averaged horizontal and vertical profiles (scaled to fit in the picture). (Right) Fit of the transmitted beam with a TEM_{00} intensity profile, plotted along with the averaged horizontal and vertical profiles.

which has the same radius of the measured field, and which is defined as:

$$\gamma_{mes,th} = \frac{(\iint I_{mes} \times I_{theory}) dS}{\sqrt{\iint {I_{mes}}^2 dS} \times \sqrt{\iint {I_{theory}}^2 dS}} \tag{6.20}$$

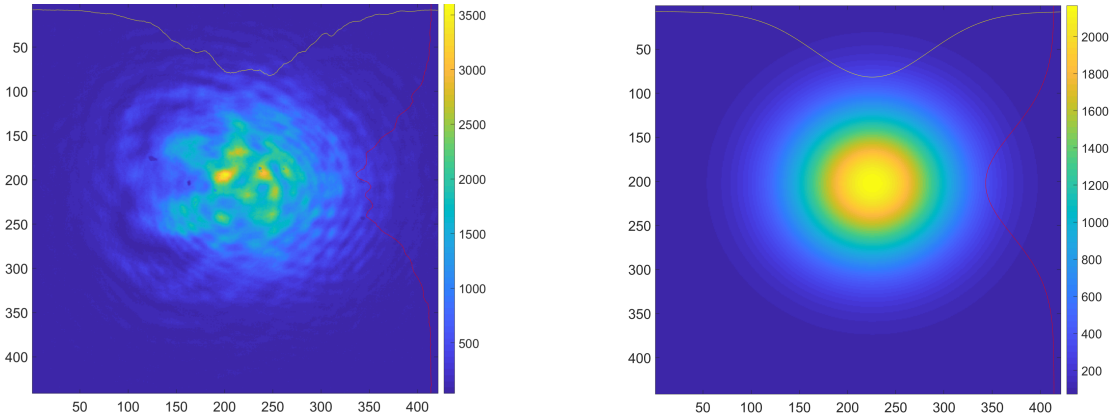

Figure 6.17 – (Left) Image of the reflected beam captured by the beam profiler at about 450 mm in the reflected path of the etalon, plotted along with its averaged horizontal and vertical profiles (scaled to fit in the picture). (Right) Fit of the reflected beam with a TEM_{00} intensity profile, plotted along with the averaged horizontal and vertical profiles.

where I_{mes} is the transverse intensity distribution acquired by a beam profiler camera, I_{theory} is the numerical fit (nonlinear curve-fitting in least-squares sense) of the transverse intensity distribution of the image from the beam profiler with a perfect Gaussian intensity distribution and dS is the infinitesimal surface element. In reality, the complete formula for the overlap integral is expressed as:

$$\eta = \frac{\left|\iint E^*_{mes} E_{theory}\right|^2 dS}{\iint |E_{mes}|^2 \iint \left|E_{theory}\right|^2 dS}, \tag{6.21}$$

where E_{mes} and E_{theory} are the complex electric fields, referring respectively, in our case, to the laser beam acquired by our beam profiler and the corresponding perfect Gaussian beam, and the integration is done for the whole beam cross-section. This formula takes into account the phase and the intensity of the laser beam whereas the equation 6.20 is an approximated formula and only uses the beams' intensity. Indeed, it is more complex to measure the phase of a laser beam as it cannot be measured by a beam profiler but requires a wavefront sensing device. Since the phase is neglected, $\gamma_{mes,th}$ is an upper limit of the mode purity of the measured beam. The numerical integration for the Equation 6.20

becomes:

$$\gamma_{mes,th} = \frac{\sum_{x=1}^{n}\sum_{y=1}^{m} I_{mes}(x,y)I_{th}(x,y)\Delta x\Delta y}{\sqrt{\sum_{x=1}^{n}\sum_{y=1}^{m} I_{mes}^2(x,y)\Delta x\Delta y}\sqrt{\sum_{x=1}^{n}\sum_{y=1}^{m} I_{th}^2(x,y)\Delta x\Delta y}} \tag{6.22}$$

where I_{mes} is the image from the beam profiler with the size $n \times m$ pixels, x and y are the indexes in the horizontal and vertical direction, Δx and Δy are the increment steps in respectively the horizontal and vertical direction and are equal to the size of one pixel. I_{th} is the fit image resulting from the function *lsqcurvefit* from the *Optimization Toolbox* of MATLAB. The nonlinear function to fit is:

$$F(X,Y) = a + be^{-2\frac{(X-c)^2+(Y-d)^2}{\sigma^2}}$$

where a is the intensity offset, b is the intensity normalization coefficient, c and d are the shift of the intensity peak for the vertical and horizontal direction and σ is the Full-Width at Half Maximum (FWHM) of the function and is proportional to the radius of the beam with $radius = \frac{FWHM}{\sqrt{2\ln 2}}$.

The resulting overlap integral is equal to 99.2% for the incident beam, 99.3% for the transmitted beam and 96.9% for the reflected beam. The result for the reflected beam is slightly worse than the other results, which may come from a residual tilt angle of the incidence beam.

6.6 Thermal stabilization

6.6.1 Temperature setting and performances of the thermal stabilization feedback

Tests were performed to evaluate our temperature controller performances and choose the PID experimentally to minimize the time needed for the etalon to be stabilized at the set temperature.

The chosen parameters are the following: $P = 60$, $I = 5$, $D = 40$. We proceed by starting the stabilization with only an arbitrary choice of P, which we tuned

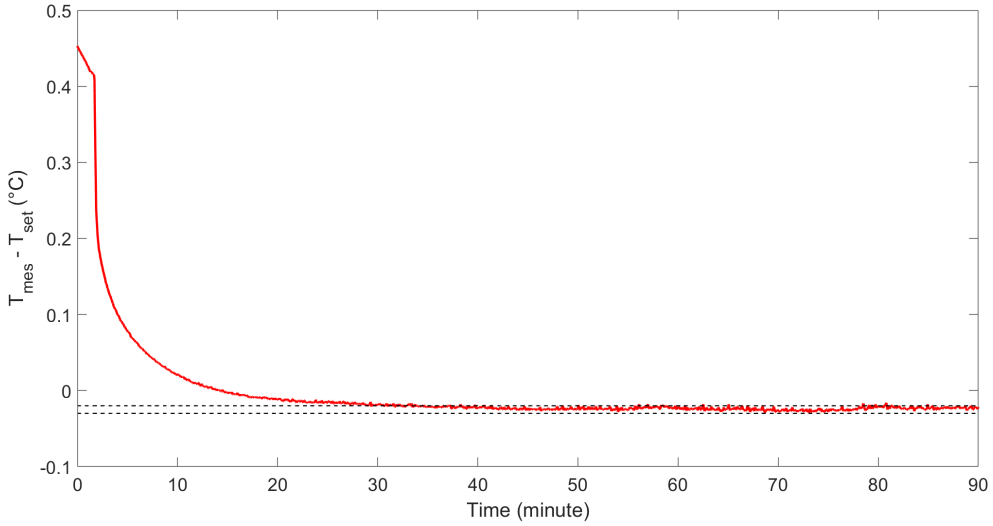

Figure 6.18 – Difference between the set temperature and the measured temperature depending on time (only the beginning of the stabilization is represented). The black-dotted lines represent the maximum fluctuations at ± 0.005 °C when the temperature is stabilized. The etalon was fixed on the optical bench and the measure lasted nearly three days. The figure only represents the first 90 minutes to show the stabilization better .

to have the smallest load to the set temperature possible. Then, we add the parameter I, then D and tune them as for the parameter P. Figure 6.18 shows the results of a nearly 3-day temperature stabilization, the etalon being fixed on the bench, in the cleanroom, with the laser off. The left figure represents the difference temperature between the set one and the measured one, only at the beginning of the stabilization. We can observe that the temperature is stabilized (at ± 0.005 °C) after less than one hour, as shown by Figure 6.18 where the temperature difference is between the two black-dotted lines. The statistical distribution, depicted in Figure 6.19 indicates that there is a fixed offset compared to the set temperature (-0.025 °C), which is not important for our purposes. The maximum temperature fluctuation is around ±0.005 °C on a 3-day time scale, which is smaller than our requirements.

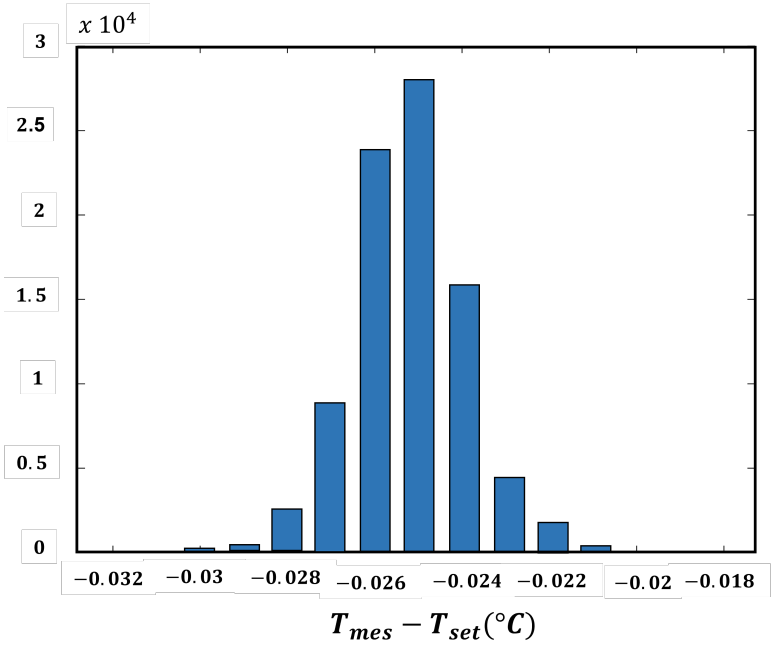

Figure 6.19 – Statistical distribution from the 3-day measurement, when the temperature is stabilized.

6.6.2 Etalon thermal stabilization tests

This long-term stabilization measurement is taken with the etalon in resonance condition, the temperature of the etalon is stabilized, the etalon and its four steering mirrors are placed inside an insulated box, as shown in Figure 6.10. The insulated box is a polystyrene box, covered with a survival blanket. The measurement is done in a period of more than 22 hours with the acquisition of the incident, transmission and reflection voltages, the room temperature, the temperature inside the insulated box, the in-loop and out-of-loop temperature . The *Agilent 34970A Data Logger Switch Unit* acquires the three photodiodes (reference: Thorlabs PDA36A-EC, Si Amplified Detector) PD_{trans}, PD_{refl} and PD_{in} and the sampling rate is 0.1 Hz. This data logger also acquires the temperatures from the out-of-loop thermistor and the room temperature thermistor. The temperature controller acquires the temperatures from the in-loop thermistor for the PID stabilization and the thermistor placed inside the insulated box, with a sampling rate of 0.2 Hz.

Results: transmission evolution

In Figure 6.20, we can observe that the transmission fluctuations follow the fluctuations of the incident power. To get rid of the effect of laser intensity fluctuations, the transmission function is calculated as follows:

$$T_{cav} = \frac{\frac{V_{trans}}{V_{inc}}}{MAX(\frac{V_{trans}}{V_{inc}})}, \tag{6.23}$$

where V_{trans} and V_{inc} are respectively the transmission and the incident voltages and MAX is the maximum. T_{cav} is then the transmission function whose values are between 0 and 1 and is shown by Figure 6.21. To measure the incident power, the $HWP2$ is tuned so that there is enough s-polarized beam power that is reflected by the PBS and detected by PD_{in}.

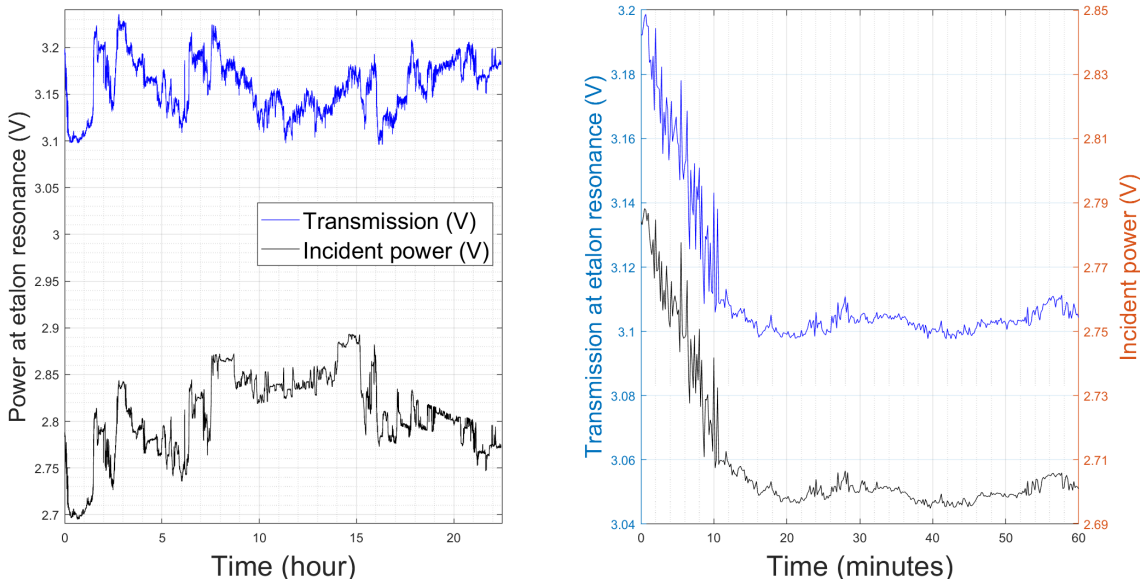

Figure 6.20 – More than 22 hours of acquisition of the transmission and a fraction of the incident power voltages, from the PD_{trans} and PD_{refl} (left) and a zoom on a 1-hour period (right). The transmission fluctuations are mostly due to the input laser intensity fluctuations.

The variations in the transmission curve seem to follow a cycle, the transmission is decreasing the first 15 hours and is dropping to 95% (as seen in Figure 6.21 or by the three last plots of Figure 6.22) and then, it increases to

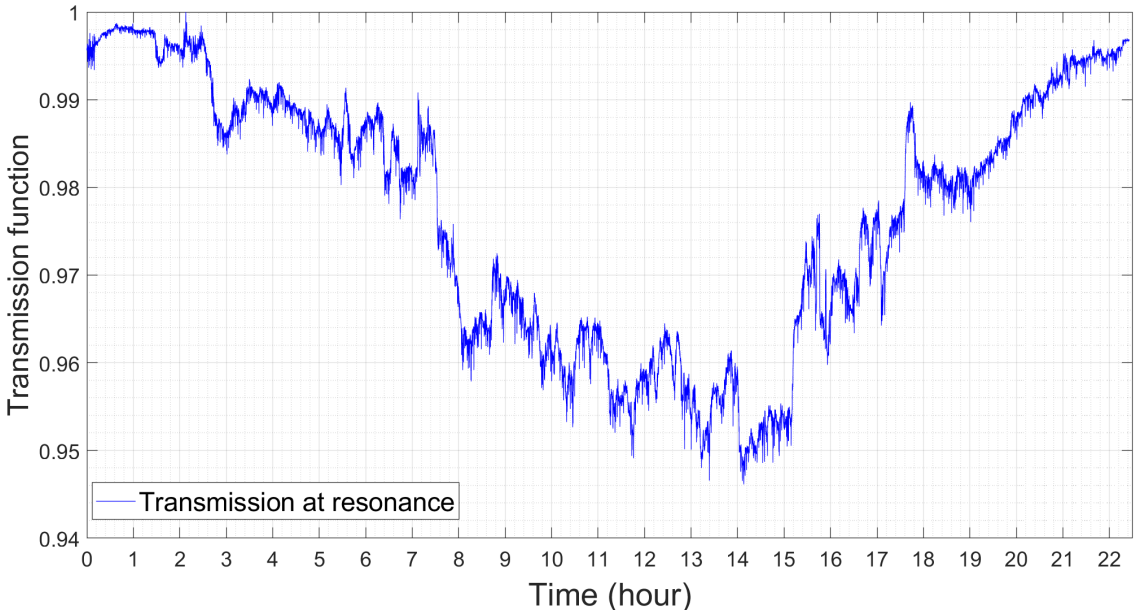

Figure 6.21 – More than 22-hour acquisition of the transmission function (transmission power normalized with the incident power) with the etalon in resonance condition.

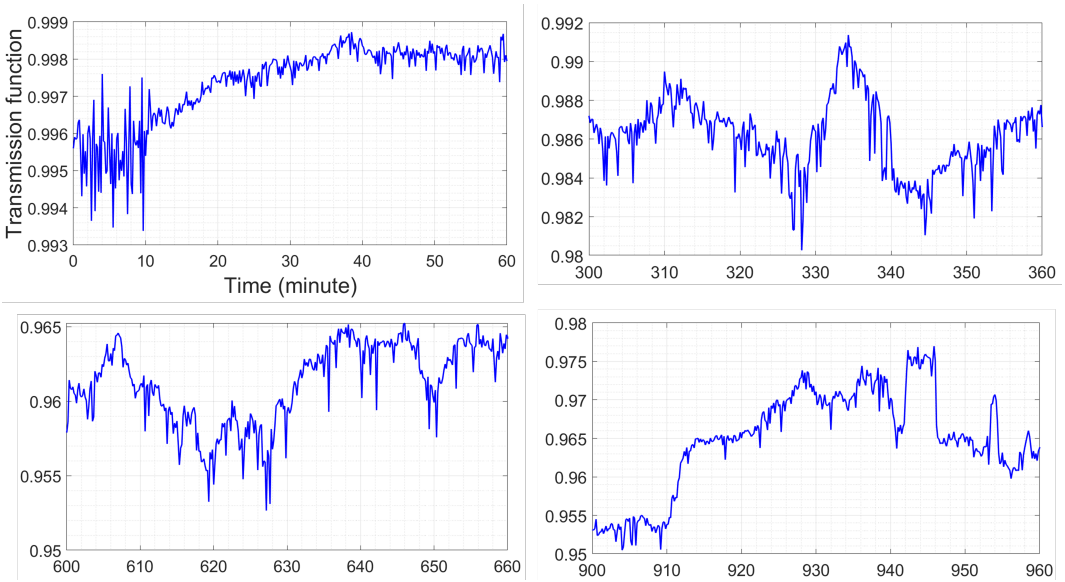

Figure 6.22 – Zoom of Figure 6.21 in a smaller time-scale: from 0 to 1 hour (top left); from 5 to 6 hours (top right); from 10 to 11 hours (bottom left) and from 15 to 16 hours (bottom right).

reach more than 99% of transmission again. The transmission stays at higher than > 95% in a one-day period. Moreover, the reflection (which is not plotted) is never higher than 2% during the whole measurement period.

6.6.3 Results: temperatures evolution

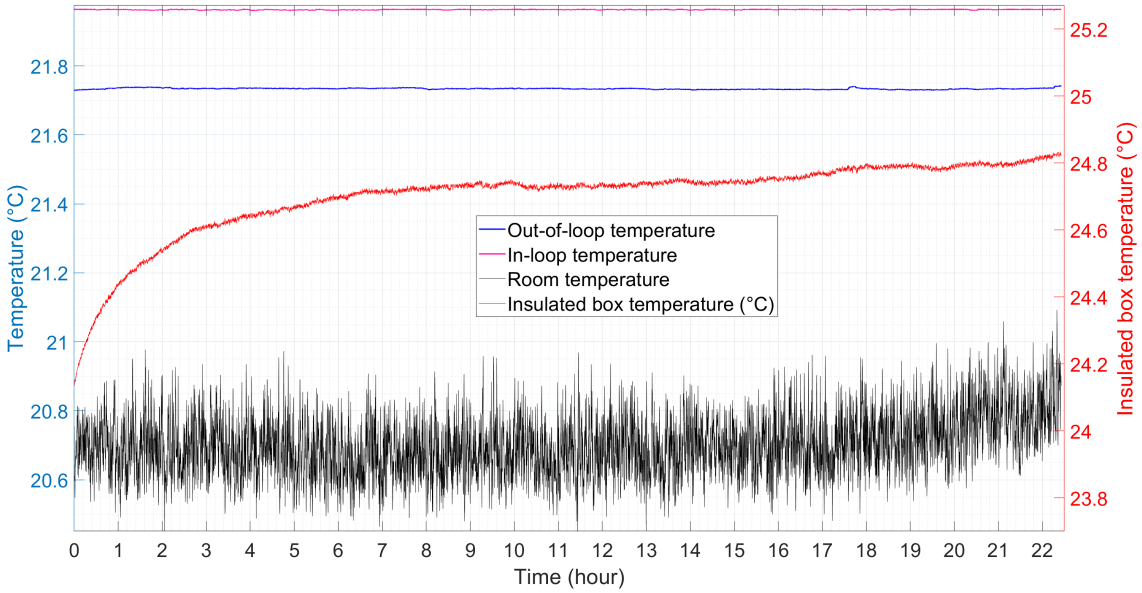

Figure 6.23 – Evolution of the different acquired temperature on more than 22 hours: in-loop (pink) and out-of-loop (blue) temperatures, room temperature (black) and insulated box (red).

The *Agilent 34970A Data Logger Switch Unit* acquires the temperatures from the out-of-loop thermistor and the room temperature thermistor. The temperature controller acquires the temperatures from the in-loop thermistor and the one placed inside the insulated box. In Figure 6.23 (left), the evolution on a 22-hour period of the four temperatures is plotted. The fluctuations in 22 hours for the in-loop and out-of-loop temperature are respectively ±0.0025 °C and ±0.007 °C. The in-loop temperature and insulated box data are down-sampled, to have the same sampling for the four temperature curves. We can observe that the in-loop and out-of-loop are very stable compared to the room temperature and the insulated box temperature and the zoom in a 1-hour period, depicted in Figure 6.25, shows that their fluctuations are respectively ± 0.0005 °C and

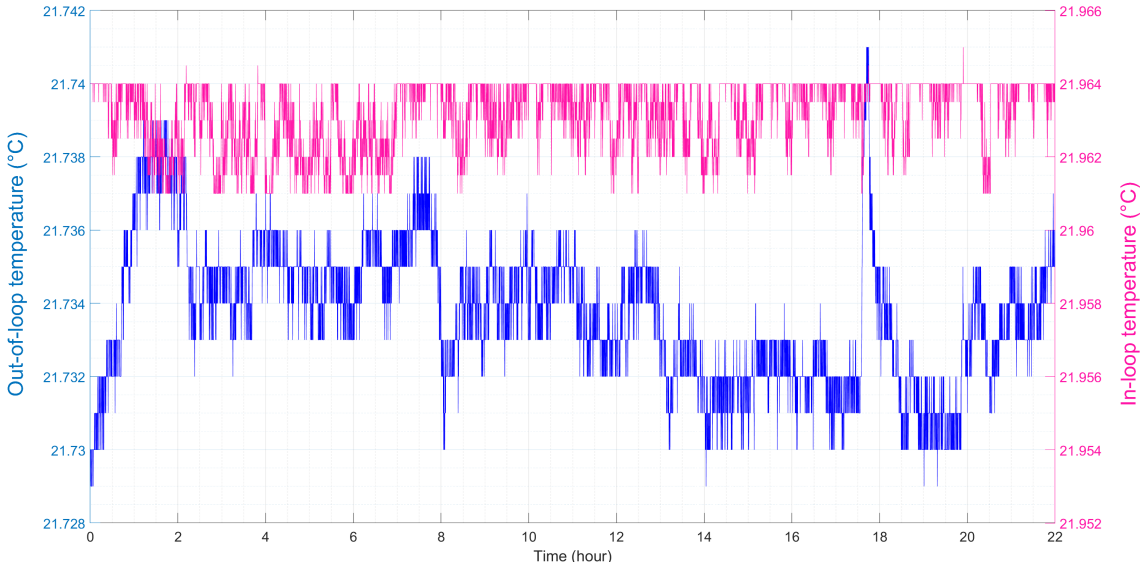

Figure 6.24 – 2 curves from Figure 6.23: in-loop (pink) and out-of-loop (blue) temperatures. Note that the two y-axes are shifted towards each other but the scale is the same.

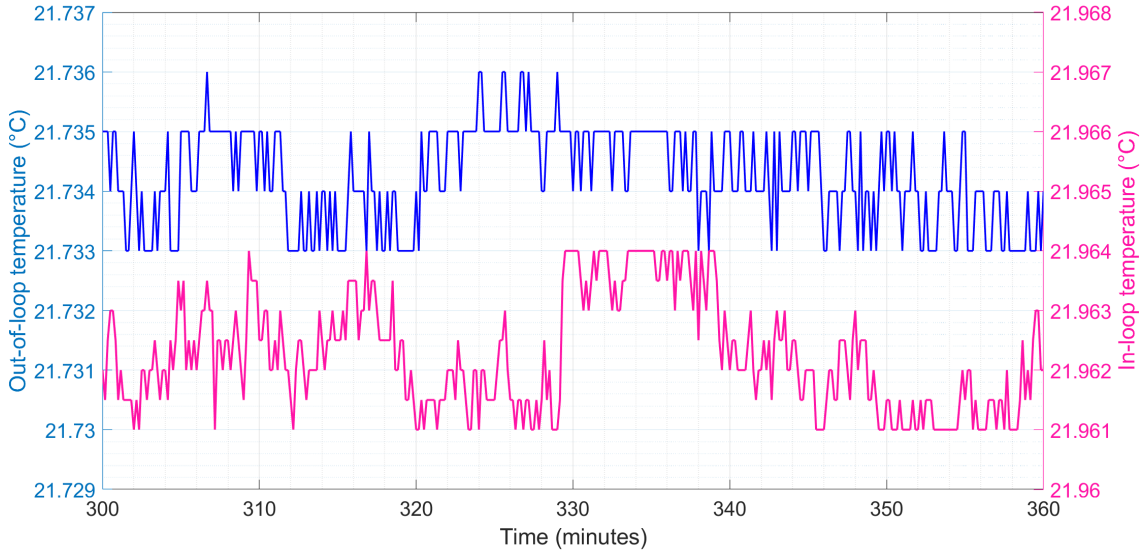

Figure 6.25 – Zoom in a 1-hour period for the in-loop and out-of-loop temperatures, to see the fluctuations. Note that the two y-axes are shifted towards each other but the scale is the same.

0.001 °C. The use of the insulated box reduces the temperature fluctuations of the in-loop temperature by a factor of 100, if we compare with Figure 6.18. We

could have tested more precise thermistors to investigate the numerical noise but we could not because of lack of time and also because the precision already obtained is sufficient.
Moreover, all the thermistors, except the one for the in-loop temperature (the model TCS10K5), are of the model TCS610. Thus, the big fluctuations in the room temperature cannot be caused by the difference in thermistors performances. They are certainly due to the room temperature itself and not from the numerical noises of the thermistor. Concerning the insulated box temperature, there is an increase of around 0.3 °C during the first five hours and after that, the temperature slightly increases. The use of the insulated box then increases the temperature inside it during the first hours.

6.6.4 Performances of the stabilization tests: discussion

The long-term stabilization measurement shows that the signal transmission can be kept higher than 95% during at least one day. The temperature, measured with an out-of-loop sensor was stable at 0.001 °*C* on 22-hour and five times better on a 1-hour period. The conclusion is that the evolution of the transmission signal cannot be explained only by a change of length in the etalon but there are other factors (alignment drifts or change in the frequency of the laser higher than expected).

From these tests we can conclude that our etalon is ready to be integrated into the EPR experiment, the tests validated the performances of the thermal stabilization.

6.7 Conclusion of the chapter

We designed and acquired a separation cavity for the EPR experiment, based on a Fabry-Perot etalon. The whole system was installed in a characterization setup in cleanroom to test its optical properties and its thermal stabilization system. A finesse of 14 ± 0.08 and an overlap integral $> 97\%$ for the transmitted and reflected beam were determined. These results guarantee respectively a good beam separation and a reasonable level of losses for homodyne measurements.

The transmission of the signal and reflection of the idler are almost equal to 98%, which meets our specification of 95%. This will guarantee to reduce losses due to readout loss for the production of EPR squeezing. The short-term and long-term stability of the temperature controlled system shows temperature fluctuations around ± 0.0005 °C on a 1-hour time scale and 0.0025 °C on a 22-hour time scale. This is respectively 20 times and four times smaller than the requirement. The stabilization on a 1-hour and a 22-hour scale thus meets the requirement on the temperature fluctuations.

Summary

Quantum noise is one of the main sources of noise, limiting the sensitivity of current second-generation gravitational-wave detectors and squeezing is the least invasive technique to reduce it. Frequency-independent squeezing has been successfully injected into the Advanced LIGO and Advanced Virgo detectors and routinely used during the third observing run, which allowed to increase their detection rate respectively up to 50% and up to about 30%. This technique only reduces the high-frequency component of quantum noise, the shot noise. The side effect consisting in the increase of the radiation pressure noise was not detrimental until the end of the science run O3, since the technical noises dominated the sensitivity in this region of the detection band. However, ongoing improvements are reducing the technical noises, making the frequency-independent squeezing technique detrimental for the low frequencies of the detection band. Consequently, the implementation of a frequency-dependent squeezing technique with the use of a long filter cavity (285 m for Advanced Virgo+) was adopted, to obtain a broadband reduction of quantum noise. My work consisted in the development of an alternative technique for frequency-dependent squeezing, using Einstein-Podolsky-Rosen entanglement. The designed demonstrator will be tested for the first time on a small-scale suspended interferometer (SIPS) to reduce radiation pressure noise, in the same frequency band as the one of GW detectors. This is thus a further step towards the direct implementation of EPR squeezing into the current GW detectors.

The first part of my thesis was dedicated to the characterization and the operation of a complete frequency-independent squeezing bench, originally built to be compatible with the Advanced Virgo detector and installed in the *1500W* optical laboratory, at the European Gravitational Observatory. I have

participated in the characterization of the main components of the experiments and to the measurement and characterization of the squeezing. The measured squeezing level is −1.6 dB. Thanks to the measurement of the propagation losses (15.3%), it was possible to evaluate the level of produced squeezing, which is -2.5 dB. An older measurement of squeezing (done more than two years ago) gave an estimated produced squeezing level of -16.4 dB for a measured level of squeezing of -5.7 dB. The estimation of the produced squeezing was done using the same measured propagation losses and other estimated losses. The discrepancy between the past and present level of squeezing can be explained by the non-optimized alignment and the aging of the cavities. The experience gained by this preliminary work enables us to understand some critical parameters for the next experiment: the room temperature control must be better stabilized, the optical design should be done in a way to facilitate precise alignment and reduce optical losses. The experiment should be shut down regularly to avoid a decrease in performance due to the aging of the cavities.

Moreover, We tested a software based on finite-state machines (FSM), with a high degree of automation for the control of the cavities locking in this bench. Several cavities are needed to run a squeezing experiment. This was the first time that a real-time FSM-based software was tested in a squeezed vacuum source. The goal is to simplify the control system to allow less human intervention and minimize dead time, which translates into a higher GW detector *science mode*. The tests have shown that the squeezer can be running for more than 99.9% of the time.

The second part of my thesis is devoted to the realization of the complete optical design of the EPR demonstrator, which will be installed on the optical bench previously used for the frequency-independent squeezing experiment. Therefore, we tried to compromise between changing this bench as little as possible (since the EPR technique uses several components of the frequency-independent squeezing experiment) and optimize the design to have enough power for the auxiliary beams, essential to run the EPR experiment. Indeed, the first part on the bench, where the squeezing is generated, used the same components but in a different configuration. The difference is that instead of one squeezed vacuum beam generated, there are two entangled beams (at

different frequencies). Then, instead of directly detecting these beams with a homodyne detector as for the FIS technique, these entangled beams need to be injected inside a test cavity which mimics the interferometer arms, separated and detected by two different homodyne detectors. These differences double the number of auxiliary beams needed to run the EPR experiment. We first realized a complete optical design by minimizing the changes with respect to the former experiment. We realized that it was impossible to have enough power for some auxiliary beams, so we made a second optical design by keeping in mind the power budget and minimizing the changes with respect to the previous experiment. Using this last complete design, at the time of writing, we are installing the new experiment. The preparation of the vacuum chamber is ongoing, for the installation of the suspended interferometer, next to the optical bench.

In the last part of my thesis, I worked on the design and the tests of a new component for the EPR demonstrator. A solid etalon will be used as an optical resonator, to separate the two entangled beams produced by the EPR technique. Specifications have been estimated on the performance of this etalon (in transmission and reflection) and the performances required for the thermal stabilization, to not degrade the EPR squeezing produced significantly. The etalon should transmit at least a significant fraction of one of the beams and reflect a significant fraction of the other beam. These performances should be maintained over time, thanks to a passive control of the etalon length, using a temperature-controlled system. This etalon, its mechanical holder, and its temperature-control system have been tested on a dedicated characterization bench, in the APC optics laboratory. The optical characterization first consisted in evaluating the separation power by measuring the finesse, equal to 14 ± 0.08. This is in accordance with the finesse chosen and specified to the manufacturer. The transmission for one of the entangled fields and reflection for the other ones were also measured to be more than 98%. In a second phase, the performances of the thermal stabilization in a 1-hour scale and 1-day scale to maintain the etalon system at the working point were tested. In particular, the etalon must have temperature fluctuations less than $\pm$ 0.01 °C and the measurements showed that the temperature fluctuations are 4-20 times smaller than the requirements.

The tests carried out allow to conclude that the requirements are met in short and long-term duration and this etalon is thus ready to be integrated on the EPR demonstrator.

Inserting my work in a broader picture: the FIS experiment allowed me to acquire a crucial experience on squeezing generation within the Virgo Collaboration and obtain some "lessons learned" about the design of future squeezing experiments. Concerning the automation software, it was the first time this real-time finite-state machine based software is used and it can potentially be used for Virgo to improve the efficiency of the controls. These controls are required in all squeezing experiments. So, this work can then be used for the squeezing injection for future GW detectors as Einstein Telescope. The work on the EPR demonstrator is a step towards the test of this technique in a suspended prototype. Even if future detectors, as Einstein Telescope, plan to use filter cavities as a baseline, a demonstration of the feasibility of the EPR technique can open the way to a reconsideration of a less expensive and logistically simple alternative, especially since ET will be built underground.

Future development & perspectives

Due to the delay caused by the COVID pandemic, I could not take care of the complete installation of the EPR demonstrator as well as the integration of the etalon. The next step is thus the installation of this demonstrator on the optical bench housing the frequency-independent squeezing, keeping in mind all the lessons learned from this previous experiment, all the technical difficulties we encountered, to limit future technical problems we may encounter and to ensure a stable experiment during time. The next step is to generate the two entangled beams, inject them inside the test cavity, separate them with the etalon, and measure the squeezing level. Moreover, we should characterize the whole bench to understand the limiting factors. Then, we have to inject this EPR squeezing into the SIPS, which will be installed in a vacuum chamber next to the EPR squeezing bench, to quantify the reduction of the radiation pressure. Since the optical propagation losses are twice as high with EPR squeezing as with the technique using an external filter cavity, it would be interesting in a second time to change all the optical components (mirrors, lenses, beam-splitters, polarizing beam-splitters, retardation plates, mode-cleaners and homodyne detectors) to replace them by components with the lowest possible losses. An in-depth study of the scattered light losses of this demonstrator is also an interesting point to understand how to reduce these optical propagation losses.

Concerning the tests done on the etalon, it would be important to do more extensive tests to understand the effects of the misalignments of the incident beam and compare the results with simulations. Finally, with the integration of the etalon on the demonstration bench, the next step is to evaluate the degradation of the EPR squeezing due to the etalon itself.

Bibliography

[1] URL: https://lisa.nasa.gov/.

[2] URL: https://en.wikipedia.org/wiki/Squeezed%5C_states%5C_of%5C_light.

[3] "A gravitational wave observatory operating beyond the quantum shot-noise limit". *Nature Physics* 7.12 (Sept. 2011), pp. 962–965. DOI: 10.1038/nphys2083.

[4] J. Aasi et al. "Advanced LIGO". *Classical and Quantum Gravity* 32.7 (2015), p. 074001. DOI: 10.1088/0264-9381/32/7/074001.

[5] B. P. Abbott et al. "Gravitational Waves and Gamma-Rays from a Binary Neutron Star Merger: GW170817 and GRB 170817A". *The Astrophysical Journal* 848.2 (2017), p. L13. DOI: 10.3847/2041-8213/aa920c.

[6] B. P. Abbott et al. "GW170817: Observation of Gravitational Waves from a Binary Neutron Star Inspiral". *Phys. Rev. Lett.* 119 (16 2017), p. 161101. DOI: 10.1103/PhysRevLett.119.161101.

[7] B. P. Abbott et al. "GWTC-1: A Gravitational-Wave Transient Catalog of Compact Binary Mergers Observed by LIGO and Virgo during the First and Second Observing Runs". *Phys. Rev. X* 9 (3 2019), p. 031040. DOI: 10.1103/PhysRevX.9.031040.

[8] B. P. Abbott et al. "Multi-messenger Observations of a Binary Neutron Star Merger". *The Astrophysical Journal* 848.2 (2017), p. L12. DOI: 10.3847/2041-8213/aa91c9.

[9] B.P. Abbott et al. "GW170814: A Three-Detector Observation of Gravitational Waves from a Binary Black Hole Coalescence". *Phys. Rev. Lett.* 119 (14 2017), p. 141101. DOI: 10.1103/PhysRevLett.119.141101.

[10] B.P. Abbott et al. "Observation of Gravitational Waves from a Binary Black Hole Merger". *Phys. Rev. Lett.* 116 (6 2016), p. 061102. DOI: 10.1103/PhysRevLett.116.061102.

[11] R. Abbott et al. "GW190521: A Binary Black Hole Merger with a Total Mass of 150 M2299". *Physical Review Letters* 125.10 (2020). DOI: 10.1103/physrevlett.125.101102.

[12] R. Abbott et al. "GW190814: Gravitational Waves from the Coalescence of a 23 Solar Mass Black Hole with a 2.6 Solar Mass Compact Object". *The Astrophysical Journal* 896.2 (June 2020), p. L44. DOI: 10.3847/2041-8213/ab960f.

[13] F. Acernese et al. "Advanced Virgo: a second-generation interferometric gravitational wave detector". *Classical and Quantum Gravity* 32.2 (2014), p. 024001. DOI: 10.1088/0264-9381/32/2/024001.

[14] F. Acernese et al. "Increasing the Astrophysical Reach of the Advanced Virgo Detector via the Application of Squeezed Vacuum States of Light". *Physical Review Letters* 123.23 (2019), p. 231108.

[15] F. Acernese et al. "Quantum Backaction on kg-Scale Mirrors: Observation of Radiation Pressure Noise in the Advanced Virgo Detector". *Phys. Rev. Lett.* 125 (13 2020), p. 131101. DOI: 10.1103/PhysRevLett.125.131101.

[16] F. Acernese et al. "Status of Advanced Virgo". In: *6th International Conference on New Frontiers in Physics*. Vol. 182. Kolymbari, Greece, 2017, p. 02003. DOI: 10.1051/epjconf/201818202003.

[17] Alain Aspect and Michel Brune. *"Quantum Optics 2 - Two photons and more", Coursera online course*. https://www.coursera.org/learn/quantum-optics-two-photons/home/welcome.

[18] K. J. Astrom and R. M. Murray. *Feedback Systems - An Introduction for Scientists and Engineers*. Princeton University Press.

[19] Hans-A. Bachor and Timothy C. Ralph. *A Guide to Experiments in Quantum Optics*. WILEY-VCH, 2004.

[20] Jöran Bauchrowitz, Tobias Westphal, and Roman Schnabel. "A graphical description of optical parametric generation of squeezed states of light". *American Journal of Physics* 81.10 (Oct. 2013), pp. 767–771. DOI: 10.1119/1.4819195.

[21] Jacob L. Beckey et al. "Broadband quantum noise reduction in future long baseline gravitational-wave detectors via EPR entanglement". *Phys. Rev. D* 100 (8 Oct. 2019), p. 083011. DOI: 10.1103/PhysRevD.100.083011.

[22] Eric D. Black. "An introduction to Pound–Drever–Hall laser frequency stabilization". *American Journal of Physics* 69.1 (2001), pp. 79–87. DOI: 10.1119/1.1286663.

[23] Vincenzo Boccia. "Progettazione di una cavità per il test della rotatione dell'angolo di *Squeezing* EPR nei rivelatori di One Gravitazionali". PhD thesis. Università degli studi di Napoli "Federico II", 2020.

[24] Daniel D. Brown et al. "Broadband sensitivity enhancement of detuned dual-recycled Michelson interferometers with EPR entanglement". *Physical Review D* 96.6 (Sept. 2017). DOI: 10.1103/physrevd.96.062003.

[25] Buikema et al. "Sensitivity and performance of the Advanced LIGO detectors in the third observing run". *Physical Review D* 102.6 (2020). DOI: 10.1103/physrevd.102.062003.

[26] Alessandra Buonanno. *Gravitational waves*. 2006. arXiv: 0709.4682 [gr-qc].

[27] C. M. Caves. "Quantum-mechanical noise in an interferometer". *Phys. Rev. D* 23 (8 1981), pp. 1693–1708. DOI: 10.1103/PhysRevD.23.1693.

[28] Carlton M. Caves. "Quantum-Mechanical Radiation-Pressure Fluctuations in an Interferometer". *Phys. Rev. Lett.* 45 (2 July 1980), pp. 75–79. DOI: 10.1103/PhysRevLett.45.75.

[29] Carlton M. Caves and Bonny L. Schumaker. "New formalism for two-photon quantum optics. I. Quadrature phases and squeezed states". *Phys. Rev. A* 31 (5 May 1985), pp. 3068–3092. DOI: 10.1103/PhysRevA.31.3068.

[30] Yue-Meng Chi et al. "A balanced homodyne detector for high-rate Gaussian-modulated coherent-state quantum key distribution". *New Journal of Physics* 13.1 (2011), p. 013003. DOI: 10.1088/1367-2630/13/1/013003.

[31] COHERENT, ed. *Mephisto/Mephisto S datasheet*. https://www.coherent.com/assets/pdf/COHR_Mephisto_DS_0819_4.pdf.

[32] The LIGO Scientific Collaboration, the Virgo Collaboration, and the KAGRA Collaboration. *Prospects for Observing and Localizing Gravitational-Wave Transients with Advanced LIGO, Advanced Virgo and KAGRA*. 2013. arXiv: 1304.0670 [gr-qc].

[33] The Virgo Collaboration. "Advanced Virgo Technical Design Report" (2012).

[34] Virgo Collaboration. "Advanced Virgo Plus (AdV+) Design Report" (2019).

[35] Virgo Collaboration. "Advanced Virgo Technical Design Report" (2019).

[36] Stefan L. Danilishin and Farid Ya. Khalili. "Quantum Measurement Theory in Gravitational-Wave Detectors". *Living Reviews in Relativity* 15.1 (Apr. 2012). DOI: 10.12942/lrr-2012-5.

[37] Stefan L. Danilishin, Farid Ya. Khalili, and Haixing Miao. "Advanced quantum techniques for future gravitational-wave detectors". *Living Reviews in Relativity* 22.1 (Apr. 2019). DOI: 10.1007/s41114-019-0018-y.

[38] Matteo Di Leonardi. "Development of a squeezed light source prototype for Advanced Virgo". PhD thesis. University of Trento, 2016.

[39] Nicolas Dubreuil. *Chapter 1: Introduction to nonlinear optics*. Lecture Notes, pedagogical website of Institut d'Optique Graduate School - Libres savoirs.

[40] Wavelength Electronics. *"Thermistor Basics"*. Application Note AN-TC11 Rev.A.

[41] Donatella Fiorucci et al. "Impact of infrasound atmospheric noise on gravity detectors used for astrophysical and geophysical applications". *Physical Review D* 97.6 (2018). DOI: 10.1103/physrevd.97.062003.

[42] Barbara Garaventa. "Acousto-optic modulator test for the EPR experiment". *Internal Presentation for the EPR weekly meeting - VIR-0554A-21* (2020).

[43] *GaussianBeam project*. URL: http://gaussianbeam.sourceforge.net/.

[44] Christopher Gerry and Peter Knight. *Introductory Quantum Optics*. Cambridge University Press, 2004. DOI: 10.1017/CBO9780511791239.

[45] Laura Giacoppo et al. "Towards ponderomotive squeezing with SIPS experiment". *Physica Scripta* (2021).

[46] Alain Aspect Gilbert Grynberg and Claude Fabre. *Introduction to QUANTUM OPTICS. From the Semi-classical Approach to Quantized Light*. Cambridge University Press.

[47] M. Granata et al. "Progress in the measurement and reduction of thermal noise in optical coatings for gravitational-wave detectors". In: *Optical Interference Coatings Conference (OIC) 2019*. Optical Society of America, 2019, FA.1. DOI: 10.1364/OIC.2019.FA.1.

[48] H. Grote et al. "First Long-Term Application of Squeezed States of Light in a Gravitational-Wave Observatory". *Physical Review Letters* 110.18 (May 2013).

[49] *GW190412: Observation of a Binary-Black-Hole Coalescence with Asymmetric Masses*. Aug. 2020. DOI: 10.1103/PhysRevD.102.043015.

[50] Gregory M. Harry et al. "Thermal noise from optical coatings in gravitational wave detectors". *Appl. Opt.* 45.7 (2006), pp. 1569–1574. DOI: 10.1364/AO.45.001569.

[51] Alexander Khalaidovski. “Beyond the quantum limit: a squeezed-light laser in GEO600, PhD thesis”. PhD thesis. AEI Hannover, MPI for Gravitational Physics, Max Planck Society", 2011.

[52] Alexander Khalaidovski et al. “Long-term stable squeezed vacuum state of light for gravitational wave detectors”. *Classical and quantum gravity* 29.7 (2012), p. 075001.

[53] Imran Khan. “Squeezed states of light generation for Short Noise limited Interferometric measurements in the next generation of Gravitational Waves Detectors”. PhD thesis. 2019.

[54] H. J. Kimble et al. “Conversion of conventional gravitational-wave interferometers into quantum nondemolition interferometers by modifying their input and/or output optics”. *Physical Review D* 65.2 (Dec. 2001). DOI: 10.1103/physrevd.65.022002.

[55] P. Kwee et al. “Decoherence and degradation of squeezed states in quantum filter cavities”. *Physical Review D* 90.6 (Sept. 2014). DOI: 10.1103/physrevd.90.062006.

[56] Yiqiu Ma et al. “Proposal for gravitational-wave detection beyond the standard quantum limit through EPR entanglement”. *Nature Physics* 13.8 (2017), pp. 776–780.

[57] M. Maggiore et al. “Science case for the Einstein telescope”. *Journal of Cosmology and Astroparticle Physics* 2020.03 (Mar. 2020), pp. 050–050. DOI: 10.1088/1475-7516/2020/03/050.

[58] Michele Maggiore et al. “Science case for the Einstein telescope”. *Journal of Cosmology and Astroparticle Physics* 2020.03 (Mar. 2020), pp. 050–050. DOI: 10.1088/1475-7516/2020/03/050.

[59] D. McCarron. “A Guide to Acousto-Optic Modulators”. In: 2007.

[60] L. McCuller et al. “Frequency-Dependent Squeezing for Advanced LIGO”. *Phys. Rev. Lett.* 124 (17 Apr. 2020), p. 171102. DOI: 10.1103/PhysRevLett.124.171102.

[61] M Mehmet and H Vahlbruch. “High-efficiency squeezed light generation for gravitational wave detectors”. *Classical and Quantum Gravity* 36.1 (Dec. 2018), p. 015014. DOI: 10.1088/1361-6382/aaf448.

[62] C. Nguyen et al. “Automated source of squeezed vacuum states driven by finite state machine based software”. *Review of Scientific Instruments* 92.5 (2021), p. 054504.

[63] Sibilla Di Pace et al. "Small scale Suspended Interferometer for Ponderomotive Squeezing (SIPS) as test bench for EPR squeezer integration in Advanced Virgo". *Zenodo* (Jan. 2020). DOI: 10.5281/zenodo.3569196.

[64] Sibilla Di Pace et al. "Thermal noise study limited optical cavity with fused silica mirror suspensions". 74.227 (2020). DOI: 10.1140/epjd/e2020-10183-7.

[65] R. Paschotta. "acouto-optic modulators". *RP Photonics Encyclopedia* (2021).

[66] *RP Photonics Encyclopedia*. https://www.rp-photonics.com/electro_optic_modulators.html.

[67] B. S. Sathyaprakash and Bernard F. Schutz. "Physics, Astrophysics and Cosmology with Gravitational Waves". *Living Reviews in Relativity* 12.1 (2009). DOI: 10.12942/lrr-2009-2.

[68] Peter R. Saulson. *Fundamentals of interferometric gravitational wave detectors*. World Scientific, 1994.

[69] Roman Schnabel. "Squeezed states of light and their applications in laser interferometers". *Physics Reports* 684 (Apr. 2017), pp. 1–51. DOI: 10.1016/j.physrep.2017.04.001.

[70] Klaus Schneider et al. "1.1-W single-frequency 532-nm radiation by second-harmonic generation of a miniature Nd:YAG ring laser". *Opt. Lett.* 21.24 (Dec. 1996), pp. 1999–2001. DOI: 10.1364/OL.21.001999.

[71] Bonny L. Schumaker and Carlton M. Caves. "New formalism for two-photon quantum optics. II. Mathematical foundation and compact notation". *Phys. Rev. A* 31 (5 May 1985), pp. 3093–3111. DOI: 10.1103/PhysRevA.31.3093.

[72] V. Sequino et al. "EPR experiment for a broadband quantum noise reduction in gravitational wave detectors". In: *Proceedings of GRAvitational-waves Science&technology Symposium*. 2019. DOI: 10.5281/zenodo.3554320.

[73] Valeria Sequino. "Development of a squeezed light source for the gravitational wave detector Advanced Virgo". PhD thesis. Università degli studi di Roma "Tor Vergata", 2016.

[74] R. E. Slusher et al. "Observation of Squeezed States Generated by Four-Wave Mixing in an Optical Cavity". *Phys. Rev. Lett.* 55 (22 Nov. 1985), pp. 2409–2412. DOI: 10.1103/PhysRevLett.55.2409.

[75] *SPECIFICATION OF THERMOELECCTRIC MODULE AMS-71-1.0-1.5 (23 × 23) HT120 E L2 69K*. AMS Technologies.

[76] MS Stefszky et al. "Balanced homodyne detection of optical quantum states at audio-band frequencies and below". *Classical and Quantum Gravity* 29.14 (2012), p. 145015.

[77] Jan Südbeck et al. "Demonstration of interferometer enhancement through Einstein–Podolsky–Rosen entanglement". *Nature Photonics* 14.4 (Feb. 2020), pp. 240–244. DOI: 10.1038/s41566-019-0583-3.

[78] Yuishi Takeno et al. "Observation of -9 dB quadrature squeezing with improvement of phase stability in homodyne measurement". *Opt. Express* 15.7 (Apr. 2007), pp. 4321–4327. DOI: 10.1364/OE.15.004321.

[79] Yuishi Takeno et al. "Observation of -9 dB quadrature squeezing with improvement of phase stability in homodyne measurement". *Opt. Express* 15.7 (Apr. 2007), pp. 4321–4327. DOI: 10.1364/OE.15.004321.

[80] M. Tse et al. "Quantum-Enhanced Advanced LIGO Detectors in the Era of Gravitational-Wave Astronomy". *Phys. Rev. Lett.* 123 (23 2019), p. 231107. DOI: 10.1103/PhysRevLett.123.231107.

[81] Henning Vahlbruch et al. "Coherent Control of Vacuum Squeezing in the Gravitational-Wave Detection Band". *Physical Review Letters* 97.1 (July 2006). DOI: 10.1103/physrevlett.97.011101.

[82] Henning Vahlbruch et al. "Detection of 15 dB Squeezed States of Light and their Application for the Absolute Calibration of Photoelectric Quantum Efficiency". *Phys. Rev. Lett.* 117 (11 Sept. 2016), p. 110801. DOI: 10.1103/PhysRevLett.117.110801.

[83] Marco Vardaro. "Toward a fully automated and digitally controlled squeezed vacuum source for gravitational wave detectors". PhD thesis. Università degli studi di Padova, 2018.

[84] R. M. Waxler and G. W. Cleek. "The Effect of Temperature and Pressure on the Refractive Index of Some Oxide Glasses". *Journal of research of the National Bureau of Standards. Section A, Physics and chemistry* 77A 6 (1973), pp. 755–763.

[85] Min Jet Yap et al. *Generation and control of frequency dependent squeezing via EPR entanglement*. 2020. DOI: 10.1038/s41566-019-0582-4.

[86] Jean-Pierre Zendri, Jean-Francois Cohadon, Fulvio Ricci, et al. "Advanced Virgo Squeezer Technical Design Report". *Internal report (VIR-0411C-15* (2016).

[87] Yuhang Zhao et al. “Frequency-Dependent Squeezed Vacuum Source for Broadband Quantum Noise Reduction in Advanced Gravitational-Wave Detectors”. *Phys. Rev. Lett.* 124 (17 Apr. 2020), p. 171101. DOI: 10.1103/PhysRevLett.124.171101.

Appendix A

Quantum mechanics in a nutshell: formalism

The symbol $|-\rangle$ or *ket* represents the state of a system, for example the state of polarization of a photon. The state kets are vectors from a complex vector space, the *Hilbert space* so adding vectors is possible with complex coefficients. This vector space can thus be described through linear superposition of n orthogonal basis kets, n being the dimension of the system [19]. For orthogonality purpose, *Bra* vectors, referred as $\langle -|$ are introduced and are related with ket vectors by the *hermitian conjugate*, written as the "dagger" symbol †. This operation is similar to the complex conjugate and can be written as:

$$z^* \langle x| = (z|x\rangle)^\dagger \tag{A.1}$$

where z is just a complex number. $\langle x|y\big|x|y\rangle$, referred as a *bracket* is similar to the dot product in real vector spaces of $\langle x|$ and $\big|y\rangle$.

To understand the physical meaning of this formalism, we assume a system in the state $\big|\phi\rangle$ and want to know with our analyzer if this state is in the state $|\sigma\rangle$, we define the probability P, equal to:

$$P = |\langle \phi \big| \sigma \rangle|^2 \tag{A.2}$$

and represents the probability amplitude for the state $\big|\phi\rangle$ to be in the state $|\sigma\rangle$ and is generally a complex number. If the state $\big|\phi\rangle$ and $|\sigma\rangle$ are orthogonal states, the probability is equal to zero if the system was in state $|\sigma\rangle$.

The **commutator** of two operators $\hat{x}$ and $\hat{y}$ is an operator defined by:

$$[\hat{x}, \hat{y}] = \hat{x}\hat{y} - \hat{y}\hat{x} \tag{A.3}$$

Two observables $\hat{A}$ and $\hat{B}$ commute when their commutator is null, which means that "measuring"(in the sense of the mean value) $\hat{A}$ then $\hat{B}$ will give the same physical state than the one obtained by measuring $\hat{B}$ then $\hat{A}$.

An **observable** or *Hermitian operator* is an operator whose mean value on a physical state is always real. To understand the difference between classical mechanics and quantum mechanics, let's take an example of an observable quantity, the position of a photon, referred as the variable x. In classical mechanics, x is just a number, that may varies in function of different parameters such as time and that can be measured in a dedicated experiment. However, in quantum mechanics, we are dealing with the position operator, called $\hat{x}$ describing the type of measurement and the *kets*, such as $|\phi\rangle$ which contain the information of the possible outcomes of a dedicated experiment. The average value of an observable is thus:

$$\langle \hat{x} \rangle = \langle \phi | \hat{x} | \phi \rangle \tag{A.4}$$

The equation A.4 make predictions on the average value of measurements of the observable represented by the operator $\hat{x}$, for a large number of measurements prepared in the state $|\phi\rangle$.

The variance of an observable at a state $|\phi\rangle$ is defined as:

$$\left\langle \Delta \hat{x}^2 \right\rangle = \left\langle \phi \middle| \hat{x}^2 | \phi \right\rangle - \langle \phi | \hat{x} | \phi \rangle^2 \tag{A.5}$$

Appendix B

Mechanical drawings

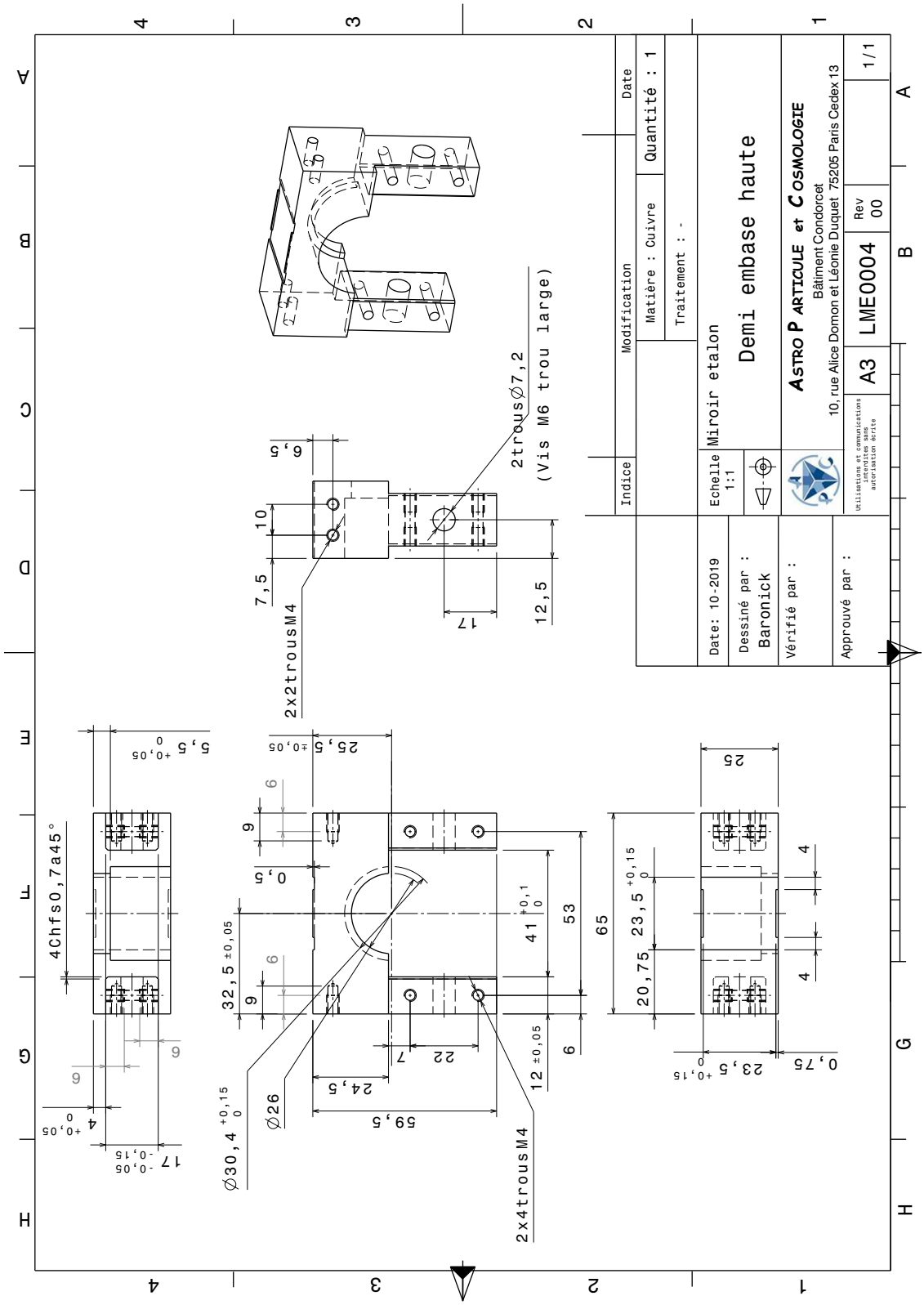

Figure B.1 – Mechanical drawing of the upper part of the etalon holder (in copper), by Jean-Pierre Baronick.

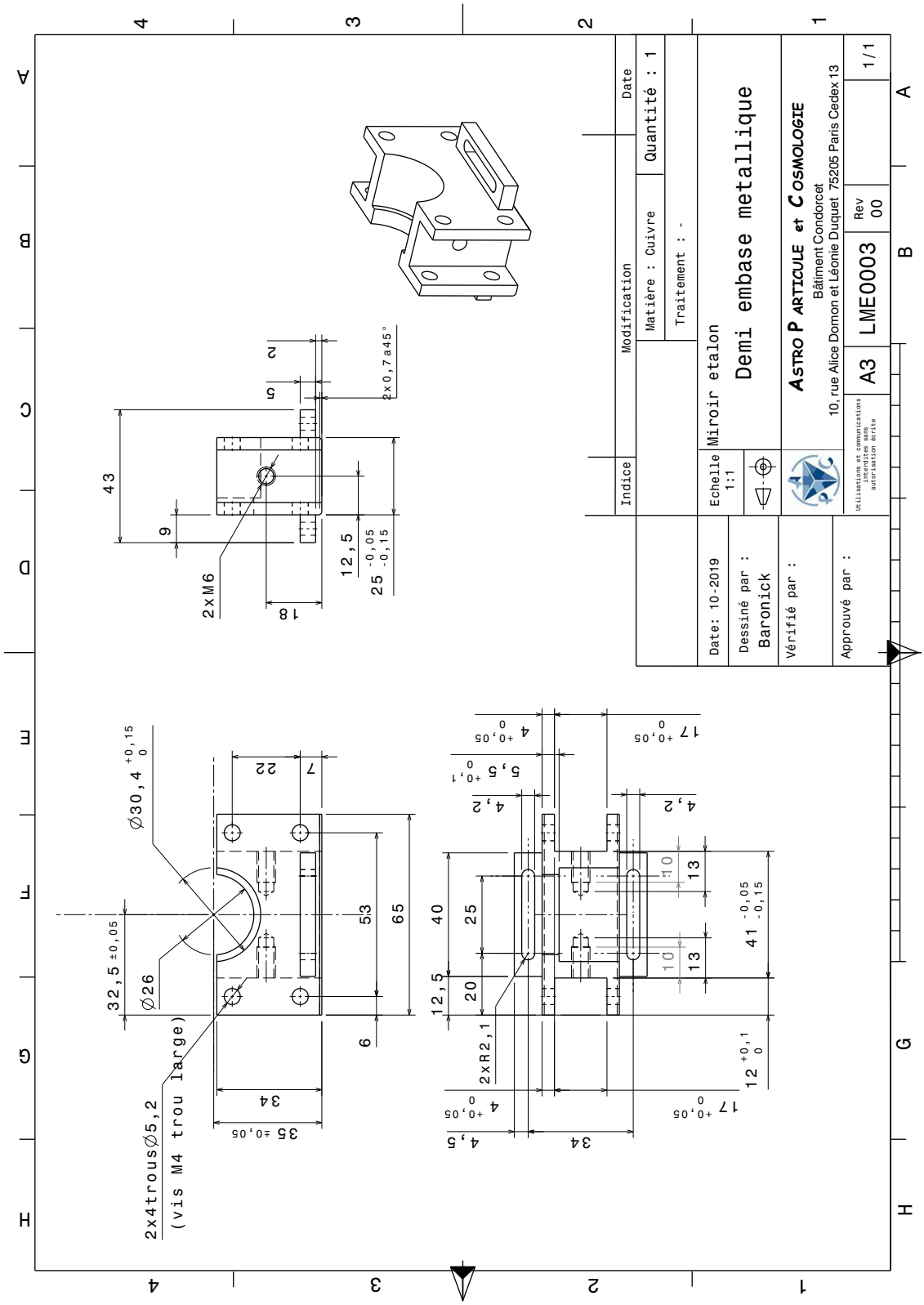

Figure B.2 – Mechanical drawing of the bottom part of the etalon holder, by Jean-Pierre Baronick.

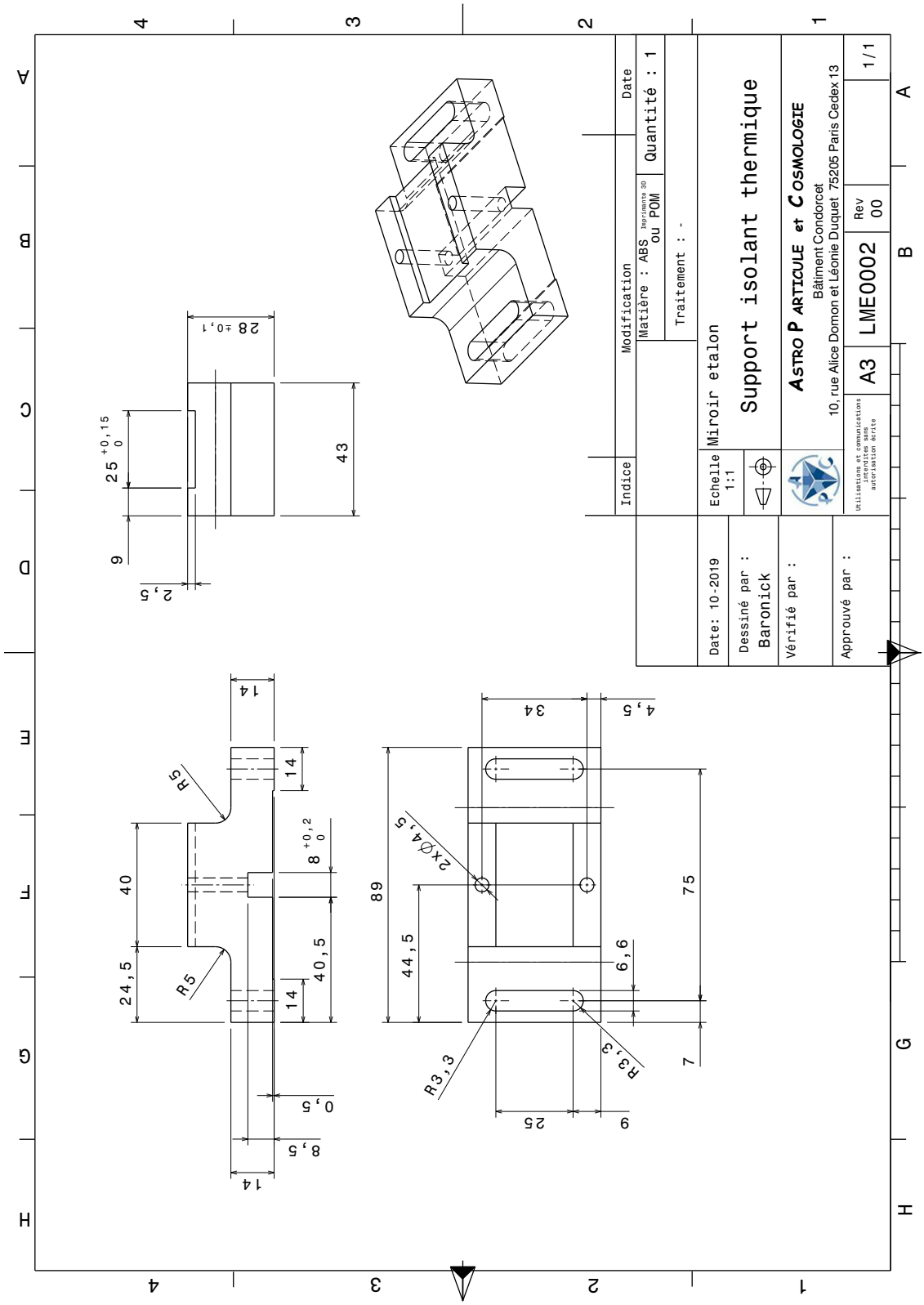

Figure B.3 – Mechanical drawing of the base in ABS, by Jean-Pierre Baronick.

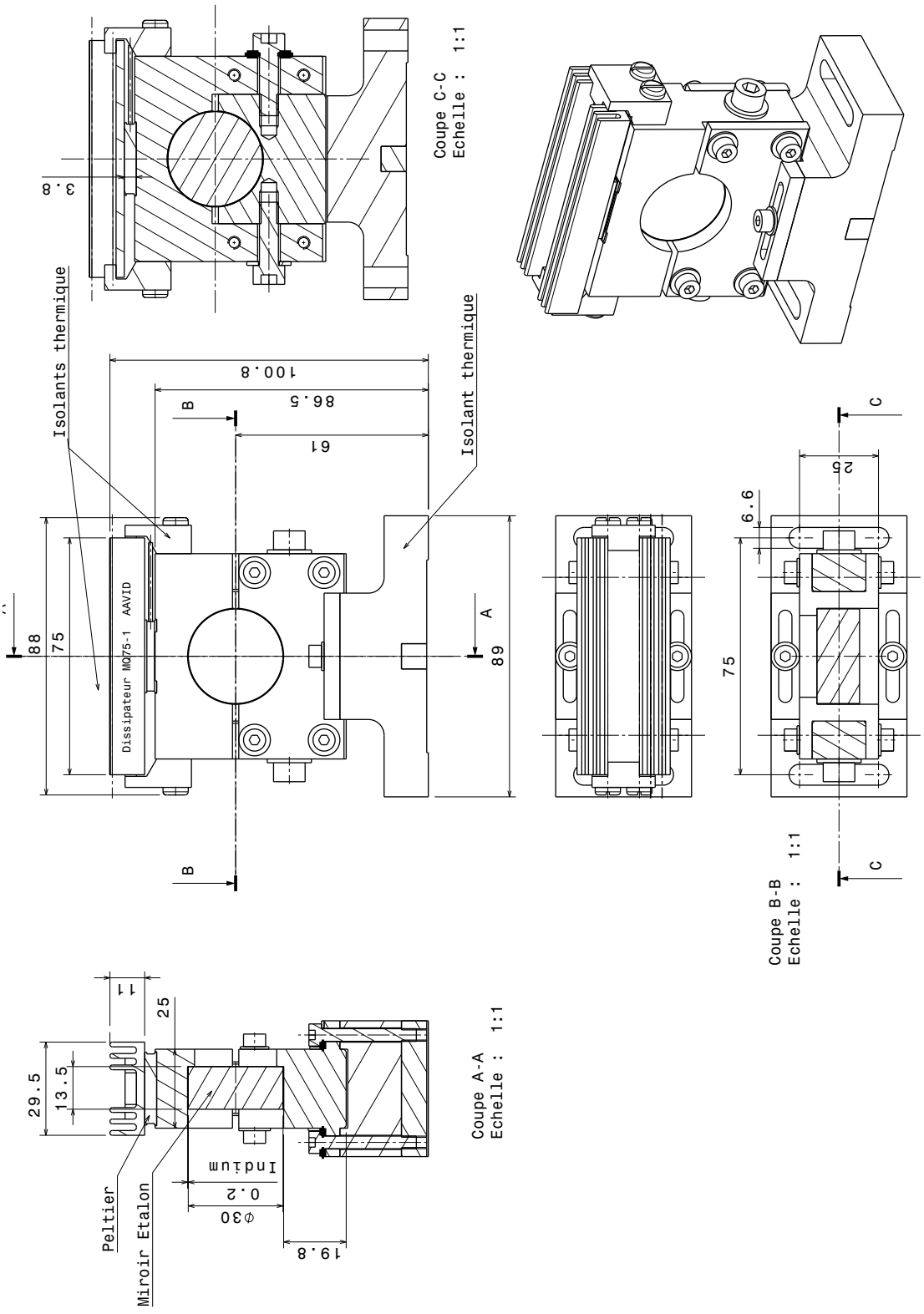

Figure B.4 – Mechanical drawing of the mounted etalon with the holder in copper, the base in ABS and the cooler, by Jean-Pierre Baronick.